Francis Leonard Deepak · Alvaro Mayoral
Raul Arenal *Editors*

Advanced Transmission Electron Microscopy

Applications to Nanomaterials

Springer

Advanced Transmission Electron Microscopy

Francis Leonard Deepak • Alvaro Mayoral
Raul Arenal
Editors

Advanced Transmission Electron Microscopy

Applications to Nanomaterials

Springer

Editors
Francis Leonard Deepak
International Iberian Nanotechnology Laboratory
Braga, Portugal

Raul Arenal
Advanced Microscopy Laboratory
Nanoscience Institute of Aragon
University of Zaragoza
Zaragoza, Spain

Alvaro Mayoral
Advanced Microscopy Laboratory
Nanoscience Institute of Aragon
University of Zaragoza
Zaragoza, Spain

ISBN 978-3-319-15176-2 ISBN 978-3-319-15177-9 (eBook)
DOI 10.1007/978-3-319-15177-9

Library of Congress Control Number: 2015939736

Springer Cham Heidelberg New York Dordrecht London

Printed on acid-free paper

Springer International Publishing AG Switzerland is part of Springer Science+Business Media (www.springer.com)

Preface

The book entitled *Advanced Transmission Electron Microscopy: Applications to Nanomaterials* is an effort to try to bring an update in the field of nanomaterials that have been explored employing *state-of-the-art* electron microscopic techniques. Electron microscopy has undergone remarkable changes since the invention of the transmission electron microscope (TEM) in 1931 by Max Knoll and Ernst Ruska (Nobel Prize in Physics 1986). The invention of the TEM was a major significant effort to move forward, in terms of spatial resolution, from optical microscopes that were predominant in that era. The efforts and achievements in the field of aberration corrected microscopes would not have happened today if not for the vision of Otto Scherzer who predicted that the limiting factor in the resolution of the microscopes originated from spherical and chromatic aberrations (*Spherical and Chromatic Correction of Electron Lenses*, *Optik*, 1947 and *J. Appl. Phys.*, 1949). The dream of imaging atoms without the "blur" of the optics owes its efforts to several people and projects in this field. The importance on several such developments and building of new prototype corrector optics as well as providing the theoretical and experimental understanding towards achieving atomic resolution has been highlighted with the award of the Wolf prize in Physics (2011) to Harald Rose, Maximilian Haider, and Knut Urban.

In parallel, there have been significant advances in the development of analytical methods—EDS and EELS, 3D techniques, electron tomography, in situ electron microscopy, advances in sample preparation, data detection, monochromators, etc. Simultaneously, there has been an explosion in the kind of materials that are being explored under the electron microscope to obtain both qualitative and quantitative information. The materials include carbon in all kinds of forms, boron nitride, and other carbon-based nanomaterials, metal, and metal oxide nanoparticles, highly beam-sensitive structures: zeolites and mesoporous materials; all of it with the final purpose of pushing the information limit down to the single structural bricks conforming matter that is the single atoms (or atomic column). Owing to this kind of information, many properties which remained unknown until now can be explained better than before, thereby allowing for enhanced material design.

The chapters in this book have been organized in order to bring an update to the field both in terms of the advanced techniques as well as to enhance the understanding of nanomaterials under the electron microscope.

The first chapter *Aberration Corrected Electron microscopy of Nanoparticles* (Miguel José Yacamán, Ulises Santiago, and Sergio Mejía-Rosales) provides an introduction to the field of electron microscopy, spectroscopy, diffraction, and aberration-corrected electron microscopy. This chapter highlights the significant historical advances that have been made in the field of transmission electron microscopy and highlights a few specific examples related to clusters and nanoparticles. This is followed by the chapter entitled *Electron Diffraction and Crystal Orientation Phase Mapping Under Scanning Transmission Electron Microscopy* (Francisco Ruiz-Zepeda, J. Alejandro Arizpe-Zapata, Daniel Bahena, Arturo Ponce, and Domingo Garcia) which highlights the use of STEM for purposes of electron diffraction and phase mapping of nanostructured and thin film materials. The subsequent chapter *Advanced Electron Microscopy in the Study of Multimetallic Nanoparticles* (Nabraj Bhatatrai, Subarna Khanal, J. Jesus Velazquez-Salazar, and Miguel Jose-Yacaman) explores the area of bimetallic/multimetallic nanoparticles as investigated by advanced electron microscopic techniques. The fourth chapter *Zeolites and Ordered Mesoporous Materials Under the Electron Microscope* (Alvaro Mayoral, Yasuhiro Sakamoto, and Isabel Diaz) deals with the most important heterogeneous catalysts which are the zeolites. In addition, it also covers the other big family of ordered porous structures, silica mesoporous materials, showing the capabilities of advanced electron microscopy methods to tackle the problem of the beam-sensitive materials. The fifth chapter *Local TEM Spectroscopic Studies on Carbon- and Boron Nitride-Based Nanomaterials* (Raul Arenal and Odile Stephan) explores local spectroscopy (including chemical analyses and the study of physical properties) on nanostructures based on carbon and other related materials (boron nitride, BxCyNz). The sixth chapter *3D-Nanometric Analyses via Electron Tomography: Application to Nanomaterials* (Simona Moldovan, Raul Arenal, and Ovidiu Ersen) provides a critical update in the field of electron tomography, while the seventh chapter *In Situ TEM of Carbon Nanotubes* (Pedro M. F. J. Costa and Paulo J. Ferreira) provides a current update in the field of in situ electron microscopy studies that have been carried out focusing especially on carbon nanotubes. The final chapter *Physical Characterization of Nanomaterials in Dispersion by Transmission Electron Microscopy in a Regulatory Framework* (Jan Mast, Eveline Verleysen, and Pieter-Jan De Temmerman) addresses the different steps required to analyze dispersed nanomaterials to obtain homogeneous and stable dispersions of colloidal nanomaterials and powders while exploring a descriptive, qualitative as well as quantitative analysis on the TEM images.

It is hoped that this book will be suitable not only for an audience that uses advanced electron microscopic techniques in their current day-to-day investigations of nanomaterials for various applications but also for materials scientists, physicists, and chemists who carry out active research in nanoscience and nanotechnology. In addition, the topics and the chapters, which are written by the various authors, are aimed at a beginner who intends to pursue such investigations for his/her study. Finally, there is a tremendous and significant pileup of new information in terms of advances in instrumentation, techniques, methodologies, etc. and we have sought to address some of these major topics that we thought necessary to highlight at the present point of time.

Braga, Portugal — Francis Leonard Deepak
Zaragoza, Spain — Alvaro Mayoral
Zaragoza, Spain — Raul Arenal

(All the Editors contributed equally to the final output of this book).

Contents

About the Editors

Raul Arenal received his Ph.D. in Solid State Physics from Univ. Paris-Sud (Orsay, France, 2005) and in 2013, he obtained his Habilitation (HDR) also at this University. In 2007, he became research scientist (chargé de recherches) at the CNRS (France), working at the LEM, CNRS-ONERA (Chatillon, France). Since 2012, Dr. Arenal is on leave from the CNRS, and he is currently ARAID research scientist at the LMA—INA of the Universidad de Zaragoza (Spain). His broad area of research interest lies in electron microscopy focused on materials science and nanoscience: TEM (HR(S)TEM, electron diffraction, EELS), as well as in Raman spectroscopy. These studies are mainly focused on the growth mechanism, structural and physical (electronic, optical, vibrational, mechanical) properties of nanomaterials based on carbon, boron, and nitrogen as well as other nanostructures.

Francis Leonard Deepak received his Ph.D. in 2005 from Jawaharlal Nehru Centre for Advanced Scientific Research, Bangalore, India. Subsequently, he was a post-doctoral fellow (2006–2008) at the Weizmann Institute of Science, Israel. He joined the International Iberian Nanotechnology Laboratory (INL) Braga, Portugal, in 2009 as a research fellow. Since 2013, he is a Staff Researcher and currently leads the Advanced Electron Microscopy Group at INL. His broad area of research is focused on the use of advanced electron microscopic techniques (Aberration Corrected TEM/STEM, Analytical Electron Microscopy, and Electron Diffraction) in the investigation of materials/nanomaterials for catalytic as well as other applications. He also employs the Focused Ion Beam (FIB) technique extensively in the investigations of nanodevices.

Alvaro Mayoral obtained his degree in Chemistry by the University of Alcala (Spain) in 2003; he was awarded with the Ph.D. title by the University of Birmingham in 2009 studying the production of metal nanowires from different porous structures such as zeolites and ordered mesoporous structures. Afterwards, he moved to the University of Texas at San Antonio where he worked with Prof. Miguel Yacaman on the synthesis and characterization of noble metal nanoparticles for applications in catalysis and cancer treatment. Since June 2010, Dr. Mayoral belongs to the Advanced Microscopy Laboratory within the Nanoscience Institute of Aragon at the University of Zaragoza. His research is now mainly focused on the observation of nanocatalysts under the electron microscope and the application of the most advanced techniques into the observation of beam-sensitive materials.

Chapter 1
Aberration-Corrected Electron Microscopy of Nanoparticles

Miguel José Yacamán, Ulises Santiago, and Sergio Mejía-Rosales

1.1 Introduction to Electron Microscopy

1.1.1 Beginnings

The very rich history of electron microscopy started with the discovery of the duality wave–particle. In the 1920s, the beginning of the twentieth century, it was shown that electrons could also behave as a wave. The optical microscopy based on Abbe's theory already achieved the resolution limit $\sim \lambda / 2 \sim 2{,}500\text{Å}$. The electrons are located at high voltages and hence will have much shorter wavelengths ~0.05 Å. Therefore, since occasionally Abbe's theory also holds for electromagnetic lenses, a sub-Å resolution could be achieved, and atomic resolution will be possible. The job to build an electron microscope was passed from the physicists to the electric engineers. Shortly after obtaining his doctoral degree, Ernst Ruska took the job. As Ruska describes in his Nobel lecture,

> After having shown in my Studienarbeit of 1929 that sharp and magnified images of electron-irradiated hole apertures could be obtained with the short coil, I was now interested in finding out if such images—as in light optics—could be further magnified by arranging a second imaging stage behind the first stage. Such an apparatus with two short coils was easily put together and in April 1931 I obtained the definite proof that it was possible. This apparatus is justifiably regarded today as the first electron microscope even though its total magnification of $3.6 \times 4.8 = 14.4$ was extremely modest. [1]

M.J. Yacamán (✉) • U. Santiago
Department of Physics and Astronomy, University of Texas at San Antonio,
One UTSA Circle, San Antonio, TX 78249, USA
e-mail: miguel.yacaman@utsa.edu

S. Mejía-Rosales
Facultad de Ciencias Físico Matemáticas, Universidad Autónoma de Nuevo León,
San Nicolás de los Garza, Nuevo León 66455, Mexico

F.L. Deepak et al. (eds.), *Advanced Transmission Electron Microscopy*,
DOI 10.1007/978-3-319-15177-9_1

The first industrial electron microscope built by Ruska's team at the Siemens labs was a microscope with a very disappointing practical performance (see Fig. 1.1). The resolution was worse than that of an optical microscope, even when, as Ruska and Knoll had already calculated in 1932, the theoretical resolution limit for a 75 kV transmission electron microscopy (TEM) was close to 2.2 Å [2]. The need of vacuum severely limited the study of biological material, and in addition the vacuum techniques at the time provided contamination on the sample by hydrocarbons deposited on the sample. However, Ruska demonstrated that the possibility of building a TEM was a concrete reality. Ruska's original design included the basic setup present in past and present electron microscopes that in essence was the same as of an optical microscope: a beam source, a condenser lens, an aperture control, a specimen stage, and an image plane where a photographic plaque could be impressed. After the Second World War when scientists were finally able to retake the low resolution problem, the road map was very clear:

- Improve the electron emission.
- Improve the electro-optics to reduce aberrations such as astigmatism, coma, and others.
- Improve the vacuum and make it cleaner.
- Develop techniques to prepare samples.

Electron emission was obtained (and still *is* in many systems) using a thermionic source, where a filament is heated to the point of emitting electrons. These electrons are accelerated by a potential difference between the filament and an anode. The electron beam is made convergent by the use of an electrostatic lens—the *Wehnelt* cylinder, as it is called. Two intrinsic limitations in the use of thermionic emission guns are that the electron beam is not monochromatic and that there is a practical limit to the current density imposed by the melting point of the materials of which the cathode filament is made of. On Ruska's time, all of the electron microscopes used tungsten filaments. One of the most important improvements in electron emission was the substitution of tungsten by lanthanum hexaboride (LaB_6), which gives a substantially higher current density operating at lower temperatures [3].

Another considerable improvement in the performance of the electron emission in TEM was the use of field emission sources that give a more monochromatic beam than thermionic sources and increase the current density several orders of magnitude. Field emission guns take advantage of the principle that an electric field produced by a potential difference is considerably large in pointy ends of a material. This increase in electric field can be enough for electron to tunnel out of the material. The main problem with field emission guns is their cost, since they have to be structurally strong enough to handle inner stress and the material has to be highly monocrystalline and well oriented to perform optimally. The use of magnetic lenses into the gun brings a more focused beam, which is particularly important in scanning techniques.

As in any microscopy equipment (electron based or otherwise), aberrations affect tremendously the resolution capabilities of the equipment. Chromatic aberration is directly related to the kind of electron gun being used, but these aberrations are not difficult to correct using magnetic quadrupoles [4]. More critical from the technological point of view are the spherical aberrations that are usually related to

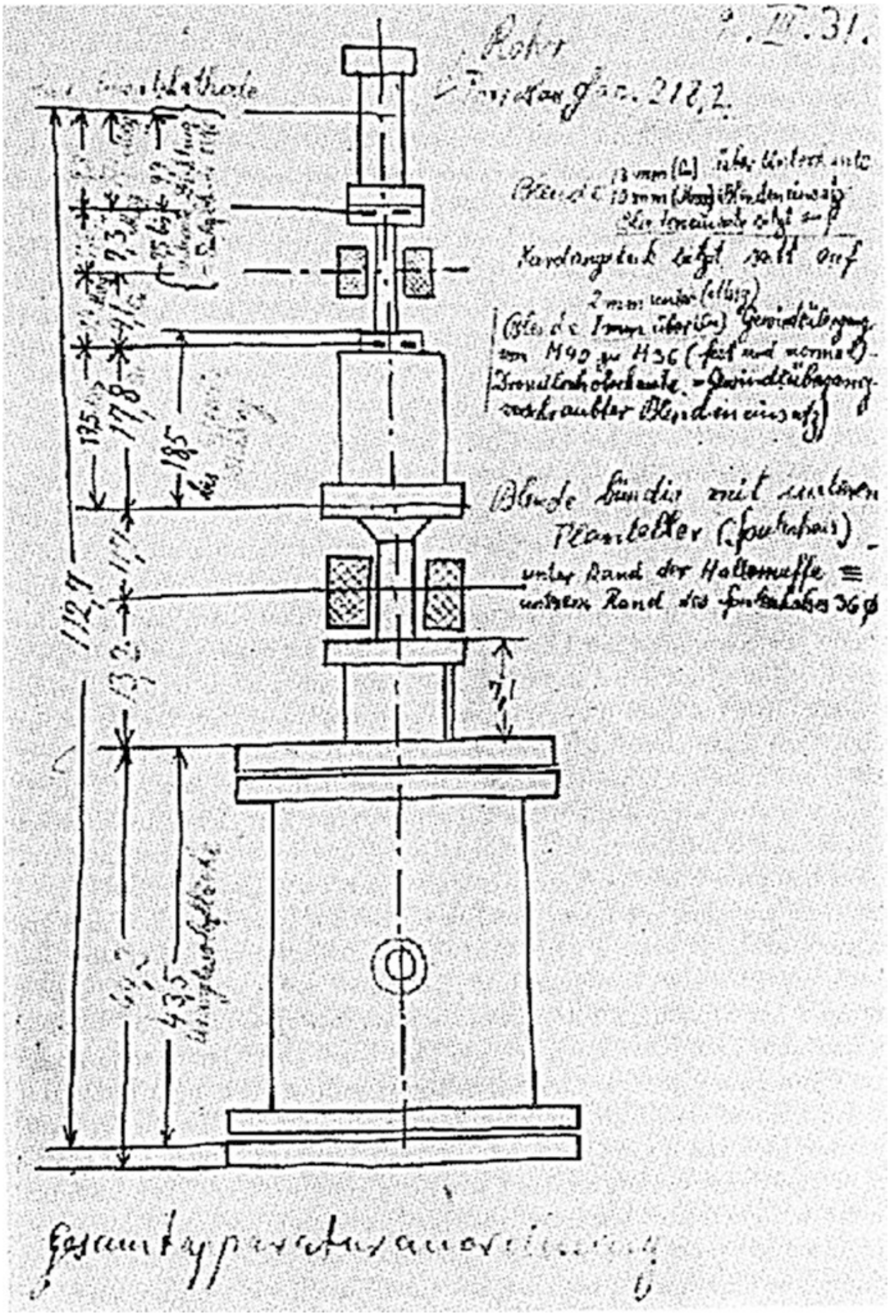

Fig. 1.1 Sketch by Ernst Ruska, dated 9 March 1931 of the cathode ray tube for testing one-stage and two-stage electro-optical imaging by means of two magnetic electron lenses (electron microscope). Source: Nobelprize.org Copyright © The Nobel Foundation (1986)

imperfections on the objective lens and may limit the resolution of the microscope to the degree of making atomistic resolution impossible. Some improvements were proposed to control spherical aberration in the 1950s, but the technology to truly avoid aberrations would not be developed until several decades later.

Vacuum may be a critical issue from two different standpoints. First, if a field emission source is being used, a way of avoiding contamination of the tip is to keep it operating in vacuum. Second, the path of the electron beam should be kept in vacuum to avoid the electrons to be scattered by the air molecules. Vacuum techniques have experienced great advances in the last decades, but even on the early stages of electron microscopy, the use of powerful mechanical pumps improved greatly the performance of the microscopes.

Simultaneously with the development of the instrument, the preparation of TEM specimens was refined. Samples were meticulously prepared using slicing and dimpling techniques that allow to get thin areas that were basically transparent to the electron beam. Ion beam techniques were and still are used to remove contaminants from the sample's surface.

By the mid-1950s, it was possible to design microscopes with a much better resolution, clean vacuum, and better illumination using double condenser lenses. Probably the most significant discovery was the first direct observation of dislocation on a metal by Hirsh and its group (then at Cambridge). That was the culmination of the work of Orowan, Polanyi, and Taylor (who postulate the edge dislocations), of Burgers (that predicted the screw dislocation), and of Frank and Reed who provided a mechanism to multiply dislocations [5]. The impact of these discoveries was monumental. In less than a half century, researchers were able to explain metallurgical problems that had remained unsolved for more than 3,000 years. Thanks to those researchers metallurgy became truly a science and the mankind was now ready for developing new materials with "on-demand" properties. The amazing fact is that no big publicity was made on those discovering in contrast with the discoveries on quantum mechanics. No Nobel Prize was ever awarded on those discoveries. Later in the mid-1960s, researchers had available very robust mechanics with a resolution better than 10 Å and with a great number of attachments such as goniometers, cold and heating stages, tensile stress stages, and so on. The preparation techniques were much improved. The theoretical foundations of image contrast were established, and it was possible for the first time to simulate electron microscope images.

By the mid-1980s, the resolution was improved to ~2 Å or better. It was possible to obtain atomic column images under the right focusing conditions and for very thin specimens. The multislice theoretical approach of Cowley and Moodie [6] had opened the way to a serious comparison of experimental and theoretical images. Between 1970 and 1985, electron microscopy was used in many research areas, and thousands of materials and biological problems were solved using TEM. A lot of the rapid progress on electronic materials can be attributed to the availability of TEM.

Perhaps one of the most celebrated discoveries was the carbon nanotubes by Sumio Iijima [7] which was one of the detonators of nanotechnology. During the 1990s, the electron microscope became a powerful analytical machine. The introduction of field emission guns provided enough electron current for the X-ray analysis (EDS) and the electron energy loss spectroscopy (EELS) to become standard techniques. They both save a great impulse to electron microscopy, and by the end of the century, electron microscopy and X-ray diffraction became the canonical techniques to characterize materials.

On the biological front, electron microscopy has been also a key technique. Back in 1665, the physicist Robert Hooke described the cells using an earlier optical microscope. That opened a brilliant era of discoveries using optical microscopes. After the discovery of the TEM, the impact has been very important. Practically all the cellular organelles (mitochondria, Golgi, vacuoles, and vesicles) were discovered using TEM. This was due to the staining methods of Claude and Palade plus the development of ultramicrotoming. The use of TEM allowed the understanding of the functional organization of the cell and was a cornerstone of the development of modern cell biology. The development of cold stages and preparation methods resulted in the cryo-electron microscopy. This has been a fundamental technique to study viral ultrastructure. Combined with electron tomography, cryo-TEM has shown how viral structural components fit together. The electron microscopy has been historically very important and has led to the discovery of new viruses such as the first image of polioviruses or the parvovirus, most intestinal virus, and very long list of others [8–11].

In the last few years, a quantum leap on the capabilities has unfolded mostly due to the development of aberration-corrected microscopy. We will describe it in the next few sections.

1.1.2 Aberration-Corrected Microscopy

In general, any optical instrument can be considered that transfers information from the object to a recording device (photographic plate or CCD or any other recording device). If the transfer is perfect, we will have true information from the object. The final image can be magnified (microscope) or demagnified (telescope) or with no magnification (our eyes). In the case of our eyes, any physical deformity will lead to a blur on the image. In this case, we can easily correct all the aberrations of the eye by making a glass with that proper combination of divergent and convergent lenses. The same is true for the optical microscopes. In the case of the electron microscopy for almost 70 years, divergent lenses were not available. However, during the last decade of the twentieth century, there was a monumental advance on the electron optics, and hexapole and octupole lenses were available [12–14]. The key advance in modern microscopy is the aberration-corrected TEM and STEM.

One of the great minds of the twentieth century Richard P. Feynman said in his famous talk in 1959 in an American physical society meeting [15, 16]:

> “The electron microscope is not quite good enough, with the greatest care and effort; it can only resolve about 10 angstroms. I would like to try and impress upon you while I am talking about all of these things on a small scale, the importance of improving the electron microscope by a hundred times. It is not impossible; it is not against the laws of diffraction of the electron. The wavelength of the electron in such a microscope is only 1/20 of an

> angstrom. So it should be possible to see the individual atoms. What good would it be to see individual atoms distinctly? We have friends in other fields—in biology, for instance. We physicists often look at them and say, "You should use more mathematics like we do." They could answer us—but they're polite, so I'll answer for them: "What you should do in order for us to make more rapid progress is to make the electron microscope 100 times better and continued" The reason the electron microscope is so poor is that the f-value of the lenses is only 1 part to 1,000; you don't have a big enough numerical aperture. And I know that there are theorems which prove that it is impossible, with axially symmetrical stationary field lenses, to produce an f-value any bigger so and so; and therefore the resolving power at the present time is at its theoretical maximum. But in every theorem there are assumptions. Why must the field be axially symmetrical? Why must the field be stationary? Can't we have pulsed electron beams in fields moving up along with the electrons? Must the field be symmetrical? I put this out as a challenge: Is there no way to make electron microscope more powerful?"

To meet the Feynman Challenge will mean to construct a microscope with a resolution of 0.1 Å or 10 pm. Commercial instruments have not reached the 50 pm level. It is not clear that it will be possible to reach the 10 pm, and some debate exists [17, 18]. However, it is clear that there are no materials with interatomic distances <50 pm. That means that most (if not all) of the material science problems can be solved using a 50 pm resolution microscope. In the following sections are the physical principles of aberration correction.

1.1.3 TEM Aberration Correction

We can consider (as in Fig. 1.2) that if the incident beam goes through that sample, the exit wave will be $\psi_{\text{exit}}(r)$, with r being the coordinates in real space. The exit wave is formed by scattered beams of wave vector k_g (g is a reciprocal lattice vector). All the beams will be focused by the objective lens to a single spot on the back focal plane. The wave function on the back focal plane is the superposition of the individual beams and is given as

$$\psi_{\text{back}}(q) = F\left[\psi_{\text{exit}}(r)\right] = \phi(q) \tag{1.1}$$

where F denotes the Fourier transform and q is the coordinates on the reciprocal space. Now we can recover the original wave function as

$$\psi(r) = F^{-1}\left[\psi_{\text{exit}}(q)A(q)\right] \tag{1.2}$$

where F^{-1} denotes the inverse Fourier transform and $A(q)$ is a function that describes the behavior of the lenses. In a perfect microscope, $A(q)=1$. Since the

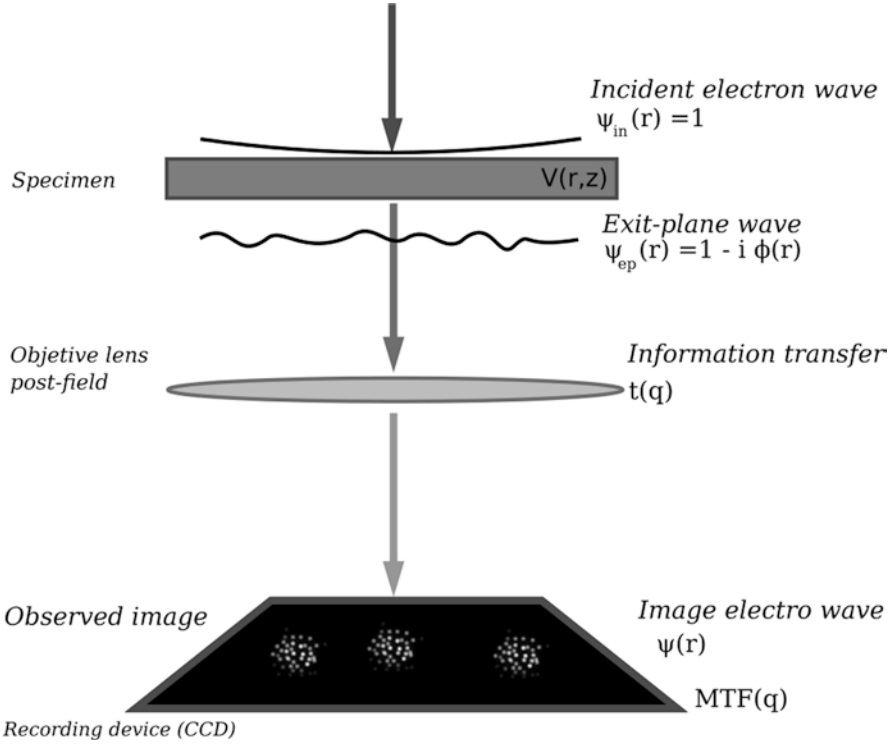

Fig. 1.2 The information transfer diagram in an electron microscope

product of two functions in Fourier space is equal to the convolution of the same two functions in real space, our final expression for the wave function is

$$\psi(r) = \psi_{\text{exit}}(r) \otimes A(r). \tag{1.3}$$

And the intensity on the image is

$$I = |\psi(r)|^2. \tag{1.4}$$

This equation is independent of the approximation used for calculating the $\psi_{\text{exit}}(r)$. Now we focus our attention in $A(q)$. This function has been calculated for the case of coherent images as

$$t_i(q) = \exp\left\{-\frac{2\pi i}{\lambda}\chi(q)\right\} \tag{1.5}$$

where

$$\chi(q) = \frac{1}{2}\theta^2 \Delta f + \frac{1}{4}\theta^4 C_3 \tag{1.6}$$

where Δf is the defocus and $\theta \approx q\lambda$ is the scattering angle, and C_3 is the third-order spherical aberration. Equation (1.6) is valid when only isotropic aberration, defocus, and spherical aberration are present. However, if the microscope has an aberration corrector, then, since C3 » 0, other aberration terms might become significant, such as the fifth-order spherical aberration; in a case like this, Eq. (1.5) would still be valid, but the function $\chi(q)$ should include a more general aberration function. In this case, additional axial aberrations need to be considered. The expression is much more complex, and if one takes up to the seventh order of aberration, we can have up to 44 coefficients which have to be taken into account including astigmatism, spherical aberration, axial coma, and star, rosette, and chaplet aberration. For a full analysis, we refer the reader to the excellent book by Erni [19].

Figure 1.3 shows the plot of the χ function for different cases (corrected and uncorrected TEM) as a function of the scattering angle.

We can modify the equation χ, in the first approximation as

$$\chi(q) = \frac{1}{2}\theta^2 \Delta f + \frac{1}{4}\theta^4 C_3 + \frac{1}{6}\theta^6 C_5 \tag{1.7}$$

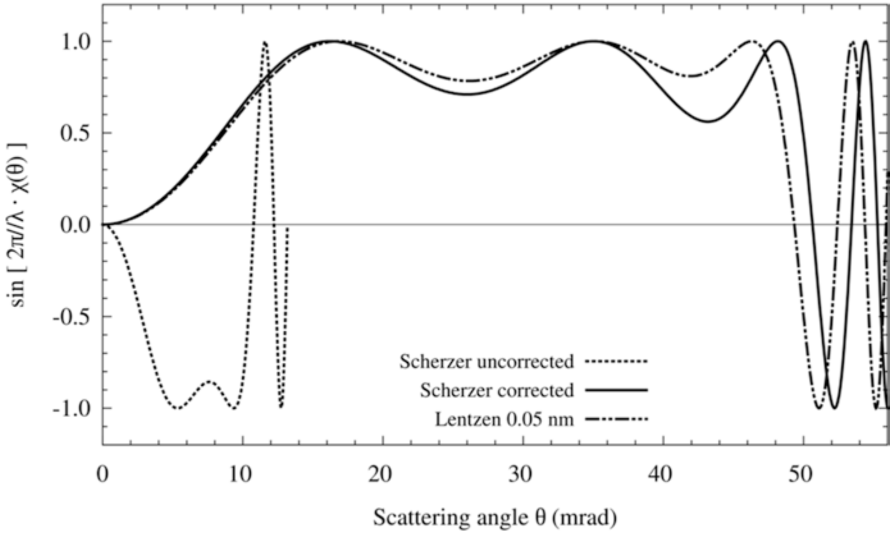

Fig. 1.3 Plot of the contrast transfer function χ for TEM. Different conditions corresponding to Scherzer condition for the corrected and uncorrected case and the Lentzen condition for the corrected case are shown

where we have included the fifth-order spherical aberration C_5. We have now a flexible situation. Even if C_3 and C_5 are zero, we can still get phase contrast with the defocus ±0. On the other hand, we can make C_3 positive or negative, and we can adjust for different frequencies to be transferred. A particularly important condition for optimum contrast is the Scherzer focus for a corrected microscope which is given by (1.9):

$$\begin{aligned} \Delta f_{\text{Scherzer}} &= A_1 \sqrt[3]{\lambda^2 C_5} \\ C_{3\text{Scherzer}} &= -A_2 \sqrt[3]{\lambda C_5^2} \end{aligned}. \tag{1.8}$$

A_1 and A_2 are constants with the values around 2 and 3.2, respectively. Lentzen [20] has proposed a different set of values of the defocus. We have added in Fig. 1.2 the contrast transfer under Scherzer conditions in an aberration-corrected TEM. In any case, it is clear that aberration correction and the possibility of adjusting C_3 and C_5 give an extra capability to the microscope. An image of a corrected and uncorrected Si crystal is shown in Fig. 1.4.

An additional important advantage of aberration-corrected TEM (shown in Fig. 1.5) is that in the case of bent samples, which is a common case due to sample preparation, it is possible to compensate by beam tilt without introducing extra aberrations.

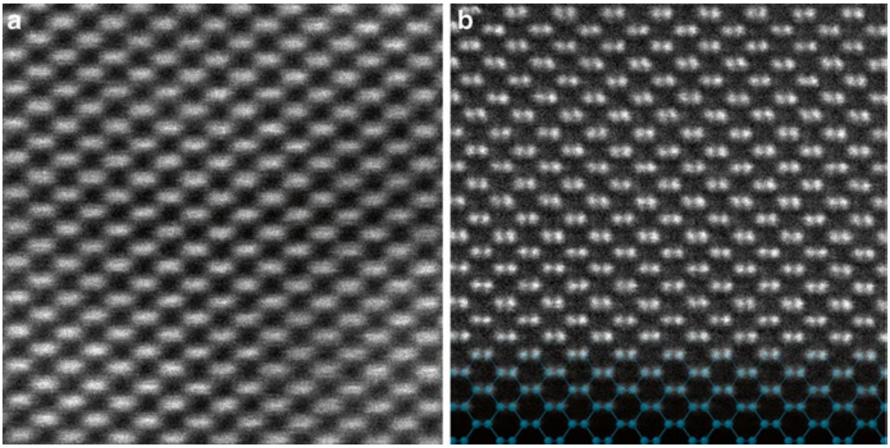

Fig. 1.4 Image of an uncorrected (**a**) and corrected (**b**) Si crystal. Dumbbells separated at 1.3 Å in silicon [110]

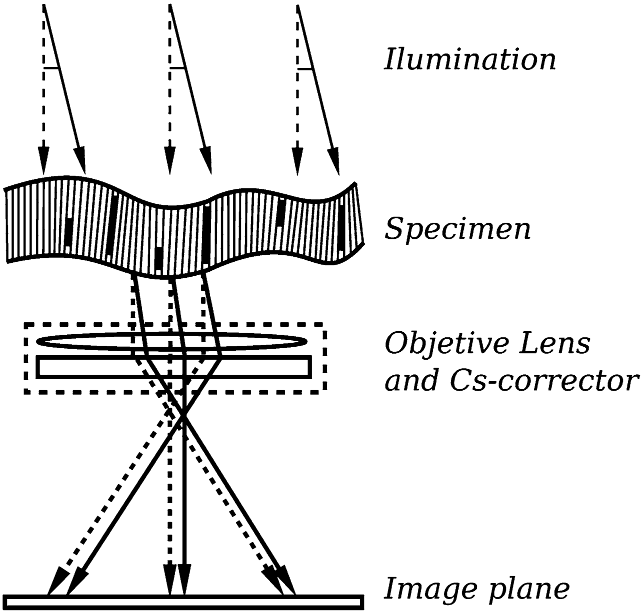

Fig. 1.5 Schematic representation of aberration-corrected HRTEM. In the case of bend samples, it is possible to compensate by beam tilt without introducing extra aberrations

1.1.4 Scanning Transmission Electron Microscopy

Unlike conventional TEM, where the whole magnified image is generated by a simultaneous interaction of the electron beam with a large area of the specimen, in a scanning electron microscope, the image is produced by a scanning process. In scanning electron microscopy (SEM), the image is produced by secondary electrons or electrons scattered by the surface of the sample, while in a scanning transmission electron microscope (STEM), the electron beam is rastered across a thin sample, and the transmitted beam is collected by a detector located at a location posterior to the sample. In a sense, STEM combines features of TEM and SEM, and since the optical arrangement of a STEM is basically the same of an inverted TEM, there exist microscopes capable of working on both modes (although not simultaneously). In STEM mode, the electron beam is condensed to a small area (the probe), whose size will be limited by spherical aberrations. The first STEM was attributed to the German physicist and inventor Manfred von Ardenne in 1938, who was granted a US patent for his invention in 1941 (the title was "Electronic-Optical Device"). In the description of its invention, von Ardenne states that:

> The present invention overcomes the above mentioned difficulties by point-for-point scanning of the object with the aid of an electron beam focal spot, the diameter of which is less than one-thousandth of a millimeter. Carrying out this method, the electrons coming from

> the electronically-optically illuminated image element are registered, a basis is established for the building-up of an electronic-optical image of the object, and, in fact, with a resolving factor which depends solely on the point sharpness of the scanning focal spot in the object plane subjected to investigation. [21]

On his breakthrough 1938 paper, von Ardenne shows an image of ZnO, produced with a resolution of 40 nm. While there were important improvements to the original design in the following years, they were mostly small refinements to the already established designs [22]. Cosslett proposed in 1965 that the use of a ring-shaped detector would improve the differentiation of elements present in the TEM sample [23]. A year later, Crewe reaches a resolution of 50 Å using a field emission gun [24]. Two years later, Crewe sets a new resolution record at 30 Å [25]. Crewe's team published in 1974 a paper in the Proceedings of the National Academy of Sciences, describing the operation of a STEM capable of a resolution of less than 3 Å [26]. They used a tungsten field emission gun to produce electrons of 30–45 keV. With this experimental setup, they were able to produce dark-field micrographs of well-defined atomic chains and crystallites of uranium.

There are different ways an electron from an electron beam may interact with a sample. Some of the electron will be backscattered, while others will be absorbed and generate secondary electrons of different kinds. If the sample is thin enough, most of the electrons will be transmitted, and some of them will barely modify their original trajectory; these electrons can be used to generate bright-field (BF) images. Electron transmitted at higher angles can be collected using an annular detector to produce high-angle annular dark-field (HAADF) images or can be used not for imaging but for different kinds of spectroscopy. Figure 1.6 represents the different signals that can be obtained from the interaction of the sample with the electron beam.

On their PNAS paper, Crewe's team used an annular detector, and because of this, "since elastic scattering increases approximately as $Z^{3/2}$, where Z is the atomic number of the material, this annular detector signal is a strong function of the atomic number." In this same paper, Crewe suggested that the use of higher voltages would allow the atomistic visualization of lighter elements and that an operation voltage of 100 keV should be sufficient to visualize individual atoms of "more than half the periodic table." While the specific dependence of the intensity signal on the atomic number may not be as simple as $Z^{3/2}$, the approximation is quite good if the sample is very thin. It is remarkable that the basic setup for a STEM built 40 years ago is basically the same for the state-of-the-art STEM systems: a field emission gun, a condenser lens, a set of optical lenses to minimize aberrations, a deflection coil to raster the beam, the specimen, and the detectors. Figure 1.7 shows this basic setup.

The set of lenses that are identified as condenser has, together with the objective lens, the function of focusing the electron beam into a small spot, with dimensions comparable to the interatomic distances. The objective lens is the optical element that produces the largest aberrations.

The scan coils have the function of scanning the probe over the sample. Independently of how this scan is made, there are several transmitted signals that can be collected with different kinds of detector to be used for the generation of an image

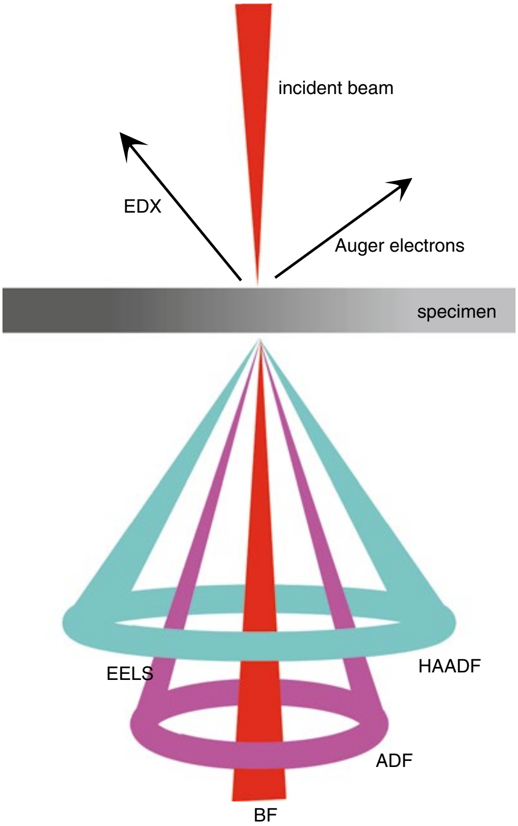

Fig. 1.6 Signals and techniques in electron microscopy. Transmitted electrons are used to generate bright-field, dark-field, and high-angle ADF micrographs

or spatial map. To detect electrons transmitted at relatively low angles with respect to the incident beam axis, a bright-field (BF) detector is used. If the electrons transmitted at relatively high angles are detected with an annular detector, it is possible to generate dark-field (DF) images. It is also possible to generate an EELS map (electron energy loss spectroscopy) discriminating the electron on function of the amount of energy lost in its interaction with the sample or to measure the X-ray generated when the beam ejects an electron from a low-energy electronic shell and a second electron fills the hole left by the ejected electron. Dark-field imaging is particularly relevant because in this technique, an annular detector is used to collect the signal that produces the image. Using this annular detector, only those electrons scattered at an angle higher than a minimum are collected, which minimized Bragg scattering [3], and so it makes the intensity signal in the image to depend almost solely on the individual contribution of the atoms present on the sample. As Crewe et al. already had established in their 1974 paper, the signal collected by the annular detector has an intensity directly dependent on the scattering cross section and thus in the atomic number of the atoms being detected. This dependence on Z is more remarked at high angles (more than 50 mrad), and when an annular detector is used at this range of angles, the STEM technique is called high-angle annular dark-field or HAADF.

Fig. 1.7 Schematic diagram of an electron microscope working on STEM mode

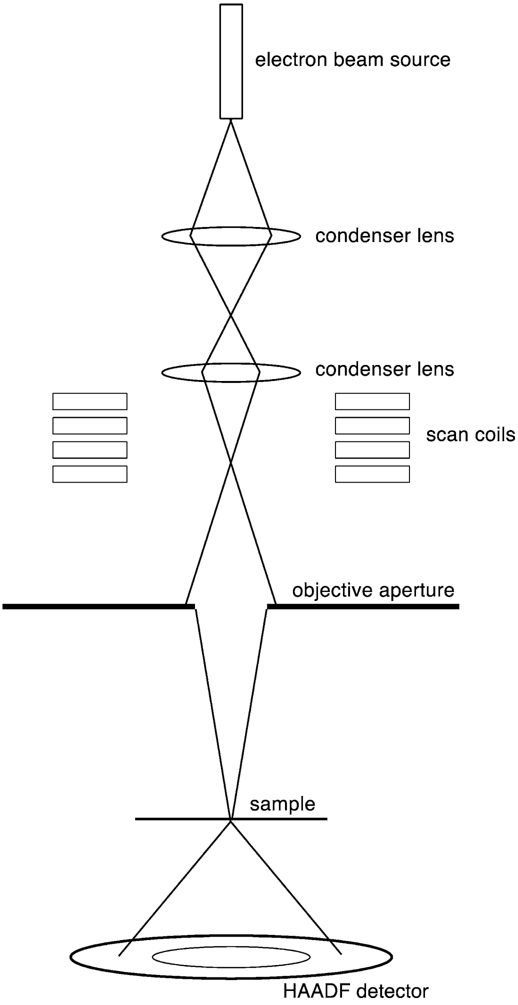

1.1.5 STEM Aberration Correction

In the case of STEM, a critical factor is the electron probe. In principle, the resolution of STEM is defined by the probe size. However, the characteristics of the probe are also important. A very important characteristic of STEM images is the depth of field or focal depth. Of course, this allows the possibility of having the appearance of 3D in the images. The depth of focus ΔF depends on the semi-angle illumination as

$$\Delta F = \frac{\lambda}{\alpha^2} \tag{1.9}$$

where λ is the wavelength. In the case of STEM, there is also influence of the aberrations on the probe. Several aberrations affect the probe such as the STEM, the fourfold astigmatism, and the spherical aberration (C_3 and C_5). Again, there are optimum conditions for maximum contrast [27]:

$$\begin{aligned} \Delta f &= -1.56\sqrt[3]{\lambda^2 C_5} \\ C_3 &= -2.88\sqrt[3]{\lambda C_5^2} \end{aligned} . \tag{1.10}$$

These options show the critical importance of the C_5 parameter. On the other hand, different factors play a role in an uncorrected STEM, such as the diffraction limit, the partial temporal coherence, the chromatic aberration Cc, and possible disturbances of high frequency which alter the stability of the probe $S_{5\,\mathrm{noise}}$. All those factors are important to consider. However, the chromatic aberration and the spherical aberration are by far the most significant.

Another important factor is the depth of focus. For a noncorrected STEM operated at 200 keV with a $C_3 = 1\mathrm{mm}$ and $\alpha = 10\mathrm{mrad}$, the depth of focus is 25 nm, so a typical nanocrystal with ~100 atomic layers can be seen in focus. For an aberration-corrected STEM, the depth of focus radius is ~4 nm. That means that we can observe in focus ~18–20 atomic layers. This means that only small particles can be observed in focus. This on the other hand opens the possibility of focusing different thickness of the sample doing a kind of reconstruction similar to a confocal microscope.

In the next sections, we will use the case of nanoparticles for illustrating aberration correction.

1.2 The Study of Clusters and Nanoparticles Using Aberration-Corrected Microscopy

1.2.1 Introduction

The study of nanoparticles with a nanometric size is one of the key aspects of nanotechnology. Indeed, knowledge of the particle structure is fundamental to understand its properties. Nanoparticles can be studied at atomic level if a spherical aberration-corrected microscope is used. Modern mechanics can achieve resolutions around 70 pm in both objective lens-corrected (TEM) and probe-corrected (STEM) microscopes. However, the study of nanoparticles has several difficulties that should be addressed. In this chapter, we will discuss the methods to study nanoparticles.

1.2.2 Difference Between Clusters and Nanoparticles

A very important distinction on the physical properties depends on the size of the nanoparticle. A first distinction should be when the particle has very few atoms. In this case, quantum effects are dominant, and it is better to call this particle a nanocluster or a super-atom. When the number of atoms increases, the plasmonic effect starts to appear. The size at which setting of the plasmon resonance is produced should be considering the boundary between clusters and nanoparticles. This is illustrated in Fig. 1.8.

In the case of clusters, it is necessary to stabilize them using an organic ligand [28]. This is required to generate well-defined structures called super-atoms [29]. The organic molecule has to contain an element that binds to the metal. An example is the thiol compounds. Those contain a carbon sulfhydryl (–C–SH) or R–SH where R represents an alkane or alkene. The –SH thiol group bonds to metals such as silver and gold. An example of a cluster passivized by thiols is shown in Fig. 1.9. Researchers have been able to synthesize many stable clusters [30–32], which include $Au_{25}, Au_{38}, Au_{102}, Au_{114}, Au_{130}, Au_{44}$, and several others. A new trend has been to produce bimetallic clusters such as of Au–Ag [33, 34].

When a cluster with few atoms is not passivated with thiols, a very particular situation happens. There is no sharp minimum in the total energy of the cluster, but many configurations here have similar energy. Then, an energy landscape is

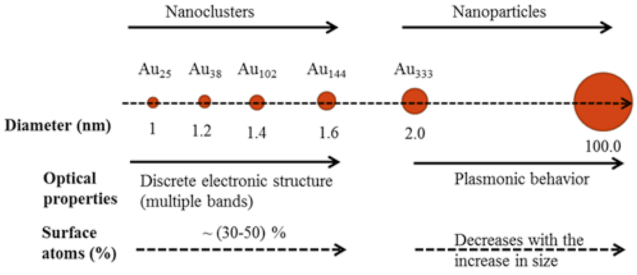

- ❖ Extremely high surface area
- ❖ Molecular like discrete energy level
- ❖ Size dependent optical properties

Size (nm)	Radius (nm)	Total Number of atoms (N)	Total number of surface atoms $N_s = 4*N^{2/3}$	% of surface atoms
1	0.5	31	39	
5	2.5	3861.5	985	25
10	5	30886	3938	12.7
20	10	$24.662 * 10^4$	15730	6.37
100	50	$30.89*10^6$	393767	1.27

Fig. 1.8 Nanoparticles and nanoclusters. When the quantum effects are dominant and it is better to call a group of atoms a nanocluster or a super-atom and when the plasmonic effect starts to appear, we can call them nanoparticles

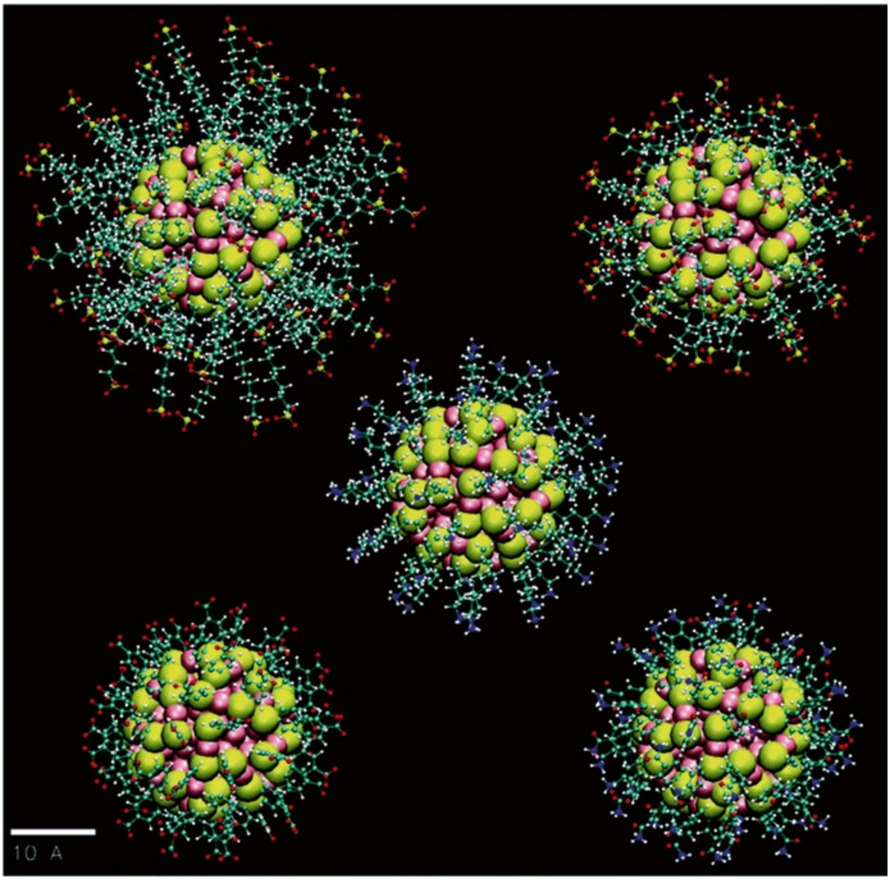

Fig. 1.9 Equilibrium structures of the five $Au_{144}(SR)_{60}$ nanoclusters shown on a common scale. Au, *pink*; S, *yellow*; O, *red*; C, *cyan*; N, *blue*; H, *white*

produced which results in many configuration results. Since the energy differences are so small, at room temperature, we will expect fluctuations on the shape [33–35]. This phenomenon is known as quasimelting [36], and it is illustrated in Fig. 1.10. When doing electron microscopy of clusters, this phenomenon is very important and can lead to misinterpretation of results. This happens when clusters are supported on carbon or graphene grids. Those substrates have a very weak interaction with the cluster. If the substrate tends to form a bond with the particle or there are van der Walls forces acting between substrate and cluster, a stable configuration is produced.

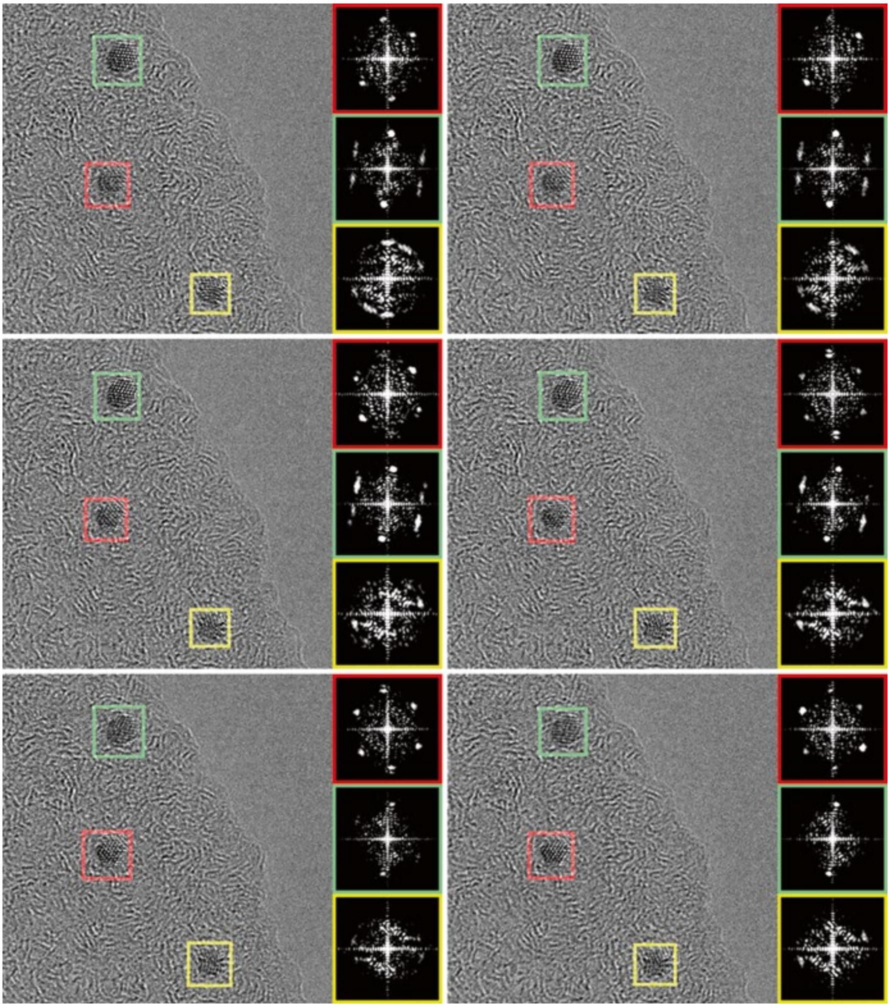

Fig. 1.10 Quasimelting observed in Au nanoparticles. The FFT corresponds to the particle on the left enclosed in a *square*. Every frame corresponds to 2 s elapsed time

1.3 Radiation Damage in Clusters

STEM in probe correction microscopy is a fundamentally important technique to characterize clusters and nanoparticles since we can achieve atomic resolution. In addition, electron diffraction of clusters is in most instances kinematical which means that by measuring the intensities in at least two crystal axes, we can determine the full crystal structure. The great advantage of electron diffraction is that no large crystals (as in the case of X-rays) are needed. In fact, nanocrystals can be easily diffracted. The number of passivized clusters whose structure has been determined by X-rays is very limited. The reason is that not all clusters can be crystallized. Unfortunately, STEM, TEM, and electron diffraction have a great limitation, which is radiation damage. This may be the most important limiting factor that prevents obtaining reliable results. The main sources of radiation damage that affect the cluster or nanoparticle observation are radiolysis (or ionized) due to inelastic scattering and knock on, which is the displacement of atoms due to inelastic scattering. The energy loss E suffered by primary electron may be transferred to a single atomic electron, which then undergoes a single-electron transition. In the case of a metal, the transition mostly involves conduction band electrons that are excited to empty states above the Fermi level E_{f}. A vacancy (hole) is produced in the valence band, which is filled very rapidly because of the high density of conduction electrons. This results in a temperature rise but no permanent damage. So the metal core is scarcely damaged by radiolysis. In the case of the organic capping, the situation is very difficult: transitions will produce electron–hole pairs, which are not filled fast. This might result in bond breaking, and also valence band electron might travel on the molecule producing more electron–hole pairs. Secondary electrons multiply the damage and eventually become the dominant source of radiolysis [37, 38]. It might also happen that the incoming electron excites an inner shell electron. In this case, the energy loss is much higher, and damage becomes considerable. When the core hole is filled with a valence electron, an Auger electron is released with the energy ~260 eV creating more bond damage. When the electron beam destroys the passivating molecule, the cluster will be altered. It is well established in the case of nanoparticles that when particles are "naked," instabilities are produced by the electron beam as a result of the structure–composition relation.

A calculation of the effect of radiolysis damage on a thiolate molecule is shown in Fig. 1.11. The curve shows different atoms composing the cluster. As can be seen, hydrogen is extremely sensitive to radiation, and most likely, despite of observation conditions, hydrogen is removed from the thiolate molecules. A very important point is whether the metal–sulfur bond is still intact. Figure 1.11 shows that around <80 keV, the maximum transferred energy is less than the energy of desorption of a sulfur ion on the surface and also smaller than that of the metal. We can conclude that a voltage of 60 keV will be adequate for observation. Since clusters and nanoparticles are very thin, lower voltage gives higher image contrast, due to the larger elastic scattering cross section (proportional to $1/v^2$) where v is the electron speed). An additional reason for operating at low voltage is to reduce or avoid knock-on displacement, the radiation damage process that predominates in electrically conducting specimens; low-voltage (<60 keV) TEM or STEM is attractive for nanoparticles. Effects produced at high current densities such as atom displacement from lattice sites or along a surface or sputtering of atoms from surfaces are reduced at low voltage. An example of this effect on MoS_2 crystals is shown in Fig. 1.12. As can be seen, atomic resolved images can be obtained at 80 keV.

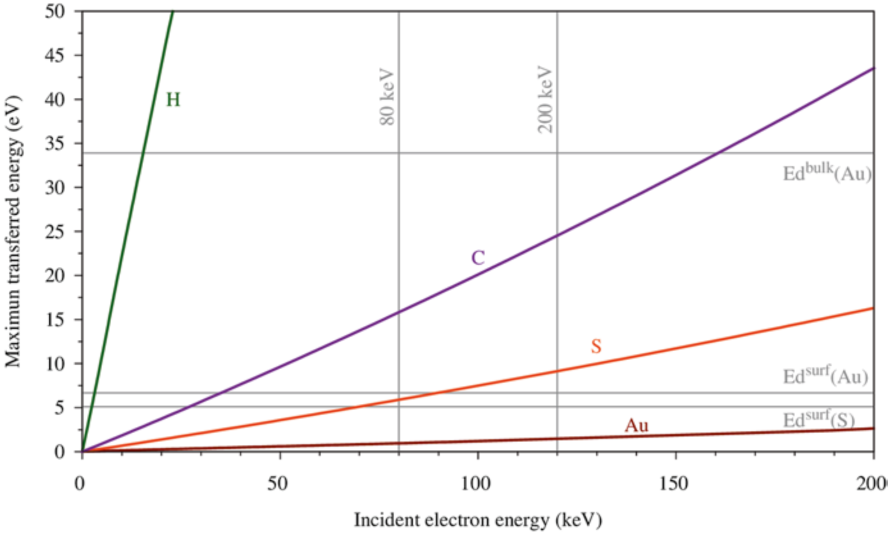

Fig. 1.11 Effect of radiolysis damage on a thiolate molecule. Hydrogen is extremely sensitive to radiation. Around <80 keV, the maximum transferred energy is less than the energy of desorption of a sulfur ion on the surface and also smaller than that of the metal. The voltage of 60 keV will be adequate for observation

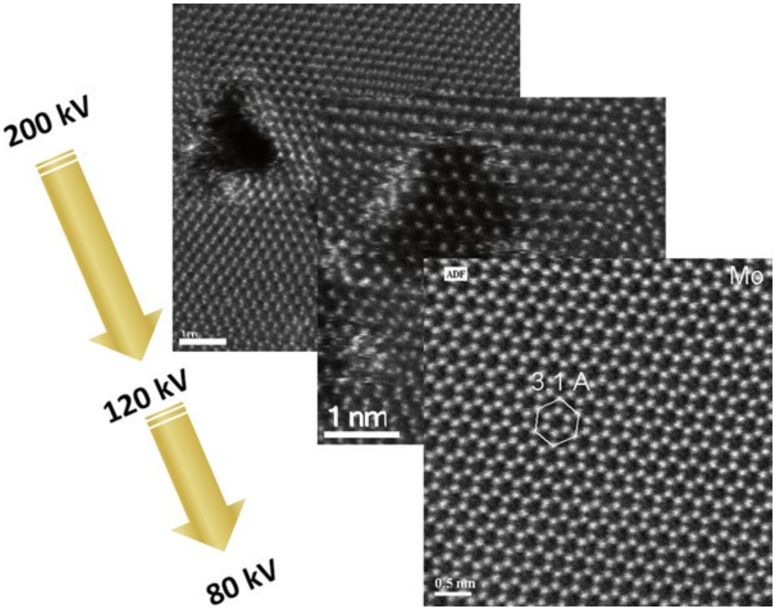

Fig. 1.12 Effects produced on MoS_2 by the electron beam as a function of the acceleration voltage. The damage in this case is due to atom displacement

1.4 STEM Contrast

One of the most interesting properties of the HAADF is the dependence of the signal with the thickness and with the atomic number. This has been documented in several excellent reviews [39, 40]. An average equation is that the intensity goes as $Z^{1.7}$. However, significant care should be taken when analyzing clusters or nanoparticles with STEM. A calculation for a hypothetical crystal with the shape of a ramp is shown in Fig. 1.13a. Here, we have considered two crystals of Au and Ag

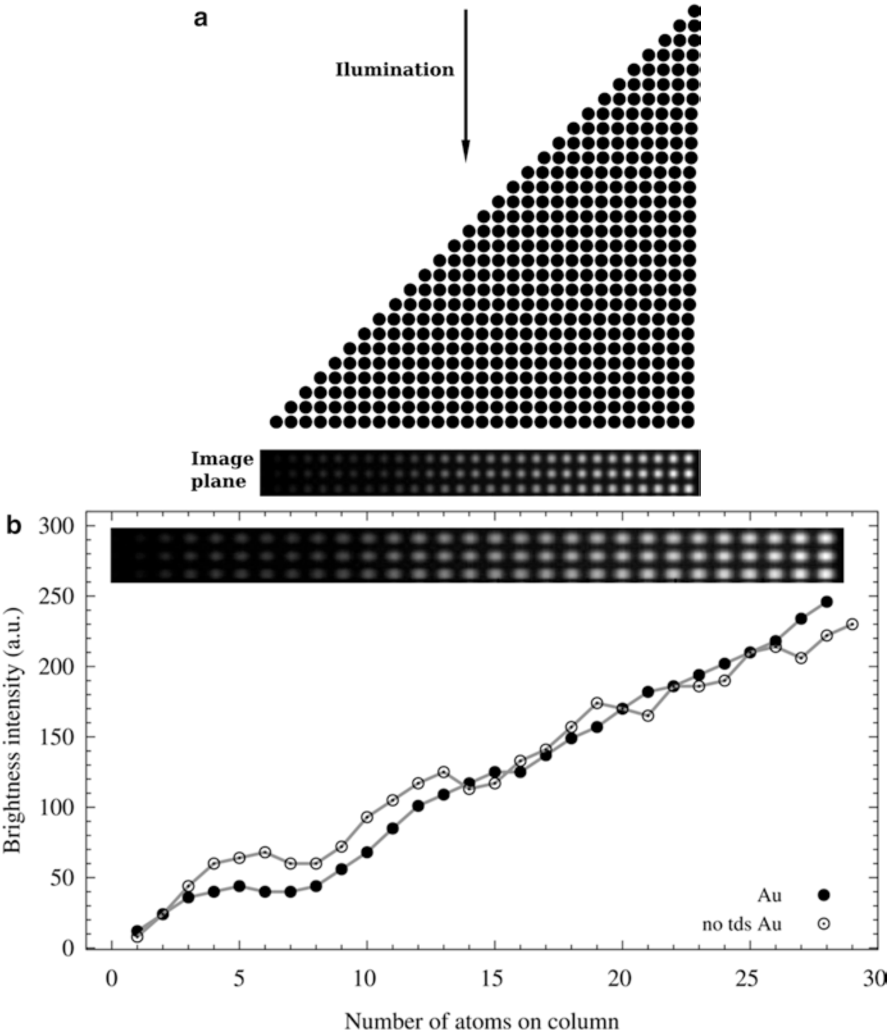

Fig. 1.13 Calculation for a hypothetical crystal with the shape of a ramp. (**a**) Model structure, where the height of the atomic columns goes from one to thirty atoms; the image plane shows the intensity dependence on the number of atoms in the column. The HAADF intensity of the signal as a function of the number of atoms in the atomic columns is calculated for (**b**) Au and (**c**) Ag. A multislice method was used with and without thermal diffusion scattering (TDS)

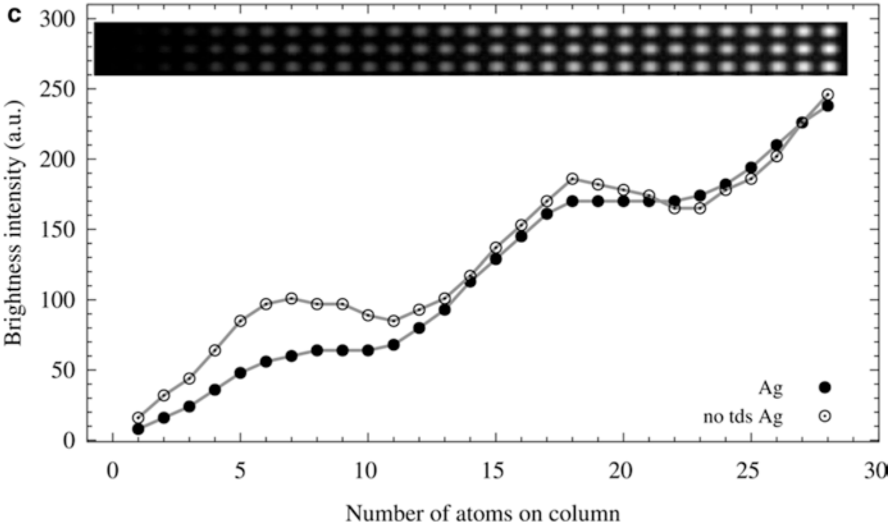

Fig. 1.13 (continued)

(Fig. 1.13a, b), and we have plotted the intensity of the signal as a function of the number of atoms in the atomic columns. We consider two cases, one with thermal diffuse scattering factoring and the other without. As can be seen, the intensity is linear up to five atoms; then there is a plateau and then an increase again. That means that a simple *Z* contrast analysis is valid for a particle of a diameter of 1.5 nm (assuming a spherical free particle). The same is valid for the case of Au. Of course, it is clear that a more involved calculation is necessary for setting an accurate atom counting [41, 42].

1.5 Radiation Damage in Nanoparticles

1.5.1 Small Nanoparticles

The boundary between cluster and nanoparticles is dependent of the type of metal (or semiconductor) forming the nanoparticle. However, the transition occurs sharply. In order to study the transition, we need to separate clusters size by size. In order to separate the clusters or nanoparticles, we used polyacrylamide gel electrophoresis (PAGE) using Tris–borate–EDTA (TBE) buffer (pH 8.0) in a Mini-PROTEAN Gel Electrophoresis System (Bio-Rad). Separation and purification of Au nanoclusters can be performed with 10 % PAGE gel using 2–5 μL of concentrated nanoclusters per well with 20 % v/v glycerol. Separation is performed at 110 V for 60 min or until verification of formation of discrete bands. Sections corresponding to bands to different nanoparticle sizes are recovered from PAGE gels by cutting with stainless

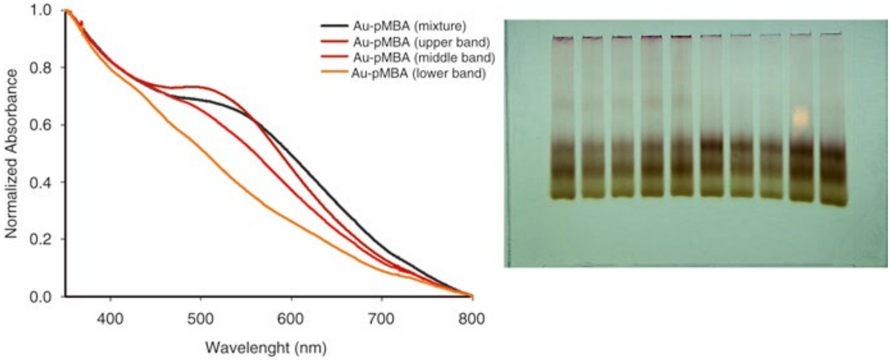

Fig. 1.14 Absorbance spectroscopy for PAGE, 10 %, TBE buffer, 100 V; Au–pMBA (*upper*), Au288, 2.46 nm, 88 kDa; Au–pMBA (*middle*), Au144, 2.01 nm, 51 kDa; Au–pMBA (*lower*), Au102, 1.55 nm, 23 kDa. As can be seen, the cluster with 288 atoms shows the plasmonic behavior

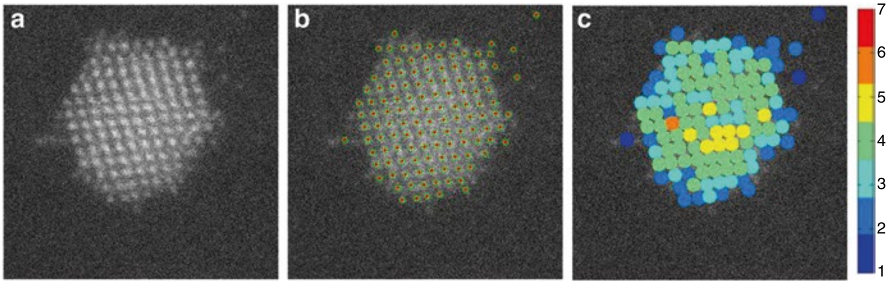

Fig. 1.15 HAADF image obtained on a probe-corrected STEM of a mass of 67 kDa gold cluster. As it is possible to see in (**a**), atoms are already stripped out of the particle. In (**b**, **c**) the intensity of each atomic column was measured and plotted on a color scale. The difference on the colors represents variations on the number of atoms. This indicates that the cluster has already suffered knock-on radiation damage

steel knife. Every PAGE gel fraction is put in a 2 mL Eppendorf tube, covered with 2 mL ddH_2O, and incubated at 37° to favor diffusion of nanoclusters from gel matrix to solvent. Finally, the separated nanoclusters are concentrated with a rotary evaporator analyzed by electron microscopy and mass spectrometry. An example of the fractions in Au–pMBA clusters is shown in Fig. 1.14. In the case of pure gold particles, the separated fractions correspond to particles with average sizes of 2.5 nm and 1.5 in diameter; we will determine the same fractions for the bimetallic particles. Figure 1.14 shows an example of the separated fractions in the case of Au–pMBA clusters. The electron microscopy of one of the fractions shows the monodispersion and the absorption spectra of the clusters. It is possible to see that the larger cluster already shows a plasmon peak. This cluster with 88 kDa corresponds to 288 atoms. This shows how the transition occurs with relative few atoms. Therefore, according to our definition, a cluster this size should be considered a nanoparticle.

In general, nanoparticles are also sensitive to radiation damage. As the size increases, radiation resistance also increases. However, it is again a very important factor to consider. Figure 1.15 shows the HAADF-STEM image of a particle of 67 kDa (333 atoms as determined by mass spectroscopy). The image in Fig. 1.15a shows that around the particle, there are single atoms. Most likely, those were stripped from the particle by the electron beam by knock-on damage. The particle appears to have a very well-defined FCC structure. However, if we made an atom counting analysis (Fig. 1.15b), we can see that there are important variations on the atomic columns. In fact, we can see that, in the color code image Fig. 1.15c, there are more single atoms which are still on the surface of the particle. Significant variations on the thickness of the layers of atoms can be seen. We can conclude that despite the very clear HAADF image, the nanoparticle has already suffered a significant damage by knock-on process. An excellent review of radiation damage can be found in Egerton's work [43].

1.5.2 Larger Nanoparticles

When larger nanoparticles >20 nm are irradiated by the electron beam, there is no increase on the temperature of the particle. Although in some cases this can be released through the substrate if a good contact exists, this increases the mobility of the nanoparticles and coalescence results. Coalescence will generate larger particles; a result of coalescence is shown in Fig. 1.16. As can be seen, several occur during coalescence such as reorientation of the nanoparticles in order to have planes of the same type, fluctuations on the shape of the nanoparticles, and reshaping of the combined particle. For instance, in Fig. 1.16a–c, it is possible to see that $\langle 110 \rangle$ planes of the two particles become aligned with each other. Then, in a second stage, twins are formed on the particle, which propagate through the particle. Finally, when the combined particle is formed, it shows several shape adjustments. When analyzing larger particles, one must be convinced that the observed size distribution is not the result of coalescence and represents the original size distribution. This sometimes is induced by common practices in TEM such as "beam shower" which many microscopists use to clean the sample. That will result in changes on the particle size and structure.

1.6 Biological Methods Applied to TEM of Nanoparticles

The biological community has developed over the years a number of methods to observe radiation-sensitive samples. Nanoclusters and nanoparticles should be considered sensitive to radiation damage. The use of biological methods is a great help in studying nanoparticles. A very important parameter that should be controlled is the electron dose that reaches the sample. Reducing the incident beam current lengthens the time needed to record an image or spectrum, increasing the likelihood of specimen, electron beam, or high-voltage drift; however, it ensures that radiolysis

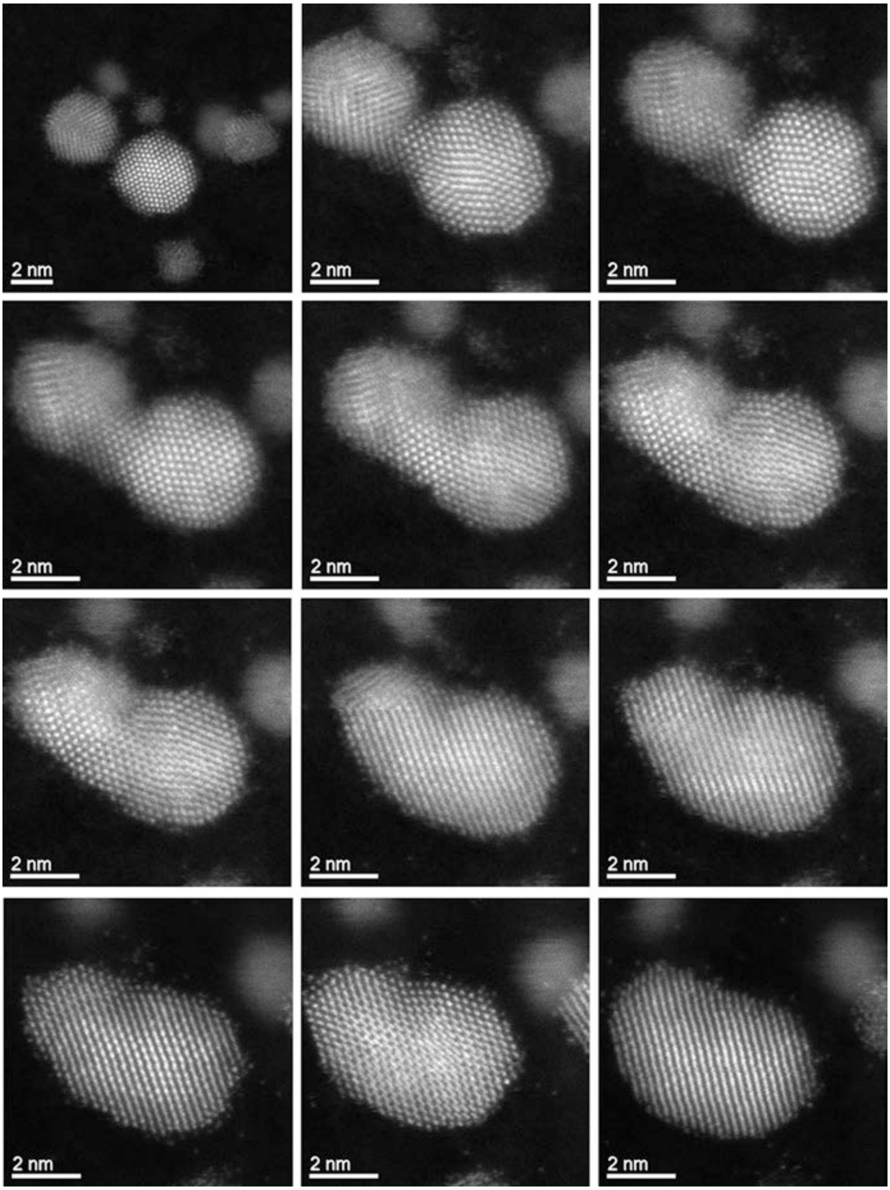

Fig. 1.16 Sequence of HAADF images of gold nanoparticles showing coalescence. The time between frames is 2 s. The coalescence is induced by the electron beam. Note how planes are aligned in each particle before the actual contact. Also twins on the structure can be seen moving along the combined particle

will not be enhanced as a result of beam heating, and it reduces the risk of thermal decomposition or electrostatic charging effect. According to Egerton's [43] calculations, a dose rate less than 0.03 A/cm^2 is required to minimize the electron beam heating. A total accumulated electron dose of ~0.01 C/cm^2 will be required for cluster observation. In order to achieve a low dose, it is necessary to use a CMOS-based camera on the TEM. CMOS architecture uses lowest noise sensors resulting in high dynamic range (>10,000:1) and single-electron sensitivity and a very low dose.

In addition [43], the mass loss (and structural damage) can be reduced by cooling the specimen with liquid nitrogen. Under these conditions, it might be expected that damage would also depend on the irradiation time. Dose rate as well as the accumulated dose delivering the electrons in a time shorter than that required for significant diffusion might produce less mass loss; therefore, cryomicroscopy is very convenient for cluster structure analysis. In most cases, liquid nitrogen cooling is enough to study clusters.

In a recent paper, Azubel et al. [44] studied the monometallic cluster $Au_{69}(SR)x$ using a very similar concept to the one described in this proposal. They use cryo-TEM and standard low-dose methods. A major difference is that they used bright-field image averaging 939 particles acquired in this which was processed with the EMAN2 software package [45] which yielded an electron density map with 68 peaks. From that map, the authors reconstruct the structure. This work is a fine example of the use of biological methods in cluster research.

1.7 Nanodiffraction of Nanoparticles

When CMOS camera is being used in a TEM, it is possible to obtain diffraction patterns of clusters and nanoparticles from which the structure of the cluster can be extracted. A combination of low intensity (1 pA/cm^2) and ultrafast detection allows the diffraction of clusters of Au_{144}. An example is shown in Fig. 1.17. Every frame was taken each 0.2 s. The sequence of patterns of Fig. 1.17 shows that diffraction patterns containing a large number of spots are obtained. If the initial pattern appears stable in subsequent frames (a few of them), we can then be sure that this corresponds to the original structure and it is not modified by the radiation damage. Then using the diffraction results combined with the data from HAADF-STEM images, we have matched the image, the FFT, the mass spectrometry, and the diffraction pattern with models obtained by DFT calculations. This iteration process is a continuous trial and error until the model can explain all the experimental data. We have applied this method to the case of $Au_{144}(SR)_{60}$ [26] and $Au_{130}(SR)_{50/80}$ [46]. The very complex structure obtained for Au_{144} is shown in Fig. 1.18. The cluster is made of three layers each one with a different symmetry.

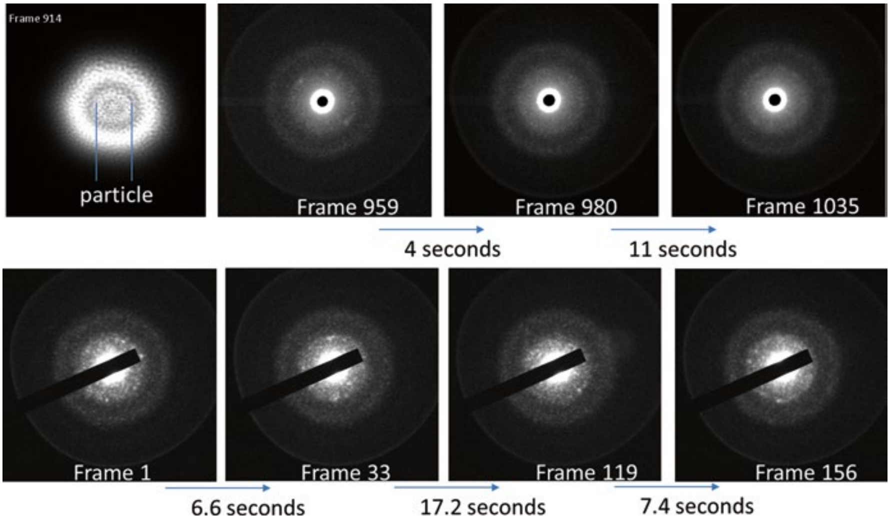

Fig. 1.17 Electron diffraction patterns of clusters of Au_{144} obtained with a CMOS camera. The beam intensity was 1 pA/cm^2. In this condition, it was possible to obtain stable patterns, which indicate that the pristine structure of the cluster was preserved. The elapsed time between frames is shown on the figure

In summary we can say that the best methods to study nanoclusters and nanoparticles imply to perform microscopy and diffraction under the following methods:

- Low-voltage operation (60–80 keV) of aberration-corrected microscope.
- Low-dose observations at an electron dose of ~0.01 C/cm^2. This can be achieved using a CMOS camera.
- Cryo-electron microscopy (liquid nitrogen).
- Ultrafast recording of images and diffraction patterns approximately less than 1 frame per second.
- Obtain STEM-HAADF, combined single particle diffraction.
- Only images which are stable at the beginning of irradiation for 10 s will be analyzed.

By the use of such methods, a new era of characterization of nanoparticles will allow a full understanding of its structure and physical properties.

Acknowledgment This project was supported by grants from the National Center for Research Resources (5 G12RR013646-12) and the National Institute on Minority Health and Health Disparities (G12MD007591) from the National Institutes of Health. In addition, the authors would like to acknowledge the support of the Welch Foundation grant No. AX-1615.

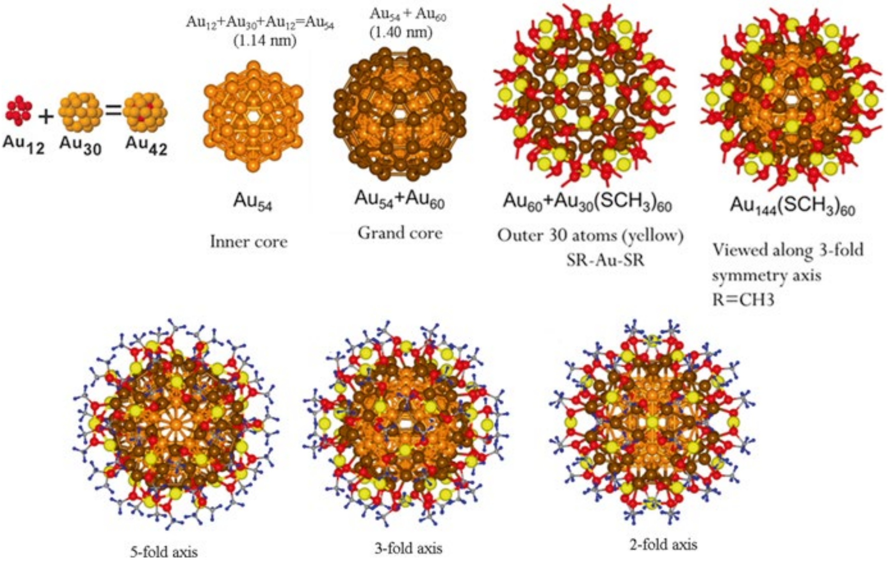

Fig. 1.18 Structure obtained for cluster Au$_{144}$ (SCH3)60, the HAADF images, the experimental FFT, the diffraction pattern among images, and DFT calculations. By matching all the information, it is possible to construct the model

References

1. The Nobel Prize in Physics 1986. Nobelprize.org. Nobel Media AB 2014. Web, http://www.nobelprize.org/nobel_prizes/physics/laureates/1986/. Accessed 6 Feb 2015
2. M. Knoll, E. Ruska, Das Elektronenmikroskop (The electron microscope). Z. Phys. **78**, 318–339 (1932), submitted 16 June 1932
3. D.B. Williams, C.B. Carter, *Transmission Electron Microscopy: A Textbook for Materials Science* (Springer, Berlin, 2009)
4. C.T. Koch, Determination of core structure periodicity and point defect density along dislocations. ProQuest Dissertations and Theses; Thesis (PhD)–Arizona State University, 2002. Publication Number: AAI3042580; ISBN: 9780493562612; Source: Dissertation Abstracts International, vol 63–02, Section: B, pp. 0846. 214 (2002) pp. 1–175
5. J. Weertman, J.R. Weertman, *Elementary Dislocation Theory* (Mac Millan, New York, 1964)
6. J.M. Cowley, A.F. Moodie, The scattering of electrons by atoms and crystals. I. A new theoretical approach. Acta Crystallogr. **10**, 609–619 (1957). See also J. Cowley, *Diffraction Physics* (North Holland, Amsterdam, 1981)
7. S. Ijima, Helical microtubules of graphitic carbon. Nature **354**, 56–58 (1991)
8. J.F. Enders, T.H. Weller, F.C. Robbins, Cultivation of the Lansing strain of poliomyelitis virus in cultures of various human embryonic tissues. Science **109**, 85–87 (1949)
9. M. Adrian, J. Dubochet, J. Lepault, A.W. McDowall, Cryo-electron microscopy of viruses. Nature **308**, 32–36 (1984)
10. L.F. Kourkoutis, J.M. Plitzko, W. Baumeister, Electron microscopy of biological materials at the nanometer scale. Annu. Rev. Mater. Res. **42**, 33–58 (2012)

11. P.W. Hawkes (ed.), *Advances in Imaging and Electron Physics,* vol 182 (Academic Press, San Diego, 2014), pp. 1–94
12. A. Howie, Aberration correction: zooming out to overview. Phil. Trans. R. Soc. A **367**, 3859–3870 (2009)
13. H.H. Rose, Historical aspects of aberration correction. J. Electron Microsc. **58**, 77–85 (2009)
14. P.W. Hawkes, Aberration correction past and present. Phil. Trans. R. Soc. A **367**, 3637–3664 (2009)
15. Richard Feynman gave a classical talk on December 29th 1959 at the annual meeting of the American Physical Society at the California Institute of Technology (Caltech) was first published in Caltech Engineering and Science, vol 23, 5 Feb 1960, pp 22–36. It has been made available on the web at http://www.zyvex.com/nanotech/feynman.html with their kind permission. The scanned original is available
16. E.S. Reich, Imaging hits noise barrier. Nature **499**, 135–136 (2013)
17. S. Ulemann, H. Müller, P. Hartel, J. Zach, M. Haider, Thermal magnetic field noise limits resolution in transmission electron microscopy. Phys. Rev. Lett. **111**, 046101 (2013)
18. S.J. Pennycook, S.V. Kalinin, Microscopy: Hasten high resolution. Nature **515**, 487–488 (2014)
19. R. Erni, *Aberration Corrected Imaging in Transmission Electron Microscopy: An Introduction* (Imperial College Press, London, 2010)
20. M. Lentzen, Contrast transfer and resolution limits for sub-angstrom high-resolution transmission electron microscopy. Microsc. Microanal. **14**, 16–26 (2008)
21. M. von Ardenne, Electronic-optical device. U.S. Patent 2,257,774, filed 15 Feb 1938, and issued 7 Oct 1941
22. M. von Ardenne, Das Elektronen-Rastermikroskop. Praktische Ausführung. Z. Tech. Phys. **19**, 407–416, as reproduced in S.J. Pennycook, P.D. Nellist, *Scanning Transmission Electron Microscopy: Imaging and Analysis* (Springer, New York, 2011)
23. V.E. Cosslett, Possibilities and limitations for the differentiation of elements in the electron microscope. Lab. Invest. **14**, 1009–1019 (1965)
24. A.V. Crewe, Scanning electron microscopes: is high resolution possible? Science **154**(3750), 729–738 (1966)
25. A.V. Crewe, J. Wall, L.M. Welter, A high-resolution scanning transmission electron microscope. J. Appl. Phys. **39**(13), 5861–5868 (1968)
26. J. Wall et al., Scanning transmission electron microscopy at high resolution. Proc. Natl. Acad. Sci. U. S. A. **71**(1), 1–5 (1974)
27. L.Y. Chang, A.I. Kirkland, J.M. Titchmarsh, On the importance of fifth-order spherical aberration for a fully corrected electron microscope. Ultramicroscopy **106**, 301–306 (2006)
28. M.M. Alvarez, J.T. Khoury, T.G. Schaaff, M.N. Shafigullin, I. Vezmar, R.L. Whetten, Optical absorption spectra of nanocrystal gold molecules. J. Phys. Chem. B **101**, 3706–3712 (1997)
29. M. Walter, J. Akola, O. Lopez-Acevedo, P.D. Jadzinsky, G. Calero, C.J. Ackerson, R.L. Whetten, H. Gronbeck, H. Hakkinen, A unified view of ligand-protected gold clusters as superatom complexes. Proc. Natl. Acad. Sci. U. S. A. **105**, 9157–9162 (2008)
30. A. Dass, P. Ninmala, V. Jupally, N. Kothalawa, $Au_{103}(SR)_{45}$, $Au_{104}(SR)_{45}$, $Au_{104}(SR)_{46}$ and $Au_{105}(SR)_{46}$ nanoclusters. Nanoscale **5**, 12082–12085 (2013)
31. A. Dass, Nano-scaling law: geometric foundation of thiolated gold nanomolecules. Nanoscale **4**, 2260–2263 (2012)
32. Y. Negishi, N.K. Chaki, Y. Shichibu, R.L. Whetten, T. Tsukuda, Origin of magic stability of thiolated gold clusters: a case study on $Au_{25}(SC_6H_{13})_{18}$. J. Am. Chem. Soc. **129**, 11322–11323 (2007)
33. C. Kumara, C.M. Aikens, A. Dass, X-ray crystal structure and theoretical analysis of Au_{25-} xAg$x$$(SCH_2CH_2Ph)_{18}$–alloy. J. Phys. Chem. Lett. **5**, 461–466 (2014)
34. W. Krakow, M. Jóse-Yacamán, J.L. Aragón, Observation of quasimelting at the atomic level in Au nanoclusters. Phys. Rev. B **49**, 10591–10596 (1994)

35. D.J. Smith, A.K. Petford-Long, L.R. Wallenberg, J.O. Bovin, Dynamic atomic-level rearrangements in small gold particles. Science **233**, 872–875 (1986)
36. P.M. Ajayan, L.D. Marks, Experimental evidence for quasimelting in small particles. Phys. Rev. Lett. **63**, 279–282 (1989)
37. R.F. Egerton, F. Wang, P.A. Crozier, Beam-induced damage to thin specimens in an intense electron probe. Microsc. Microanal. **12**, 65–71 (2006)
38. M. Malac, M. Beleggia, R. Egerton, Y. Zhu, Bright-field TEM imaging of single molecules: dream or near future? Ultramicroscopy **107**, 40–49 (2007)
39. G. van Tendeloo, S. Bals, S. Van Aert, J. Verbeeck, D. van Dyck, Advanced electron microscopy for advanced materials. Adv. Mater. **24**, 5655–5675 (2012)
40. S.J. Pennycock, P.D. Nelist (eds.), *Scanning Transmission Electron Microscopy: Imaging and Analysis* (Springer, New York, 2011), p. 762
41. A. De Backer, G. Martinez, A. Rosenauer, S. Van Aert, Atom counting in HAADF STEM using a statistical model-based approach: methodology, possibilities, and inherent limitations. Ultramicroscopy **134**, 23–33 (2013)
42. J.M. LeBeau, S.D. Findlay, L.J. Allen, S. Stemmer, Standardless atom counting in scanning transmission electron microscopy. Nano Lett. **10**, 4405–4408 (2010)
43. R. Egerton, Control of radiation damage in the TEM. Ultramicroscopy **127**, 100–108 (2013)
44. M. Azubel, J. Koivisto, S. Malola, D. Bushnell, G.L. Hura, A.L. Koh, H. Tsunoyama, T. Tsukuda, M. Pettersson, H. Häkkinen, Electron microscopy of gold nanoparticles at atomic resolution. Science **345**, 909–912 (2014)
45. G. Tang, L. Peng, P.R. Baldwin, D.S. Mann, W. Jiang, I. Rees, S.J. Ludtke, EMAN2: an extensible image processing suite for electron microscopy. J. Struct. Biol. **157**, 38–46 (2007)
46. D. Bahena, N. Bhattarai, U. Santiago, A. Tlahuice, A. Ponce, S.B. Bach, B. Yoon, R.L. Whetten, U. Landman, M. Jose-Yacaman, STEM electron diffraction and high-resolution images used in the determination of the crystal structure of the $Au_{144}(SR)_{60}$ cluster. J. Phys. Chem. Lett. **4**, 975–981 (2013)

Chapter 2
Electron Diffraction and Crystal Orientation Phase Mapping Under Scanning Transmission Electron Microscopy

Francisco Ruiz-Zepeda, J. Alejandro Arizpe-Zapata, Daniel Bahena, Arturo Ponce, and Domingo I. Garcia-Gutierrez

2.1 Introduction

Creation of new materials used for nanotechnology applications, with specific properties, could not be possible without a direct correlation with their crystalline structure; for this purpose, conventional X-ray and neutron diffraction are typically used. However, even with the advanced powerful synchrotron sources, those

---

F. Ruiz-Zepeda • A. Ponce
Department of Physics and Astronomy, University of Texas at San Antonio,
One UTSA Circle, San Antonio, TX 78249, USA

J.A. Arizpe-Zapata
Universidad Autónoma de Nuevo León UANL, Fac. de Ingeniería Mecánica y Eléctrica,
FIME, Av. Universidad S/N, Cd. Universitaria, San Nicolás de los Garza,
Nuevo León 66450, Mexico

Universidad Autónoma de Nuevo León UANL, Centro de Innovación, Investigación y
Desarrollo en Ingeniería y Tecnología, CIIDIT, Apodaca, Nuevo León, Mexico

D. Bahena
Department of Physics and Astronomy, University of Texas at San Antonio,
One UTSA Circle, San Antonio, TX 78249, USA

CINVESTAV, Mexico city, Mexico

D.I. Garcia-Gutierrez (✉)
Universidad Autónoma de Nuevo León UANL, Fac. de Ingeniería Mecánica y Eléctrica,
FIME, Av. Universidad S/N, Cd. Universitaria, San Nicolás de los Garza,
Nuevo León 66450, Mexico

Universidad Autónoma de Nuevo León UANL, Centro de Innovación, Investigación y
Desarrollo en Ingeniería y Tecnología, CIIDIT, Apodaca, Nuevo León, Mexico

Km. 10 de la Nueva Carretera al Aeropuerto Internacional de Monterrey, PIIT Monterrey,
Apodaca, Nuevo León 66600, Mexico
e-mail: domingo.garciagt@uanl.edu.mx

F.L. Deepak et al. (eds.), *Advanced Transmission Electron Microscopy*,
DOI 10.1007/978-3-319-15177-9_2

diffraction techniques are quite often limited since the diffraction is not collected from a selected region at nanometric scale. Signals obtained by powder diffraction in a sample with different crystalline phases produce overlapped peaks, and it is not possible to register simultaneously a real-time image of the analyzed region and its diffraction pattern. In this context, structure analysis by electron-beam-based diffraction techniques (selected area electron diffraction, SAED; convergent beam electron diffraction, CBED; nano beam diffraction, NBD), obtained in a transmission electron microscope (TEM), have advantages over the mentioned diffraction techniques with a spatial resolution that can be better than 1 nm. Therefore, individual phases in crystalline powders (nm size) can be examined. SAED collects the images with a parallel illumination in TEM mode; in order to ensure this illumination condition, the selected aperture used must be small enough or the analyzed crystal large enough, and SAED patterns depend basically upon aperture size and camera length. In CBED, the electrons are focused in a probe at the specimen, rather than illuminating the sample in a parallel fashion, traveling in a range of directions inside a cone. A convergent-beam pattern has an array of bright disks, one for each Bragg reflection present in the pattern. CBED is widely used for determination of structure and space group to obtain the crystal symmetry. Large angle CBED (LACBED) is typically used to study structural defects in materials; the reflections registered contain inelastic diffraction, which produces Kikuchi lines in the center of each reflection and are used mainly to determine lattice distortions in crystals. Bulk materials, with “large grains” (>100 nm) are good candidates to be analyzed by SAED and CBED; however, nanostructured materials, such as nanoparticles, 2D (monolayers), 1D (nanowires), and quantum dots, require a combination of the convergent and parallel illumination, to ensure a small illuminated region with an electron beam as parallel as possible. For this purpose, a NBD technique is used. As indicated by the name of the technique, this diffraction analysis involves using an electron probe in the nanometer scale. This technique was developed to obtain diffraction patterns from areas smaller than the ones analyzed by SAED; to achieve this goal, it is necessary to reduce the area illuminated by the electron beam to the smallest possible. For this reason, NBD obtained simultaneously in STEM mode becomes a powerful technique to study the crystalline structure in nanomaterials. Originally proposed by J.M. Cowely, he stated that electron diffraction patterns may be obtained from regions 1 nm or less in diameter when a field emission gun is used to form a very small bright source, as is usual in STEM instruments [1]. In order to achieve this goal, Cowley et al. [2, 3] showed that the use of a convergent beam in the STEM mode, combined with the use of a small aperture and optimum defocus of the electron beam on the specimen, produced an electron probe of approximately 1–2 nm; it also reduced the size of the diffraction disks, making them to look more like diffraction points in a SAED [2, 4]. The procedure proposed to ensure the formation of this small electron probe relied importantly on varying the strength of the pre-specimen lenses, which are located just above the specimen plane; this provided a greater flexibility to the entire illumination system, due to the ability of these lenses to control the convergence angle of the electron beam on the specimen plane [2]. This small electron probe is useful to determine local structure in materials with complicated micro- and nanostructures, including interfaces. As mentioned, this technique uses a parallel electron beam of nanoscale dimensions, with the parallel illumination achieved by reducing the crossover's convergence angle of the condenser lens 2 (C2), using condenser lens 3 (C3), taking this crossover point to the focal plane of the objective lens, producing a parallel illumination on the specimen plane. Using such configuration, in combination with a condenser aperture 2 of 10 μm, an electron probe of approximately 1 nm was achieved [2, 4]. This electron probe is capable to illuminate an area much smaller than the areas illuminated using SAED (~100 nm). The diffraction patterns acquired with this technique are very similar to the SAED patterns, being the major difference the size of the region where the diffraction pattern is coming from, which is directly defined by the electron probe size in this technique [1]. One of the first applications of this D-STEM technique was used to study the average helicity and the local variations of helicity of the individual carbon nanotubes within the ropes of single-walled carbon nanotubes [5]. Kolb et al. followed this approach in a Tecnai F-30 field emission gun (FEG) TEM/STEM equipped with a condenser aperture 2 of 10 μm to obtain a quasi-parallel beam for coherent electron diffraction while in STEM mode and were able to generate probe sizes between 15 and 50 nm at the specimen [6]. Subsequently, He and Nelson using a Libra 200 FEG obtained a parallel beam with a probe size of approximately 80 nm altering the condenser defocus [7]. More recently, Alloyeau et al. proposed a method combining STEM illumination and NBD on a JEOL 2010F using a four-stage condenser system getting a probe size around 1–2 nm, but with a very challenging method of astigmatism correction of the probe [8]. One of the latest reports related to improving this technique was developed with the goal of increasing the certainty of the area analyzed, as well as to a subsequent automation, to maximize the speed in the analysis of a greater number of nanostructures [9]. In their work, Ganesh et al. report electron probes with parallel illumination between 1 and 2 nm formed in a JEOL 2010F; this electron probe is optimized in STEM mode, which allows to record images in bright field or in dark field of a high quality. The high quality of the images permits to locate the electron probe right on top of the nanostructure of interest with great accuracy, allowing for the recording of high-quality electron diffraction patterns. In both cases, the microscopes used had a four-stage condenser system (C1, C2, C3, and condenser minilens, CM), which is necessary to achieve smaller electron probe sizes. Ganesh et al. called this technique D-STEM [9]. It is stated by Ganesh et al. that in D-STEM, the first condenser lens (C1) is strongly excited to produce a strong demagnification of the electron source; furthermore, the smallest condenser aperture 2 available is used to ensure low convergence angle on the specimen, in order to obtain sharper maxima in the diffraction plane. Using these parameters, results in convergence angles smaller than 1 mrad also reducing the area of illumination [9]. The major distinction of D-STEM among the other techniques obtaining diffraction patterns in STEM mode is that in D-STEM, the CM is used at maximum excitation. Under this condition, as stated by Ganesh et al., by adjusting the C3 lens such that a demagnified source is formed just before the CM, the strongly excited CM forms a crossover close to the front focal plane of the objective prefield lens. This results in a nearly parallel illumination on the specimen. The strong excitation of the CM also reduces the size of the crossover formed before the objective prefield lens, consequently resulting in a reduction of the probe size on the specimen [9]. This research group has extensively used this D-STEM technique, applying it to a wide range of nanostructured materials, like downscaling nanoscale Cu interconnects used in the semiconductor industry, where this technique, in combination with precession microscopy, was determinant in the acquisition of quantitative local texture information in damascene copper interconnects (1.8 μm–45 nm in width) with a spatial resolution of less than 5 nm. Their results revealed strong variations in texture and grain boundary distribution of the copper lines upon downscaling, observations that have been very useful for the semiconductor industry [10–12]. This D-STEM technique has also been used by this research group to study lithium-rich layered oxide materials used as cathode materials in Li-ion batteries [13, 14]. They analyzed lithium-rich layered $\mathrm{Li[Li_{1/32\mathit{x}/3}Mn_{2/3\mathit{x}/3}Ni_{\mathit{x}}]O_2}$ ($0 < x \leq 1/2$) oxide cathodes, which show promising characteristics as a potential candidate for Li-ion batteries due to their high capacity, and they were able to observe how the oxygen loss from the lattice during the first charge, and the discharge capacity in subsequent cycles increase with increasing lithium content. D-STEM was fundamental in the observation of a transition in the studied samples from an $\mathrm{R\bar{3}m}$ structure to a C2/m structure with increasing lithium content and decreasing nickel to manganese ratio, indicating that the maximum oxygen loss and discharge capacity were achieved with a single C2/m phase [14]. This D-STEM technique has also demonstrated its use as a useful tool to acquire nanoscale orientation maps in the TEM, observing an order of magnitude improvement in spatial resolution, compared against the conventionally used technique for this application. Using this technique, it was possible to quantify the five-parameter grain boundary distribution in nanocrystalline materials, like nanocrystalline Cu thin films [15].

2.2 Evaluating the Parameters Affecting the Probe Size and Convergence Angle

Different parameters were identified to have a possible impact on the convergence angle, α, of the electron beam; among these we can mention condenser aperture 2 size, spot number, camera length, CM excitation, gun lens value, and extraction voltage. These parameters were selected based on the different reports found in the literature consulted [1–9, 16–18]. All the evaluation experiments were performed on a monocrystalline silicon [100] sample, using a TEM FEI Titan G^2 80–300 operated at 300 kV, with scanning transmission electron microscopy (STEM) capabilities and equipped with a high-angle annular dark-field (HAADF) detector from Fishione, a bright-field (BF) STEM detector from Gatan, an annular dark-field (ADF) STEM detector from Gatan, and an EDAX energy dispersive X-ray spectroscopy (EDXS) detector. The reference monocrystalline Si [100] sample was mounted on a double-tilt TEM holder for all performed analysis. Once the sample

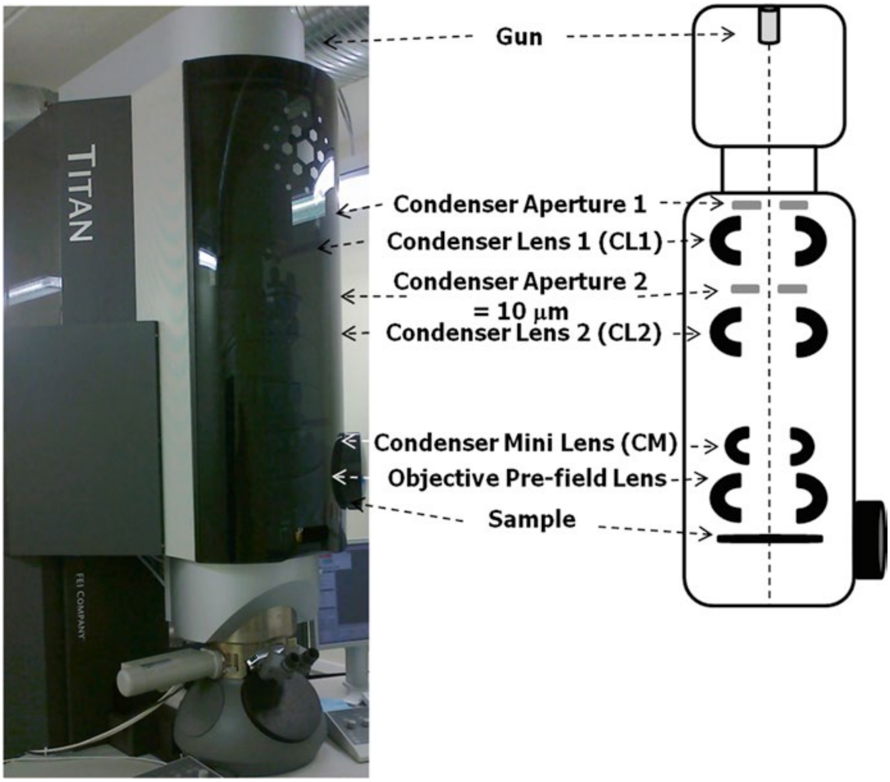

Fig. 2.1 Diagram of the TEM indicating the location of the relevant features used during the experiments

was introduced into the microscope, a conventional alignment of the microscope in bright-field mode was performed. Afterward, the proper alignment procedure was followed in the STEM mode. Figure 2.1 shows a diagram of the TEM, indicating the location of the relevant features used during the studies.

Once the microscope was properly aligned, data acquisition continued, starting with the experiments to measure the reference parameters using the monocrystalline Si reference sample previously mentioned. Variation of the different parameters was carried out based on the results obtained during the literature search and then selecting those parameters known to have a greater impact on the convergence angle. The parameters varied, in the following order, were camera length, condenser aperture 2 size, CM excitation, spot size number, gun lens number, and extraction voltage. The followed methodology can be summarized in Scheme 2.1.

This methodology was developed based on the feasibility of producing a measurable change on the diffraction pattern. All the experimental conditions analyzed are presented and summarized in Appendix.

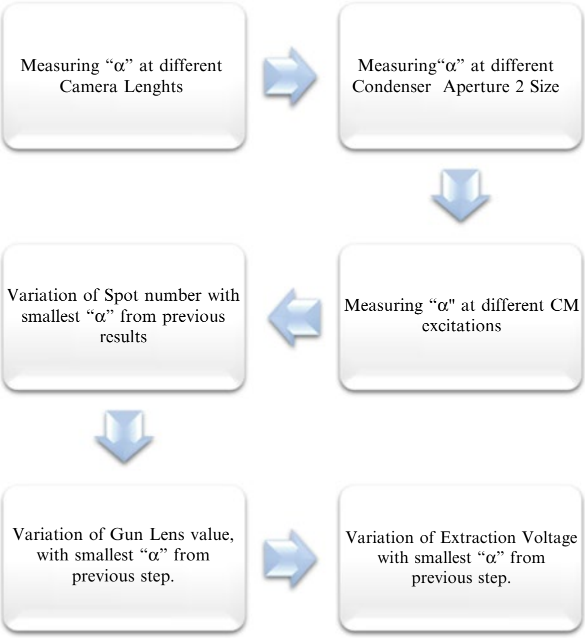

Scheme 2.1 Methodology followed for the variation of the different parameters in the TEM to evaluate their effect in the convergence angle, α

After the data was acquired, following the previous methodology, the convergence angle, α, was calculated for all the experiments performed. The methodology and equation followed for the calculation of the convergence angle was the same reported in Ref. [9]. As it has been mentioned earlier, the value of the convergence angle is in very close relationship to the electron probe diameter that will be used to illuminate the sample; thus, calculating the effect of the different parameters on the convergence angle enables the opportunity to make a correlation between the effect of the parameters varied and the electron probe size as well. In order to calculate the convergence angle obtained in each experiment, (2.1) was used:

$$2\alpha = \frac{X}{Y}\left(\frac{\lambda}{d_{hkl}}\right) \tag{2.1}$$

In this equation X represents the diameter of the central beam (transmitted beam) in the electron diffraction pattern; Y represents the distance between the center of the transmitted beam and the center of diffracted beam hkl; λ is the wavelength of the electron beam, and d_{hkl} is the interplanar distance associated to the hkl planes.

For the actual calculation of the convergence angle from the electron diffraction patterns acquired in the different experiments, the software Gatan DigitalMicrograph (DM) was used in order to perform the different measurements required. The diffraction patterns acquired corresponded to the [100] zone axis of the Si monocrystalline sample used as reference in this study.

2.2.1 Camera Length Variations

The following diffraction patterns shown in Fig. 2.2 were acquired in TEM mode and correspond to the modification of the camera length of the microscope. Figure 2.3 shows the graph of the convergence angle vs. camera length; in this graph, it can be observed that a decrement in the camera length produces a

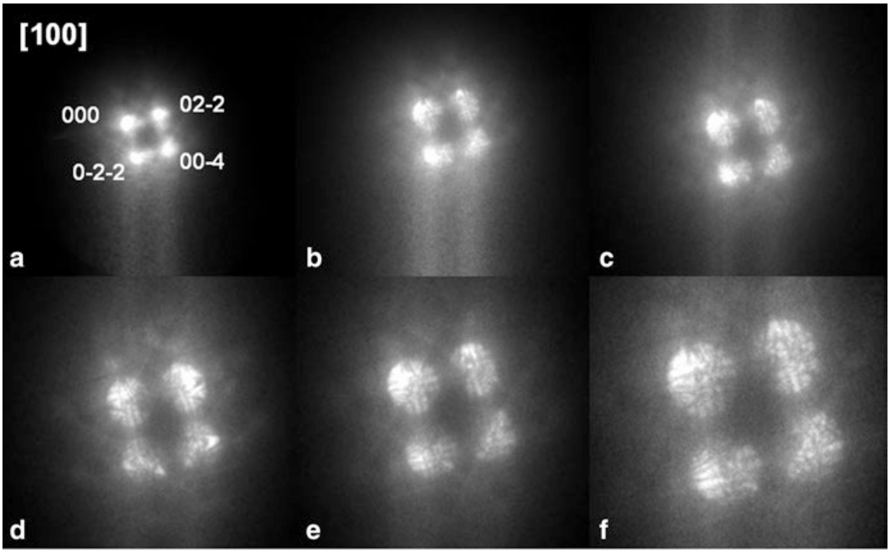

Fig. 2.2 Electron diffraction patterns in TEM mode from the Si monocrystalline sample acquired with a camera length of (**a**) 108 mm, (**b**) 128 mm, (**c**) 160 mm, (**d**) 196 mm, (**e**) 245 mm, (**f**) 301 mm

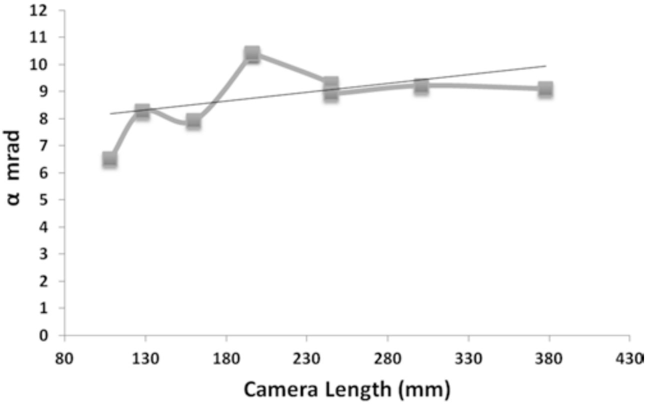

Fig. 2.3 Camera length vs. convergence angle, α (TEM mode)

decrement in the convergence angle; however, this trend is not observed in all the points. These small variations in the convergence angle, and the lack of a clear trend on the effect of varying the camera length, could be related to some of the camera lengths not being properly calibrated, particularly because the lenses involved in changing the camera length are the post-specimen lenses, which in theory should not affect the convergence angle on the sample [18]. Nevertheless, variations in the camera length had a major impact on the practical aspects of the acquisition of the diffraction patterns with the charge-coupled device (CCD) camera of the microscope, aspects that will become very important in the actual acquisition and recording of data in the D-STEM mode.

2.2.2 Condenser Aperture 2 Size Variations

Figure 2.4 shows the results for the convergence angle calculated from (2.1) against the different condenser aperture 2 sizes available in the microscope used. A clear decrement in the convergence angle can be observed as the condenser aperture 2 size decreases. Leading to a reduction in the convergence angle down to 0.85 mrad, which corresponds to a reduction close to 70 % compared to the highest value. The observed results agree with previous reports found in the literature [9, 17–19] and also shows that the condenser aperture 2 size is one of the parameters with the highest impact on the convergence angle. Figure 2.5 shows the electron diffraction patterns used to calculate the convergence angles for these experiments.

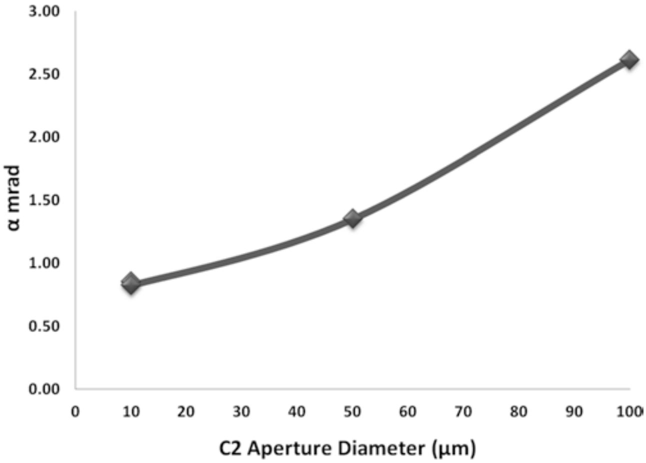

Fig. 2.4 Condenser aperture 2 diameter vs. convergence angle, α (TEM mode)

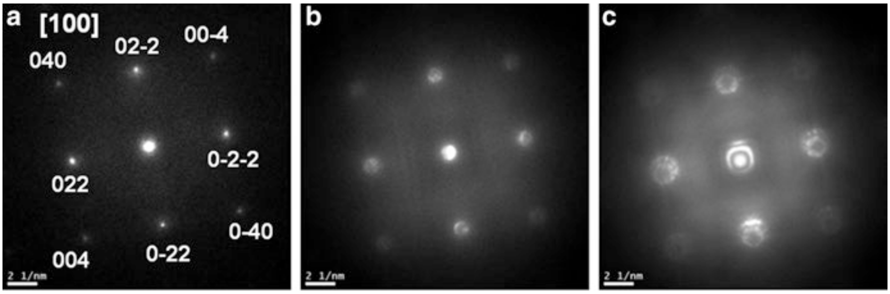

Fig. 2.5 Electron diffraction patterns in TEM mode from the Si monocrystalline sample acquired with a condenser aperture 2 size of (**a**) 10 μm, (**b**) 50 μm, and (**c**) 100 μm

Fig. 2.6 Variation of condenser minilens (CM) excitation: (**a**) CM slightly excited and (**b**) CM highly excited. Scale bar equals 10 nm^{-1}

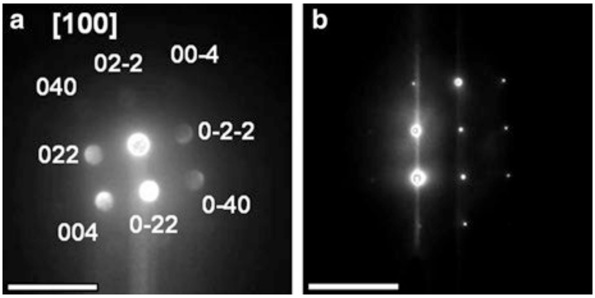

2.2.3 *Condenser Minilens (CM) Excitation Variation*

Changing the excitation of the CM in a TEM Titan G^2 80–300 is related to changing from one beam mode called "nanoprobe," where the CM is slightly excited, to a beam mode called "microprobe," where the CM is highly excited. When working on STEM mode, the CM is slightly excited; however, even in STEM mode, the beam mode can be changed to "microprobe," thus exciting the CM while in STEM mode. Figure 2.6 shows the two different cases; Fig. 2.6a shows the diffraction pattern of the Si monocrystalline sample in the [100] zone axis with a condenser aperture 2 size of 50 μm, a camera length of 0.196 mm, a gun lens value of 5, a spot size number of 9, and extraction voltage of 4,400 V with the CM slightly excited, while Fig. 2.6b shows the diffraction pattern for the same conditions with the CM highly excited.

Under these conditions, for the case of the CM slightly excited, the convergence angle calculated was approximately 9 mrad, while for the highly excited case, the convergence angle calculated was approximately 1.5 mrad. Once the CM was highly excited, there were seven different levels available to increase the strength of the CM. Figure 2.7 shows the graph with the results of increasing the strength of the CM and the effect on the convergence angle.

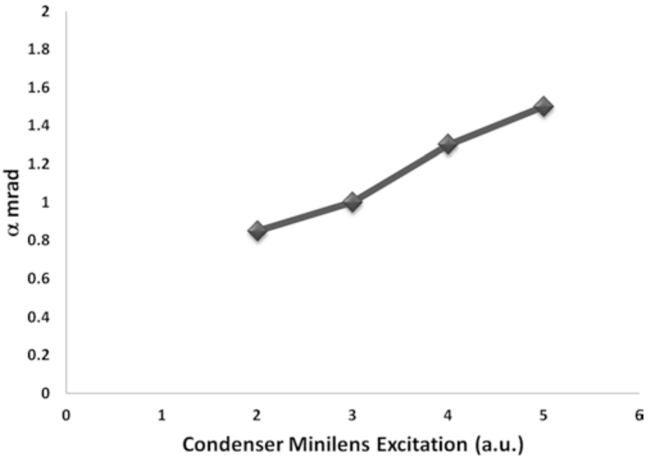

Fig. 2.7 Condenser minilens excitation vs. convergence angle, α (STEM mode)

Increasing the strength of the CM (decreasing the arbitrary units number) decreased the convergence angle value; with the highest excitation of the CM, it was possible to obtain the smallest convergence angle value of 0.85 mrad. This is consistent with what was observed by Ganesh et al., since they observed the same relationship between the CM excitation and the convergence angle; highly excited CM produced smaller convergence angles [9].

2.2.4 *Spot Number Variation*

For the variation of the spot number, a condenser aperture 2 of 50 μm was used, with a camera length of 0.196 m; the CM was highly excited with a strength of 5 (arbitrary units); a gun lens value of 5 (arbitrary units) and an extraction voltage of 4,000 V were used for the reported experiments. Changing the spot size in the TEM instrument used involves the variation of the current through C1 lens, which has the effect on the beam of changing the crossover of the electron beam position between C1 lens and C2 lens; higher spot number values bring the crossover closer to C1 lens [18]. Figure 2.8 shows the electron diffraction patterns of three different spot numbers; in the image no clear effect on the convergence angle can be observed.

Figure 2.9 shows the graph for the results of varying the spot number and their effect on the convergence angle; these results indicate a slight decrement on the convergence angle as the spot number decreases, which means a displacement of the crossover of the electron beam closer to the C2 lens. The main effect of varying the spot number was observed on the intensity of the electron beam; the smaller the spot number, the higher the intensity of the electron beam; this had a major impact at the time of recording the diffraction pattern on the CCD camera, because very

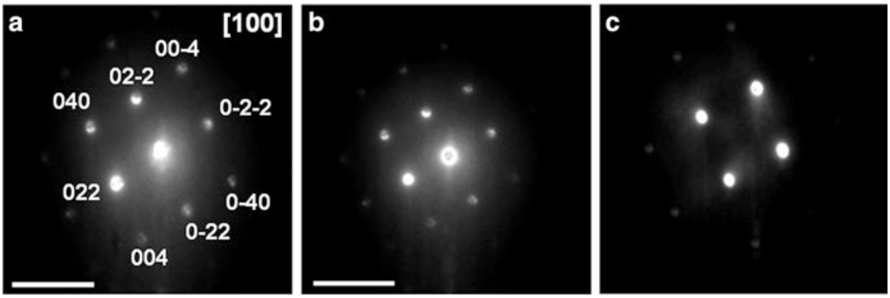

Fig. 2.8 Effect on the convergence angle by the variation of the current through C1 lens (spot number): (**a**) spot number 3, (**b**) spot number 4, and (**c**) spot number 5. Scale bar equals 10 nm^{-1}

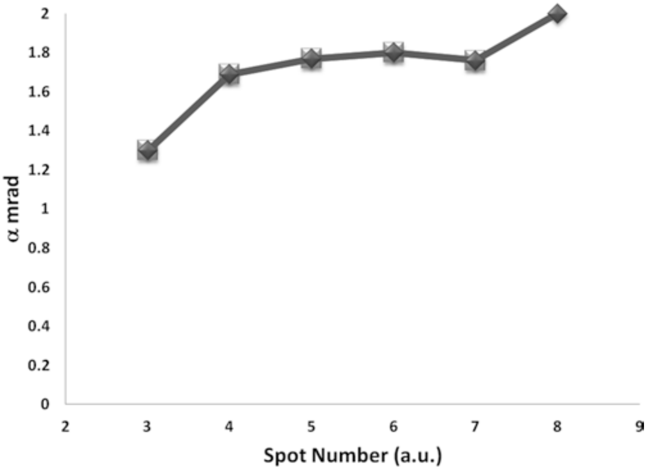

Fig. 2.9 Spot number vs. convergence angle, α (STEM mode)

intense electron beams can damage the camera. This relationship observed implied a compromise between a smaller convergence angle and a bright electron beam which could damage the CCD camera.

2.2.5 Gun Lens Value Variation

Varying the gun lens value involves changing the position of the crossover of the electron beam between the acceleration ring of the microscope and the C1 lens. Changing this parameter has no clear effect on the convergence angle, as can be seen in Fig. 2.10. However, just like in the case previously described, this parameter has a major influence on the electron beam intensity reaching the CCD camera, which makes it an important parameter determining the acquisition conditions for the electron diffraction patterns.

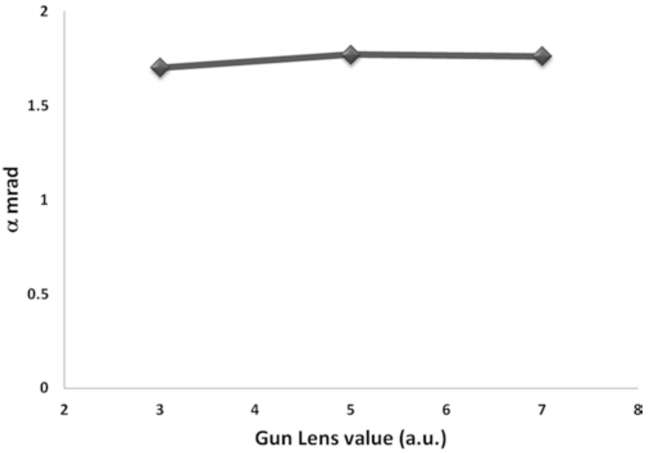

Fig. 2.10 Gun lens value vs. convergence angle, α (STEM mode)

2.2.6 *Extraction Voltage Variation*

This parameter had no clear effect on the convergence angle, just like varying the gun lens value previously described; likewise, it was an important parameter controlling the electron beam intensity, which, as it has been already mentioned, is an important factor determining the final acquisition conditions for the electron diffraction patterns.

2.3 STEM Diffraction (D-STEM) Analysis of Semiconductor Nanoparticles

After these sets of experiments were performed, and the effect of each studied parameter on the convergence angle was determined, an optimal combination of these parameters was established to ensure the smallest convergence angle possible with the highest electron beam intensity that didn't damaged the CCD camera used for the data acquisition. Based on the experimental results obtained, it was determined for a TEM Titan G^2 80–300 that the combined used of a condenser aperture 2 size of 10 μm, a camera length value of 0.196 m, a beam mode of "microprobe" (CM highly excited) with the smallest convergence angle available, a spot number 3, a gun lens value of 5, and an extraction voltage of 4,000 V allows to obtain an electron beam with a convergence angle of approximately 0.85 mrad and a diameter of approximately 2 nm.

Using the conditions previously described, electron diffraction patterns in STEM mode were acquired from lead chalcogenide nanoparticles (PbSe, PbTe, and PbS),

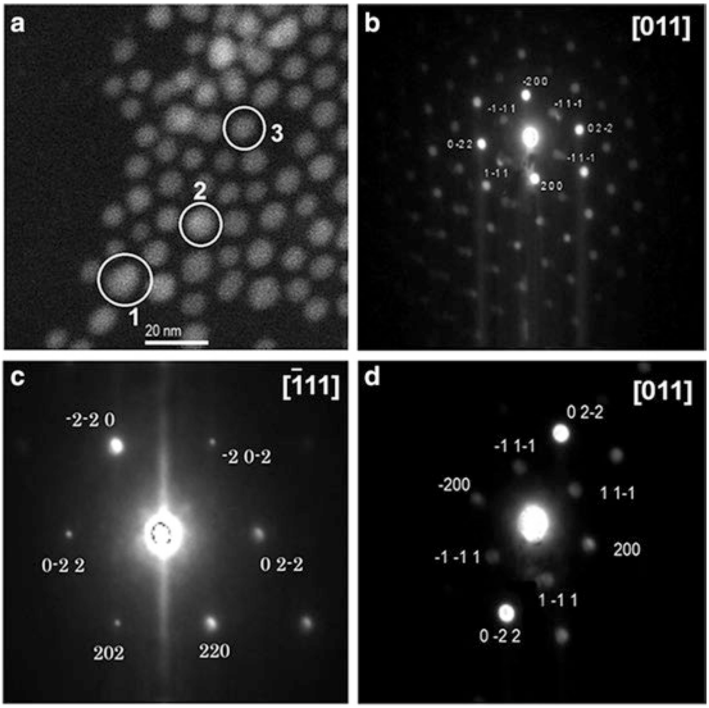

Fig. 2.11 (**a**) HAADF image acquired with the D-STEM conditions indicating the three different PbSe nanoparticles analyzed. Electron diffraction pattern corresponding to the nanoparticles indicated by (**b**) number 1, (**c**) number 2, and (**d**) number 3

to determine the crystal structure from isolated nanoparticles. These nanoparticles present different morphologies, cubic and quasi-spherical, and have a size between 3 and 20 nm, depending mostly on the reaction time used for their synthesis, as reported in the literature [20].

Figure 2.11 shows the results of the analyses performed on PbSe nanoparticles. Figure 2.11a shows the HAADF image acquired with the parameters previously described; in this image, we can clearly observe PbSe nanoparticles with sizes between 12 and 5 nm. Three different nanoparticles are circled and labeled with the numbers 1, 2, and 3, while Fig. 2.11b–d shows the electron diffraction pattern corresponding to these nanoparticles, respectively.

Electron diffraction patterns from isolated nanoparticles were successfully acquired using the D-STEM conditions previously described. In this case, the nanoparticles analyzed had a size of approximately 12, 10, and 7 nm for nanoparticles 1, 2, and 3, respectively. All three nanoparticles presented the FCC crystal structure (JCPDS # 06-0356), while nanoparticles 1 and 3 were oriented on the [011] zone axis, and nanoparticle 2 was oriented on the $\left[\bar{1}11\right]$ zone axis.

Figure 2.12 shows the results for the analyzed PbTe nanoparticles; Fig. 2.12a, c show HAADF images of the PbTe nanoparticles, and marked by a circle are the

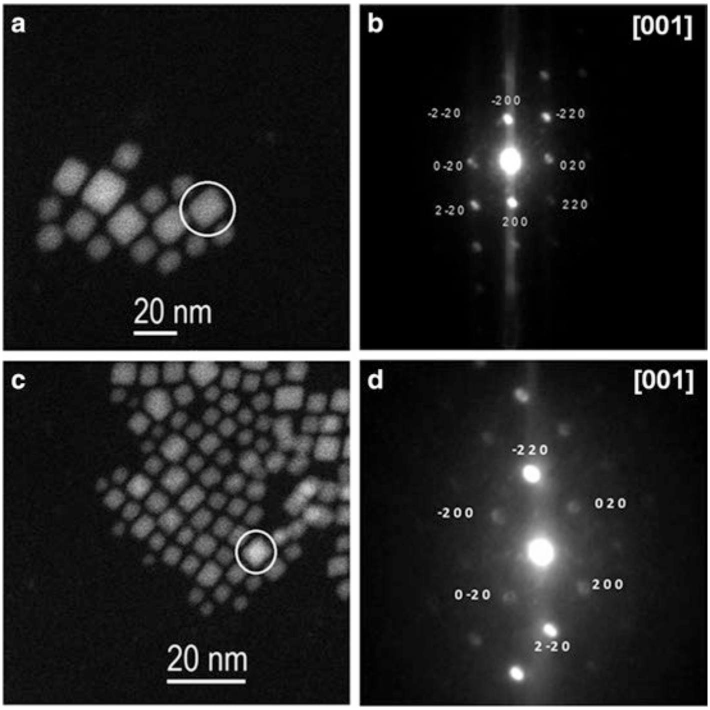

Fig. 2.12 (**a**, **c**) HAADF image of the analyzed PbTe nanoparticles with sizes between 5 and 20 nm. (**b**, **d**) D-STEM electron diffraction patterns from the nanoparticles marked by the circles in figure (**a**, **c**), respectively

nanoparticles from which an electron diffraction pattern was acquired. Their corresponding electron diffraction patterns are shown in Fig. 2.12b, d. In this case, the nanoparticles analyzed had a size of approximately 10 and 15 nm, and both presented a cubic morphology. The D-STEM electron diffraction patterns confirmed their FCC crystal structure (JCPDS # 38-1435) and that both were oriented in the [001] zone axis.

Figure 2.13 shows the results for the analyses of PbS nanoparticles; in this case, the nanoparticles presented a quasi-spherical morphology, with sizes between 3 and 8 nm, as can be observed in the HAADF image in Fig. 2.13a. Figure 2.13b, c show the D-STEM electron diffraction patterns acquired from the nanoparticles marked by the circles in Fig. 2.13a. The smallest of the nanoparticles analyzed had a size of approximately 3 nm and could be analyzed without any complication with the D-STEM conditions used, which suggests an electron probe smaller than 3 nm. Both nanoparticles presented the FCC crystal structure (JCPDS # 050592), while nanoparticle 1 was oriented in the [011] zone axis and nanoparticle 2 was oriented in the $\left[1\bar{1}\bar{2}\right]$ zone axis.

The current study allowed us to identify the effect of different parameters of the microscope in the convergence angle, α, of the electron beam; it was also possible

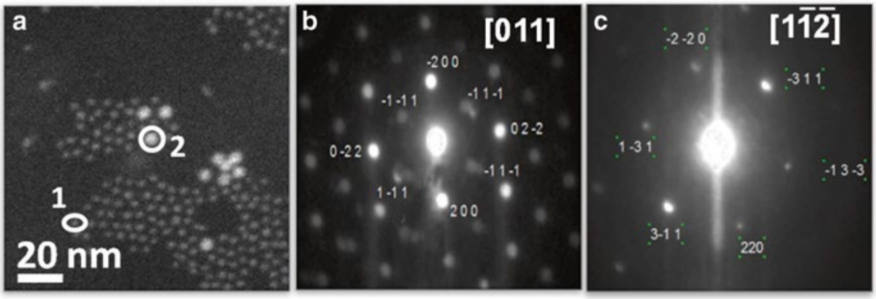

Fig. 2.13 (**a**) HAADF image of the PbS nanoparticles analyzed. (**b**) D-STEM electron diffraction pattern from the nanoparticle marked with number 1; this nanoparticle had a size of approximately 3 nm. (**c**) D-STEM electron diffraction pattern from nanoparticles marked with number 2

to identify the optimum conditions that allow obtaining a convergence angle below 1 mrad with electron beam intensities that do not damage the CCD camera and permit to obtain HAADF images of a sufficient quality to identify isolated nanoparticles with size around 3 nm and to locate the electron beam on top of these nanoparticles to record their electron diffraction pattern. The electron probe size obtained with the D-STEM conditions studied was smaller than 3 nm, since nanoparticles of this size were easily identified and analyzed. These results establish the effect of different parameters of a TEM on the convergence angle, in order to identify the optimum conditions to perform D-STEM studies.

In the following section, an example of the D-STEM technique in a Cs-corrected microscope is presented.

2.4 STEM Diffraction (D-STEM) Using a Cs-Probe Corrector

Aberrations are artifacts produced by the imperfections on the equipment. Astigmatism and coma can be easily corrected using magnetic quadrupoles. Spherical aberrations, denoted by Cs, are much harder to correct, but the corrections are necessary to produce images of atomic resolution, particularly in the STEM mode, when the corrections are intended in the electron probe itself. The objective lens, located after the sample in a TEM, focuses the electron beam, which mathematically can be described by the Fourier transform of the wave at the exit of the sample. Imperfections in the objective lens are the source of Cs, and additional optics is needed after this element to make the appropriate corrections. A very useful tool is the Ronchigram which is a shadow image formed by a focused and stationary electron probe on amorphous material. The quality and resolution of the

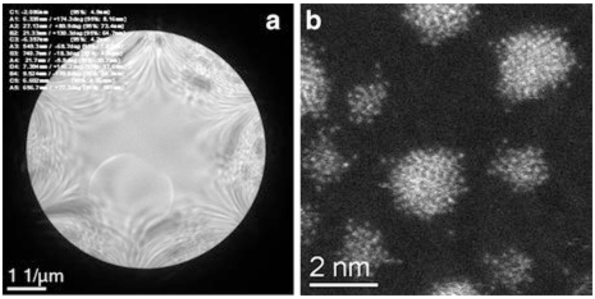

Fig. 2.14 (**a**) Ronchigram using a Cs-probe corrector, (**b**) Cs-probe corrected HAADF-STEM image of a thiol-protected gold nanoparticle

STEM images depend directly on the proper alignment of the Ronchigram. It is easily observable in FEG microscopes, but it might be difficult to obtain in the lanthanum hexaboride (LaB6) filaments, because the effective probe size is too large, and therefore both the spatial resolution and the brightness decrease dramatically, even using microscopes with voltages higher than 200 kV. All the parameters used to adjust different sets of contrast, spatial resolution, etc., are directly related to the Ronchigram. The Ronchigram can be registered in a CCD camera (Fig. 2.14). The electrons coming out of the sample can be observed directly in a circle called the Gabor hologram, the Ronchigram, or the central zero-order disk of the CBED pattern.

The combination of NBD and STEM (diffraction-STEM, D-STEM) is important in order to study nanoparticles with different morphologies and crystalline structures, including compound nanostructures, like the ones previously discussed, in which lattice parameters and lattice distortions affect their properties. In addition, probe-corrected microscopy plays an important role in D-STEM because the electron probe governs the NBD in the condenser lens system. Setting up the proper combination between STEM imaging and quasi-parallel beam diffraction (D-STEM) in a Cs-probe-corrected JEOL ARM microscope has been used to study metallic nanoparticles and thin-film nanostructured samples. D-STEM patterns are obtained by positioning the beam in the STEM image using the Digiscan control; the scan is stopped in a region of interest, and subsequently the pattern is recorded in a CCD camera. All the parameters previously discussed affecting the convergence angle, α, have the same effect both in uncorrected and Cs-probe corrected microscopes; however, since D-STEM mode works in the diffraction plane, in Cs-probe corrected microscopes, the overlapping of the convergent disks can be additionally optimized by a compensation of the latest condenser lens (C3) and the excitation of the adaptor lens (ADL) in the hexapole coils of the CEOS corrector; subsequently the beam is aligned by the beam tilt and beam-shift deflectors, providing additional parameters that allow for a better and more precise control on the convergence angle. The ADL is the last lens in the Cs corrector, which contributes in the STEM mode to make the beam as convergent as possible; hence, varying the strength in this lens directly affects the convergence angle of the beam. As previously mentioned, changing the

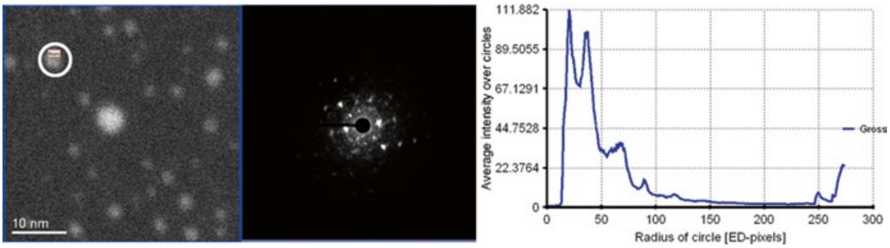

Fig. 2.15 (*Left*) D-STEM pattern obtained from a single gold cluster (*white circle*), (*right*) radial distribution function of the D-STEM pattern to determine the crystalline structure of the cluster

values of C3 and ADL implies an adjustment in the beam shift and beam tilt to realign the beam. A set of values used in the C3 and ADL for the D-STEM mode are presented in Appendix.

D-STEM studies on a Cs-probe corrected microscope were performed on Au clusters, in which the number of atoms can be controlled very precisely. Acquiring Au clusters extracted from toluene by thiolate interaction is a promising way to have a precise control of the number of atoms [21]. The gold clusters are stabilized by thiolate groups; the atomic arrangement details and their precise crystalline structure are still under study. In Fig. 2.15, small clusters with different number of atoms are showed. Acquiring a diffraction pattern of each individual cluster under CBED or SAED is not possible. D-STEM in a Cs-probe corrected microscope is proposed in the current section to allow the systematic study of the structure transformation of these clusters under electron beam irradiation. The samples studied by STEM are very sensitive to the electron beam irradiation. Samples exposed to a continuous broad illumination are modified by the elimination of the thiolate groups, and subsequently a coarsening evolution takes place. The changes in structure can be studied by D-STEM, in which the radial distribution function is obtained, and it can be compared to the radial distributions calculated theoretically, as shown in Fig. 2.16 [22].

As can be observed in Fig. 2.15, Au clusters smaller than 2 nm could be analyzed, which suggests an electron probe size smaller than 2 nm, with convergence angles smaller than 1 mrad.

Combining this D-STEM capability in a Cs-probe corrected TEM with precession electron diffraction capabilities opens up the possibility to obtain crystallographic maps from samples with spatial resolution of approximately 1 nm or below.

In the following sections, different applications of the D-STEM technique coupled with precession electron diffraction and automated diffraction pattern recognition software are presented and their advantages discussed.

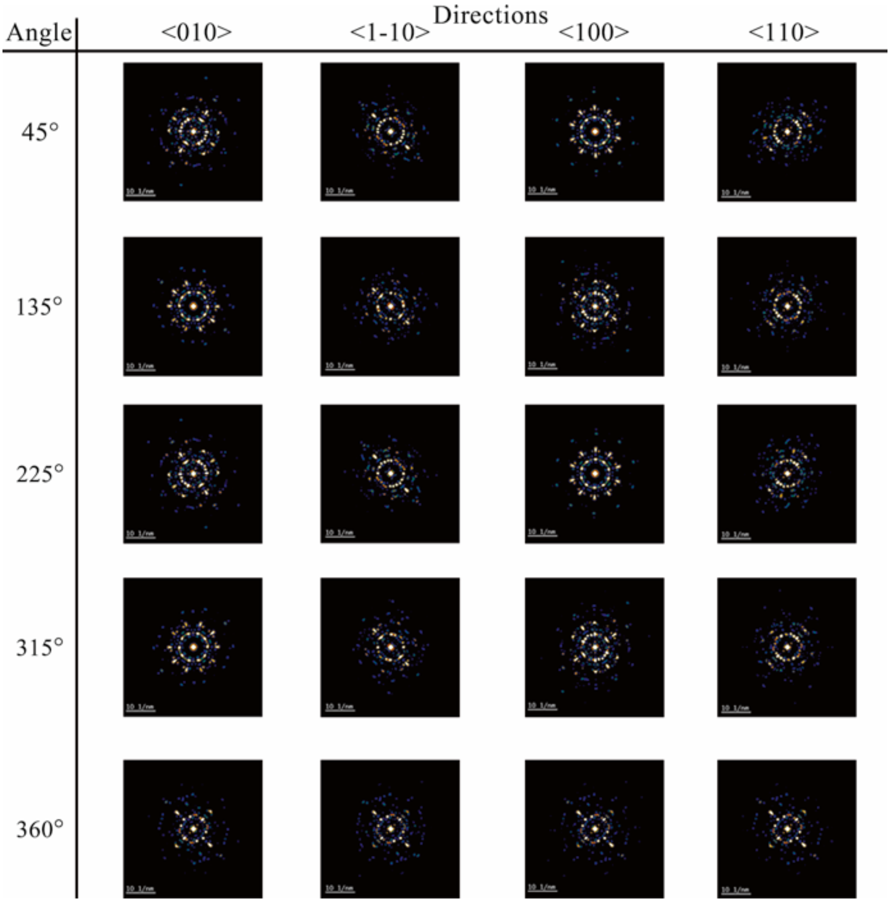

Fig. 2.16 Map of rotations of the simulated electron diffraction patterns obtained from the calculated Au144(SR)60 model. Simulated electron diffraction patterns were used to compare with the experimental ones

2.5 Precession Electron Diffraction

Paul Midgley and Roger Vincent developed a diffraction technique to achieve near-kinematical conditions in the diffraction pattern in order to measure the diffracted intensities for structure determination [23]. In precession electron diffraction (PED), the beam tilt coils are used to rock the electron beam in a conical fashion around a pivot point in the specimen plane. Then the image shift coils are used to de-scan the electron beam and obtain a quasi-kinematical diffraction pattern on the diffraction plane (Fig. 2.17a). The precession frequency is variable, but usually is adjusted to 50 or 100 Hz. In PED the beam can be parallel or convergent, and it is tilted away

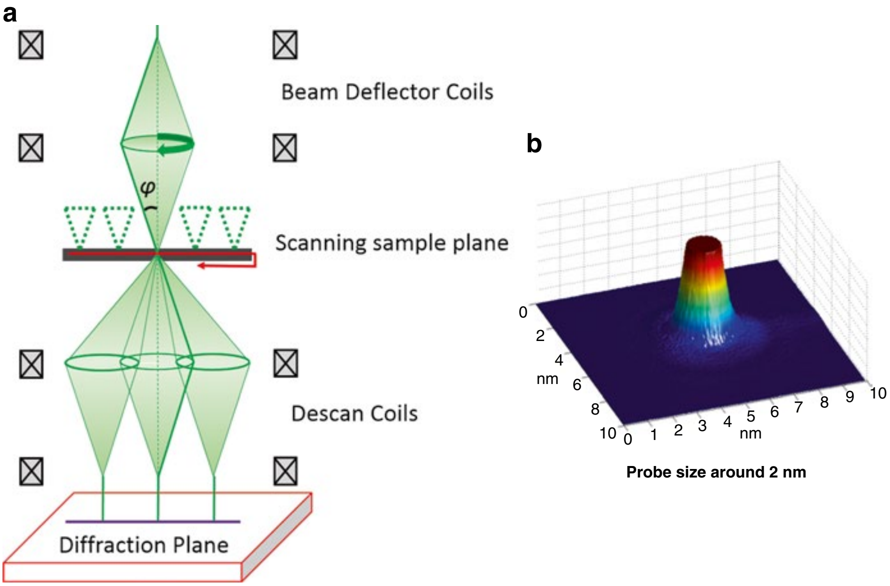

Fig. 2.17 (**a**) Schematic representation of the precession geometry in a TEM. The incident electron beam is tilted and rotated in a conical hollow surface around the optical axis using the beam tilt coils. The diffracted intensities are then de-scanned in a complementary way, with the image shift coils, so that the diffraction pattern appears as a stationary spot pattern. (**b**) Probe size of around 2 nm in NBD mode. The probe size will define the spatial resolution of the mapping

from the optical axis forming the precession angle, φ, typically between 0° and 3°. During the precession of the electron beam, the reflections are scanned by the Ewald sphere with only a few reflections in Bragg condition at each moment, making the dynamical effects less pronounced in the diffraction pattern obtained, which represents the sum of a continuous set of electron diffraction patterns [24]. The distributions of intensities in the diffraction spots are closer to be proportional to the square of the structure factor, and the forbidden reflections and the multiple scattering are reduced considerably. For these reasons, a more refined analysis of the structure can be obtained with PED. Increasing the precession angle will make the Ewald sphere touch more points in the reciprocal space, and more diffraction spots will be displayed in the diffraction pattern.

One of the applications of PED is coupling it with fast electron diffraction acquisition and pattern matching [25, 26]. This technique has become a useful tool to obtain crystal orientations and phase maps in relative short times [27, 28]. The principle consists in forming a small probe and then rastering the beam through the area of interest on the sample, obtaining and recording with an ultrafast (200 fps) external CCD camera an electron diffraction pattern at each step of the scanned area. Every acquired electron diffraction pattern is stored in a computer to be later compared to pre-calculated templates: the diffraction pattern is indexed using cross-correlation to select the best match. The indexing result of the whole set of diffraction patterns can be displayed as a phase or an orientation map of the scanned area [29]. In a modern TEM with a FEG tip, a small probe of around 1–2 nm size (Fig. 2.17b) can be formed in NBD mode by using a small condenser aperture; this will yield a high spatial resolution of the map. If the sample is thick, however, the trade-off of selecting the smallest spot size and aperture is to preserve enough brightness in the diffraction pattern. When using precession, the effective focused beam size on the specimen will suffer from beam broadening due to spherical aberration for the non-axial trajectories, and this will be more noticeable when increasing the precession angle [26]. At the end, the spatial resolution of the orientation/phase map will depend on the effective beam size and on the scanning step chosen. On the other hand, the angular resolution obtained in the orientation maps will depend on the angular grid used for the generation of the templates. And since the spot diffraction patterns are not sensitive to crystal tilts of less than 1°, usually values are given between 0.5° and 1° [26]. There is, though, the possibility to select a smaller sample value by increasing the number of generated templates so that between a given template and the closest one, there is 0.2°–0.5° [30]. To avoid duplicities in orientation assignation, it is necessary to use precession angles lower than 1° [29]. This has to be taken into consideration when choosing the precession angle for phase or orientation mapping. Hence the crystal orientation phase mapping consists in two main steps: the fast acquisitions of spot patterns and the reliable orientation identification. This brings the necessity of hardware equipment additionally implemented in the microscope and software to carry out the analysis.

The degree of matching between an experimental diffraction pattern and a calculated one will be given by the following equation [29]:

$$Q\left(i\right)=\frac{\sum_{j=1}^{m}P\left(x_j,y_j\right)T_i\left(x_j,y_j\right)}{\sqrt{\sum_{j=1}^{m}P^2\left(x_j,y_j\right)}\sqrt{\sum_{j=1}^{m}T_i^2\left(x_k,y_j\right)}} \tag{2.2}$$

The pattern is represented by the intensity function $P(x, y)$ while every template i is given by the function $Ti(x, y)$. The highest Q value corresponds to the solution.

In this way, the quality of the pattern matching can be evaluated by the assigned pixel values of the index maps. Additionally, a reliability index value is determined between the two highest optimum solutions Q_1 and Q_2 of the matching $R = 100(1 - Q_2/Q_1)$. A reliability index value will be low when more than one orientation or phase is contained in a diffraction spot pattern. This value is assigned to each pixel corresponding to an indexed diffraction pattern; in this way a reliability map can be generated. A lower value will correspond to a darker pixel, and a higher value will correspond to a brighter pixel. The range will depend on the maximum reliability value calculated.

To reconstruct a bright-field image of the objet, the average intensity is calculated in a disk that surrounds the transmitted beam from the recorded diffraction pattern (Fig. 2.18). The inner part of the transmitted beam saturates leaving the

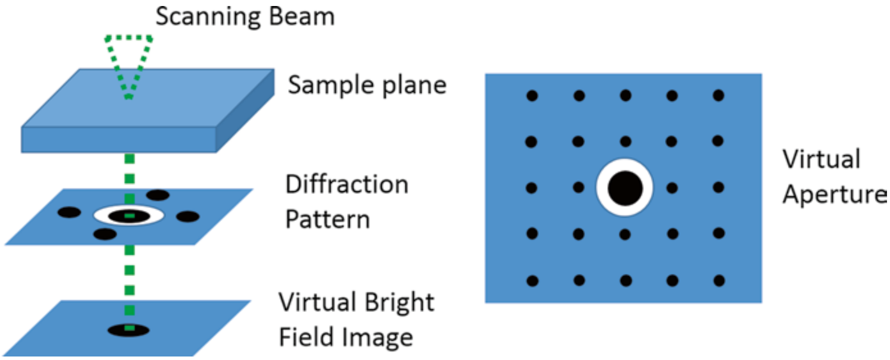

Fig. 2.18 Schematic representation of the virtual bright-field reconstruction. A virtual aperture is used to select only the transmitted beam and then plotted on the image. This is equivalent to introduce an aperture in the beam path

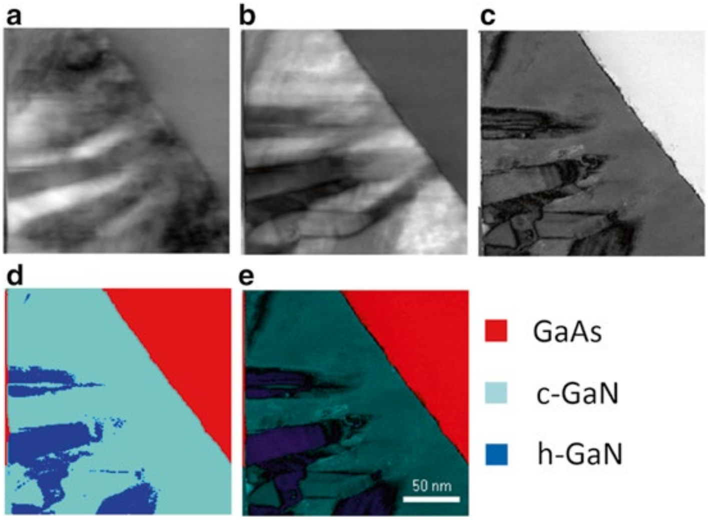

Fig. 2.19 GaN film grown on GaAs substrate. (**a**) Virtual bright-field image, (**b**) index map, (**c**) reliability map, (**d**) phase map, and (**e**) phase map combined with reliability map for better interpretation

contrast information in the outer part. Therefore, the virtual aperture needs to be larger than the transmitted beam. In this virtual bright-field STEM mode, it is the beam diameter that delimits the virtual bright-field image resolution [29]. In a similar way, the virtual aperture may be displaced on one of the spots of the diffraction pattern and form a virtual dark-field image.

In Fig. 2.19a, it is shown a virtual bright-field image of a GaN film grown on GaAs (001) cubic substrate. Growing the cubic metastable nitride phase is a challenge due to the crystalline nature of the nitrides to grow in the hexagonal phase. By using precession electron diffraction-assisted phase mapping, it is possible to distinguish the two different phases in the film. In Fig. 2.19b, c, the index and the reliability map are shown respectively. Reliability maps can show dark features at grain or phase boundaries, as can be seen in Fig. 2.19c. The phase map (Fig. 2.19d) is obtained after a precessed electron diffraction pattern was recorded every 1 nm in an automated way by scanning the precessed beam along the sample with an angle of 0.4° at 100 Hz, over an area of 200 nm × 200 nm with D-STEM conditions, spot size 1.1 nm, and using a 20 µm condenser lens aperture. The set of diffraction patterns is then indexed, and a phase map is built after considering the possible structures of the compounds present in the sample, in this case cubic GaAs (f-43m), cubic GaN (f-43m), and hexagonal GaN (P63mc). In Fig. 2.19e, the phase map is combined with the reliability map to show the degree of confidence. The map illustrates with colors the phases present in the GaN film. The dark regions correspond to lower reliability values, which are due to overlapping of both phases because of high density of stacking faults or because of overlapped orientations contributing to the diffraction pattern making it hard to index. The GaN film shows, overall, a cubic phase structure (cyan color) with some inclusions of the hexagonal phase (blue color). At the first stage of growth, the film presents only the cubic phase; this means that the hexagonal inclusions are not formed in the nucleation layer. The creation of inclusions of the hexagonal GaN phase are due to misorientations or stacking faults created during growth and are found in a columnar shape [31].

A similar analysis is shown in Fig. 2.20, where it depicted an InN film grown on a GaAs (001) substrate. The virtual bright-field image of the film and the substrate is shown in Fig. 2.20a, and the phase map combined with the reliability map is shown Fig. 2.20b. Only the cubic phase of the InN was found in the film in this analysis, and apparently not a trace of hexagonal phase inclusions can be seen from the phase map. Instead, a thin layer of InAs on the substrate is formed due to the special growth conditions employed to grow the InN on the GaAs substrate. The PED pattern acquisition conditions were the following: D-STEM mode with 1.1 nm

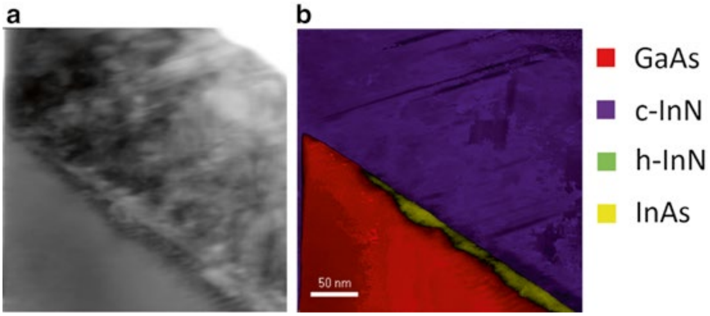

Fig. 2.20 InN film grown on GaAs. (**a**) Virtual bright-field image and (**b**) phase map combined with the reliability map

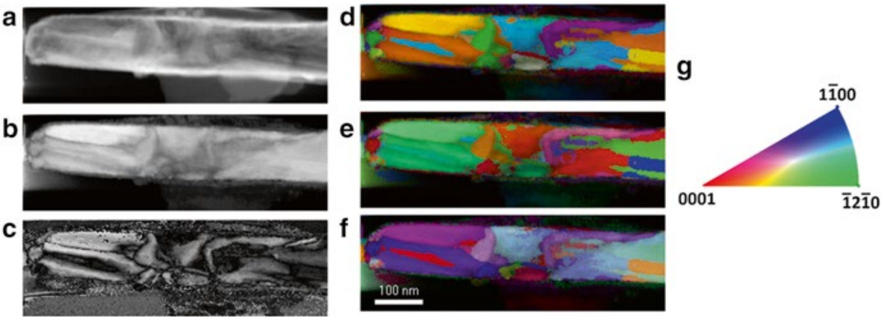

Fig. 2.21 Cobalt nanowire. (**a**) Virtual bright-field image, (**b**) index map, (**c**) reliability map, (**d**) crystal orientation map with respect to *x*, (**e**) crystal orientation map with respect to *y*, (**f**) crystal orientation map with respect to *z*, (**g**) color key for the hexagonal crystal orientation map

spot size, 10 µm aperture, precession angle 0.22° at 50 Hz, and scanning with a step size of 1 nm. The banks used to calculate the templates were cubic GaAs (f-43m), cubic InN (f-43m), hexagonal InN (P63mc), and InAs (f-43m).

In Fig. 2.21, a section of a hexagonal phase cobalt nanowire is shown. The virtual bright-field image, the index map, the reliability map, and the crystal orientation map with respect to *x*, *y*, and *z* are displayed in Fig. 2.21. In the orientation maps, *z* is the axis of the incident beam; *x* is the horizontal direction; and *y* is the vertical direction of the scanned area. The correlation index map, which is an indication of the degree of matching between a particular electron diffraction spot pattern and all of the possible calculated templates generated for the matching, is combined with the crystal orientation maps and displayed in Fig. 2.21d–f for a better interpretation of the mapping. Usually the crystalline orientation map with respect to *z* is the one used to display the information of tilt with respect to the zone axis. The *x* and *y* orientation maps are useful to understand the rotation of the crystallites observed in the *z* orientation map. This is because a single map is not sufficient to adequately describe the orientations measured. In this case, as can be seen from Fig. 2.21d–f, the nanowire looks highly texturized. This is also reflected in the reliability map where dark areas may correspond to grain boundaries or polycrystalline grains. The knowledge of the growth orientation in the Co nanowires is of great importance, mainly because of the influence of the crystallinity in the magnetic properties of the wire. A crystallographic texture may favor one direction of magnetization or another. The PED pattern acquisition conditions for this sample were the following: D-STEM mode with 1.1 nm spot size, 20 µm aperture, precession angle 0.9° at 50 Hz, and scanning with a step size of 2 nm.

Another example of orientation mapping is shown in Fig. 2.22 where the gold decahedral nanoparticle is orientated along the observation axis *z* (zone axis). The orientation map with respect to *z* is colored in green, showing the orientation of [110] of the whole nanoparticle. The index map shows dark areas along the twin boundaries of the particle due to the double-spot feature in the diffraction pattern.

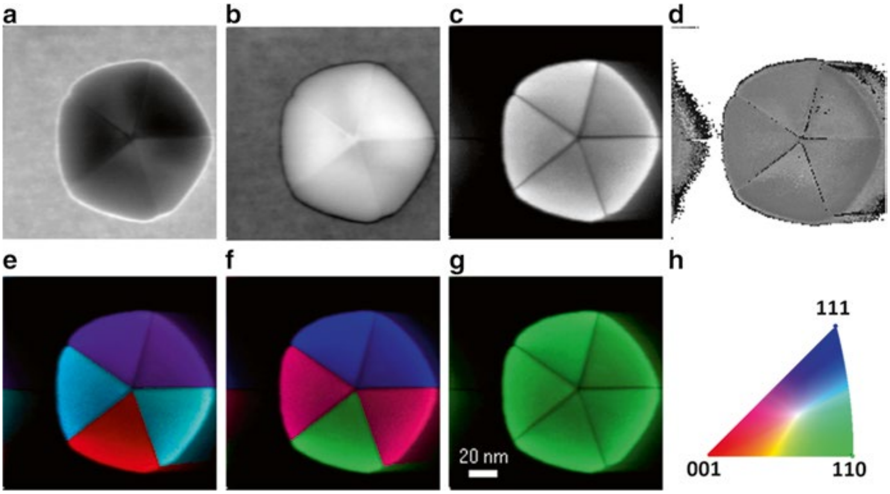

Fig. 2.22 Gold decahedral nanoparticle. (**a**) Virtual bright-field image, (**b**) negative virtual bright-field image, (**c**) index map, (**d**) reliability map, (**e**) crystal orientation map with respect to *x*, (**f**) crystal orientation map with respect to *y*, (**g**) crystal orientation map with respect to *z*, (**h**) color key for the cubic crystal orientation map

This is also observed in the reliability map along the twin boundaries of the nanoparticle. In Fig. 2.22e–g, the orientation maps have been combined with the index map, and this feature allows distinguishing the twins. Crystal orientation maps with respect to *x* and *y* show a degree of rotation between each tetrahedron, two pairs of them having similar orientation. The PED pattern acquisition conditions were the following: D-STEM mode with 0.8 nm spot size, 20 μm aperture, precession angle 0.5° at 50 Hz, and scanning with a step size of 1 nm.

Using PED increases greatly the quality of the orientation/phase maps because the PED patterns contain more information in the diffraction spots than in SAED patterns. With precession, the intensities of the diffraction spots are proportional to the square modulus of the structure factor of the material, and when compared to the templates, this will result in high index correlation values. The precession angle can be increased to obtain a more kinematical diffraction pattern, but the beam will suffer from beam broadening, and the resolution of the map will degrade [26]. This of course will require a balance between the two parameters. Here, we have shown some examples of different materials mappings acquired with different precession angles. This process has been done by scanning the precessed electron beam in D-STEM mode through the area of interest and acquiring each diffraction pattern to be used later to reconstruct the maps. To reveal information about the crystal orientation at the nanoscale level is a key element to elucidate the growth mechanisms of the materials. Also, if this information is known, the microstructural properties can be correlated with other particular properties of interest in specific areas of the material.

As it can be seen in the different examples presented, the combination of the D-STEM technique with the PED technique enabled the acquisition of crystal orientation phase mapping with a spatial resolution mainly determined by the electron probe size, which in the case of the Cs-corrected probe TEM used in these studies, can be as good as 0.8 nm, thus allowing crystal orientation phase mapping with a subnanometer resolution. These combined techniques hold a very promising future on the characterization of the crystallographic nature of nanostructured materials.

2.6 Appendix

All the experimental conditions analyzed during the studies related to the effect of different parameters on the convergence angle, α, are presented in the following tables. Table 2.1 summarizes conditions used for the analysis of the variations of the camera length and condenser aperture 2 size; both cases were studied in TEM mode. Table 2.2 summarizes the experimental conditions used for the variation of the CM excitation, spot size number, gun lens value, and extraction voltage. All these experiments were performed on STEM mode using the 10 μm condenser aperture 2 and the camera length of 0.196 m.

For the case of the Cs-corrected experiments, the conditions of the D-STEM data acquisition are presented in Table 2.3. All Cs-corrected D-STEM patterns were acquired with an acceleration voltage of 80 kV.

Table 2.1 Experimental conditions analyzed by varying the camera length and C2 aperture size

Experiment	C2 aperture size (μm)	Camera length (m)	Spot #	Extraction voltage (V)	GL
1	10	0.478	3	4,400	5
2	10	0.478	6	3,800	5
3	50	0.478	5	3,800	5
4	50	0.478	6	3,800	5
5	100	0.478	5	3,800	5
6	100	0.478	6	3,800	5
7	50	0.108	9	4,400	5
8	50	0.128	9	4,400	5
9	50	0.160	9	4,400	5
10	50	0.196	9	4,400	5
11	50	0.245	9	4,400	5
12	50	0.301	9	4,400	5
13	50	0.378	9	4,400	5

Table 2.2 Experimental conditions analyzed by varying the CM excitation, spot size number, gun lens value, and extraction voltage

Experiment	C2 aperture size (μm)	CM excitation	Spot #	Extraction voltage (V)	GL
1	10	6	9	4,400	5
2	10	5	9	4,400	5
3	10	4	9	4,400	5
4	10	3	11	4,400	5
5	10	3	10	4,400	5
6	10	3	9	4,400	5
7	10	3	8	4,400	5
8	10	3	9	4,000	5
9	10	3	8	4,000	5
10	10	3	7	4,000	5
11	10	3	9	4,400	7
12	10	3	8	4,000	7
13	10	3	7	4,000	7
14	10	3	11	4,000	3
15	10	3	10	4,000	3
16	10	3	9	4,000	3
17	10	2	5	4,400	5
18	10	2	4	4,400	5
19	10	2	3	4,400	5
20	10	2	3	4,400	7
21	10	2	2	4,400	7
22	10	1	3	4,000	7
23	10	1	9	4,400	5
24	10	1	8	4,400	5
25	10	1	7	4,400	5
26	10	1	5	4,400	5
27	10	1	3	4,400	5
28	10	1	8	4,400	7
29	10	1	7	4,400	7
30	10	1	5	4,400	7
31	10	1	3	4,400	7
32	10	1	3	4,400	8
33	10	1	3	4,000	8
34	10	1	2	4,000	8

Table 2.3 ADL and C3 lens values for the acquisition of the D-STEM patterns in a JEOL ARM 200F

Electron-optic element	Value
Adaptor lens (ADL)	1.806 A
Condenser 3 lens (C3)	1.64 V

Acknowledgments This project was supported by grants from the CONACYT Mexico (project number 154303), National Center for Research Resources (5 G12RR013646-12), and the National Institute on Minority Health and Health Disparities (G12MD007591) from the National Institutes of Health. The authors would like to acknowledge to the NSF for support with grants DMR-1103730 and PREM: NSF PREM Grant # DMR 0934218. Finally, the authors would like to acknowledge to the Department of Defense #64756-RT-REP and the Welch Foundation grant award # AX-1615.

References

1. J.M. Cowley, Electron nanodiffraction: progress and prospects. J. Electron Microsc. (Tokyo) **45**(1), 3 (1996)
2. J.M. Cowley, Electron nanodiffraction. Microsc. Res. Tech. **46**, 75 (1999)
3. J.M. Cowley, D.E. Janney, R.C. Gerkin, P.R. Buseck, The structure of ferritin cores determined by electron nanodiffraction. J. Struct. Biol. **131**, 210 (2000)
4. J.M. Cowley, Applications of electron nanodiffraction. Micron **34**, 345 (2004)
5. J.M. Cowley, P. Nikolaev, A. Thess, R.E. Smalley, Electron nano-diffraction study of carbon single-walled nanotube ropes. Chem. Phys. Lett. **265**, 379–384 (1997)
6. U. Kolb, T. Gorelik, C. Kubel, M.T. Otten, D. Hubert, Towards automated diffraction tomography: Part I—data acquisition. Ultramicroscopy **107**, 507 (2007)
7. H. He, C. Nelson, A method of combining STEM image with parallel beam diffraction and electron-optical conditions for diffractive imaging. Ultramicroscopy **107**, 3404 (2007)
8. D. Alloyeau, C. Ricolleau, T. Okiawa, C. Lanlois, Y.L. Bouar, A. Loiseau, STEM nanodiffraction technique for structural analysis of CoPt nanoparticles. Ultramicroscopy **108**, 656 (2008)
9. K.J. Ganesh, M. Kawasaki, J.P. Zhou, P.J. Ferreira, D-STEM: a parallel electron diffraction technique applied to nanomaterials. Microsc. Microanal. **16**, 614–621 (2010)
10. K.J. Ganesh, S. Rajasekhara, D. Bultreys, P.J. Ferreira, *Rapid and Automated Grain Orientation and Grain Boundary Analysis in Nanoscale Copper Interconnects*. IEEE IRPS Proceedings, IRPS11 (2011), pp. 500–502
11. K.J. Ganesh, A.D. Darbal, S. Rajasekhara, G.S. Rohrer, K. Barmak, P.J. Ferreira, Effect of downscaling nano-copper interconnects on the microstructure revealed by high resolution TEM-orientation-mapping. Nanotechnology **23**, 135702 (2012)
12. L. Cao, K.J. Ganesh, L. Zhang, O. Aubel, C. Hennesthal, M. Hauschildt, P.J. Ferreira, P.S. Ho, Grain structure analysis and effect on electromigration reliability in nanoscale Cu interconnects. Appl. Phys. Lett. **102**, 131907 (2013)
13. K.A. Jarvis, Z. Deng, L.F. Allard, A. Manthiram, P.J. Ferreira, Atomic structure of a lithium-rich layered oxide material for lithium-ion batteries: evidence of a solid solution. Chem. Mater. **23**, 3614–3621 (2011)
14. K.A. Jarvis, C.-C. Wang, A. Manthiram, P.J. Ferreira, The role of composition in the atomic structure, oxygen loss, and capacity of layered Li–Mn–Ni oxide cathodes. J. Mater. Chem. A **2**, 1353 (2014)
15. A.D. Daral, K.J. Ganesh, X. Liu, S.-B. Lee, J. Ledonne, T. Sun, B. Yao, A.P. Warren, G.S. Rohrer, A.D. Rollett, P.J. Ferreira, K.R. Coffey, K. Barmak, Grain boundary character distribution of nanocrystalline Cu thin films using stereological analysis of transmission electron microscope orientation maps. Microsc. Microanal. **19**(01), 111–119 (2013)
16. X. Zou, S. Hovmöller, P. Oleynikov, *Electron Crystallography: Electron Microscopy and Electron Diffraction*, vol. 16 (Oxford University Press, Oxford, 2010)
17. C.B. Carter, D. Williams, *Transmission Electron Microscopy: A Textbook for Materials Science. Diffraction. II*, vol. 2 (Springer, Berlin, 1996)
18. S.J. Pennycook, P.D. Nellist, Z-contrast scanning transmission electron microscopy, in Impact of electron scanning probe microscopy on materials research, ed. by D. Rickerby, G. Valdrè, U. Valdrè (Kluwer Academic, Amsterdam, 1999), p. 161. ISBN 0-7923-5939-9

19. T. Mulvey, B. Kazan, P.W. Hawkes, *The Growth of Electron Microscopy*, vol. 96 (Academic Press, San Diego, 1996)
20. D.I. Garcia-Gutierrez, L.M. De Leon-Covian, D.F. Garcia-Gutierrez, M. Treviño-Gonzalez, M.A. Garza-Navarro, S. Sepulveda-Guzman, On the role of Pb0 atoms on the nucleation and growth of PbSe and PbTe nanoparticles. J. Nanopart. Res. **15**, 1620 (2013)
21. I. Dolamic, S. Knoppe, A. Dass, T. Bürgi, First enantioseparation and circular dichroism spectra of Au38 clusters protected by achiral ligands. Nat. Commun. **3**, 798 (2012)
22. D. Bahena, N. Bhattarai, U. Santiago, A. Tlahuice, A. Ponce, S.B.H. Bach, B. Yoon, R.L. Whetten, U. Landman, M. Jose-Yacaman, STEM electron diffraction and high-resolution images used in the determination of the crystal structure of the Au144(SR)60 cluster. J. Phys. Chem. Lett. **4**, 975–981 (2013)
23. R. Vincent, P.A. Midgley, Double conical beam-rocking system for measurement of integrated electron diffraction intensities. Ultramicroscopy **53**, 271 (1994)
24. X. Zou, S. Hovmöller, P. Oleynikov, *Electron Crystallography: Electron Microscopy and Electron Diffraction* (Oxford University Press, Oxford, 2011), pp. 113–117
25. E.F. Rauch, M. Véron, J. Portillo, D. Bultreys, Y. Maniette, S. Nicolopoulos, Automatic crystal orientation and phase mapping in TEM by precession diffraction. Microsc. Anal. **22**, S5 (2008)
26. D. Viladot, M. Véron, M. Gemmi, F. Peiró, J. Portillo, S. Estradé, J. Mendoza, N. Llorca-Isern, S. Nicolopoulos, Orientation phase mapping in the transmission electron microscope using precession-assisted diffraction spot recognition: state-of-the-art results. J. Microsc. **252**, 23 (2013)
27. S. Estradé, J. Portillo, J. Mendoza, I. Kosta, M. Serret, C. Müller, F. Peiró, Assessment of misorientation in metallic and semiconducting nanowires using precession electron diffraction. Micron **43**, 910 (2012)
28. G. Brunetti, D. Robert, P. Bayle-Guillemaud, J.L. Rouviere, E.F. Rauch, J.F. Martin, J.F. Colin, F. Bertin, C. Cayron, Confirmation of the domino-cascade model by LiFePO(4)/FePO(4) precession electron diffraction. Chem. Mater. **23**, 4515 (2011)
29. E.F. Rauch, M. Veron, Coupled microstructural observations and local texture measurements with an automated crystallographic orientation mapping tool attached to a tem. Materwiss. Werksttech. **36**, 552 (2005)
30. E.F. Rauch, K. Barmak, K.J. Ganesh, P.J. Ferreira, A. Darbal, D. Choi, T. Sun, B. Yao, K.R. Coffey, S. Nicolopoulos, Automated crystal orientation and phase mapping for thin film applications by transmission electron microscopy. Microsc. Microanal. **17**, 1086 (2011)
31. F. Ruiz-Zepeda, Y.L. Casallas-Moreno, J. Cantu-Valle, D. Alducin, U. Santiago, M. José-Yacaman, M. López-López, A. Ponce, Precession electron diffraction-assisted crystal phase mapping of metastable c-GaN films grown on (001) GaAs. Microsc. Res. Tech. **77**(12), 980–985 (2014). doi:10.1002/jemt.22424

Chapter 3
Advanced Electron Microscopy in the Study of Multimetallic Nanoparticles

Nabraj Bhattarai*, Subarna Khanal*, J. Jesus Velazquez-Salazar, and Miguel Jose-Yacaman

3.1 Introduction

Nanoalloys are interesting for several reasons. One of the most exciting features of metal nanoparticles and nanoalloys is that their properties depend on size. This size dependence is related to several phenomena: quantum effects, surface effects, and modification of thermal behavior, among others [1–5]. Chemical mixing is another factor that affects the physical and chemical properties of a nanoparticle. Thus the spectrum of possibilities is quite diverse, since the same set of metals A and B may form different structures, depending on the individual elements, thermal conditions, and the synthesis procedure: core–shell nanoparticles [6, 7], mixtures, *Janus* nanoparticles [8], onion-like nanoparticles (see Fig. 3.1) [9, 10], or combinations of several of these kinds of structure. If we also include the shape of the particle in the scene, the *phase* diagram for nanoalloys becomes very rich. To appropriately investigate this phase diagram, a battery of characterization techniques is required.

In the last decade, several works have been done in the synthesis of well-controlled shape and size-selected metallic and bimetallic nanostructures [11–18]. Au-, Pd-, and Pt-based bimetallic nanoparticles were extensively studied since they

---

*Author contributed equally with all other contributors.

N. Bhattarai
Emergent Atomic and Magnetic Structures, Division of Materials Sciences and Engineering,
Ames Laboratory, Ames, IA 50011, USA
e-mail: miguel.yacaman@utsa.edu

S. Khanal
University of Pittsburgh, Mechanical Engineering & Materials Science Department,
636 Benedum Hall, 3700 O'Hara Street, Pittsburgh, PA 15261, USA

J.J. Velazquez-Salazar • M. Jose-Yacaman (✉)
Department of Physics and Astronomy, University of Texas at San Antonio,
One UTSA Circle, San Antonio, TX 78249, USA
e-mail: miguel.yacaman@utsa.edu

F.L. Deepak et al. (eds.), *Advanced Transmission Electron Microscopy*,
DOI 10.1007/978-3-319-15177-9_3

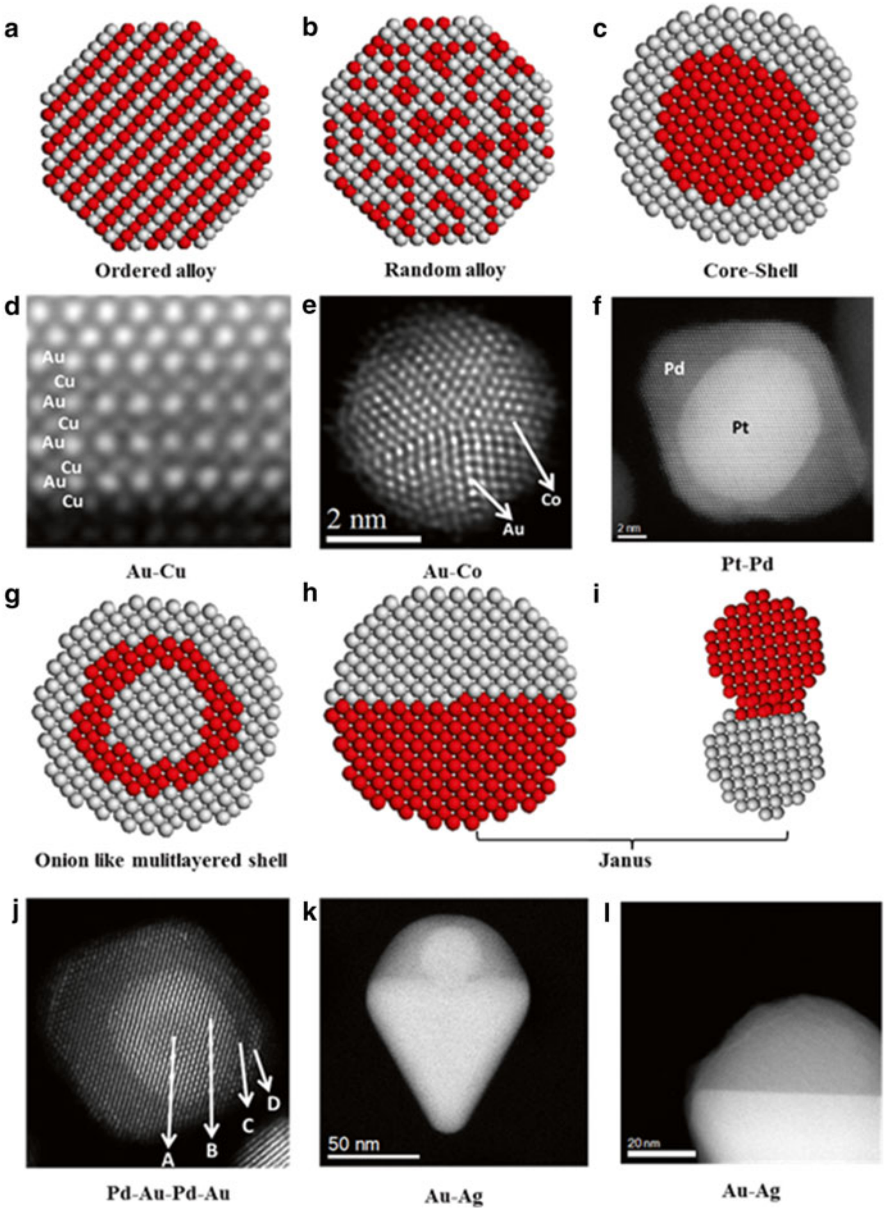

Ordered alloy

Random alloy

Core-Shell

Au-Cu

Au-Co

Pt-Pd

Onion like mulitlayered shell

Janus

Pd-Au-Pd-Au

Au-Ag

Au-Ag

Fig. 3.1 Comparison between theoretically predicted structures and experimentally obtained results in mixing two different metals. Atomistic model and atomic resolution STEM images for possible structures in bimetallic nanoparticles. Frames (**a**–**c**, **g**–**i**) represent the atomistic model for possible structures and (**d**–**f**, **j**–**l**) represent HAADF-STEM images for bimetallic nanoparticles obtained from the experiment. Particularly, frames (**a, d**) represent an ordered alloy, (**b**, **e**) represent random alloy, (**c**, **f**) represent core–shell, (**g**, **j**) represent onion-like multilayered shells, (**h**, **i**, **k**, **l**) represent *Janus* nanoparticles. All those structures were synthesized and imaged in our laboratory exhibit enhanced catalytic activities for several industrial reactions [19–31]. In particular, Pt-based bimetallic nanoparticles have been used in catalytic reactions for fuel cell applications [19, 20, 32–40]. Kobayashi et al. reported a method to change the atomic arrangement in bimetallic nanoparticles (Pd/Pt) by a process of hydrogen adsorption/desorption and also demonstrated that the hydrogen adsorption can be controlled by changing the alloy compositions of Pd and Pt [41]. More recently, Goodman and Gao extensively studied the alloying effects in Pd–Au bimetallic catalyst systems and explained the enhanced catalytic activity of Pd [42]. On the other hand, Au/Co nanoparticles have been extensively studied for the synthesis of Au@Co magnetic core–shell structural NPs through a one-step seeding growth method at room temperature, and it exhibited high-catalytic activity and long-term stability for the hydrolytic dehydrogenation of aqueous ammonia borane [43]. Bao et al. synthesized Au–Co and Au–Ni core–shell nanoparticles with well-controlled shell thickness and demonstrated high (factor of 10^{-3}–10^{-4}) surface-enhanced Raman scattering effect for adsorbed pyridine [44]. In the case of larger nanostructures, the reactivity of metal nanocrystals with polyhedral shapes can be increased with the synthesis of small (relative size) nanocrystals with high-index facet (HIF) surfaces. The concave nanostructure and hollow nanostructure present HIF surface that will provide more surface atoms with kinks, terraces, and steps thereby increasing the reactivity of the nanocrystals [45–49].

Despite an enhanced catalytic activity in bimetallic nanoparticles, only a small fraction of atoms are in the surface, and hence most of the atoms will be catalytically inactive. In order to design the most effective catalyst, mass specific activity (MSA) of the nanoparticle should be maximized. The fabrication of tri- and multimetallic nanostructure with the decoration of catalytically active precious metal in the surface (shell) in tri- and multimetallic nanostructure will be model systems. In recent years, numerous research efforts have been devoted to the optimization of the existing mono- and bimetallic (particularly precious metal Au, Pt, Pd, Re, etc. based) nanoparticle catalysts and to design new catalysts with less or no usage of expensive materials. In addition to nanoparticle morphology control, recent research has been focused on fabrication of trimetallic nanoparticle (TNP) and multimetallic nanoparticle (MNP) catalysts due to their tunable properties implemented in diverse potential applications. The addition of a third metal into the nanoparticle catalyst is expected to produce a combination of effects such as modification of the electronic structure, change in the *d*-band center, reduction of the lattice distance, and enhancement of the overall electronic charge shift. Therefore, TNPs and MNPs possess higher catalytic activity and selectivity in comparison to mono- and bimetallic counterparts [50–53]. Wang and Yamauchi [54, 55] have established the successful synthesis of Au@Pd@Pt TNPs, composed of an Au core, a Pd inner layer, and a nanoporous Pt outer shell by using a one-step aqueous-phase reaction, that exhibit significantly enhanced catalytic performance compared to Au@Pt core–shell bimetallic nanoparticles in the methanol oxidation reactions as well as demonstrating its promising potential as an effective catalyst. In addition, the Au@Pd@Pt TNPs revealed high activity of electro-oxidation of formic acid and exhibits a synergistic effect between the three different nanostructure components (sphere, shell, and islands), albeit the amount of Pt and Pd used is extremely small [56].

The special properties of nanoparticles (high aspect ratio and quantum size effects) make them very suitable to manipulate the electronic, optical, catalytic, and magnetic properties, which are eventually determined by the shape, size, composition, and crystallinity of the nanomaterials. For practical application, the synthesis of well-controlled nanoparticles and in-depth characterization at atomic scale is very essential. There are some well-controlled synthesis methods and several characterization techniques like UV-Vis spectrometer, XRD, AFM, electron microscopy, NMR, FTIR, Raman, etc. The electron microscopy (EM) (SEM, TEM, and STEM) can be used to study an individual nanoparticle at atomic scale, and the use of different detectors in EM makes them useful to investigate the chemical information of the individual nanoparticles. By the use of aberration-corrected scanning/transmission electron microscopy (STEM), several groups including ours have already explored the insight mechanisms in metallic, BM, and TM NPs. In this chapter, we will briefly introduce different synthesis methods, characterization techniques using TEM and STEM, STEM microanalysis, and some results from our group in BM and TM NPs.

3.2 Synthesis Methods

It is well established that nanoparticle's properties strongly depend on the shape, size, composition, and crystallinity, which is mostly controlled by the synthesis methods of the nanoparticles. Different nanoparticles for different functionalities can be synthesized using physical, chemical, and biological methods. The physical method (top down) includes electric arc discharge, flame pyrolysis, ball milling, physical vapor deposition, atomic layer deposition, laser ablation, etc. In the laser ablation technique, the material is heated using a laser source, and the penetration of the laser source depends on the optical properties of materials and the wavelengths of the source. For example, carbon nanotubes are synthesized by this technique. Chemical method (bottom up) is the process for the precise control of the shape and size of the nanoparticles. In chemical methods, the metal ions are reduced to neutral atoms and the particle growth takes place. The chemical synthesis process is widely used where shape, size, and chemical composition can be precisely controlled. The eco-friendly, biocompatible, and very cheap nanoparticles can be obtained by using microbes and plants with green synthesis technique [57]. These methods are called biological methods. The metabolic activity of the cell is used to synthesize the structures where the shape, size, and nature of nanostructures can be controlled by controlling the pH, temperature, and nutrition media [58]. The commonly used synthesis processes in the laboratory are explained below.

3.2.1 Seed-Mediated Growth Method

The seed-mediated growth method is the most versatile method for synthesizing metallic and bimetallic nanoparticles that can yield controlled shape, size, and structure of various morphologies of nanoparticles, such as triangles, rods, wires, stars, decahedral, polyhedral, and so on. The reaction is carried out in air and water at room temperature so that it does not require any special conditions. This process starts with the reduction of the metal salts in aqueous solution by a strong reducing agent, in the presence of stabilizing agents forming a nanoparticle that is called the seed. The seed is grown to desired size, and metal salts will be reduced on the surface of the seed nanoparticles. The surfactant molecules will form suitable templates that facilitate the growth process to produce nanoparticles of desired morphology, and the addition of the amount of seed nanoparticles changes their size. The seed-mediated growth process can separate the nucleation and growth stages of the nanocrystals in comparison with other methods so that by controlling the shape, size, and crystalline structure of seed, the final structure can be well controlled. Moreover, the facets and crystallinity of the nanocrystal can be controlled by changing the kinetics and thermodynamical conditions. The schematic of reaction pathways with possible morphology is presented in Fig. 3.2. In this method, cetyltrimethylammonium bromide (CTAB) is commonly used as a surfactant,

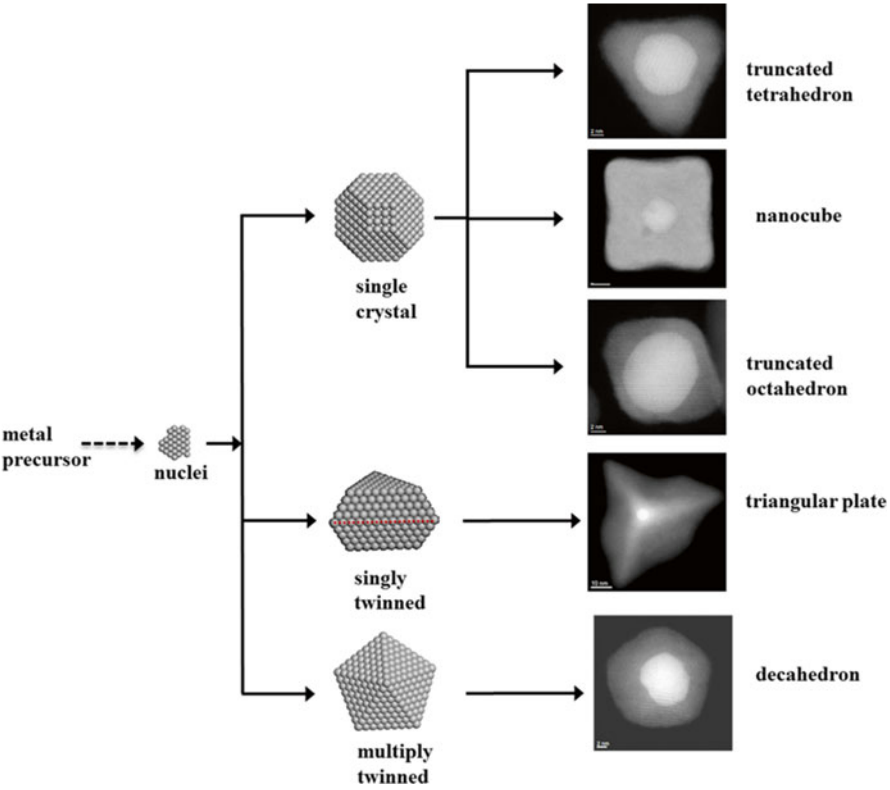

Fig. 3.2 Reaction pathways that lead to face-centered cubic (FCC) metal nanocrystals having different shapes. First, a metal precursor is reduced or decomposed to form the nuclei (*small clusters*). Once the nuclei have grown past a certain size, they become seeds with a single-crystal, singly twinned, or multiply twinned structure. If stacking faults are introduced, then plate-like seeds will be formed. The final morphology of the nanoparticles is based on the seed morphology

sodium borohydride ($NaBH_4$) as a strong reducing agent, and citric acid and ascorbic acid as weak reducing agents.

3.2.2 Phase Transfer Method

This method was first introduced by Brust [59] in 1994 and is used to produce relatively smaller (<5 nm)-sized nanoparticles and can even be used for the synthesis of atomically precise metallic and bimetallic nanoclusters [60]. The metal precursor in aqueous medium is transferred into organic medium using a phase transfer reagent, for example, tetraoctylammonium bromide (TOAB). The change in color from light yellow to deep red indicates the transfer in phase from aqueous to organic, and the deep red color is from the formation of $Oct_4N^+ AuBr^{4-}$ compound. The thiolate ligand is added to the deep red-colored solution and allowed sufficient time to be capped; the change in color from deep red to colorless indicated the capping by thiolate ligands. The size of nanoparticles and nanoclusters can be controlled by the ratio of metal precursor to thiolate ligands used. The thiolate-capped metal complexes are reduced using $NaBH_4$ (a strong reducing agent). The advantage of this process is that a very high concentration of metal nanoparticles can be readily synthesized with high monodispersity. The photographs of the entire reaction pathways are presented in Fig. 3.3.

3.2.3 Chemical Reduction Method

The nanoparticles can be synthesized from chemical reduction process in two ways: simultaneous reduction and successive reduction. In simultaneous reduction process, the reduction of metals takes place simultaneously in an appropriate solvent in

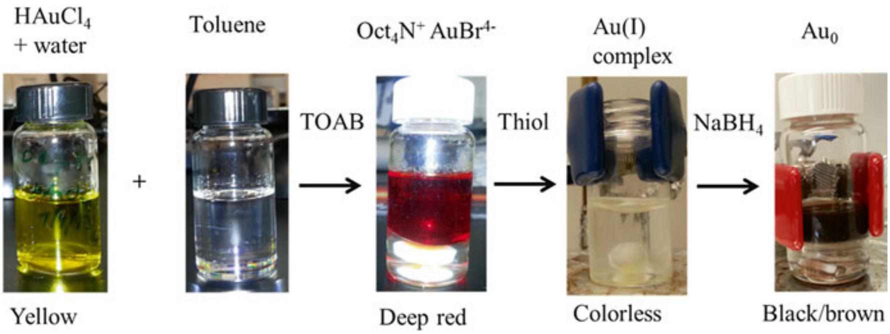

Fig. 3.3 Photographs of the reaction pathways in the phase transfer process. The metal precursor in aqueous phase is transferred into organic phase (toluene) using a phase transfer catalyst (TOAB). The use of TOAB forms $Oct_4N^+ AuBr^{4-}$ compound producing deep red color. The suitable thiol (e.g., 1-dodecanethiol, 2-phenylethylenethiol, 1-hexanethiol) is added to the deep red-colored compound to produce a colorless Au(I) compound. The change in color from deep red to colorless is the indication of thiolate capping. The thiolate-capped Au(I) complexes are reduced by adding $NaBH_4$ (strong reducing agent) producing black/brown Au^0 nanoparticles

the presence of a stabilizing ligand, and an alloyed nanoparticle will be obtained. In successive reduction process, the reduction of the first metal ions takes place followed by the reduction of second metal ions such that the metal having higher-reduction potential gets reduced faster and serves as the seed for the reduction of the metal with lower-reduction potential, and a strong metallic bond will be formed between the two metals, thereby forming the first metal at the core and the second metal at the surface: the core–shell nanostructure.

3.2.4 Polyol Method

This is a well-established versatile method for the production of well-controlled nanoparticles with higher crystallinity using polyethylene glycol as the polyol. In this process, the precursor is thoroughly mixed with liquid polyol and heated to the boiling point of polyol. The used polyol acts as solvent, reducing agent, and stabilizer, thereby controlling the growth of particles and also preventing the aggregation of particles. In this method, precursor compounds such as hydroxides, oxides, nitrates, sulfates, and acetates are either dissolved or suspended in a polyol, and the reaction mixture is then heated to reflux. As the temperature is increased, the reduction potential of the ethylene glycol increases, which leads to nucleation. During the reaction, the soluble metal precursor in polyol forms an intermediate compound and reduced to metal nuclei which will nucleate to metal nanoparticles. Polyvinylpyrrolide (PVP) is also used as a stabilizer and shape-controlling reagent for the polyol synthesis methods. The particle size can be controlled by adding foreign nuclei for heterogeneous nucleation and increasing temperature for thermal degradation of the polyol (Fig. 3.4).

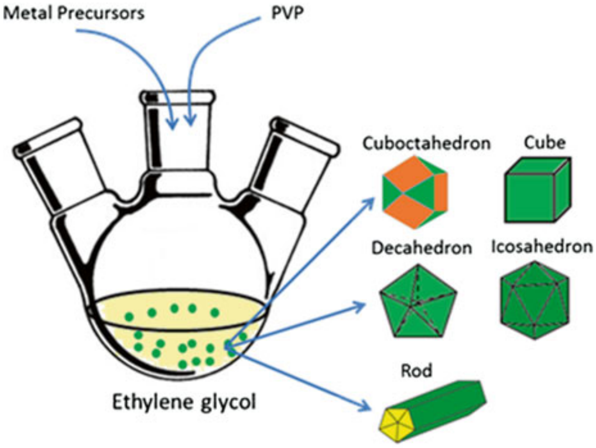

Fig. 3.4 Schematic of the polyol method with the formation of possible morphologies cuboctahedron, decahedron, rod, cube, and icosahedron

Nr	t	E [W]	T1 [°C]
1	[illegible]	1000	90
2	01:00:00	1000	90
3	00:20:00	0	20

Fig. 3.5 Photograph of microwave technique (*left*), Teflon vessel (reference and material inserted) (*upper right*), and the programmed panel with power and temperature for different time. The temperature sensor is inserted inside the reference vial and provides the temperature inside the microwave system

3.2.5 Microwave Method

In this method, the interaction between materials and microwaves are based on two specific mechanisms: dipole interaction in solvent and conducting ions in a solid which requires effective coupling between components of the target material and rapidly oscillating electrical field of the microwave [22] that minimizes the energy required for a reaction to take place. Furthermore, this technique dramatically reduces the reaction times and uniform, is energy efficient, and extensively enhances product purities by reducing unwanted side reactions compared to conventional heating methods. The rapid and uniform heating on the overall volume produces the size-controlled metallic nanoparticles, with very narrow particle size distribution. The reaction takes place very rapidly. Different solvents (ethanol, methanol, water, ethylene glycol, etc.) are used for different reactions (Fig. 3.5).

3.3 Characterization Techniques

The NPs are characterized using several characterization techniques like UV-Vis-NIR spectroscopy, XRD techniques, Raman spectroscopy, and FTIR. The use of these techniques provides the collective properties of the nanostructures. For real application, the shape, size, and crystalline structure of individual particles play a crucial role. Hence the use of electron microscopy is a very important technique in the field of nanoscience and nanotechnology.

3.3.1 TEM and HRTEM

TEM is a technique that uses the interaction of energetic electrons with the sample and provides morphological, compositional, and crystallographic information. The electrons emitted from the filament pass through the multiple electromagnetic lenses and interact with the sample. The interacted electrons make contact with the screen where the electrons are converted into light and an image is formed. The energy of electrons is directly related with the electron wavelength and determines the image resolution. A modern TEM is composed of an illumination system, a condenser lens system, an objective lens system, a magnification system, and the data recording system. The electron gun is the central part of a source of electron, which is made out of single-crystal tungsten as either a thermionic emission source or as a field emission source. Field emission source is unique for performing high coherence lattice imaging and high spatial resolution microanalysis. A set of condenser lens focus the beam on the sample, and an objective lens collects all the electrons after interacting with the sample, forms an image of the sample, and determines the limit of image resolution. Finally, a set of intermediate lenses magnifies this image and projects them on to a phosphorous screen or a charge-coupled device (CCD). TEM can be used in imaging and diffraction mode.

The high-resolution transmission electron microscopy (HRTEM) uses both the transmitted and the scattered beams to create an interference image. It is a phase contrast image and can be as small as the unit cell of crystal. In this case, the outgoing-modulated electron waves at very low angles interfere with itself during propagation through the objective lens. All electrons emerging from the specimen are combined at a point in the image plane. HRTEM has been extensively and successfully used for analyzing crystal structures and lattice imperfections in various kinds of advanced materials on an atomic resolution scale. It can be used for the characterization of point defects, stacking faults, dislocations, interferences, precipitates grain boundaries, and surface structures.

3.3.2 Diffraction

In diffraction mode, TEM can be used for both selected area electron diffraction (SAED) and nanobeam diffraction (NBD) mode. In SAED, the condenser lens is defocused to produce parallel illumination at the specimen, and the selected area aperture is used to limit the diffracting volume. The diffraction patterns obtained at small portion of the specimen give the information about the related crystallographic axis, thereby giving the characteristic property of the image. In addition, the NBD is a TEM technique that is used to determine the strain distributions in crystalline material with high spatial resolution and is also used to study the growth mechanism in the formation of bimetallic nanoparticles. The specimen is oriented along specific axis and very small (10 nm) diameter beam size is passed through the

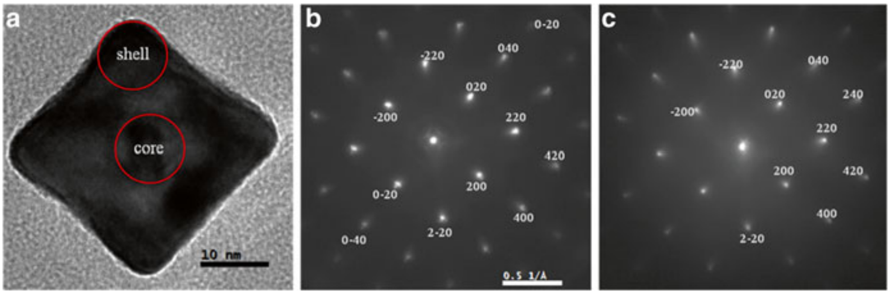

Fig. 3.6 (**a**) NBD patterns of core–shell Au–Pd nanoparticles oriented along the [001] zone axis obtained from (**b**) Au (core) and (**c**) Pd (shell). The beam size used was about 10 nm

specimen, and the diffraction pattern of very small area was obtained and recorded in the CCD camera. The NBD of an Au–Pd core–shell nanocube is presented in Fig. 3.6, showing that there is no loss in crystallinity in the core and shell.

3.3.3 Weak-Beam Dark-Field Imaging in TEM

The TEM can also be used for weak-beam dark-field (WBDF) imaging technique, which is used in order to study the defects present in the specimen. The dislocations and strain distribution defects can be directly imaged by producing the diffraction contrast images of weakly excited beams in DF mode. In this technique, the specimen is properly oriented and SAED is obtained. The objective aperture is inserted and centered, making sure that the spot G is centered at the aperture. The different reflection points are focused at the center by adjusting, and the DF image is recorded at different reflection points along with SAED patterns. The contrasts produced in the images are directly related with the surface structures, strain in the specimen, steps, wedges, stacking faults, dislocations, planar defects, etc. The contrast present in the image can be explained as from the precipitate (core) contrast and matrix (shell) contrast. The matrix (shell) contrast comes from the strain distributions in the interface and should be clearly analyzed for dislocation or other defects present. For reciprocal lattice vector **g** and displacement vector **R** from lattice imperfection, if the scalar product $\mathbf{g} \cdot \mathbf{R}$ is zero, the line of no contrast will be produced. The line of contrast is perpendicular to the direction of **g** and gives the strain field. It is also possible to calculate the misfits of particles from the observed contrast. A typical example is presented in Fig. 3.7. The nanocube was oriented along the [114] zone axis as shown in Fig. 3.7a. The SAED patterns obtained can be indexed as shown in Fig. 3.7b. DF images in Fig. 3.7c–f were recorded using different reflections. It is possible to see some contour fringes at the top of the particle and also the stresses at the core. This is to be expected since there is lattice mismatch (~4.8 %) between Au and Pd, creating a strained zone surrounding the Au core and alleviating it toward

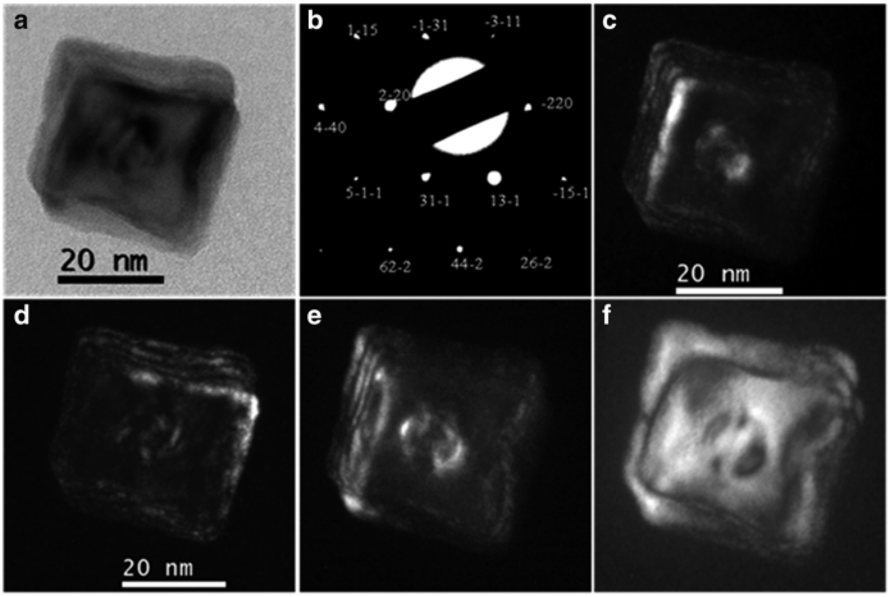

Fig. 3.7 WBDF in Au–Pd core–shell nanocube. (**a**) Bright-field image. (**b**) SAED pattern of nanocube along the [114] zone axis. (**c**–**f**) Dark-field image of the sample by inserting the objective aperture at different reflection points

the surface of the particle. The alternate bright and dark fringes in Fig. 3.7c–e correspond to the thickness of the cube.

Despite using SEM and TEM, the use of aberration-corrected STEM allows to probe the atomic structure of nanostructures and is one of the most significant advancements in studying nanomaterials.

3.4 High-Resolution Scanning Transmission Electron Microscopy (HRSTEM)

In the case of STEM, the beam of electrons is focused to form a small spot, or probe, which is incident on the very thin electron transparent sample. All the lenses except the final objective lens are called condenser lenses and are used for enough demagnification of the finite-sized electron source in order to form an atomic-scale probe at the sample. The upper objective lens provides the final and largest demagnification step that controls the size of the probe. Scan coils are arranged to scan the probe over the sample in a raster, and a variety of scattered signals can be detected and plotted as a function of probe position to form a magnified image [61]. The schematic of STEM is presented in Fig. 3.8. A STEM technique which is particularly important in the study of nanoalloys is the one that uses an annular dark-field (ADF)

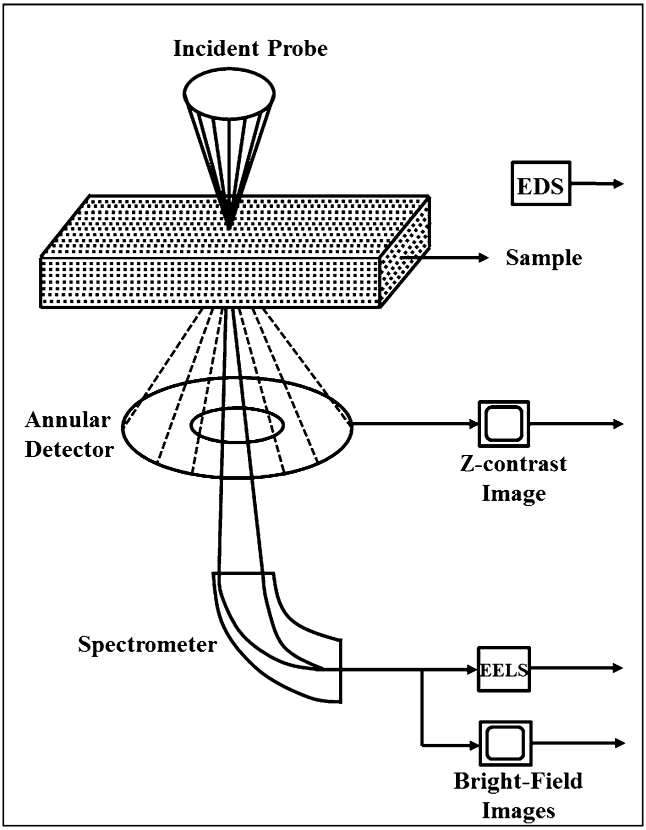

Fig. 3.8 Schematic of scanning transmission electron microscopy (STEM), the figure is redrawn from reference [66]

detector to collect the signal that produces the image. With the annular detector, only the electrons scattered more than a minimum angle θ are able to reach the detector and contribute to the image. At high angles (more than 50 mrad), the electron is scattered incoherently, with essentially no Bragg scattering present [62]. The image intensity is then mostly due to the individual contribution of each atom to the scattering. Crewe et al. demonstrated that the signal collected by the high-angle annular dark-field (HAADF) detector will have an intensity directly related to the scattering cross section, and thus it will depend on the atomic number of the atoms in the specimen [63]. Due to this dependence on the atomic number of the atoms on the specimen, the contrast in this imaging technique is strongly dependent on the chemical composition, and for this reason, it is called Z-contrast imaging. The Z-contrast technique works remarkably well in metal nanoparticles because the intensity dependence is close to $Z^{3/2}$ [64], with minimum dependence on microscope defocus [65]. This is definitely different from what is expected of bright-field imaging, where the signal varies weakly and non-monotonically with Z. The Z-dependence technique allows identifying easily the elements present in the sample. Moreover, as the electron beam interacts with the sample, the electrons are elastically or inelastically scattered. Those elastically scattered electron signals are the sources of STEM images that can be recorded either in HAADF or ADF detectors. The signals of inelastically scattered electrons are the sources of chemical information present in the sample.

3.5 STEM Microanalysis

There is a wide range of possible signals available in STEM that can be used for microanalysis of the sample, but the commonly collected signals for the characterization are bright field (BF), annular dark field (ADF), electron energy-loss spectroscopy (EELS), and energy dispersive X-ray spectroscopy (EDX). In BF mode, only those transmitted electrons are collected that leave the sample at relatively low angles with respect to the optic axis (smaller than the incident beam convergence angle). The transmitted electrons that leave the sample at relatively higher angles with respect to the optic axis are collected as ADF. Transmitted electrons losing measureable amount of energy are collected for EELS, and X-ray generated from the electron excitation in the sample is collected for EDS analysis.

3.5.1 EDX

This technique is used in order to quantify the chemical information present in the sample. The atoms within the sample are ionized by the high-energy electrons thereby ejecting inner-shell electrons. The electron from higher-energy level jumps to the vacancy of ejected electron losing some energy with the characteristic energy of specific electronic transitions within the target atoms. The characteristic X-rays emitted from the specimen are collected in the solid-state detector forming X-ray energy dispersive spectrum (EDX). The collected spectrum contains a wealth of chemical information about the specimen. The schematic diagram of EDX and X-ray spectra is presented in Fig. 3.9. This technique can be used as the finger print for detecting the various elements present in the specimen and can also be used for obtaining the composition.

3.5.2 EELS

EELS is an analytical technique measuring the change in kinetic energy of electrons after the interaction with the specimen. The change in KE is related with the atomic structures of specimen of atoms. The structural and chemical information of

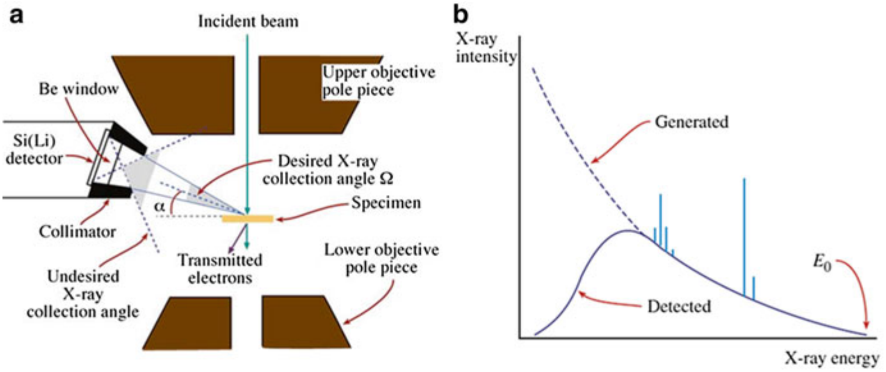

Fig. 3.9 (**a**) Schematic diagram shows the XEDX and the AEM stage showing how the detector can detect X-rays from regions other than the beam–specimen interaction volume over the (relatively large) undesired collection angle, (**b**) X-ray spectrum showing the bremsstrahlung X-ray background as a function of energy (*purple line*) and two families of characteristic X-rays (*blue lines*) (*Reprinted with permission from Williams and Carter 1996, Copyright (1996) Plenum Press*) [67]

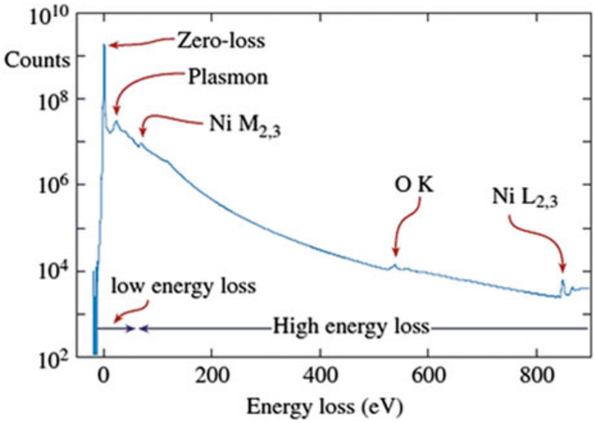

Fig. 3.10 An EELS spectrum in logarithmic intensity mode. The zero-loss region has more intensity than low loss (0–50 eV) and high loss (>50 eV) (*Reprinted with permission from Williams and Carter 1996, Copyright (1996) Plenum Press*) [67]

specimen can be inferred at the atomic level. All the incident electrons have the same energy, but the energy gets distributed after transmission through the very small specimen. This energy distribution is the characteristics of material. This technique is suitable for the detection of low-atomic-number elements but not applicable for high-atomic-number elements. There are three regions: zero loss, low loss, and high loss as shown in Fig. 3.10. The zero-loss region is from the elastically scattered electrons and electrons with minor energy losses. The low-loss region corresponds to the energy from 0 to 50 eV and corresponds to the energy of plasmon peaks and gives the information about the valence electrons. The high-loss region with energy greater than 50 eV gives the information about the core electrons that corresponds to bonds and ionization energy.

3.5.3 Tomography

This technique is used in order to get 3D visualization of 2D images. In this process, a series of 2D images of a 3D object is taken by tilting the specimen sequentially, and these 2D images are back projected using DM software to get the 3D reconstruction. The experimental data for tomography were acquired by means of STEM using a JEOL JEM-ARM200F microscope operating at 200 kV. A focused electron beam is scanned across the specimen and recorded using a HAADF detector. Digital micrograph acquisition software was used in order to tilt the specimen by an angle of 1° increments between +60° and −60°; giving the total of 121 images in 2D. The defocus and the drift shift of specimen are manually corrected in each tilting angle. The tilt series of HAADF images were recorded using 512×512 pixels in HAADF detector for the acquisition time of 20 μs with the probe size 0.095 nm and probe current 32 pA. As the tilt series acquisition is completed, the stack of 2D images is obtained. The stack of these images is back projected using 3D SIRT or 3D WBP algorithm iterative approach, and the 3D reconstruction of images is obtained [68]. It can be viewed using a 3D visualization. An example is shown in Fig. 3.11 [69].

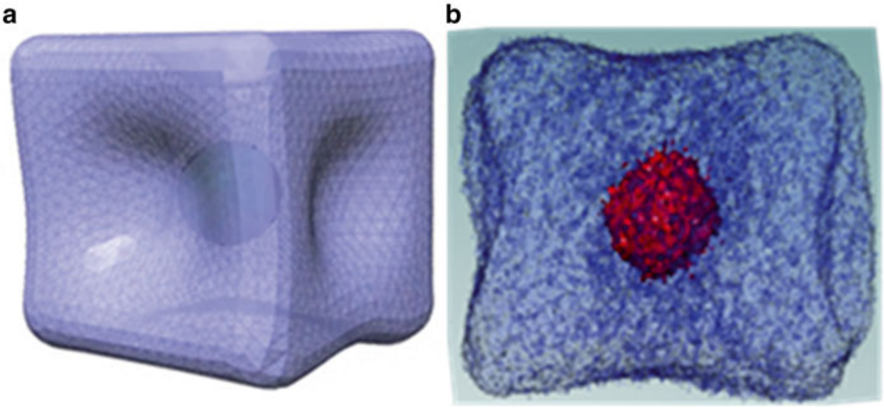

Fig. 3.11 (**a**) Model of an Au–Pd core–shell nanocube (Au–core, Pd–shell) and (**b**) 3D tomography reconstruction of the nanocube

3.5.4 GPA

Geometrical phase analysis (GPA) is a technique that is used in order to quantify the strain present in the nanostructures [70]. The lattice mismatch between two metals in BM nanoparticles generates the lattice strain thereby making the nanoparticles stable. The GPA method produces a two-dimensional map of strains in an area imaged at high resolution. It measures the displacement of crystalline lattice layer strained part (across the junction of core and shell) with reference to unstrained part of shell [71]. In GPA, amplitude and geometric phase are mapped in reciprocal space by the measurement of the displacement of lattice fringes in the Fourier transform of the image. The squared modulus of the Fourier transform of the micrograph is calculated. Each bright spot in the power spectrum represents a periodicity, and the inner structure of a particular spot is related to distortions in the lattice. Here, the displacement field comes from phase image, in the direction of the reciprocal lattice vector $\mathbf{g}$, so, between two reflections, it is possible to calculate the vectorial displacement field $\mathbf{u}(\mathbf{r})$ in the whole image. The beam shift between the scanning lines produces 1D artifacts also called the fly back error and can be eliminated by scanning the specimen parallel to the principal axis of strain [71]. Other scanning errors from sample drifts, mechanical vibrations, and electromagnetic fields must be considered as errors. In GPA technique, the power spectrum of the original image gives the same information as the diffraction pattern. Two noncollinear reflections are chosen from the power spectrum of the image, the most orthogonal one provides higher signal, and the intensity of each reflection is given by both amplitude and phase images. The phase is related with the displacement field that is $Pg(\mathbf{r}) = -2\mathbf{g} \cdot \mathbf{u}(\mathbf{r})$, where $Pg(\mathbf{r})$ is the phase image, $\mathbf{u}(\mathbf{r})$ is the displacement field, and $\mathbf{g}$ is the reciprocal lattice vector. Here, the displacement field comes from phase image, in the direction of the reciprocal lattice vector $\mathbf{g}$; therefore, between two reflections, it is possible to calculate the vectorial displacement field $\boldsymbol{u}(\mathbf{r})$ in the whole image. The mask (usually cosine mask) applied in the reflection points of power spectrum affects the spatial resolution of the image where the precision and spatial resolutions are inversely related. The software calculates the displacement field in the direction of reciprocal lattice vector g, and the vectorial displacement field $u(r)$ of the image is obtained that gives the strain tensor (σxx, σxy, σyx, σyy) [72].

Figure 3.12a presents HAADF-STEM image of Au–Pd core–shell nanoparticle oriented along the [110] zone axis. The (200) and (111) reflections were selected for the analysis (as shown in the inset) with the spatial resolution of 1.73 nm. Figure 3.12b shows the phase image with the reference at the shell with the resulting x component of the stress tensor σxx. Here, we can see that there is an expansion of about 3.5 ± 0.5 % at the core and a contraction of 4.2 ± 0.5 % to both sides of the core. This elastic strain of the particle comes from lattice distortion, chemical deformation gradient, and lattice deformation gradient [73] and contributes to the stability of the nanoparticles. Moreover, the particle is oriented in a [110] zone axis, and no dislocations at the interfaces are observed by the GPA analysis. Similarly, GPA analysis of Pt–Pd core–shell decahedral structure oriented along the [011] zone axis

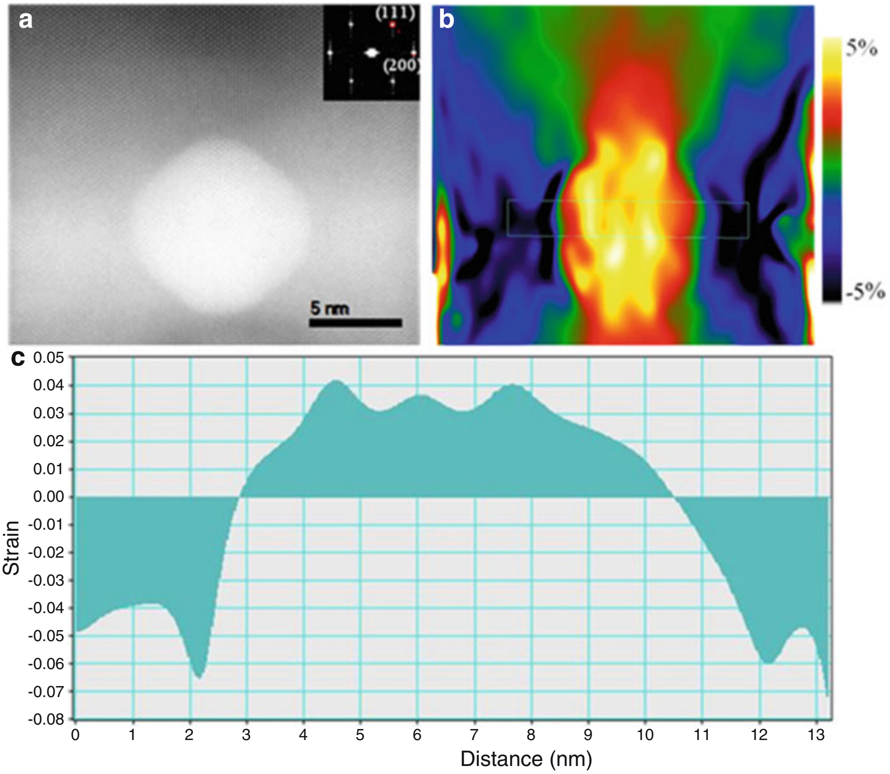

Fig. 3.12 (**a**) High-resolution HAADF-STEM image of Au–Pd core–shell nanocube. (**b**) σxx component of the strain tensor obtained from (**a**) using GPA. (**c**) Strain profile along the rectangular region of frame (**b**) showing that contraction and expansion takes place in the boundary of core and shell and in the core, respectively. The *inset* in frame (**a**) shows the power spectrum of sample, the mask is applied at *red spots*, and the color-scale *inset* in frame (**b**) changes from −5 % to +5 %

is presented in Fig. 3.13. The (111) and (200) reflections in the Fourier transform of an individual segment of that image were chosen for the analysis. Masks (e.g., Gaussian) were placed around these reflections to isolate them, and the geometric phase images analyzed. A separate analysis allows us to determine the strain distribution within the segments. Figure 3.13b shows evidence about a nearly constant phase at each segment of the Pd shell layer, and thus the center of each segment of shell layers was considered as a reference. Taking this, the methods reveal that the strain is localized along the boundaries and possesses a sharp interface between the surface layer (Pd) and core (Pt) particles. This contrast is shown by change in color, and it is due to the change in lattice parameters of core and shell atoms. The homogeneous red color region in the strain map (in Fig. 3.13b) depicts the Pd shell layer. The green layer of the strain map indicates the interface region between Pt and Pd, and the red and light-green colors correspond to the Pt core region.

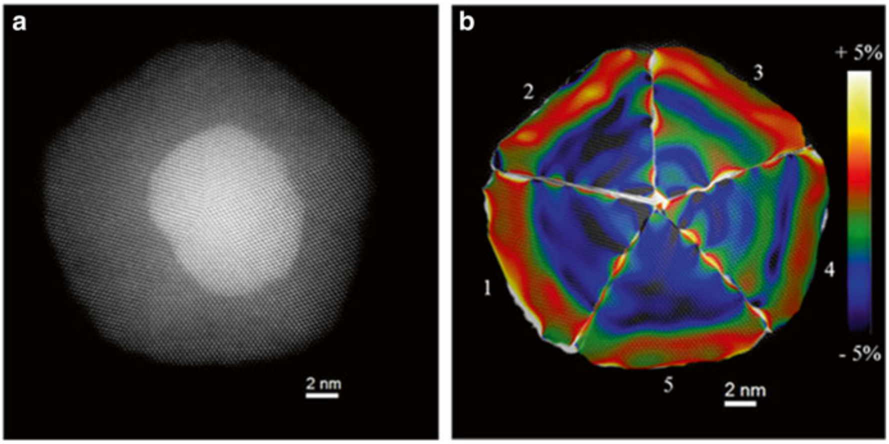

Fig. 3.13 (**a**) HAADF-STEM image of decahedral Pt–Pd core–shell nanoparticles. (**b**) Strain distribution of each segment of the decahedral Pt–Pd core–shell nanoparticles using geometric phase analysis (GPA) techniques. The scale bar is 2 nm and the color scale shows –5 % to +5%

3.5.5 Holography

One of the most exciting areas related to the characterization of nanoparticles is by employing electron holography. Using electron holography, it is possible to extract the morphology and shape of individual nanoparticles via the reconstruction of the phase hologram. Particularly in polyhedral nanoparticles, there is no TEM-related technique capable to extract the 3D shape with a single-projected image and provide surface information of the nanoparticles. For metallic nanoparticles, we consider in the holograms the contribution of the mean inner potential within the nanoparticle, which is given by the zero-order Fourier coefficient. In the reconstructed phases, an unwrap phase process should be applied in order to avoid a $\pm 2\pi n$ thickness jump of the phases; this process has been developed in the current work using HoloWorks v5.0.4 [74]. At UTSA, we set the optimal conditions for the off-axis electron holography using the flexible dual-lens system in a JEOL ARM200F, and this work was reported for the first time [75]. The parameters calibrated in the JEOL ARM200F microscope for nanoparticles are basically the voltage applied in the objective lens (OL), the voltage in the biprism, and the fringe contrast. These parameters were optimized for a gold decahedral nanoparticle (see Fig. 3.14). The phase image can be calibrated using the mean inner potential of the FCC Au. The model shown in Fig. 3.14b shows that the nanoparticle has steps, wedges in the corners, and complicated rough surface which is consistent with a structure produced by the kinetics, as has been recently discussed by Patala et al. [76]. The steps with kinks correspond to the morphology obtained by growth by step movement, i.e., atoms are added to the steps which provoke their movement; this is a classical mechanism of crystal growth.

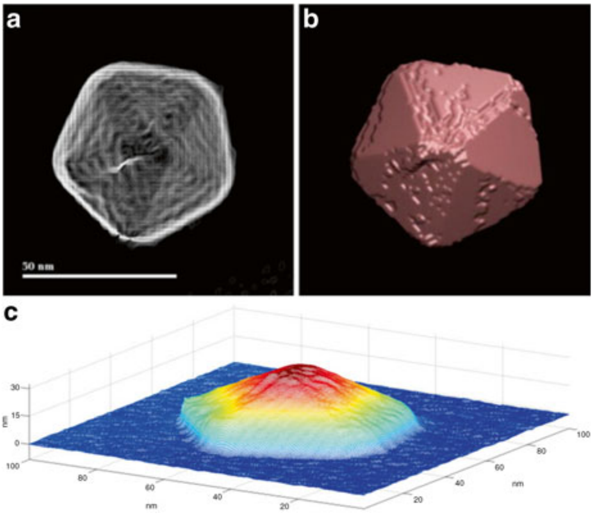

Fig. 3.14 (**a**) Reconstructed phase from the hologram for Au nanoparticle, (**b**) geometrical continuum model, (**c**) surface plot in a pseudo-isometric view of the reconstructed phase (*Reprinted with permission from Cantu-Valle et al. (2013), Copyright (2013), Elsevier*) [75]

In addition, we can observe the growth of two-dimensional isolated islands on the surface and the formation of wedges along the twin boundaries which are consistent with previous reports [77]. The growth of a nanoparticle can be the result of equilibrium, and then a minimum-energy shape structure is produced or the result of growth kinetics that can result in a complicated shape.

3.6 Examples of Bimetallic Nanoparticles

The importance of BM NPs was presented in the introduction section. In this section, we are presenting some of the results for BM nanoparticles produced in our laboratory.

3.6.1 Au/Pd

HRS/TEM micrographs can be used to study the growth mechanism in nanoparticles from the first nucleation step to the formation of the final nanostructures (Fig. 3.15) [69]. The shape evolution of Au–Pd core–shell nanoparticles from single-crystal and singly twinned seed to final concave nanocube and triangular plates is presented at the atomic level by Cs-corrected scanning transmission electron microscopy (STEM). The schematic of the reaction pathway is presented in the

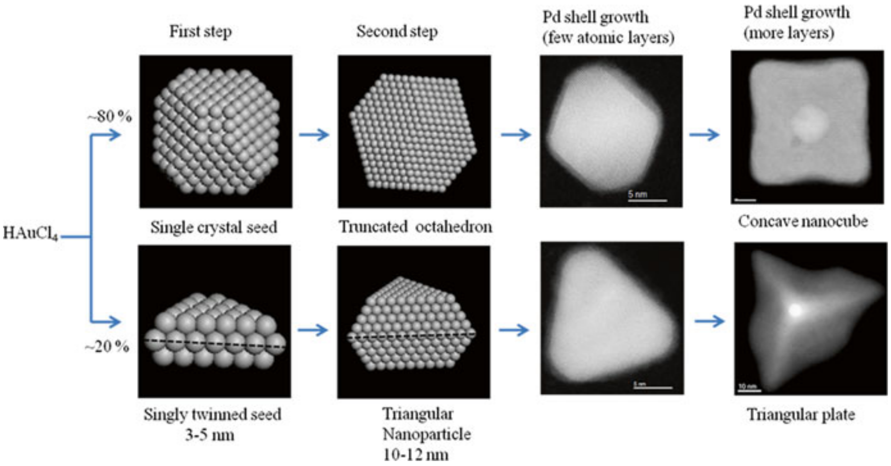

Fig. 3.15 Schematics of the reaction pathways for the formation of Au–Pd core–shell nanostructures from Au precursors. In the first step, single-crystal and singly twinned Au seeds (3–5 nm size) were formed. In the second step, single-crystal and singly twinned Au seeds were grown to larger truncated octahedron and triangular plate (10–12 nm size) nanoparticles, respectively. On the expense of volume of K2PdCl4 (10 mM) added, the Pd layers can be tuned from few atomic layers to many layers (*Reprinted with permission from Bhattarai et al. (2013). Copyright (2013) Springer*) [69]

upper part of Fig. 3.15. The growth mechanism of both morphologies was studied throughout different sizes, and it was found that the concave nanocubes grew from octahedral Au seeds due to fast growth along <111> directions, while the triangular nanoparticles grew from singly twinned Au seeds, growing twice as fast in <110> directions along the twin boundary, compared to the <111> direction perpendicular to the twin boundary. Furthermore, both the concave nanocubes and triangular nanoparticles presented HIF surfaces that will increase the catalytic activity of different reactions (Fig. 3.16).

The beauty of HAADF-STEM image is that it can be used to investigate the structural defects (Shockley partial dislocation (SPD), stacking faults (SF), partial dislocation (PD), and dislocation). The introduction of structural defect is investigated using HRSTEM images in our recent publications (Fig. 3.17) [78]. The strain release mechanism between Au and Pd is explained from the direct observation in Au–Pd core–shell nanoparticles that SPD combined with SF appears at the last Pd layers for smaller sizes. As the shell grows, the SPDs and SF appear in the interface and combine with misfit Pd, and finally it disappears because of diffusion of Au toward Pd sites. For more details, the readers should refer to reference [78].

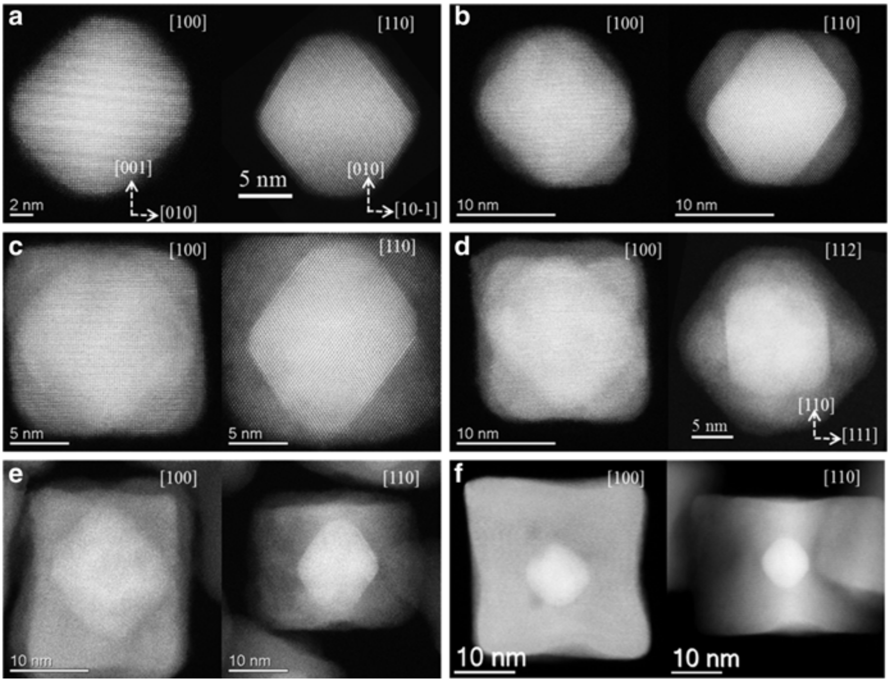

Fig. 3.16 For simplicity, the crystallographic directions are inserted on each images for [100], [110] and [112] zone axis. The zone axis is inserted in the corresponding images and the crystallographic orientation is also inserted (*Reprinted with permission from Bhattarai et al. (2013). Copyright (2013) Springer*) [69]

3.6.2 Au/Co

The magnetoplasmonic Au/Co NPs is investigated using aberration-corrected STEM for both imaging and chemical characterization. Thus the HAADF-STEM images allowed to investigate the possible Au- and Co-rich atomic columns and enable confirmation of the nanoalloyed phenomena as presented in Fig. 3.18 [79, 80]. The elemental distribution between Au and Co in the nanoalloy was confirmed by using EDX. Representative EDX line profile and mapping are presented in Fig. 3.19. The EDS line spectra of Fig. 3.18b were measured over the line drawn in Fig. 3.19a; the red and green lines in the plot correspond to the contribution from Au–L (9.71 KeV) and Au–M (2.12 KeV), while the blue line is the contribution from Co–L (0.77 KeV). Area EDX maps taken over a whole particle are presented in Fig. 3.19c–g. Both line profile and map spectra confirmed the mixing of Au and Co forming an alloyed structure. The atomically resolved HAADF-STEM images obtained from Cs-corrected STEM allowed investigating the elemental distribution in individual atomic columns in the nanoparticles, revealing the diffusion of Co atoms into Au lattice site.

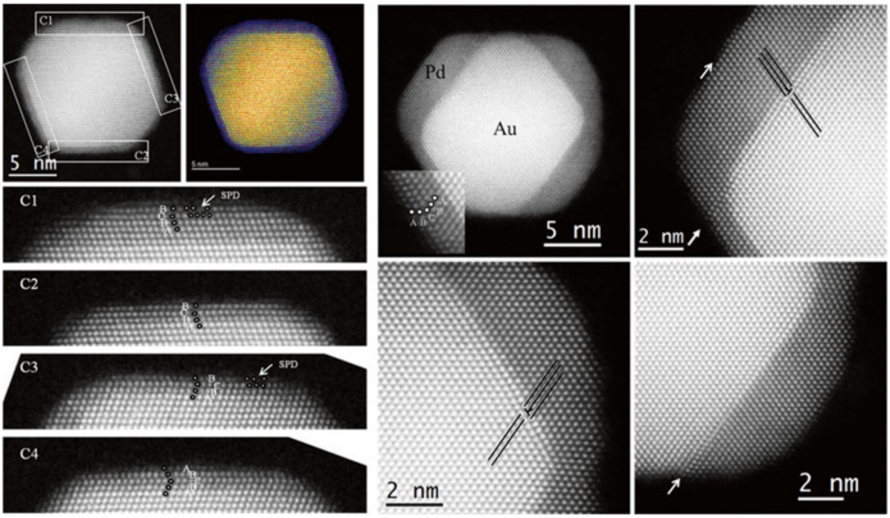

Fig. 3.17 Strain released mechanisms as seen from HRSTEM images. *Left* frame: HAADF-STEM images of an Au–Pd core–shell nanoparticles with few Pd layers in the [110] zone axis. Fully grown Pd(111) surfaces are easily observed. SPDs and SF are indicated in the figure. *Right* frame: HAADF-STEM images of a core–shell nanoparticles with larger Pd thickness. The presence of SPDs and PD is shown in the magnified portion (*Reprinted with permission from Bhattarai et al. (2012). Copyright (2012) Elsevier*) [78]

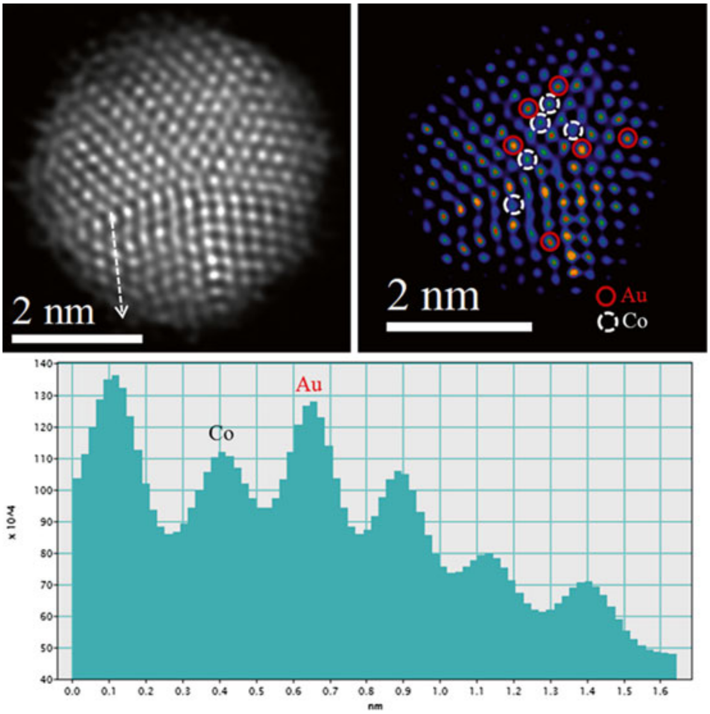

Fig. 3.18 HAADF-STEM image of Au/Co decahedral nanostructure with different intensity for atomic columns: the higher intensity for Au-rich atomic columns and lower intensity for Co-rich atomic columns. A line profile shows the variation in intensities along that direction

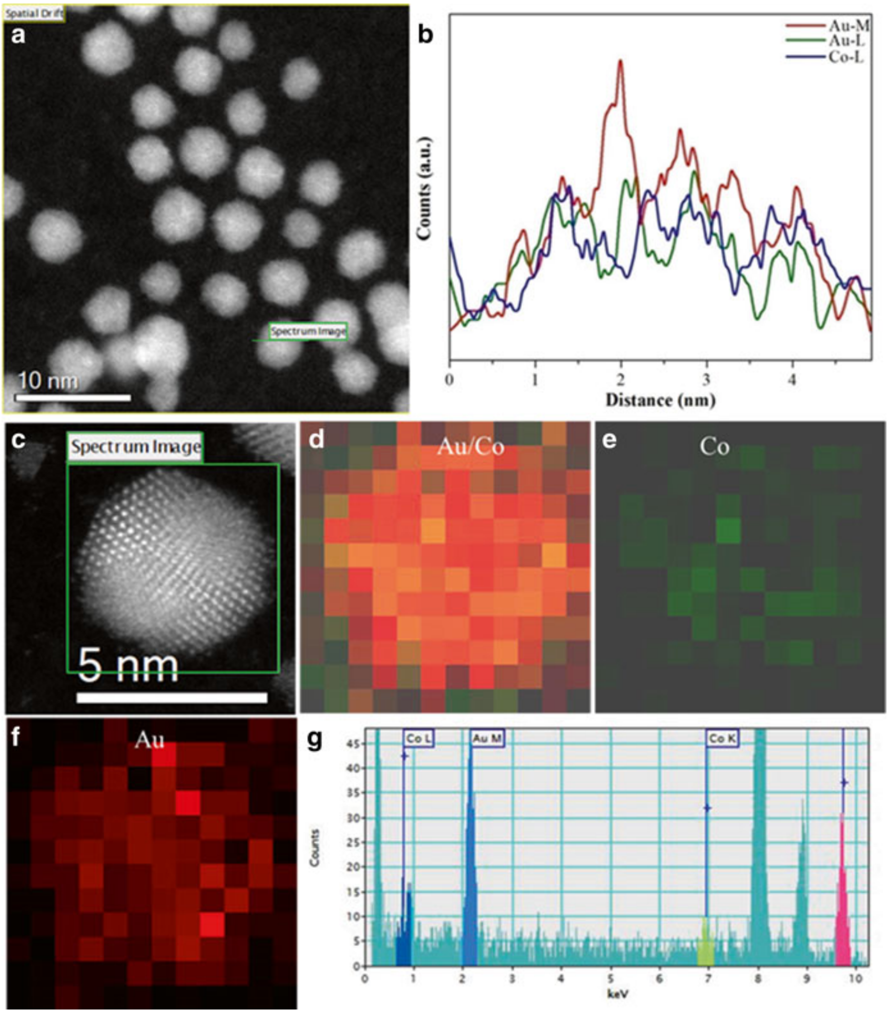

Fig. 3.19 EDX line profile and mapping of a single Au/Co nanocluster. (**a**) HAADF-STEM images, (**b**) the line profile spectrum (number of counts in arbitrary unit vs. position in nm) obtained during EDX line scan from the nanoparticles in figure (**a**), (**c**) Au/Co nanoparticle that was chosen for the EDX mapping, (**d**) combined Au/Co maps showing the Au–L and Co–L maps, (**e**, **f**) individual Co and Au maps, (**g**) line spectrum of different elements present in the sample. The signal contributions from Au–M, Au–L, and Co–L are represented by *red*, *green*, and *blue* spectra profiles in figure (**b**). The intensity recorded at different positions of Au and Co shows intermixing and confirms the alloyed structure (*Reprinted with permission from Bhattarai et al. (2013). Copyright (2013) Cambridge*) [79]

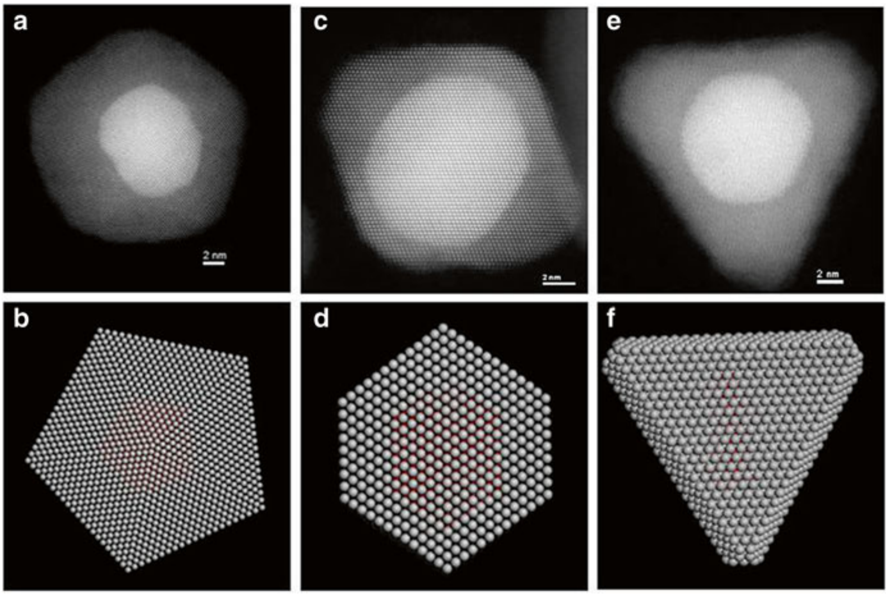

Fig. 3.20 HAADF-STEM images of the decahedral, octahedral, and triangular plates Pt–Pd core–shell nanoparticles (*top*) and their respective atomistic models (*bottom*) (*Reprinted with permission from Khanal et al. (2012). Copyright (2012), American chemical Society*) [81]

3.6.3 Pt/Pd

The polyhedral morphology of Pt–Pd core–shell nanoparticles synthesized by the polyol method clearly showed Pt seeds with two distinctive morphologies: single-crystal and multiple-twinned structures [81]. The final polyhedral structures are octahedral, triangular plates, and decahedral core–shell nanostructure as shown in Fig. 3.20. By controlling the crystalline structure of the seed, the final structure can be controlled. The aberration-corrected scanning transmission electron microscopy (STEM) techniques were complemented with microanalysis and revealed insight mechanism at the atomic resolution level. The intensity profiles of the nanoparticles in the outer layer suggest that these particles present kinks and adatoms on the outer layers as shown in Fig. 3.21. Moreover, stacking faults (SFs) and Shockley partial dislocation (SPD) are found in octahedral-shaped nanoparticles, the close-ups of the four {111} surfaces revealing that each one of them presents a SF, along with different defects. T_1 presents an ABCBC sequence due to a SF; T_2 and T_3 presents an ABCB sequence, while T_4 presents a twin sequence ABCBA. Interestingly, T_2 presents a SPD accompanied by a SF to the left (marked by an arrow), which have been known to release strain in core–shell nanoparticles. These novel decahedral Pt–Pd core–shell nanoparticles were reported for the first time.

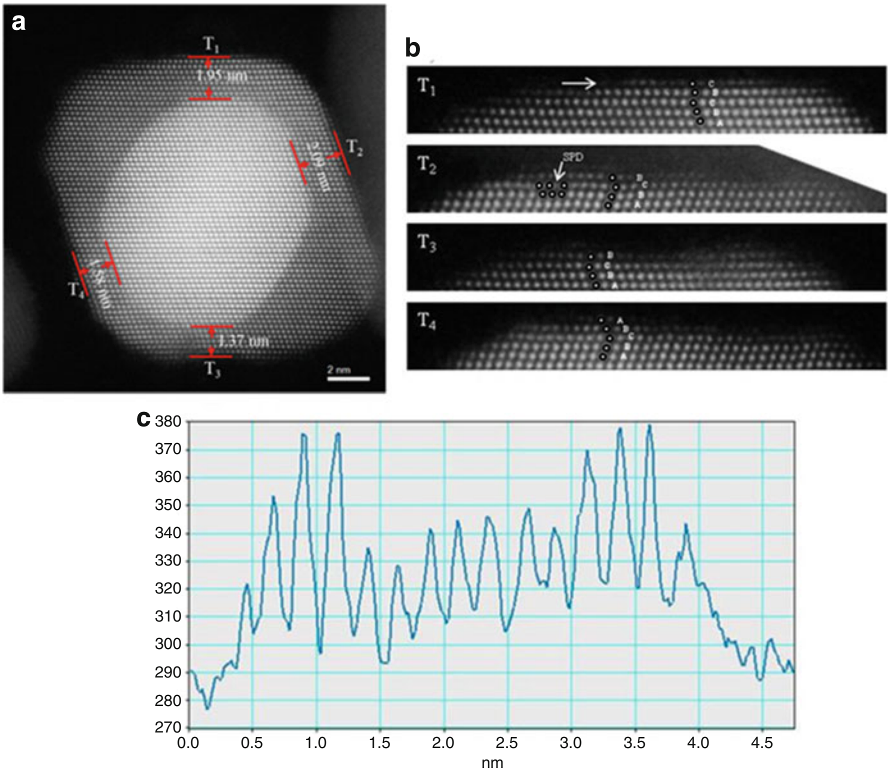

Fig. 3.21 (**a**) Atomic-resolution HAADF image of an octahedral Pt–Pd core–shell nanoparticle in a [011] zone axis. (**b**) Close-ups of the (111) surfaces where the defects are readily observable. (**c**) Intensity profile of the top surface layer in T_1, where the disparity of the intensity in the atomic columns can be observed (*Reprinted with permission from Khanal et al. (2012). Copyright (2012), American chemical Society*) [82]

3.6.4 Au/Cu

In this system, CuS_2-passivated Au core and Au_3Cu-alloyed shell nanoparticles by the polyol method were synthesized and characterized by Cs-corrected STEM [83]. The analysis of the high-resolution micrographs revealed that these nanoparticles have a decahedral structure with shell periodicity and that each of the particles is composed by Au core and Au_3Cu-alloyed shell surrounded by CuS_2 surface layer. It was also observed that the Cu layers interpenetrated into the Au lattice site. The atomistic model was constructed to exemplify the structure shown in Fig. 3.22(I) where an Au core, Au_3Cu-alloyed shell, and CuS_2 surface layer are evident. In addition, the intensity profiles showed the dramatic difference in the intensity due to the differences in atomic number. The EDX line scan in the interface region revealed

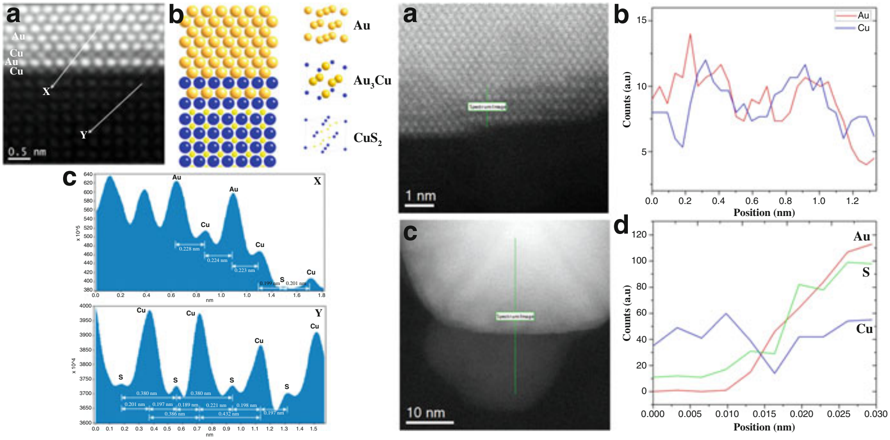

Fig. 3.22 *Left panel*: (**a**) HAADF image of Au–Cu core–shell nanoparticle showing the interface region. (**b**) Model structure which exhibits the Au, diffusion of the Cu atoms into the Au lattice site in the shell region (Au_3Cu alloy), and the CuS_2 surface layer. (**c**) Intensity profiles of shell region (Au_3Cu alloy) and CuS_2 surface layer. *Right panel*: STEM–EDX line scan (**a**, **b**) along the interface showing the presence of Au and Cu. (**c**, **d**) along the core–shell region with the surface layer showing the presence of Au, S, and Cu (*Reprinted with permission from Khanal et al. (2013). Copyright (2013), American chemical Society*) [83]

the presence of Au and Cu along the core–shell region, with the surface layer showing the presence of Au, Cu, and S signals as shown in Fig. 3.22(II). Additionally, the formation of an ordered superlattice of Au_3Cu and a self-capping layer made from one of the alloyed metals was observed for the first time.

3.7 Examples of Trimetallic Nanoparticles

3.7.1 Ag/Pd/Pt

The advanced electron microscopy techniques together with microanalysis were used in order to study the structure of the trimetallic nanoparticles made from three different metals. As an example, the study of AgPd/Pt trimetallic nanoparticles is presented in Fig. 3.23. Here, the synthesis, structural characterization, and atomistic simulations of AgPd/Pt trimetallic nanoparticles are presented. Two types of structure were synthesized using a relatively facile chemical method: multiply twinned core–shell and hollow particles. The nanoparticles were small in size, with an average diameter of 11 nm and a narrow size distribution. The EDX mapping and line scans enable to study the atomic positions of Ag, Pd, and Pt, finding that the Pt atoms are partially distributed on the surface. Furthermore, the growth mechanism of the nanoparticles was investigated using grand canonical Monte Carlo

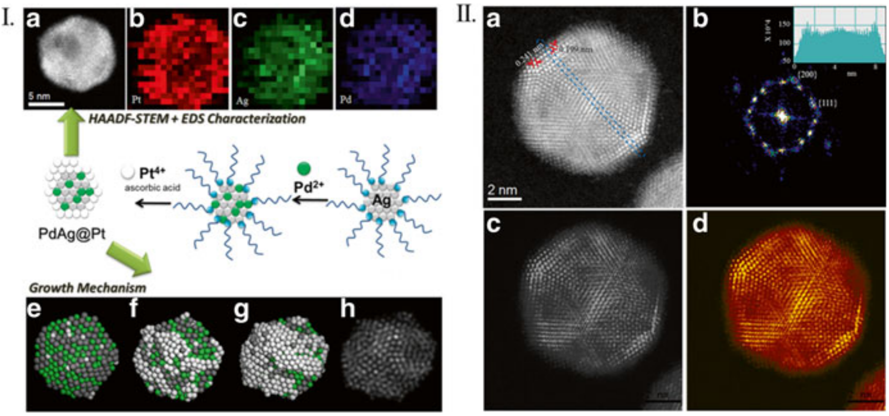

Fig. 3.23 *Left panel*: Schematic of growth process, HAADF-STEM images, EDS elemental mapping, and the growth mechanism of the nanoparticles using grand canonical Monte Carlo simulations, where Pt regions grow at overpotentials on the top of AgPd nanoalloys. *Right panel*: Cs-corrected HAADF-STEM image of (**a**) AgPd–Pt nanoparticles with a Pt-rich shell and AgPd-rich core with a twofold symmetry axis oriented along the [011] zone axis. (**b**) Fast Fourier transform (FFT) of corresponding nanoparticles. The inset intensity profile (in arbitrary units) of the area marked in (**a**) showing the difference in the intensity due to the facts that $Z_{Pd}<Z_{Ag}<Z_{Pt}$, (**c**, **d**) indicate that the different color contrast, showing the Pt shells, partially covered the AgPd core surface (*Reprinted with permission from Khanal et al. (2013). Copyright (2013), Royal Society of Chemistry*) [82]

simulations, and it was found that the Pt regions grow at overpotentials on the AgPd nanoalloys, forming 3D islands at the early stages of the deposition process. In addition, it was also observed that there was a tendency of Ag atoms to migrate toward the surface, which frequently results in the formation of hollow, cage-like structures as shown in Fig. 3.24.

3.7.2 Au/Cu/Pt

Recently, we have also started to investigate trimetallic nanostructure where catalytically active and precious metals can be decorated in the surface [84]. Thus we have obtained preliminary data for AuCu/Pt nanoparticles, where Pt atoms are deposited in the surface alloying with Cu. We have obtained a new way to control the nanoparticle morphologies by the presence of third metal (Pt), Which is overgrowth on top of the as prepared AuCu core by Frank–van der Merwe (FM) layer-by-layer and Stranski–Krastanov (SK) island-on-wetting-layer growth modes. With this, we are now a step closer to produce optimum catalysts in which the active phase forms only surface monolayers as shown in Fig. 3.25. The presence of islands and incomplete surface layers is observed in the outermost layers that will lead to the formation of {211} and {321} HIF surface. High-index facets are highly open-structure surfaces,

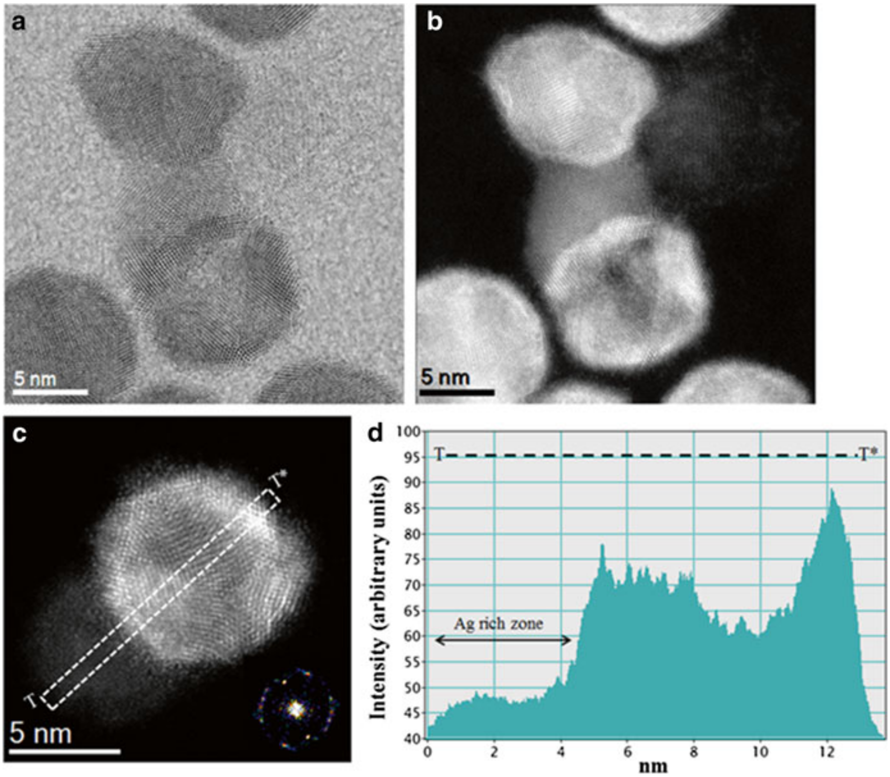

Fig. 3.24 (**a**, **b**) Bright-field and HAADF-STEM images of AgPd/Pt hollow structure nanoparticles showing that the Ag atoms have moved to the surface region and are also segregated from the structure, (**c**) AgPd/Pt nanoparticles with an Ag-rich zone (*left*) and Pt-rich shell hollow structure (*right*), and (**d**) intensity profile (in arbitrary units) (*Reprinted with permission from Khanal et al. (2013). Copyright (2013), Royal Society of Chemistry*) [82]

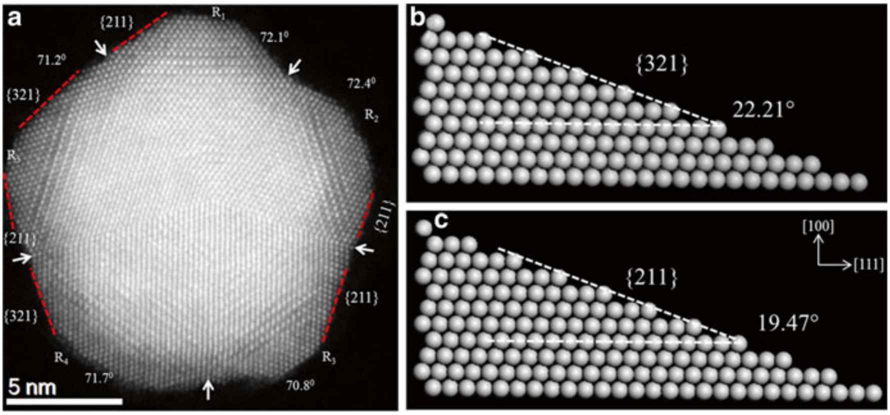

Fig. 3.25 (**a**) HAADF-STEM image of a penta-twinned AuCu/Pt core–shell nanoparticle. Each tetrahedron ($R1$, $R2$, $R3$, $R4$, and $R5$) is identified by *white arrow*, and the angles measured between the {111} twinning plane are 72.1°, 72.4°, 70.8°, 71.7°, and 71.2° as indicated. (**b**, **c**) atomistic model for high-index facets {321} and {211} with steps and terraces

which have high density of atomic steps and kinks, and these low-coordinated atoms can easily interact with other molecules and perform as the active catalysts. This research carries significant impact since most part of the nanoparticle is made from Cu and Au which are cheaper than Pt, and also the decoration of Pt in the surface presents HIF surface which will be more reactive than the low-index surfaces. Hence, this is a topic that deserves a great deal of further research.

3.8 Conclusions

The use of advanced electron microscopic techniques in the understanding of bimetallic and trimetallic nanoparticles has been highlighted in this chapter. In combination with spectroscopic tools such as EDX and EELS, it is now clearly possible to enhance our understanding of the atomic structure, morphology, and chemical constitution of these complex nanoalloys. A large number of bimetallic and trimetallic nanoalloy examples have been presented in this chapter to illustrate this. It is hoped that with the unprecedented enhancement in the understanding of these nanoalloys in the light of the advanced electron microscopic techniques in combination with theoretical calculations and simulations that are readily available, many more possible applications of these nanoalloys can now be envisaged.

Acknowledgments This project was supported by grants from the National Center for Research Resources (5 G12RR013646-12) and the National Institute on Minority Health and Health Disparities (G12MD007591) from the National Institutes of Health. The authors would like to acknowledge the NSF for the support with grants DMR-1103730, “Alloys at the Nanoscale: The Case of Nanoparticles Second Phase and PREM: NSF PREM Grant # DMR 0934218,” and “Oxide and Metal Nanoparticles—The Interface Between Life Sciences and Physical Sciences.” In addition, the authors would like to acknowledge the support of the Welch Foundation (grant no. AX-1615, “Controlling the Shape and Particles Using Wet Chemistry Methods: The Case of Bimetallic Nanoparticles”).

References

1. R. Ferrando, J. Jellinek, R.L. Johnston, Nanoalloys: from theory to applications of alloy clusters and nanoparticles. Chem. Rev. **108**, 845–910 (2008)
2. J. Jellinek, Nanoalloys: tuning properties and characteristics through size and composition. Faraday Discuss. **138**, 11 (2008)
3. J. Mock, M. Barbic, D. Smith, D. Schultz, S. Schultz, Shape effects in plasmon resonance of individual colloidal silver nanoparticles. J. Chem. Phys. **116**, 6755 (2002)
4. S. Sao-Joao, S. Giorgio, J.-M. Pénisson, C. Chapon, S. Bourgeoism, C. Henry, Structure and deformations of Pd–Ni core-shell nanoparticles. J. Phys. Chem. B. **109**, 342 (2005)
5. S. Khanal, A. Spitale, N. Bhattarai, D. Bahena, J.J. Velazquez-Salazar, S. Mejía-Rosales, M.M. Mariscal, M. José-Yacaman, Synthesis, characterization, and growth simulations of Cu-Pt bimetallic nanoclusters. Beilstein J. Nanotechnol. **5**, 1371 (2014)
6. W. Schärtl, Current directions in core–shell nanoparticle design. Nanoscale **2**, 829 (2010)

7. T. Toai, G. Rossi, R. Ferrando, Global optimisation and growth simulation of AuCu clusters. Faraday Discuss. **138**, 49 (2008)
8. B. Wang, B. Li, B. Zhao, C.Y. Li, Amphiphilic Janus gold nanoparticles via combining "solid-state grafting-to" and "grafting-from" methods. J. Am. Chem. Soc. **130**, 11594 (2008)
9. D. Ferrer, D.A. Blom, L.F. Allard, S. Mejía, E. Pérez-Tijerina, M. José-Yacamán, Atomic structure of three-layer Au/Pd nanoparticles revealed by aberration-corrected scanning transmission electron microscopy. J. Mater. Chem. **18**, 2442 (2008)
10. M. Mariscal, N. Oldani, S. Dassie, E. Leiva, Atomistic computer simulations on the generation of bimetallic nanoparticles. Faraday Discuss. **138**, 89 (2008)
11. Y. Xia, Y. Xiong, B. Lim, S.E. Skrabalak, Shape-controlled synthesis of metal nanocrystals: simple chemistry meets complex physics? Angew. Chem. Int. Ed. Engl. **48**, 60 (2009)
12. J. Zhang, H. Liu, Z. Wang, N. Ming, Shape-selective synthesis of gold nanoparticles with controlled sizes, shapes, and plasmon resonance. Adv. Funct. Mater. **17**, 3295 (2007)
13. Y. Xiong, Y. Xia, Shape-controlled synthesis of metal nanostructures: the case of palladium. Adv. Mater. **19**, 3385 (2007)
14. H.M. Chen, R.-S. Liu, Architecture of metallic nanostructures: synthesis strategy and specific applications. J. Phys. Chem. C. **115**, 3513 (2011)
15. T.T. Tran, X. Lu, Synergistic effect of Ag and Pd ions on shape-selective growth of polyhedral Au nanocrystals with high-index facets. J. Phys. Chem. C. **115**, 3638 (2011)
16. M.R. Langille, M.L. Personick, J. Zhang, C.A. Mirkin, Defining rules for the shape evolution of gold nanoparticles. J. Am. Chem. Soc. **134**, 14542 (2012)
17. X. Xia, J. Zeng, Q. Zhang, C.H. Moran, Y. Xia, Recent developments in shape-controlled synthesis of silver nanocrystals. J. Phys. Chem. C. **116**, 21647 (2012)
18. N. Bhattarai, S. Khanal, P.R. Pudasaini, S. Pahl, D. Romero-Urbina, Citrate stabilized silver nanoparticles: study of crystallography and surface properties. Int. J. Nanotechnol. Molecul. Comput. **3**, 15 (2011)
19. W. Yu, M.D. Porosoff, J.G. Chen, Review of Pt-based bimetallic catalysis: from model surfaces to supported catalysts. Chem. Rev. **112**, 5780 (2012)
20. H. Zhang, M. Jin, Y. Xia, Enhancing the catalytic and electrocatalytic properties of Pt-based catalysts by forming bimetallic nanocrystals with Pd. Chem. Soc. Rev. **41**, 8035 (2012)
21. N.S. Porter, H. Wu, Z. Quan, J. Fang, Shape-control and electrocatalytic activity-enhancement of Pt-based bimetallic nanocrystals. Accounts Chem. Res. **46**, 1867 (2013)
22. G.J. Hutchings, C.J. Kiely, Strategies for the synthesis of supported gold palladium nanoparticles with controlled morphology and composition. Accounts Chem. Res. **46**, 1759 (2013)
23. K.-S. Lee, M.A. El-Sayed, Gold and silver nanoparticles in sensing and imaging: sensitivity of plasmon response to size, shape, and metal composition. J. Phys. Chem. B. **110**, 19220 (2006)
24. P.K. Jain, X. Huang, I.H. El-Sayed, M.A. El-Sayed, Noble metals on the nanoscale: optical and photothermal properties and some applications in imaging, sensing, biology, and medicine. Accounts Chem. Res. **41**, 1578 (2008)
25. S.I. Choi, S. Xie, M. Shao, J.H. Odell, N. Lu, H.-C. Peng, L. Protsailo, S. Guerrero, J. Park, X. Xia, Synthesis and characterization of 9-nm Pt–Ni octahedra with a record high activity of 3.3 A/mgPt for the oxygen reduction reaction. Nano Lett. **13**, 3420 (2013)
26. S. Xie, H.-C. Peng, N. Lu, J. Wang, M.J. Kim, Z. Xie, Y. Xia, Confining the nucleation and overgrowth of Rh to the {111} facets of Pd nanocrystal seeds: the roles of capping agent and surface diffusion. J. Am. Chem. Soc. **135**, 16658 (2013)
27. V. Petkov, B.N. Wanjala, R. Loukrakpam, J. Luo, L. Yang, C.-J. Zhong, S. Shastri, Pt–Au alloying at the nanoscale. Nano Lett. **12**, 4289 (2012)
28. J. Li, Y. Zheng, J. Zeng, Y. Xia, Controlling the size and morphology of Au@ Pd core–shell nanocrystals by manipulating the kinetics of seeded growth. Chem. Eur. J. **18**, 8150 (2012)
29. L. Kesavan, R. Tiruvalam, M.H. Ab Rahim, M.I. bin Saiman, D.I. Enache, R.L. Jenkins, N. Dimitratos, J.A. Lopez-Sanchez, S.H. Taylor, D.W. Knight, Solvent-free oxidation of primary carbon-hydrogen bonds in toluene using Au–Pd alloy nanoparticles. Science **331**, 195 (2011)

30. V.L. Nguyen, M. Ohtaki, T. Matsubara, M.T. Cao, M. Nogami, New experimental evidences of Pt–Pd bimetallic nanoparticles with core–shell configuration and highly fine-ordered nanostructures by high-resolution electron transmission microscopy. J. Phys. Chem. C. **116**, 12265 (2012)
31. M.S. Nashner, A.I. Frenkel, D. Somerville, C.W. Hills, J.R. Shapley, R.G. Nuzzo, Core shell inversion during nucleation and growth of bimetallic Pt/Ru nanoparticles. J. Am. Chem. Soc. **120**, 8093 (1998)
32. A.X. Yin, X.Q. Min, W. Zhu, W.C. Liu, Y.W. Zhang, C.H. Yan, Pt–Cu and Pt–Pd–Cu concave nanocubes with high–index facets and superior electrocatalytic activity. Chem. Eur. J. **18**, 777 (2012)
33. A.-X. Yin, X.-Q. Min, Y.-W. Zhang, C.-H. Yan, Shape-selective synthesis and facet-dependent enhanced electrocatalytic activity and durability of monodisperse sub-10 nm Pt–Pd tetrahedrons and cubes. J. Am. Chem. Soc. **133**, 3816 (2011)
34. Y. Wu, S. Cai, D. Wang, W. He, Y. Li, Syntheses of water-soluble octahedral, truncated octahedral, and cubic Pt–Ni nanocrystals and their structure–activity study in model hydrogenation reactions. J. Am. Chem. Soc. **134**, 8975 (2012)
35. N. Tian, Z.-Y. Zhou, S.-G. Sun, Platinum metal catalysts of high-index surfaces: from single-crystal planes to electrochemically shape-controlled nanoparticles. J. Phys. Chem. C. **112**, 19801 (2008)
36. L. Wei, Y.-J. Fan, N. Tian, Z.-Y. Zhou, X.-Q. Zhao, B.-W. Mao, S.-G. Sun, Electrochemically shape-controlled synthesis in deep eutectic solvents a new route to prepare Pt nanocrystals enclosed by high-index facets with high catalytic activity. J. Phys. Chem. C **116**, 2040 (2011)
37. Z.-C. Zhang, J.-F. Hui, Z.-C. Liu, X. Zhang, J. Zhuang, X. Wang, Glycine-mediated syntheses of Pt concave nanocubes with high-index {hk 0} facets and their enhanced electrocatalytic activities. Langmuir **28**, 14845 (2012)
38. X. Huang, Y. Li, Y. Li, H. Zhou, X. Duan, Y. Huang, Synthesis of PtPd bimetal nanocrystals with controllable shape, composition, and their tunable catalytic properties. Nano Lett. **12**, 4265 (2012)
39. B. Lim, M. Jiang, P.H. Camargo, E.C. Cho, J. Tao, X. Lu, Y. Zhu, Y. Xia, Pd–Pt bimetallic nanodendrites with high activity for oxygen reduction. Science **324**, 1302 (2009)
40. F. Lima, E. Gonzalez, Ethanol electro-oxidation on carbon-supported Pt–Ru, Pt–Rh and Pt–Ru–Rh nanoparticles. Electrochim. Acta **53**, 2963 (2008)
41. H. Kobayashi, M. Yamauchi, H. Kitagawa, Y. Kubota, K. Kato, M. Takata, Atomic-level Pd–Pt alloying and largely enhanced hydrogen-storage capacity in bimetallic nanoparticles reconstructed from core/shell structure by a process of hydrogen absorption/desorption. J. Am. Chem. Soc. **132**, 5576 (2010)
42. F. Gao, D.W. Goodman, Pd–Au bimetallic catalysts: understanding alloy effects from planar models and (supported) nanoparticles. Chem. Soc. Rev. **41**, 8009 (2012)
43. J.-M. Yan, X.-B. Zhang, T. Akita, M. Haruta, Q. Xu, One-step seeding growth of magnetically recyclable Au@ Co core–shell nanoparticles: highly efficient catalyst for hydrolytic dehydrogenation of ammonia borane. J. Am. Chem. Soc. **132**, 5326 (2010)
44. F. Bao, J.-F. Li, B. Ren, Jian-LinYao, R.A. Gu, Z.-Q. Tian, Synthesis and characterization of Au@ Co and Au@ Ni core-shell nanoparticles and their applications in surface-enhanced Raman spectroscopy. J. Phys. Chem. C **112**, 345 (2008)
45. T. Ming, W. Feng, Q. Tang, F. Wang, L. Sun, J. Wang, C. Yan, Growth of tetrahexahedral gold nanocrystals with high-index facets. J. Am. Chem. Soc. **131**, 16350 (2009)
46. C.-L. Lu, K.S. Prasad, H.-L. Wu, J.-A.A. Ho, M.H. Huang, Au nanocube-directed fabrication of Au–Pd core–shell nanocrystals with tetrahexahedral, concave octahedral, and octahedral structures and their electrocatalytic activity. J. Am. Chem. Soc. **132**, 14546 (2010)
47. F. Wang, C.-H. Li, L.-D. Sun, H.-S. Wu, T. Ming, J.-F. Wang, J.C. Yu, C.-H. Yan, Heteroepitaxial growth of high-index-faceted palladium nanoshells and their catalytic performance. J. Am. Chem. Soc. **133**, 1106 (2011)
48. Z. Quan, Y. Wang, J. Fang, High-index faceted noble metal nanocrystals. Accounts Chem. Res. **46**, 191 (2012)

49. M. Jin, H. Zhang, Z. Xie, Y. Xia, Palladium concave nanocubes with high–index facets and their enhanced catalytic properties. Angew. Chem. Int. Ed. **50**, 7850 (2011)
50. N. Toshima, R. Ito, T. Matsushita, Y. Shiraishi, Trimetallic nanoparticles having a Au-core structure. Catal. Today **122**, 239 (2007)
51. S.-H. Tsai, Y.-H. Liu, P.-L. Wu, C.-S. Yeh, Preparation of Au–Ag–Pd trimetallic nanoparticles and their application as catalysts. J. Mater. Chem. **13**, 978 (2003)
52. N. Toshima, Capped bimetallic and trimetallic nanoparticles for catalysis and information technology. Macromol. Symp. **270**, 27 (2008)
53. H.-L. Jiang, Q. Xu, Recent progress in synergistic catalysis over heterometallic nanoparticles. J. Mater. Chem. **21**, 13705 (2011)
54. L. Wang, Y. Yamauchi, Strategic synthesis of trimetallic Au@Pd@Pt core–shell nanoparticles from poly(vinylpyrrolidone)-based aqueous solution toward highly active electrocatalysts. Chem. Mater. **23**, 2457 (2011)
55. L. Wang, Y. Yamauchi, Autoprogrammed synthesis of triple-layered Au@ Pd@ Pt core–shell nanoparticles consisting of a Au@ Pd bimetallic core and nanoporous Pt shell. J. Am. Chem. Soc. **132**, 13636 (2010)
56. P.-P. Fang, S. Duan, X.-D. Lin, J.R. Anema, J.-F. Li, O. Buriez, Y. Ding, F.-R. Fan, D.-Y. Wu, B. Ren, Z.L. Wang, C. Amatore, Z.-Q. Tian, Tailoring Au-core Pd-shell Pt-cluster nanoparticles for enhanced electrocatalytic activity. Chem. Sci. **2**, 531 (2011)
57. M. Montes, A. Mayoral, F. Deepak, J. Parsons, M. Jose-Yacamán, J. Peralta-Videa, J. Gardea-Torresdey, Anisotropic gold nanoparticles and gold plates biosynthesis using alfalfa extracts. J. Nanopart. Res. **13**, 3113 (2011)
58. M. Gericke, A. Pinches, Biological synthesis of metal nanoparticles. Hydrometallurgy **83**, 132 (2006)
59. M. Brust, M. Walker, D. Bethell, D.J. Schiffrin, R. Whyman, Synthesis of thiol-derivatised gold nanoparticles in a two-phase liquid–liquid system. J. Chem. Soc. Chem. Commun **7**, 801–802 (1994)
60. N. Bhattarai, S. Khanal, D. Bahena Uribe, J.A. Olmos-Asar, A. Ponce, R. Whetten, M.M. Mariscal, M. Jose-Yacaman, Structural order in ultrathin films of the monolayer protected clusters based upon 4-nm gold nanocrystals: an experimental and theoretical study. Phys. Chem. Chem. Phys. **16**, 18098 (2014)
61. S.J. Pennycook, P.D. Nellist, *Scanning Transmission Electron Microscopy* (Springer, New York, 2011)
62. D.B. Williams, C.B. Carter, *The Transmission Electron Microscope* (Springer, New York, 2009)
63. J. Wall, J. Langmore, M. Isaacson, A. Crewe, Scanning transmission electron microscopy at high resolution. Proc. Natl. Acad. Sci. U. S. A. **71**, 1 (1974)
64. P. Nellist, S. Pennycook, The principles and interpretation of annular dark-field Z-contrast imaging. Adv. Imag. Elect. Phys. **113**, 147 (2000)
65. S. Pennycook, L. Boatner, Chemically sensitive structure-imaging with a scanning transmission electron microscope. Nature **336**, 565 (1988)
66. N.D. Browning, D.J. Wallis, P.D. Nellist, S.J. Pennycook, EELS in the STEM: determination of materials properties on the atomic scale. Micron **28**, 333 (1997)
67. D.B. Williams, C.B. Carter, *Transmission Electron Microscopy: Diffraction* (Plenum, New York, 1996)
68. P.A. Midgley, R.E. Dunin-Borkowski, Electron tomography and holography in materials science. Nat. Mater. **8**, 271 (2009)
69. N. Bhattarai, G. Casillas, S. Khanal, J.J.V. Salazar, A. Ponce, M. Jose-Yacaman, Origin and shape evolution of core–shell nanoparticles in Au–Pd: from few atoms to high Miller index facet. J. Nanoparticle. Res. **15**, 1 (2013)
70. M. Hÿtch, E. Snoeck, R. Kilaas, Quantitative measurement of displacement and strain fields from HREM micrographs. Ultramicroscopy **74**, 131 (1998)
71. J. Chung, G. Lian, L. Rabenberg, Practical and reproducible mapping of strains in si devices using geometric phase analysis of annular dark-field images from scanning transmission electron microscopy. Electron Devic. Lett. IEEE. **31**, 854 (2010)

72. F. Calvo, *Nanoalloys: From Fundamentals to Emergent Applications* (Elsevier, Amsterdam, 2013)
73. T.D. Young, J. Kioseoglou, G.P. Dimitrakopulos, P. Dłużewski, P. Komninou, 3D modelling of misfit networks in the interface region of heterostructures. J. Phys. D App. Phys. **40**, 4084 (2007)
74. E. Völkl, L. Allard, B. Frost, A software package for the processing and reconstruction of electron holograms. J. Microsc. **180**, 39 (1995)
75. J. Cantu-Valle, F. Ruiz-Zepeda, E. Voelkl, M. Kawasaki, U. Santiago, M. José-Yacaman, A. Ponce, Determination of the surface morphology of gold-decahedra nanoparticles using an off-axis electron holography dual-lens imaging system. Micron **54**, 82 (2013)
76. S. Patala, L.D. Marks, M. Olvera de la Cruz, Elastic strain energy effects in faceted decahedral nanoparticles. J. Phys. Chem. C. **117**, 1485 (2013)
77. A.S. Barnard, N.P. Young, A.I. Kirkland, M.A. Van Huis, H. Xu, Nanogold: a quantitative phase map. ACS Nano **3**, 1431 (2009)
78. N. Bhattarai, G. Casillas, A. Ponce, M. Jose-Yacaman, Strain-release mechanisms in bimetallic core-shell nanoparticles as revealed by Cs-corrected STEM. Surf. Sci. **609**, 161 (2012)
79. N. Bhattarai, G. Casillas, S. Khanal, D. Bahena, J.J. Velazquez-Salazar, S. Mejia, A. Ponce, V.P. Dravid, R.L. Whetten, M.M. Mariscal, M. Jose-Yacaman, Structure and composition of Au/Co magneto-plasmonic nanoparticles. MRS Commun. **3**, 177 (2013)
80. N. Bhattarai, S. Khanal, D. Bahena, R.L. Whetten, M. Jose-Yacaman, Synthesis and structural characterization of ferromagnetic Au/Co nanoparticles. MRS Proc. **1708** (2014). doi:10.1557/opl.2014.526
81. S. Khanal, G. Casillas, J.J. Velazquez-Salazar, A. Ponce, M. Jose-Yacaman, Atomic resolution imaging of polyhedral PtPd core–shell nanoparticles by Cs-corrected STEM. J. Phys. Chem. C. **116**, 23596 (2012)
82. S. Khanal, N. Bhattarai, J.J. Velazquez-Salazar, D. Bahena, G. Soldano, A. Ponce, M.M. Mariscal, S. Mejia-Rosales, M. Jose-Yacaman, Trimetallic nanostructures: the case of AgPd–Pt multiply twinned nanoparticles. Nanoscale **5**, 12456 (2013)
83. S. Khanal, G. Casillas, N. Bhattarai, J.J. Velázquez-Salazar, U. Santiago, A. Ponce, S. Mejía-Rosales, M. José-Yacamán, CuS_2-passivated Au-core, Au_3Cu-shell nanoparticles analyzed by atomistic-resolution Cs-corrected STEM. Langmuir **29**, 9231 (2013)
84. S. Khanal, N. Bhattarai, D. McMaster, D. Bahena, J.J. Velazquez-Salazar, M. Jose-Yacaman, Highly monodisperse multiple twinned AuCu-Pt trimetallic nanoparticles with high index surfaces. Phys. Chem. Chem. Phys. **16**, 16278 (2014)

Chapter 4
Zeolites and Mesoporous Crystals Under the Electron Microscope

Alvaro Mayoral, Yasuhiro Sakamoto, and Isabel Diaz

4.1 Zeolites

In 1756 the Swedish mineralogist, Axel Fredrik Crønstedt, discovered a new type of mineral [1] currently known as *stilbite*. He named this mineral "zeolite" because they appear to boil, due to the release of water adsorbed by the material, when they were heated in a blowpipe flame. The term zeolite derives from the combination of the two Greek words: *zeo* meaning "to boil" and *lithos* "stone." Years later, 1777–1800s, additional properties were described, such as adsorption properties, cation exchange, or dehydration. St. Claire Deville reported the first hydrothermal synthesis of a zeolite, *levynite*, trying to imitate natural and geological conditions that enable the formation of zeolites [2]. In 1896 Friedel observed the occlusion of different liquids in dehydrated zeolites [3–5]. In the following years, zeolites were used to adsorb different molecules [6] until that in 1925 Weigel and Steinhof reported the first molecular sieve effect [7]. In 1930 Taylor [8] and Pauling [9] reported the first crystal structure determinations (of *analcite* and *sodalite*), and in 1932, McBain established the term "molecular sieve" to define a porous structure that acts as sieve in a molecular scale [10]. By this time, the majority of the zeolite studies were mainly based on natural and synthetic work that was virtually inexistent.

A. Mayoral (✉)
Advanced Microscopy Laboratory (LMA), Nanoscience Institute of Aragon (INA), University of Zaragoza, Mariano Esquillor, Edificio I+D, Zaragoza 50018, Spain
e-mail: amayoral@unizar.es

Y. Sakamoto
PRESTO, JST, Kawaguchi 332-0012, Japan

Department of Physics, Graduate School of Science, Osaka University, Toyonaka 560-0043, Japan

I. Diaz
Instituto de Catálisis y Petroleoquímica, CSIC, Marie Curie, 2, Madrid 28049, Spain

F.L. Deepak et al. (eds.), *Advanced Transmission Electron Microscopy*,
DOI 10.1007/978-3-319-15177-9_4

However, Richard Maling Barrer, who began his zeolite studies in the mid-1930s, reported in 1948 the first definitive zeolite synthesis, describing the synthesis of *mordenite* [11] and the novel synthetic zeolite [12, 13] later identified as the KFI framework.

In 1954 Union Carbide commercialized synthetic zeolites for industrial separation and purification purposes, starting for the drying of natural gas. Five years later, the same company marketed the process for normal–isoparaffin separation, being the first time were molecular sieves were used in a bulk separation reaction. In 1962, zeolite X was introduced by Mobil Oil as cracking catalyst, and about 10 years later, zeolite A started to replace phosphates in detergents.

Molecular sieves are porous structures where the pore dimensions are of molecular dimensions ranging from 3 Å up to 2 nm in diameter, including carbon, glasses, and oxides, although nowadays they are practically all zeolites.

Zeolites are crystalline microporous (pore size below 2 nm, according to the IUPAC) aluminosilicates based on an infinitely extending three-dimensional, four-connected framework of AlO_4 and SiO_4 tetrahedra linked to each other by sharing oxygen. Each SiO_4 tetrahedron in the framework bears a neutral charge, and each AlO_4 tetrahedron in the framework bears a net negative charge that is balanced by an extra-framework cation, which usually is an alkali or alkaline earth metal. Zeolite micropore channels have very well-defined diameters so that bulky molecules are excluded from the internal surface. The general formula for a zeolite can be expressed as

$$M_{x/n}\left[\left(\mathrm{AlO}_2\right)_x\left(\mathrm{SiO}_2\right)_y\right]\cdot w\mathrm{H}_2\mathrm{O} \tag{4.1}$$

where n is the valence of cation M, w is the number of water molecules per unit cell, x is the number of AlO_2 units, and y is the number of SiO_2 units. The ratio of y/x is usually between 1 and 5. In the case of a high-silica zeolite, the ratio is 10–100 or higher, while in a purely siliceous zeolite, the ratio is infinite. The molar ratio of y/x cannot be smaller than 1 due to Löwenstein's rule which states that no Al–O–Al linkages occur [14] (if the zeolite is prepared under hydrothermal conditions).

The tetrahedra can be combined in a number of different ways which lead to different unique 176 zeolite framework types [15]. A good example of a typical zeolite (LTA structure type, zeolite A) is shown in Fig. 4.1, where oxygen atoms appear in red color while "T" atoms are in blue.

The highly selective properties due to their particular structural parameters, size and shape of the pores, have converted these molecular sieves into the most important heterogeneous catalyst [16]. The pore diameters vary from each structure, plus the great number of structures gives a wide variety of pore sizes and thus permits the ability to choose a suitably engineered zeolite for a particular reaction.

Another aspect of the versatility of the zeolites is the possibility to modify the tetrahedra which form the framework. During the synthesis process, for example, it is possible to substitute Si by P. This new family is known as *AlPO* materials [17] or *SAPO* [18] when the zeolites contain silicon, aluminum, and phosphorus as "T" atoms.

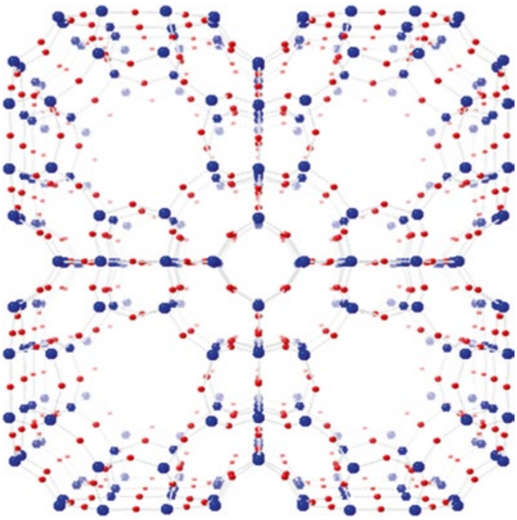

Fig. 4.1 Schematic representation of the unit cell of zeolite A (LTA framework type), observed along [100]

4.1.1 Nomenclature and Structure

The original synthesized materials discovered by Milton, Breck, and coworkers at Union Carbide used the modern Latin alphabet naming zeolite as A, B, X, or Y. The Greek alphabet was started by Mobil and also Union Carbide with the alpha, beta, and omega zeolites. As many synthetic zeolites present structural topologies as the mineral, they exhibit the mineral name such as *faujasite*, *mordenite*, and *chabazite*. Moreover, the molecular sieve literature contains a great number of acronyms: ITQ, ZSM-5, AlPO, and SAPO, among many others. Following the rules set up by the IUPAC Commission on Zeolite Nomenclature in 1979 [19], designations consisting of three capital letters have been used since then. The codes are generally derived from the names of the type materials and do not include numbers and characters other than capital Roman letters and designate framework types. For example, zeolites X and Y only differ in the Si/Al ratio, but both of them have the same framework type which is analogous to the rare mineral *faujasite* (FAU). In the case of zeolite A (LTA), it is also known as molecular sieve Linde Type 4A. For this case, the code is derived from the name of the company that discovered the zeolite, and “4” describes the maximum pore diameter (4 Å in this case). Nowadays, the terms zeolite and zeolite materials bring together three-dimensional tetrahedral oxide networks with a framework density less than about 21 T atoms per 1,000 $Å^3$.

The smallest building block of zeolites, the tetrahedron, can be arranged in a number of ways, thereby creating a large number of different structure types. In all zeolites, the T–O distances are between 1.58 and 1.78 Å and the O–T–O angles rarely differ by more than 5° from the ideal tetrahedral angle (109.46°). Most of the T–O–T angles fall between 130° and 160° [20]. The variation possible in the latter

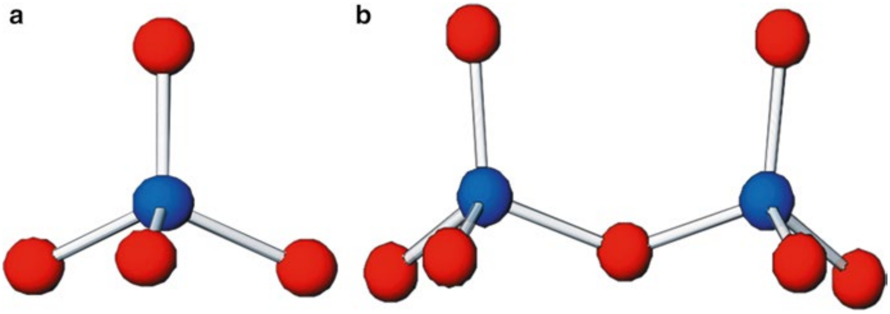

Fig. 4.2 (**a**) Single building unit, where the "T" atom appears in *blue* and the O bridges are in *red* color. (**b**) Two tetrahedra sharing corners (oxygen atoms)

angle enables the existence of the numerous different structure types. As it was mentioned previously, zeolite framework consists of uninterrupted three-dimensional nets built up by tetrahedra that share corners (Fig. 4.2).

To describe zeolite structures, the term secondary building units (SBUs) is often encountered, which are formed from the primary building unit (PBU), TO_4 shown in Fig. 4.2. The SBUs were originally (Fig. 4.3) developed to facilitate the description of zeolite structures.

By connecting the relatively basic secondary building units, complex zeolitic structures can be created. The framework formed exhibits pore sizes from 0.3 to 1.0 nm and pore volumes ranging from 0.10 up to 0.35 cm^3/g. The typical pore sizes can be classified as (a) small pores with 8 rings, diameter of 0.30–0.45 nm (zeolite A); (b) medium pores with 12 rings, 0.45–0.60 nm (ZSM-5); (c) large pores, 12 rings, 0.6–0.8 nm (zeolite X or Y); and (d) extra-large pores, with 14 rings, over 0.8 nm (UTD-1). These frameworks present some degree of flexibility, depending on the water content and/or species occluded within the zeolite cavities. For example, dramatic changes in the thermal expansion properties of zeolites with the LTA topology have been monitored depending on their cage content [21].

A good example of the connection of four and six rings leads to a tertiary building unit, the so-called β- or *sodalite* cage (Fig. 4.4a). Further, the connection of the sodalite cage via the six-ring planes in the shape of hexagonal prism leads to the *faujasite* structure (Fig. 4.4b). All known zeolite structures can be found in the International Zeolite Association (IZA) [22].

The presence of channels and cavities and the ability of reversibly incorporating water into the structure are the essential characteristics of zeolite frameworks. Several distinct cages can be found in a particular zeolite structure, and the same cage can be found in different zeolites, for example, sodalite cage can be found either in zeolite A (LTA), zeolites X and Y (FAU), and sodalite (SOD) itself. The size and shape of the channels and cavities have a great influence on the properties of the zeolites.

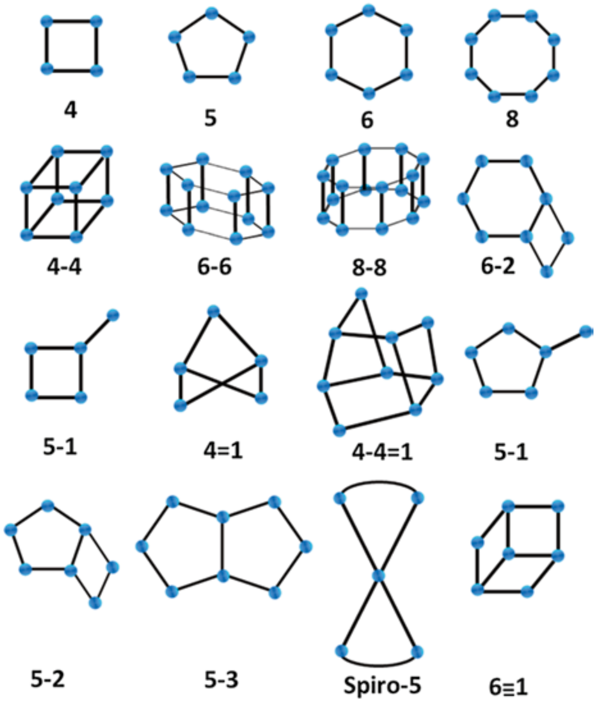

Fig. 4.3 Secondary building units (SBUs) in zeolites. The corners of the polyhedral represent tetrahedra atoms

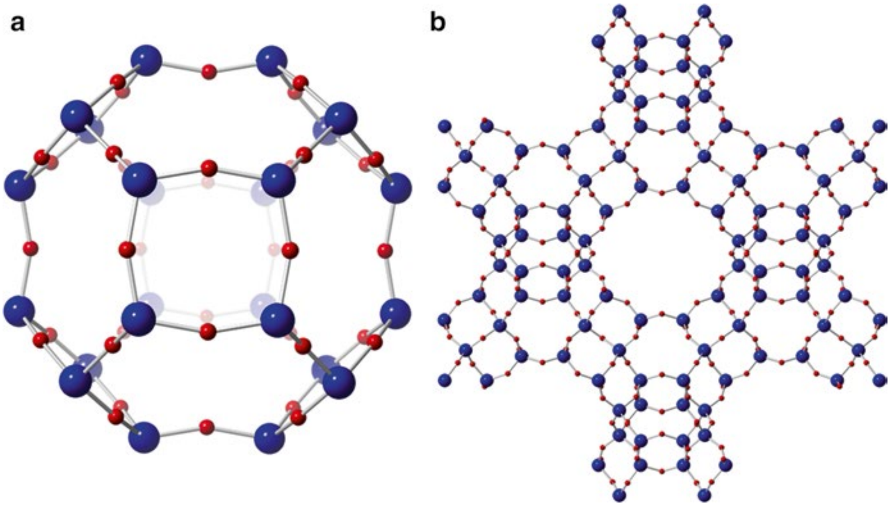

Fig. 4.4 Schematic representations of (**a**) *sodalite* cage. (**b**) *Faujasite* structure. In both diagrams, the "T" atoms appear in *blue*

4.1.2 Applications

Due to the capability of zeolites to exchange the cations containing the structure, they have replaced phosphates in detergents, becoming the single largest volume use for synthetic zeolites worldwide [4, 23], mainly zeolite A (LTA type). Taking advantage of this property, zeolites have been also used to capture nuclear elements, being of paramount importance after the Three Mile Island, Chernobyl, and Fukushima accidents.

The properties of zeolites strongly depend on their topology, making possible to distinguish in a reaction between reactants or products [24, 25] with a difference in size of only 0.05 nm. They can be used as bifunctional catalysts carrying a catalytically active metal, such as Pt, Ag, or Cu, or on their own. The large internal surface area, the strong acid sites, the possibility of selective sorption, and the molecular sieve effect are an exceptionally useful combination for a catalyst. Since their introduction in the refining process 40 years ago, zeolites have been widely used in the fields of petroleum refining and petrochemistry. Dealuminated MOR is used for the isomerization of light paraffin, usually containing a noble metal impregnated onto the zeolite. Zeolite Y is used as a catalyst for FCC (fluid catalytic cracking), with approximately 500,000 tonnes/year, about 1.05 billion dollars/year [26], used for this process.

In the area of petrochemistry, ZSM-5 is used to isomerize aromatics, in order to produce *p*-xylene. Again, the zeolite is impregnated with a noble metal. The synthesis of ethylbenzene and cumene (90 % of the ethylbenzene is used to produce styrene and polystyrene) is carried out by ZSM-5 and beta (BEA) or USY, respectively. Zeotypes (materials with zeolite structure, where Si or Al atoms are replaced by other elements) are also used in the petrochemical industry to convert methanol into olefins and gasoline; in this case, SAPO-34 [27, 28] is the catalyst more commonly used. SAPO-11 is also used to convert synthesis gas $\left(\mathrm{CO}+\mathrm{H}_2\right)$ into gasoline.

Not only petrochemical companies but also other types of industries have found different uses for these materials, such as desiccants, water softener devices, detergents and soaps, housecleaners, or heavy metal removal. Depending on the type and morphology of the metal incorporated into the zeolite framework, new potential applications are being discovered, such as decomposition of NO [29] interconnects in nanodevices [30] or chirality [31].

4.2 Zeolites and Electron Microscopy

Considering the good crystallinity and the large structural parameters that zeolites tend to exhibit in most of the cases, it would be expected that these microporous solids would provide excellent materials for transmission electron microscopy observations. Unfortunately, zeolites suffer severe drawbacks regarding their electron beam sensitivity which has been associated to radiolytic damage [32–35]. In addition to this, another major disadvantage has been associated to high-resolution transmission electron microscopy (HRTEM), which is the presence of artificial electron optical effects [36–39]. Due to these crucial factors in the observation of molecular sieves, the analysis of microporous structures by conventional TEM has represented a great challenge for scientist which has converted this field in a very active topic in material science with numerous publications. The pioneer results date back to 1958 where lattice fringes were observed in *faujasite* mineral [40]. During these years, electron microscopy (EM) studies were based on diffraction analysis [41], and it was not until 1972 when EM images were utilized to study faults in ERI [42]; later on, mainly in the 1980s, HRTEM images began to be used to elucidate structural parameters in zeolites [43]. Since then, a countless number of papers have been published dealing with molecular sieve observations under the electron beam with exceptional quality [38, 44–51].

It has been deeply studied and widely accepted that the sensitivity of zeolites is related to the ionization due to radiolytic damage. Radiolysis consists on the dissociation of chemical bonds as a result, in this case, of the high energy flux of electrons. Within an electron microscope is composed of several electron excitations: inner shell ionization, plasmon loss, creation of locally bound electron–hole pairs, and the cross section, which decreases when accelerating voltage is increased. This radiolytic damage can be expressed as [52, 53]

$$\sigma_e = \frac{8\pi a_0^2 R_\infty^2}{mc^2} \frac{Z'}{T'_{th}\beta^2} \tag{4.2}$$

where T'_{th} is the minimum energy required to break an atomic bond and Z' is the number of electrons around the atom. Fortunately, the efficiency of the electrons hitting the sample is not of 100 % and therefore not all the electrons cause bond breaking [54]. Therefore, the radiolytic damage cross section σ_r is the result of the product of σ_e and the efficiency (ζ):

$$\sigma_r = \sigma_e \zeta \tag{4.3}$$

which has been found to decrease when the acceleration voltage is increased [53]. A major factor in limiting the lifetime of zeolites under the electron beam is the Si/Al ratio. The amount of water occluded in the cavities is directly related to this relatively composition, and the ionization of water is believed to be a critical factor regarding the stability of zeolites under electron irradiation. In 1987 Tracey and Newsam [34] proposed three mechanisms for the vitrification of the framework: (1) bond breakage caused by the formation of a peroxy linkage resulting from the excitation of the 2*p* orbital of the oxygen in the oxygen bridge, (2) OH radicals combine with extra-framework cations resulting in Al–O–Si bond breakage, or (3) protonation of the Al–O–Si bridge weakens the Al–O bond and results in the formation of a Si–OH group. In addition to this, the extra-framework cations (and its order or not) has been suggested to influence the structural instability [33, 55].

Most of zeolites are obtained in powder form with large crystallites, that if they are free of defects, structural parameters can be determined by powder X-ray diffraction methods. However, there are several benefits in using EM over (or complementary) other methods:

(a) Atomic, local, and periodic structures can be also determined at the nanometer-sized crystal scale.
(b) EM is crucial for the analysis of several types of defects which affect the chemical and physical properties of molecular sieves [56, 57].
(c) Intergrowths between different materials within the same families are frequent in zeolites [58–61] or in some other cases where the structures are described as the stacking sequence of the sheets [62, 63].
(d) Acquiring information of the surface structures in order to understand the crystal growth process with the final purpose of a more rational design [57, 64].
(e) Zeolites acting as hosts are rather common. For these samples are indispensable to locate the position of the guests and to check the crystallinity after occlusion. In this sense, TEM provides unique information especially for nonperiodic structures [47, 57, 65–71].
(f) A chemical and elemental characterization of the sample can be carried out either energy-dispersive X-ray spectroscopy (EDS) or electron energy loss spectroscopy (EELS). Furthermore, point-by-point chemical information can be extracted by using a convergent beam in scanning transmission electron microscopy (STEM) mode.

4.2.1 Surface Structure of MFI

Silicalite-1 (MFI) is often industrially used as a model system to study crystal growth. Gaining information on the external surface area is imperative in order to build crystal growth models, understanding the catalytical and adsorption properties, especially when nanocrystals are synthesized where the external area becomes more important.

The effects that SDAs have in the structure of the final zeolite have intrigued synthetic scientist due to the possibility of fully controlling the formation process in order to produce novel materials with the aim of exploring new applications. One of the main structure-directing effects in the synthesis of pure or very high-silica zeolites is exerted by organic cations that remain occluded in the zeolite cages [72]. The size, flexibility, and concentration of such cations are crucial for a rational design, and their directing ability has allowed reporting novel structures as ITE, STF, and ISV, moreover, to a series of disordered materials. Thanks to a very careful and detailed analysis by HRTEM combined with electron diffraction, it showed that no extra spots or striking was observed that should appear if intergrowths or stacking faults were present. A mixture of phases was also rejected by electron diffraction analysis as every diffraction pattern was indexed as $P4_2/mmc$ [73].

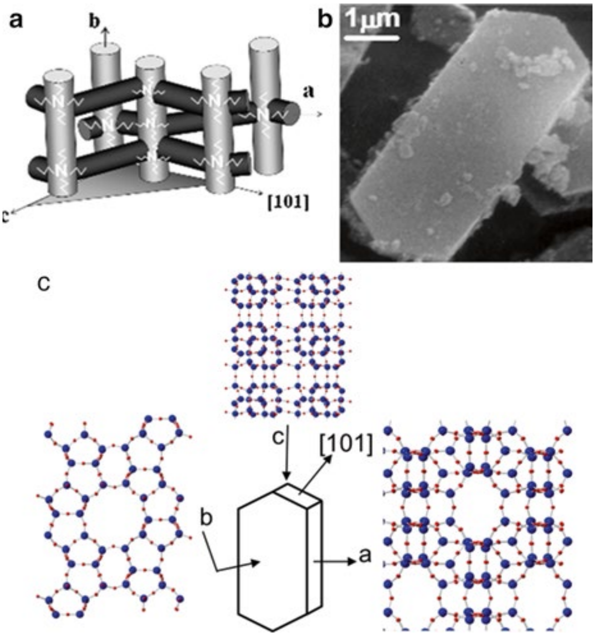

Fig. 4.5 (**a**) Schematic representation of the pore structure of TPA-MFI, where the TPA is located at channels intersections. (**b**) Typical SEM image of the coffin-shaped crystals. (**c**) Schematic representation identifying the crystal faces and directions along with the corresponding framework projections ("T" atoms in *blue* and O in *red*). Adapted from [72]

ZSM-5 zeolite belongs to the MFI-type structure, and it can be described as a combination of two interconnected systems with orthorhombic (*Pnma*) symmetry. The MFI framework is formed by sinusoidal channels along the *a*-axis, which are interconnected with ten-member ring (MR) straight channels running along the *b*-direction. On the other hand, a tortuous path can be observed along the *c*-direction. In order to obtain rich Si ZSM-5 (known as silicalite-1), tetrapropylammonium hydroxide (TPA) is used as structure-directing agent (SDA) through the incorporation at the channels intersection (Fig. 4.5), which leads to particles with coffin-shaped morphology. In these crystals, the mentioned sinusoidal channels run along the *a*-axis, and straight channels go along *b*, which corresponds to the shortest dimension of the crystal. By controlling the SDA, different morphologies can be obtained retaining the MFI-type structure [72]. Synthetic dimer TPA cations dC7, dC6, and trimer TPA (tC6) yielded new morphologies for MFI crystals, which are normally identified by scanning electron microscopy (SEM) followed by TEM and selected area electron diffraction (SAED) to index crystal faces [72]. Furthermore, the surface microstructure was evidenced for the first time on MFI-type zeolite by means of HRTEM observations [46]. Figure 4.6 shows the [010] projection of a tC6-grown MFI crystal. The termination area marked as A provides structural information of the (100) face. This confirms the termination with complete pentasil

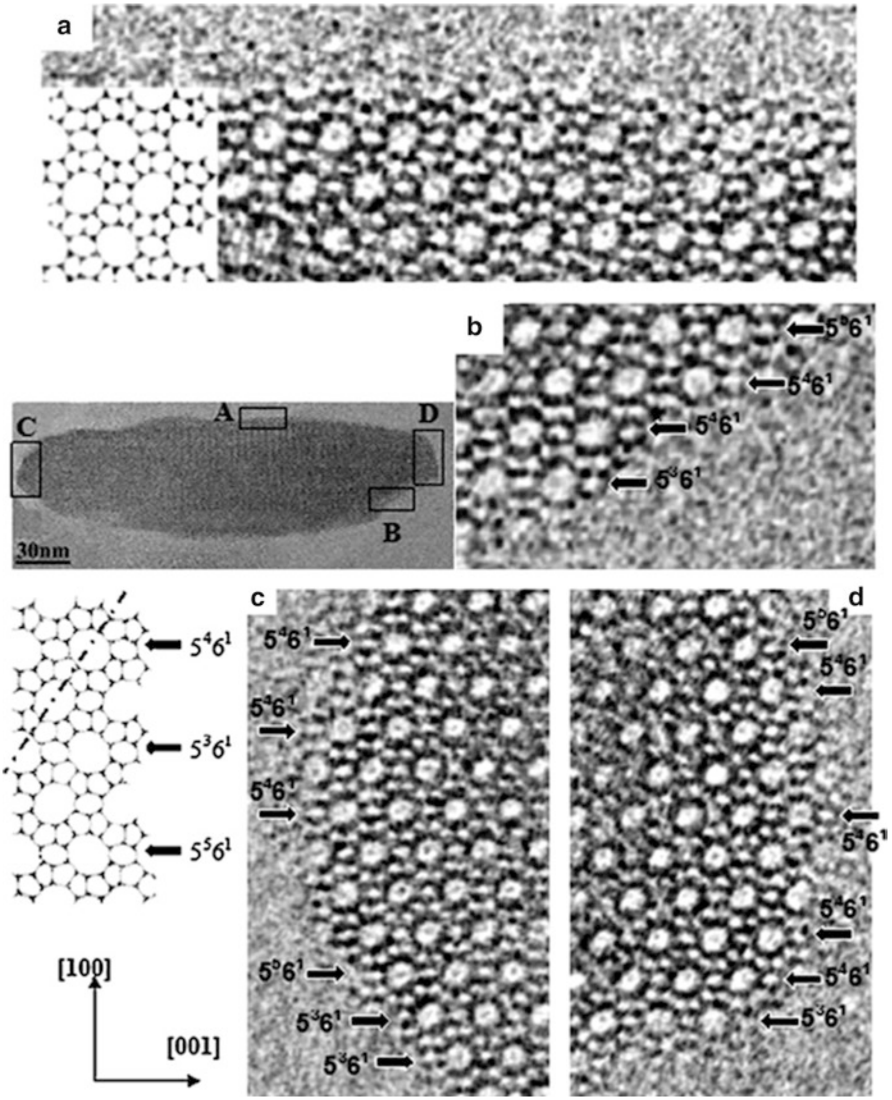

Fig. 4.6 Low- and high-magnification HRTEM images of a tC6-grown crystal orientated along the *b*-axis. Adapted from [46]

chains and incomplete six-member rings (6MRs). Areas B, C, and D suggest the absence of well-defined facets on this projection. The (*h0k*) facets are formed by various combinations of terminal 6 MRs and 5 MRs. Although groups consisting of 6 MRs surrounded by four 5 MRs (indicated by 5^46^1) are most abundant, 6 MRs surrounded by three 5 MRs (5^36^1) along with some rougher or hairy terminations with an extra 5 MRs (5^56^1) are also present [46]. Figure 4.7 shows a crystal tilted

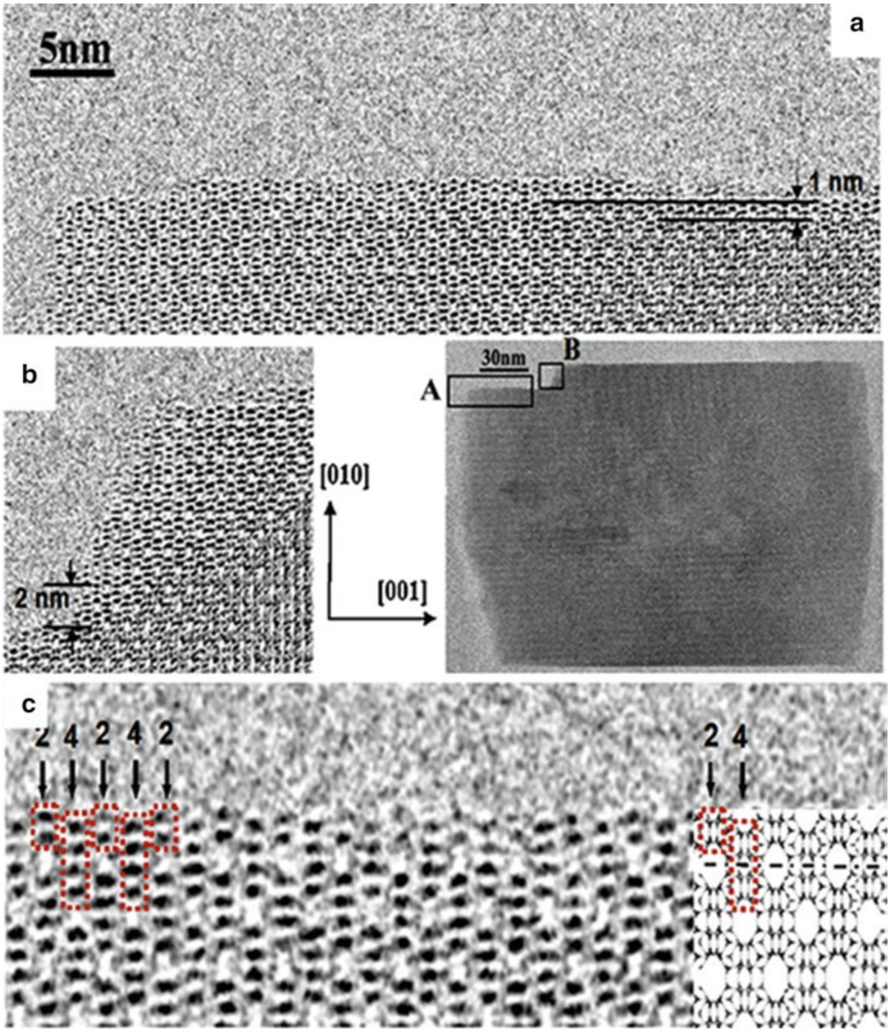

Fig. 4.7 HRTEM images recorded along the [100], *a*-axis (sinusoidal channels). Adapted from [46]

along the [100] projection where the sinusoidal channels can be identified. The area marked by A gives information on the surface termination of the (010) faces. Magnification of the mentioned area shows the presence of 1 nm steps (1/2 unit cell along the *b*-axis), while magnification B shows a rare 2 nm step (one unit cell along the *b*-axis). Figure 4.7c corresponds to a magnified image of Fig. 4.7a. The sequence of 2, 4, 2, 4 black dots, marked in the figure, clearly establishes as dominant termination of the (010) face, complete pentasil chains, and incomplete 6 MRs. This surface structure minimizes the number of Si–OH groups and has been often proposed as a possible surface termination.

4.2.2 Beam Irradiation on $AlPO_4$-5

The aluminophosphate microporous material, $AlPO_4$-5, presents AFI-type framework structure, where the “T” atoms correspond to alternative Al and P. The system is composed of one-dimensional channels that run along the [001] direction, consisting of 12-membered rings surrounded by six 4-membered rings and six 6-membered rings as shown in Fig. 4.8a. The as-synthesized material with the template still in the channels has a hexagonal structure which can be explained assuming *P*6*cc* symmetry; however, after calcination, the framework exhibits lower symmetry due to the relaxation of the framework [74, 75]. A high-resolution image of the pore structure along the [001] direction is shown in Fig. 4.8b where the main straight channels, 12-membered rings, can be elucidated. A closer observation is shown in Fig. 4.9a together with the simulated data and the framework structure, where the six and four rings around the main channels can be identified. The fact that the four-membered rings are not so clearly observed can be attributed to the low stability of this material that resulted in very fast radiation damage.

A series of ED pattern from a crystal orientated along the [001] zone axis and from the same area of the specimen is shown in Fig. 4.10. The area was selected by a selected area (SA) aperture of 200 nm on the specimen. After about 6 C/cm^2 total dose on the sample, the 550 reflection $\left(d_{550} = 1.37\text{Å}\right)$, marked by an open arrow in the figure, starts to weaken, and the relative intensity of whole ED pattern also changes. The intensity of the diffraction spots continuously decreases, while each peak becomes broader; both effects are associated to the reduction of the crystal size

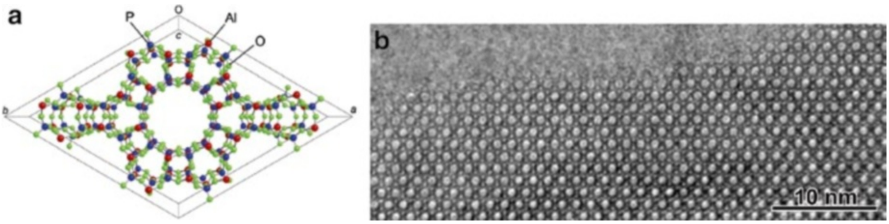

Fig. 4.8 (**a**) Crystal structure of $AlPO_4$-5 along the [001] direction. Adapted from [51]

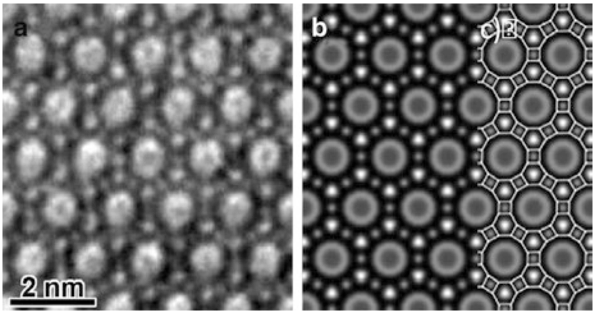

Fig. 4.9 (**a**) Experimental HRTEM image of $AlPO_4$-5 along the [001] direction, (**b**) simulated image along the same orientation, and (**c**) framework structure overlaid on the simulated image. Adapted from [51]

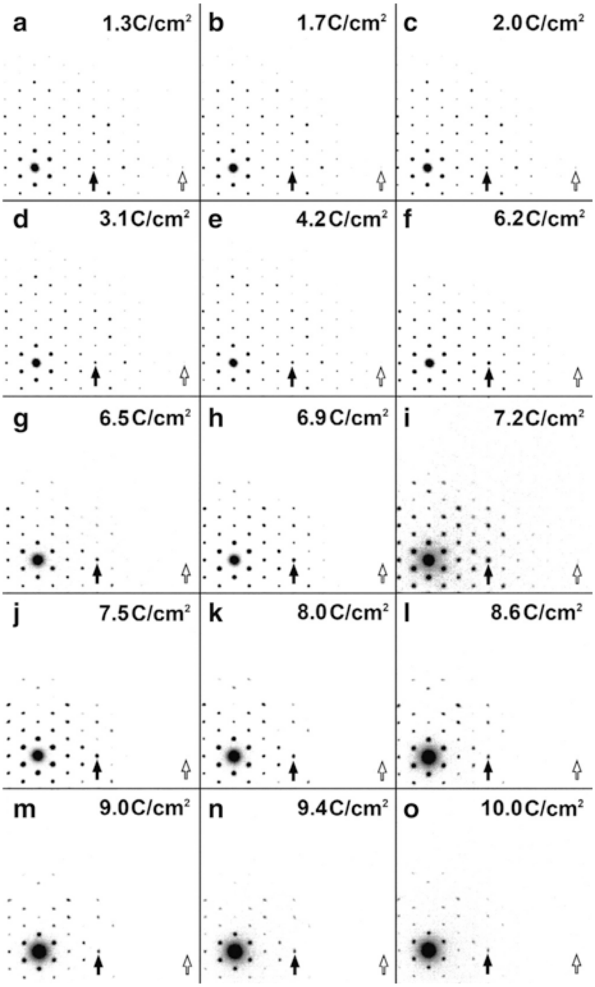

Fig. 4.10 Series of the ED patterns recorded at the same area of the specimen. *Solid* and *open arrows* indicate 220 and 550 reflections, respectively. Adapted from [51]

due to the vitrification process. When the beam dose was increased over 7.5 C/cm^2, the process accelerated.

The high-resolution images recorded from the same area revealed that for 0.9 and 1.5 C/cm^2, the 12-membered and the six-membered rings were observable exhibiting symmetrical Fourier diffractograms. When the total dose was increased above 2.5 C/cm^2, vitrification process begins to take place and electron damage becomes more apparent. In addition, the lower resolution achievable which does not allow imaging the six-membered rings, lattice distortion, and tilted diffractograms can be also observed [51]. Interestingly, lattice defects, which may originally exist in the structure, are observed in the image with 0.9 C/cm^2 total dose, but they don't enhance the vitrification under the electron beam.

4.3 Zeolites and Spherical Aberration-Corrected Electron Microscopy

All results presented through this chapter have been obtained under a very careful control of the electron beam dose applied; this is minimizing the amount of electrons per area as possible and under very low exposure times in order to avoid structural damage. This has made very difficult to obtain any benefits from the most modern electron microscopes which incorporate spherical aberration (C_s) correctors. In the early 2000s, C_s-corrected electron microscopes became commercially available overcoming the lateral resolution issue; however, the increment of the number of electron per area that comes associated with new machines would have an even more detrimental effect on the analysis of this type of solids. For the particular case of C_s-corrected STEM, the quality of the images has dramatically improved with the use of the correctors for the electron probe. However, the high current focused onto a fine spot that is scanned along the sample would easily result in burning a hole.

Fortunately, by having an exhaustive control of the electron beam current and pixel time (time that the beam is located onto the structure), new findings have been reported on molecular sieve microscopy since 2010. This mode of operation combined with a high-angle annular dark-field detector (HAADF) rises the advantage of an easier image interpretation as the contrast is proportional to Z^n (Z is the atomic number and $n \oplus 1.7$), and, furthermore, the image is not affected by the contrast transfer function (CTF) enabling the possibility of forming atomic resolution images. In addition, heavy atoms incorporated into the structure can be highlighted allowing the characterization of, for example, metal distribution.

The pioneer result using C_s-corrected STEM-HAADF described the location of Ir atoms on ultrastable dealuminated zeolite HY [65]. In these experiments, low-dose conditions for imaging were used ($1{,}200\ e^{-}\text{Å}^{-2}$) observing at atomic level the guest Ir single atoms and clusters but not the zeolitic framework. An alternative approach to the low-dose conditions has been also described, which consisted of increasing the dose up to 10^5–$10^6 e^{-}\text{Å}^{-2}$ and decreasing the pixel time [66, 76]. This allowed the observations of Ir and Au atoms in zeolites SSZ-53 and zeolite Y, respectively. For even higher resolution images with the scope of observing the zeolitic framework, the best results have been reported by decreasing the beam dose to the maximum, keeping the structure still visible confirming that nowadays it is possible to assert that truly atomic resolution images of guest species and virtually any zeolitic framework [67, 68, 77, 78] can be obtained by means of C_s-corrected EM.

4.3.1 Zeolite A (LTA Type)

Zeolite A is normally synthesized by a hydrothermal method leading into a white powder with cubic morphology [79]. It presents an ideal formula (on the sodium form) as

Fig. 4.11 C_s-corrected STEM images of NaA (**a**) using a beam current of 150 pA, *inset* the simulated image (probe size of 1.7 Å) [67], and (**b**) using beam current of 2 pA, *inset* the simulated image using a probe size of 0.7 Å [81]

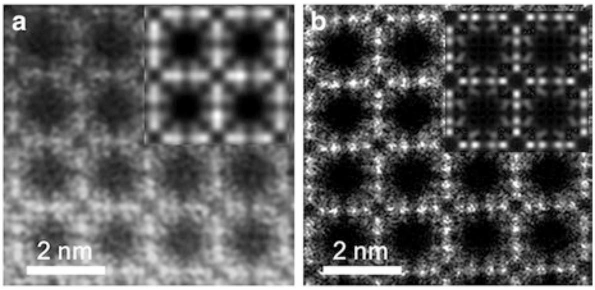

$\left|Na^{+}_{12}\left(H_2O\right)_{27}\right|_8$ $[Al_{12}Si_{12}O_{48}]_{48}$ with unit cell of $a = 24.61$Å in the *Fm*-3*c* symmetry [80]. This structure represents the lowest Si/Al ratio in a zeolite converting it in one of the most beam-sensitive materials. Figure 4.11 shows the type of images that can be obtained from a C_s-corrected equipment operated at 300 kV when the beam current is decreased. Figure 4.11a displays the FFT filtered image of NaA along the [001] orientation with a beam current of hundreds of pA, showing inset the simulated image for a probe size of 1.7 Å. On the other hand, Fig. 4.11b shows the results when the beam current was decreased below 10 pA allowing a full identification of T atoms within the structure together with the simulated image using a probe size of 0.7 Å. In these two images, the darker area corresponds to the zeolite pores that is, zeolite alpha cages, linked to each other by sodalite cages, in which the four-membered rings can clearly be observed.

The very high ion exchange capability of LTA has converted it into the most widely industrially produced zeolite, mainly for its application in detergents. The sodium can be easily exchanged by silver cations obtaining a white powder that, when dehydrated, suffers from a spectacular sequence of color changes [47, 82]. This effect has been attributed either to the presence of partially reduced Ag_6 octahedra in the sodalite cages [82] or also to the formation of linear clusters of three atoms [83]. With the purpose of gaining information of the interior of the zeolitic cages, ultrahigh-resolution C_s-corrected STEM images were recorded along the main crystallographic orientations, [001], [011], and [111]. Due to the low stability of the material under the beam, it is necessary that each orientation needs to be recorded from different crystallites. An initial major difference could be observed between the original NaA and the dehydrated AgA as a perfect distribution of white spots as images, Fig. 4.12.

A careful analysis along the [001] projection, corroborated with the other orientations, allowed for the first time imaging the silver conformation within the *sodalite* cages. Figure 4.13a shows the Ag distribution with the *sodalite* cages containing 14 Ag atoms. Eight of them (which would correspond to four signals in the projected image forming a square) forming a cube in the three-dimensional space (separated by 4.72 Å, Fig. 4.13b) that contains six Ag more (five signals in two dimensions) that would form the smallest octahedron ever reported. Meanwhile, the distance between Ag columns in the adjacent sodalite cages was found to be

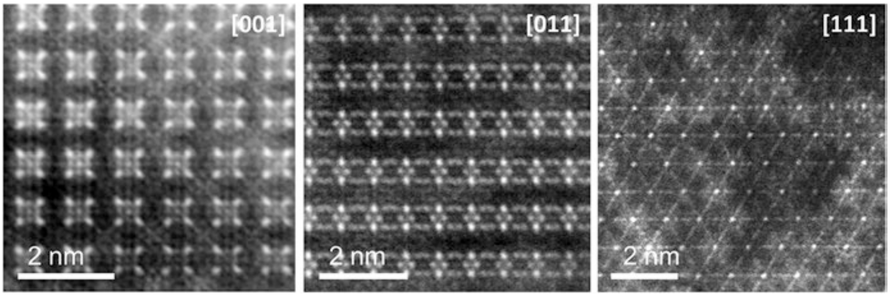

Fig. 4.12 C_s-corrected STEM-HAADF images of dehydrated AgA along the main crystallographic orientations, where Ag appears as brightest atomic columns [67]

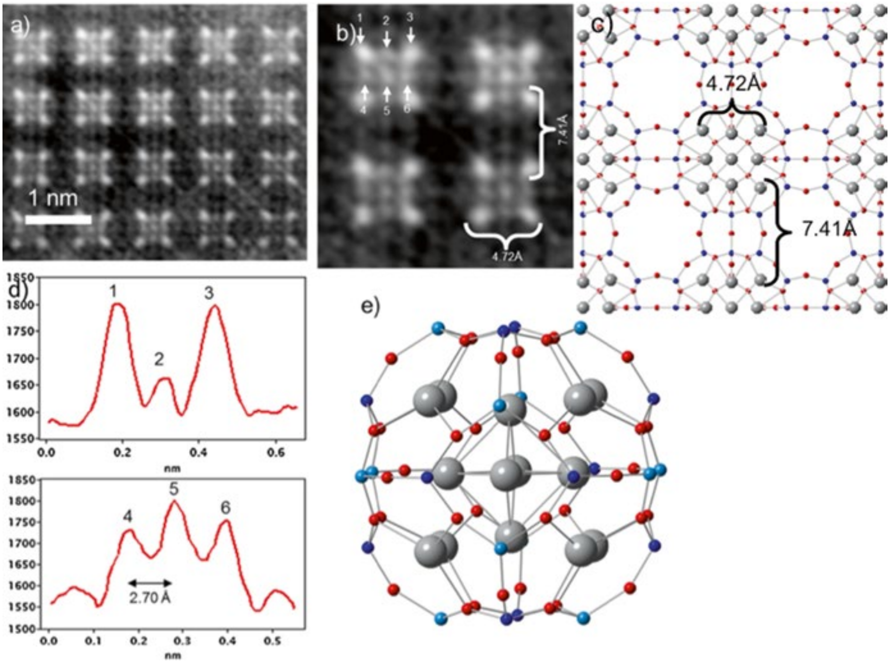

Fig. 4.13 (**a**, **b**) FFT-filtered images of AgA along the [001]. (**c**) Model proposed containing the Ag (in *gray*). (**d**) Intensity profiles of the interatomic distances marked in (**b**). (**e**) Sodalite cage slightly tilted for a better visualization of the Ag. Adapted from [81]

approximately 7.41 Å. The schematic model assuming the formation of Ag_6 octahedra is shown in Fig. 4.13c, where silver appears in gray color. The intensity profiles plotted over three atomic columns in the *sodalite* cages (Fig. 4.13d) show a higher intensity at the corners because of the higher number of atoms in those positions. For the second line intensity profile (points 4, 5, and 6), atoms forming the Ag_6 cluster, the highest value was obtained in the center of the octahedron, again

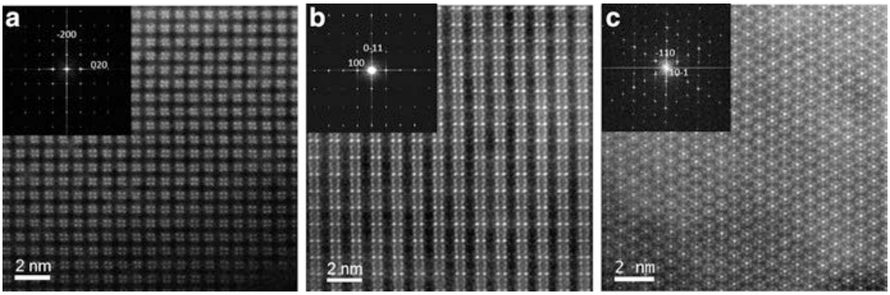

Fig. 4.14 C_s-corrected STEM-HAADF images of CdA along (**a**) [001], (**b**) [011], and (**c**) [111]. In all cases, the Fourier transforms are shown *inset* [69]

attributed to the greater number of atoms in that column. For those atoms, the interatomic distance was found to be 2.70 Å. For better understanding, a single *sodalite* cage is depicted in Fig. 4.13e.

As earlier mentioned in this chapter, a major application of certain molecular sieves is the ability that they have to capture (throughout ion exchange reaction) radioactive heavy metals. Cadmium can be inter-exchanged with the original sodium that upon dehydration also displays color transformations. Cd-containing zeolite A has been reported to exhibit better stability under the electron beam than the "parental" material. Unfortunately, conventional TEM observations failed to throw any information on the metal distribution [55]. Taking into account the much higher scattering factor of Cd with respect to the zeolite framework, it would be expected that by performing STEM-HAADF observations, the former would be highlighted compared to the Si, Al, and O. With the intention of elucidating the Cd presence and distribution, several crystallographic orientations were imaged. The electron dose for this case was also kept very low, below 30 pA. Figure 4.14 represents the [001], [011], and the [111] projected orientations of the Cd-loaded zeolite A. For all images, there is a symmetric metal distribution. A closer observation of the data acquired along [001] projection is presented in Fig. 4.15. From this image, it is possible to assume that Cd species adopted a cubic symmetry occupying the six rings of the *sodalite* cages. An analysis of the intensity of the signals obtained is presented in Fig. 4.15a, b. Intensity profiles were extracted from the arrows marked as 1 and 2 (raw data) along the center of the *sodalite* cage and along the six rings where the Cd was contained. Intensity profile "1" (Fig. 4.15b) first exhibits a maximum corresponding to the Si and Al atoms (known collectively as "T atoms"), forming the six rings that define the sodalite cage (upper part) separated from each other by 2.21 Å. The second distance measured corresponds to the T atoms sitting on the diagonal of the four rings of the *sodalite* cage and separated by 4.11 Å. The last distance measured was 7.90 Å and attributed to one T atom forming the four rings (bottom part) and the upper T atom of the four rings from the following *sodalite* cage. The intensity profile "2" was traced over four Cd atomic signals. The first interatomic distance corresponds to a T atom (very low intensity with respect to the Cd) and two Cd atomic columns, too close to each other (0.47 Å) to be considered

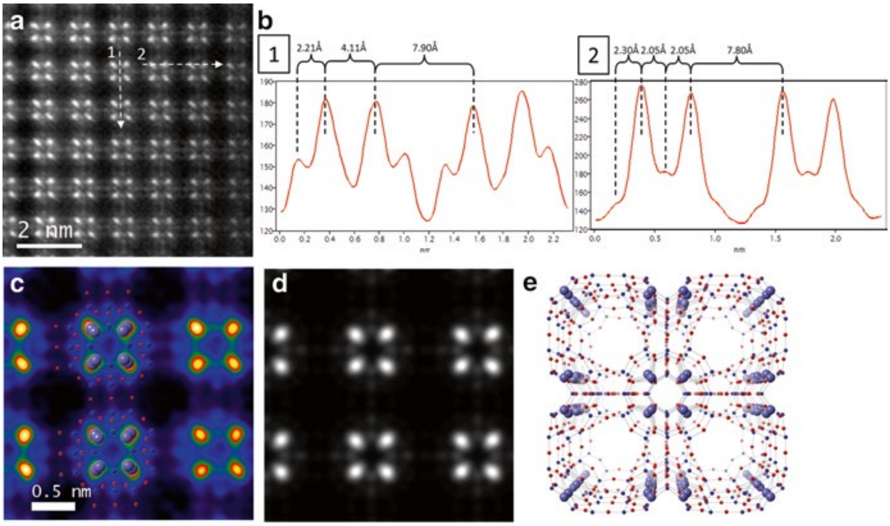

Fig. 4.15 (**a**) Atomic resolution data, where two intensity profiles were plotted, marked as *white arrows*. (**b**) Intensity profiles where the distances between maxima are shown; *1* corresponds to zeolite signals and *2* is due to Cd. (**c**) Thermal-colored atomic resolution image of a zeolite A unit cell with the model superimposed. (**d**) Simulated STEM data of the experimental data shown in panel (**c**). Schematic representation of Cd zeolite A where the Cd atoms appear in *violet*. (**e**) Ball-and-stick model of the Cd-loaded zeolite A. Cd appears in violet, O in *red*, and Si and Al in *blue*

as individual entities (situated in the six rings of the *sodalite* cage) separated by ~2.30 Å. The second distance of 2.05 Å belongs to this Cd atomic column and the T atomic signal that comes from the upper atom of the four rings of the *sodalite* cage. The next distance is the same one but taking into account the next Cd atomic column in the other six rings of the *sodalite* cage (Cd–Cd distance 4.11 Å). The last measurement corresponds to two strong signals that are coming from two of the Cd atomic columns from two different *sodalite* cages and separated by 7.80 Å. It is worth to mention the strong and very elongated signal which suggests the presence of two Cd species two close to each other (0.5 Å) to be clearly differentiated. Figure 4.15c shows the thermal-colored data with the model superimposed. The strong correlation between the experimental and simulated data, Fig. 4.15d, suggests the presence of 2 Cd species in the six rings.

4.3.2 ETS-10 Analysis

Porous titanosilicates were first discovered in 1983 [84] where a pure siliceous silicalite-1 was doped with titanium, where the Ti adopted a tetrahedral coordination. Years later, a related new class of materials containing octahedral and tetrahedral coordinated T atoms (T = Si, Al, or Ti) was synthesized [85, 86]. ETS-10 (Engelhard Corporation titanosilicate) is a member of this family formed by orthogonal TiO_6

octahedra and SiO_4 tetrahedra linked by corner-sharing oxygen atoms forming a three-dimensional pore system [87]. Each titanium unit, therefore, introduces two negative charges that must be compensated by cations to provide a material that is particularly interesting for ion exchange, adsorption, photochemistry, membrane separation, and catalysis [88, 89]. Its particular structural parameters, containing a high degree of disorder, do not allow an easy structural determination. ETS-10 has unit cell [90] (polymorph B) parameters $a = b = 21\text{Å}$, $c = 14.5\text{Å}$, $\alpha = \gamma = 90°$, and $\beta = 111.12°$, with space group $C2/c$. By combining SEM images with ED patterns and HRTEM images, it was confirmed that the ETS-10 exhibits fourfold symmetry projection along the z axis and that the projected structures along the x and y axes are identical [38, 62, 91]. The basic structure can be explained as (–O–Ti–O–Ti–O–)$_n$ chains, built from TiO_6 octahedra sharing corners which are surrounded by Si–O linkages. The typical structure of ETS-10 is shown in Fig. 4.16a, where oxygen appears in red, titanium in light blue, and silicon in dark blue. Figure 4.16b exhibits the high-resolution C_s-STEM-HAADF data along the [110] projection, where the 12-membered rings forming the large pores are clearly identified as well as the Ti–O chains and the Si–O units. An artificially colored map based on the atomic intensities for each atomic position is represented in Fig. 4.16c. Figure 4.16d

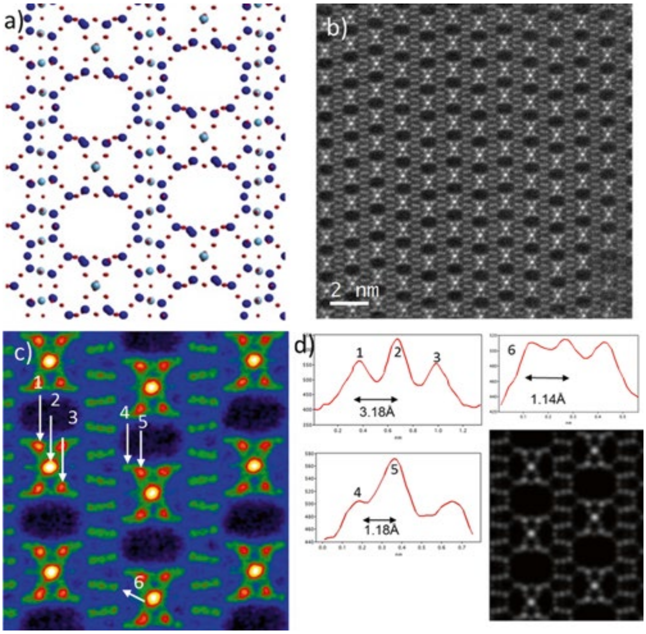

Fig. 4.16 (**a**) Model of ETS-10 along the [110] orientation. (**b**) C_s-corrected STEM-HAADF image at the same orientation, where many stacking faults are observed. (**c**) FFT filtered thermal-colored map, where the different atomic columns are identified and marked with *numbers*. (**d**) Intensity profiles of the positions denoted in (**c**), together with the simulated data. Images adapted from [77]

displays the plotted intensity profiles (arbitrary units from the raw image) of each signal, and for the case of Ti, it is observed that it is around 15 % more intense than for Si, confirming the feasibility of this method to discern, by simple image analysis, between Ti and Si; however, although the difference in *Z* number may be enough for such a contrast difference, the number of atoms composing the column must be also taken into account. If only a unit cell is considered (for simplicity), the number of Ti atoms in position "2" is 9 being 8 or 7 for Si. Positions "4" and "5" only show the presence of Si separated by 1.18 Å. In this case, for the same atomic number, the difference in intensity is related to the number of silicon atoms in those positions being 8 with respect to 3 or 7 versus 4 (again if only one unit cell is considered). The row of 3 atomic columns, marked as "6" and separated by approximately 1.14 Å, displays an overall similar intensity maximum. In this row, the central atom is always Ti. However, the number of atoms is higher for Si, and therefore they compensate the stronger scattering factor of Ti with respect to Si. The simulated image is also presented matching very well with the experimental data.

An intrinsic property of ETS-10 is the high degree of defects present in the structure, which are ultimately responsible for the properties and different applications of this material. Stacking faults have been always observed in this material, and their formation was nicely described by Anderson et al. [92, 93] in 2001 as a consequence of the layer growth. Figure 4.17a shows the Fourier-filtered image of a

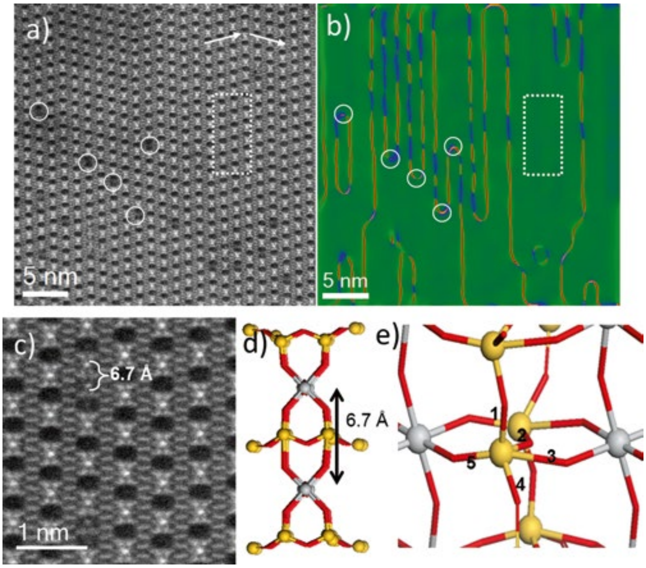

Fig. 4.17 (**a**) C_s-corrected STEM-HAADF image where the rotational analysis was performed; the defects are marked by *circles*, a stacking fault is marked by two *arrows*, and the area of reference corresponds to the *white dashed square*. (**b**) Rotational map produced using image. (**c**) Closer look at ETS-10 showing two TiO_6 octahedra linked to each other where the Ti atoms are separated by 6.7 Å. (**d**) Ball and stick model proposed for 2 TiO_6, in *yellow* the Si atoms, and in *gray* the Ti atoms. (**e**) Hypothetical model, where the Si would be linked to 5 O and therefore one of those bonds must be broken

crystal where the stacking faults are marked. In every case the disorder merged as consequence of the 12-ring layer, which is displaced from its "expected" position by the size of one pore, this is approximately 6.70 Å. Figure 4.17a shows a medium magnification image with its correspondent rotational map obtained through geometrical phase analysis (GPA) [94] and digital micrograph analysis. In both figures, the area used as reference is marked by a dashed white rectangle, which corresponds to an area free of structural defects. Therefore, all the lines appearing in different colors in the image are directly related to rotational changes (GPA nomenclature, which corresponds to dislocations) in the ETS-10 layers with respect to the area of reference and as a consequence on the growth direction. The structural defects marked with white circles (only five for the sake of clarity) have always been found to be the starting point for a change in the direction of the lines (observed in the rotational map, Fig. 4.17b). This observation suggests that this type of defects would be the point where such a "faulted structure" is formed. The change in growth direction is marked in Fig. 4.17a by white arrows corresponding to a relationship of 120° between the two regions. A closer observation of the so-called double pores revealed the presence of a weak signal suggesting the presence of another building (Fig. 4.17c) unit which has not been observed by conventional TEM. Figure 4.17d displays a schematic representation of the defect formed, which was observed in every crystal analyzed. If this conformation is extended over the three-dimensional space (Fig. 4.17e), Si atoms would be linked to five oxygen atoms (Fig. 4.16e). Clearly, Si cannot have five Si–O bonds and one bond must be broken. As a consequence of this disruption in position "1" or "4," the number of atoms in that column would be lower making it look like a double pore by conventional TEM.

4.4 Ordered Mesoporous Materials

The discovery of mesoporous silicas with tunable mesoscale pores in the early 1990s opened up new possibilities for various applications in different fields ranging from chemistry and physics to materials science and pharmacy [95–98].

Mesoporous silicas have two defining structural characteristics: (1) disorder on the atomic scale, i.e., only short-range order, and (2) distinct order on the mesoscale, i.e., long-range order. Atomic-scale structural characterization by common diffraction techniques, such as X-ray single-crystal diffraction, is challenging for these partially ordered materials. This is because of the difficulty in obtaining large (>10 μm) single crystals, and because large-distance periodic features cause diffraction intensities to fall off rapidly with scattering angle, so that only limited small-angle data are available, as shown in Fig. 4.18. With CuK_α radiation, there are several peaks in the two-theta range less than 10°, which are attributed to distinct long-range mesoscale order. At higher scattering angles, there is only diffuse scattering originating from amorphous atomic-scale character, i.e., amorphous silica.

Transmission electron microscopy (TEM) is a powerful tool for structural characterization at the mesoscale level, especially for solving three-dimensional (3D)

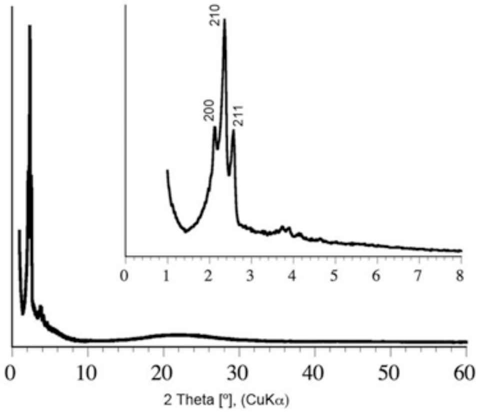

Fig. 4.18 Powder X-ray diffraction pattern of mesoporous silica SBA-1 with space group *Pm*-3*n*

structures of mesoporous silicas. Two methodologies exist for 3D structural characterization of mesoporous materials with amorphous silica wall structures. One is electron tomography and the other is electron crystallography which is actually the only method to solve structures. We will focus on electron crystallography in this chapter.

Electron crystallography for mesoporous silicas is a method where the phase and the amplitude of the crystal structure factors are obtained from HRTEM images. By collecting data from several zone axes, a 3D structure model can be obtained. The main advantage of using HRTEM images, compared with traditional X-ray single-crystal diffraction, is that the phases are experimentally available from Fourier transformation of the HRTEM images. Another advantage is the stronger interaction of electrons with matter compared with X-rays, enabling the use of small crystal sizes down to only a few tens of unit cells. Electron crystallography has been applied to a variety of mesoporous silicas, and unique structural solutions were obtained without any previous assumption of structural models [99–107]. From 3D structural solutions, it is possible to deduce, at the nanoscale level, the size, shape, arrangement, and connectivity of pores or cages, including the dimensions of cage openings, which are crucial characteristics for application development.

4.4.1 Mesoporous Silica as a Crystal

In a crystal, an atom or cluster of atoms are arranged on each of the lattice points. All crystals are classified into one of seven crystal systems and 14 Bravais lattices. These 14 lattices have translational symmetry, and each lattice point is exclusively equivalent. When the point symmetry is considered with these 14 Bravais lattices, there are 230 total crystal symmetry possibilities, called space groups. The atomic arrangement at each lattice point is generated by one of the 230 space groups.

An ideal crystal is constructed by the repetition of structural units in 3D space. The structure of crystals can be described as the convolution of lattice and basis as follows:

$$\text{Crystal structure} = \text{Lattice} \otimes \text{Basis}, \tag{4.4}$$

where "⊗" stands for the mathematical operation of convolution. The 3D lattice is defined by three translational vectors, a_1, a_2, and a_3:

$$r = r_0 + t_1 a_1 + t_2 a_2 + t_3 a_3 \tag{4.5}$$

where t_1, t_2, and t_3 are arbitrary integers. The set of points r defined by (4.5) gives a lattice, and the smallest volume defined by the three vectors, a_1, a_2, and a_3, is called a unit cell. The crystal structure consists of the basis arranged on each lattice point, which is defined by (4.5). It should be noted that the basis does not need to be an atom or cluster of atoms (e.g., a molecule) as we will see later.

If the concept of a space group is introduced, the unit cell can be divided further into an asymmetric unit, where the asymmetric unit will generate the unit cell (and subsequently the whole crystal) by symmetry operations. Therefore, atomic-scale structural determination of crystals follows the following process: (1) determination of the space group and (2) determination of the arrangements of atoms in the asymmetric unit.

The crystal structure in real space and the crystal structure factors in reciprocal space have a one-to-one correspondence with each other, where the two are mathematically related by Fourier transformation. The crystal structure factors are composed of two parts (amplitude and phase), so that when both the amplitude and phase of the crystal structure factors are determined, the crystal structure can be exactly determined by Fourier transformation of them. However, diffraction-based techniques, such as electron diffraction and X-ray diffraction, provide only amplitude information of the crystal structure factors, and phase information is not included in the diffraction intensity. For crystal structural determination with a diffraction experiment, one has to go through a structure refinement process starting from initial assumptions of the arrangement of atoms or molecules in an asymmetric unit.

However, for mesoporous silicas, the same process cannot be applied to determine their meso-structures since they have different characteristics in different length scales; that is, they are amorphous on the atomic scale and have distinct order on the mesoscale. The crystal structure of mesoporous silicas can be described as a combination of lattice and basis based on the crystal definition in (4.4), where the lattice has repeating units of mesoscale order and the basis can be thought of continuous matter. As shown in Fig. 4.19, mesoporous silica with 2D hexagonal structure can be described based on this definition, where continuous tubes (basis) are arranged on a 2D hexagonal lattice with mesoscale periodicity.

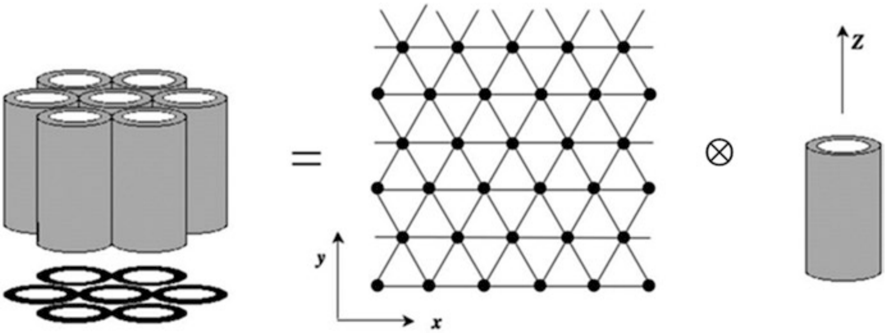

Fig. 4.19 Mesoporous silica with a two-dimensional hexagonal structure can be defined by a two-dimensional hexagonal lattice and continuous tubes arranged on each lattice point

4.4.2 Electron Crystallography

Since electrons have 10,000-fold stronger interactions with matter than X-rays, we can extract single-crystal information from a small area of several tens of nanometers. HRTEM images contain information about the phase as well as the amplitude of crystal structure factors. These are the major advantages for using HRTEM images for structural determination. 3D reconstruction of mesoporous silicas especially benefits from using HRTEM images. By using HRTEM images of mesoporous silicas, both amplitude and phase of crystal structure factors can be experimentally obtained, and the 3D meso-structure can be determined without a refinement process of an initial structural model. The reconstruction procedure for mesoporous silicas is as follows: (1) determination of the space group; (2) acquisition of HRTEM images; (3) extraction of both amplitude and phase from the HRTEM images; (4) correction of the CTF; (5) combination of the sets of amplitude and phase, corresponding to crystal structure factors; and (6) inverse Fourier transformation of the corrected crystal structure factors. Finally, the crystal structure—in this case the electrostatic potential distribution—of mesoporous silica is determined. With additional information such as pore volume from N_2 adsorption/desorption measurements and the silica density, one can calculate the threshold value, which gives the boundary between the silica wall and pore space, and determine the 3D pore structure, pore size, and silica wall thickness.

Here we will briefly examine the details of electron crystallography. Crystal structure and crystal structure factors are related to each other as follows:

$$V(x,y,z) \propto \sum_{hkl} F(hkl) \exp\left[-2\pi i(hx+ky+lz)\right] \tag{4.6}$$

where $V(x, y, z)$ is the electrostatic potential distribution and $F(hkl)$ are the crystal structure factors. Therefore, when the crystal structure factors are determined, the electrostatic potential distribution of the crystal can be obtained by Fourier transformation of the crystal structure factors with (4.6). The crystal structure factors are generally complex numbers and are written as follows:

$$F\left(hkl\right) = \left| F\left(hkl\right) \right| \exp\left[i\alpha_{hkl}\right] \tag{4.7}$$

Electron diffraction experimentally gives only amplitude information $|F(hkl)|$ and loose phase information αhkl of the crystal structure factors. However, HRTEM images give both amplitude and phase information experimentally.

Under the weak phase object approximation, where the sample thickness is thin enough, the image intensity on the image plane can be written as follows:

$$I\left(x,y\right) \infty 1 + 2\sigma V_{\mathrm{p}}\left(x,y\right) * \mathrm{FT}_{\mathrm{2D}}\left[\sin\left[\chi\left(u,v\right)\right]\right] \tag{4.8}$$

where $V_{\mathrm{p}}(x, y)$ is the projected potential of the sample, σ is the interaction constant, $\mathrm{FT}_{\mathrm{2D}}$ is the two-dimensional Fourier transform operator, and $\chi(u, v)$ is the CTF that is defined by the defocus value df, wavelength of electrons λ, and spherical aberration C_{s}:

$$\chi\left(u,v\right) = \pi\left[df\lambda\left(u^2 + v^2\right) + 0.5C_{\mathrm{s}}\lambda^3\left(u^2 + v^2\right)^2\right] \tag{4.9}$$

From (4.8), when $\sin\left[\chi\left(u,v\right)\right] = 1$, the image intensity $I(x, y)$ is proportional to the projected potential $V_{\mathrm{p}}(x, y)$. Fourier transformation of (4.8), i.e., Fourier transformation of the HRTEM image, becomes

$$\begin{aligned} F\left[I\left(x,y\right)\right] &\propto \delta\left(u,v\right) + 2\sigma \mathrm{FT}_{\mathrm{2D}}\left[V_{\mathrm{p}}\left(x,y\right)\right]\sin\left[\chi\left(u,v\right)\right] \\ &\propto \delta\left(u,v\right) + 2\sigma F\left(u,v\right)\sin\left[\chi\left(u,v\right)\right] \end{aligned} \tag{4.10}$$

where

$$V_{\mathrm{p}}\left(x,y\right) \propto \int F\left(hk, l=0\right)\exp\left[2\pi i\left(hx + ky\right)\right] dhdk. \tag{4.11}$$

From (4.10), it is clear that the structure factor $F(hk)$ can be obtained by Fourier transformation of the projected potential $V_{\mathrm{p}}(x, y)$, meaning that Fourier transformation of the image intensity $I(x, y)$ gives the crystal structure factors modified by the CTF, sin $[\chi(u, v)]$. After correcting for the CTF, and combining the structure factors extracted from each HRTEM image, the crystal structure factors defined by (4.7) can be obtained. Inverse Fourier transformation of the crystal structure factors gives us the electrostatic potential distribution in 3D space defined by (4.6).

4.5 Ordered Mesoporous Materials and Transmission Electron Microscopy

TEM directly shows the fine structures of mesoporous silicas in real space, i.e., HRTEM images, even though the mesoporous silicas display rather poor powder X-ray diffraction patterns. Figure 4.20a shows the powder X-ray diffraction pattern of mesoporous silica AMS-9 with space group $P4_2/mnm$ [105]. It has one intense broad peak around 1.9° (CuK$_\alpha$), with a few smaller peaks, unlike the diffraction pattern of SBA-1 as shown in Fig. 4.18. However, HRTEM shows highly ordered meso-structure, and its Fourier diffractogram has sharp discrete peaks even at higher scattering angles, indicating that the mesoporous silica AMS-9 has a well-ordered structure as shown Fig. 4.20.

As it can be seen from this example, the powder X-ray diffraction alone may not be enough to judge the crystallinity, and it is almost impossible to determine the structure of mesoporous silicas in this way. This example clearly shows how TEM is an indispensable tool for the characterization of mesoporous silicas. We now examine how the appearance of mesoporous silica structures can change when observed by TEM with different conditions such as defocus values or sample thickness. The HRTEM images are usually very sensitive to the observation conditions when materials have structural characteristics on an atomic scale, i.e., atomic ordering.

Figure 4.21 shows the defocus dependence of mesoporous silica MCM-48, *Ia*-3*d* space group. In under-focus conditions, white spots in the HRTEM images, as shown in the first and second rows of the figure, are always white at different defocus values, 400–1,200 nm, while the overfocus image, -400 nm, shows the opposite contrast. This is unusual for materials with atomic ordering, which generally show dramatic contrast changes depending on the defocus value, even though the difference of the value is several nanometers.

Figure 4.22 shows the thickness dependence of mesoporous silica MCM-48. As it can be observed in the HRTEM image, the contrast does not change much from the edge to the center of spherical mesoporous silica. The Fourier diffractogram

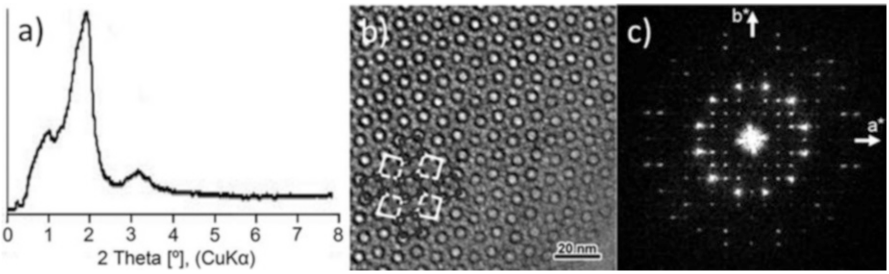

Fig. 4.20 (**a**) Powder X-ray diffraction pattern and (**b**) HRTEM image of mesoporous silica AMS-9 with tetragonal *P42/mnm*. (**c**) Fourier diffractogram of the HRTEM image in (**b**). Adapted from [105]

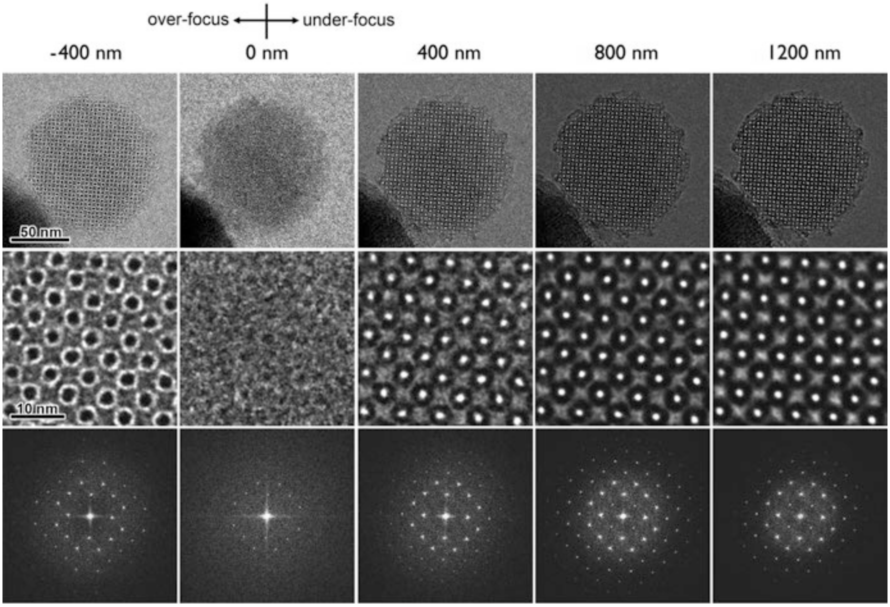

Fig. 4.21 Defocus dependence of mesoporous silica MCM-48. In the first row are low-magnification images, in the second are magnified images, and in the third are Fourier diffractograms

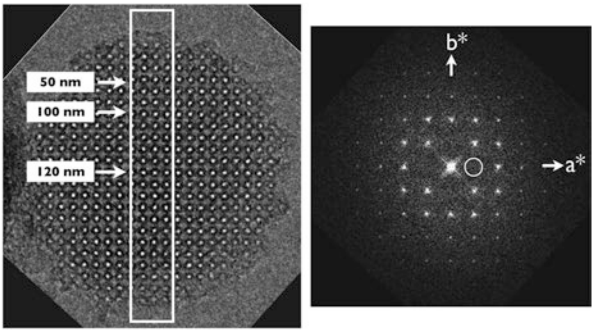

Fig. 4.22 Thickness dependence of mesoporous silica MCM-48

from the whole crystal clearly shows the extinction of the 200 reflection (marked by circle), which is not allowed in the space group *Ia-3d*. This means that the effect of dynamical scattering caused by strong interaction of electrons with matter is decreased and results in an HRTEM image that does not correspond to the real structure, i.e., projected potential of the crystal. However, as we can see at higher scattering angles, some of the reflections that should not be allowed are observed, meaning that there are still small amounts of dynamical scattering.

4.5.1 Three-Dimensional Reconstruction of Mesoporous Silica AMS-10

There have been many mesoporous silicas reconstructed by electron crystallography methods [99–107]. Their meso-structures are classified into two groups depending on their pore structures determined by the arrangement of surfactant micelles. The first group has bicontinuous meso-structures and the second has cage-type meso-structures. Here, one of the bicontinuous mesoporous silicas will be considered, AMS-10 [106]. Mesoporous silica AMS-10 was made with anionic surfactant *N*-myristoyl-L-glutamic acid (C_{14}GluA) as a structure-directing agent (SDA) and *N*-trimethoxysilylpropyl-*N*,*N*,*N*-trimethyl-ammonium chloride (TMAPS) as a co-structure-directing agent (CSDA) with a silica source. The resulting structure presents cubic symmetry with space group *Pm*-3*n* and a unit cell parameter of 96 Å. Figure 4.23 shows the main HRTEM images of AMS-10 and their corresponding Fourier diffractograms.

In order to reconstruct 3D meso-structure of AMS-10, three HRTEM images were used. Table 4.1 shows crystal structure factors extracted from these three images. It is noted that space group *Pm*-3*n* (origin choice 2) has an inversion center, resulting in all the factors having a phase of 0 or π. As we can see in Table 4.1, the structures

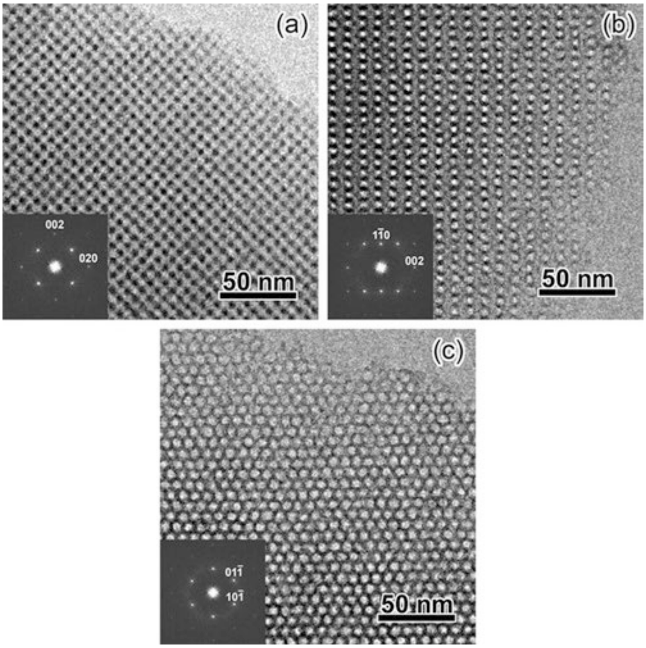

Fig. 4.23 HRTEM images of mesoporous silica AMS-10 taken along the (**a**) [100], (**b**) [110], and (**c**) [111] directions. Corresponding Fourier diffractograms are inserted in each panel. Adapted from [106]

Table 4.1 Crystal structure factors of mesoporous silica AMS-10

hkl	$h^2+k^2+l^2$	*d* [nm]	$\|F(hkl)\|/\|F(110)\|$	Phase
110	2	6.80	100.00	π
111	3	5.55	57.09	0
200	4	4.81	13.13	0
211	6	3.92	3.40	π
220	8	3.40	0.79	π
221	9	3.20	0.57	0
310	10	3.04	0.42	π
311	11	2.90	0.06	0
222	12	2.77	0.20	π
321	14	2.57	0.13	0
400	16	2.40	0.10	0
322	17	2.33	0.10	π
330	18	2.27	0.07	0
420	20	2.15	0.01	π
433	34	1.65	0.05	0
442	36	1.60	0.02	0
710	50	1.36	0.01	0
633	51	1.35	0.01	0

of mesoporous silica are decided by the first few strong reflections in the low scattering angles (such as 110, 111, and 200 reflections) so that the HRTEM images must be obtained in very under-focus conditions, as shown in Fig. 4.24a. At the same time, the intensity of each reflection is not overly sensitive to the defocus values. For example, the first three reflections at scattering angles less than 0.21 nm^{-1} can be determined within an error of 2 % when the HRTEM images are taken with the range of defocus values of 300 ± 200 nm, as shown in Fig. 4.24b. Weak reflections at higher scattering angles with $|F(hkl)|/|F(110)| < 3.4$ can be also determined with small errors. This characteristic of mesoporous silicas leads to simple interpretation of the HRTEM images and determination of the crystal structure factors with high accuracy, even though the observation conditions and the CTF corrections are not very accurate.

The 3D meso-structure of AMS-10 was reconstructed by inverse Fourier transformation of the set of crystal structure factors. Figure 4.25a shows the (100) section of the electrostatic potential distribution, where dark portions of the image correspond to the silica wall and white is the pore space. By taking into account the pore volume, in this case, 0.65 cm^3/g, obtained from N_2 adsorption/desorption measurements, and the density of amorphous silica, 2.2 g/cm, the threshold value between the silica walls and mesopores can be determined, which allows to ascertain the 3D pore structure, as shown in Fig. 4.25b. It is clear that mesoporous silica AMS-10 has two interwoven networks divided by amorphous silica walls (Fig. 4.25c). Interestingly, the silica wall follows one of the minimal surfaces referred to as the diamond surface (D-surface), as shown in Fig. 4.25d. From the 3D pore structure, we can deduce the pore size, 4.6 nm, and silica wall thickness, 2.2 nm. The pore size corresponds to that obtained from N_2 adsorption/desorption experiments, 4.7 nm.

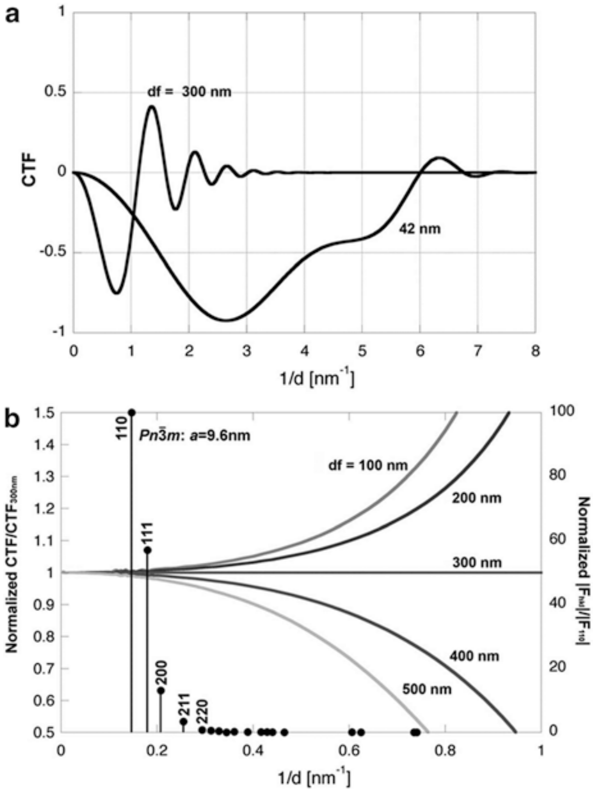

Fig. 4.24 (**a**) Contrast transfer function of the electron microscope (acc. $V = 300\text{kV}$ and $C_s = 0.6\text{mm}$) with two different defocus values. (**b**) The CTF normalized by $df = 300\text{nm}$ and the amplitude of mesoporous silica AMS-10 normalized by the intensity of 110 reflection [106]

4.5.2 Direct Observation of Intermediate Phases

One of the early reports where TEM was applied to mesoporous materials involved the validation of the growth mechanism of FSM-16. FSM-16 is made from *kanemite* and has one-dimensional pores arranged in a two-dimensional (2D) hexagonal structure. Inagaki et al. suggested the so-called folded sheet mechanism (FSM), where a single silica sheet is bended around a rod-type micelle [108]. However, there was a discussion whether *kanemite* sheet is preserved or not during the synthesis process. Sakamoto et al. made an attempt to clarify this using TEM [109]. Observations of several samples picked out from the solution during the synthesis allowed to conclude that the FSM-16 was formed through condensation of silicate species as a result of fragmentation of the *kanemite* sheet, instead of the expected folding of the *kanemite* sheets. Later on, Kimura et al. succeeded to make a real FSM structure, KSW-2, which actually follows the folded sheet mechanism [91].

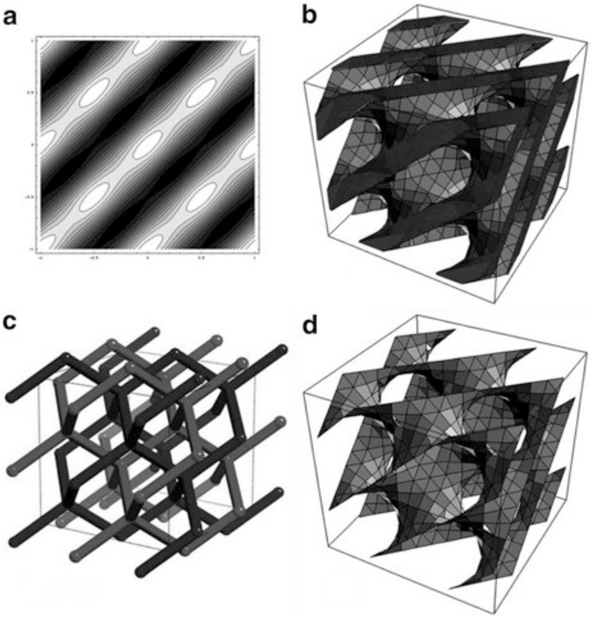

Fig. 4.25 (**a**) (100) Section of electrostatic potential distribution and (**b**) 3D pore structure of mesoporous silica AMS-10. (**c**) Two networks divided by the silica wall and (**d**) diamond surface known as minimal surface. Adapted from [106]

TEM was used in this case to confirm that KSW-2 presents a rectangular symmetry instead of the hexagonal one previously assumed, indicating that the mesostructured structure of KSW-2 was formed via bending of individual *kanemite* sheets.

Structural transformation of mesoporous material is an attractive topic because silica mesoporous system shows a wide structural diversity, something that is already well known in liquid crystal and polymer systems. On the other hand, the accurate control of the final structures in ordered mesoporous materials is extremely important from the application point of view. In this regard, it is well known that ordered mesoporous materials might alter their structures depending on the synthesis conditions such as temperature and gel composition. Especially, there are several reports about extra additives in the silica–surfactant systems that induce a structural transformation.

For example, triblock copolymer with butanol [110] or with anionic surfactants [111] and blends of diblock and triblock copolymer system [112], they cause structural variety from cage-type to 2D hexagonal and bicontinuous structure. There are many reports about the structural relationship in the M41s family, e.g., MCM-41 and MCM-48 and MCM-48 and MCM-50 (lamella structure). How these structures are related each other [113] and whether their structural transformation occurs via dissolving–reconstructing route or solid-state transition can be elucidated in terms of TEM. Diaz et al. tried to give an answer by following the transformation with TEM [114]. They showed that the structural transformation from MCM-41 to MCM-48 goes through the dissolving–reconstructing route. On the other hand, TEM images reveal clear evidence of epitaxial growth of MCM-50 (lamellar structure) on the

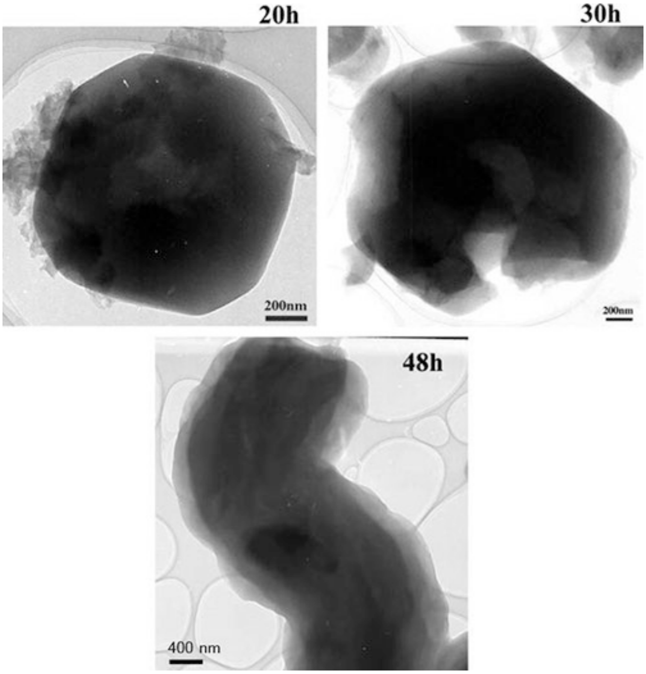

Fig. 4.26 Low-magnification transmission electron microscopy images of the 20, 30, and 48 h as-made samples prepared without crushing

cubic MCM-48 structure, indicating that this transformation occurs via a solid-state transition evidenced by the transformation of the perfectly shaped truncated octahedral crystals of MCM-48 (20 h) which start to break and "open" in the 30 h sample. When the material is treated for 48 h, the crystals are completely open with rod-shaped crystals where the lamellar meso-structure is observed (Fig. 4.26).

It has detected also epitaxial relationships in other mesoporous systems, for instance, TEM was used to observe an epitaxial growth of 2D hexagonal and *Pm*-3*n* structure with no presence of dissolution–recrystallization process [115, 116]. Interestingly, the 100 reflection of the 2D hexagonal mesophase appears to transform into the 211 reflection of the cubic mesophase, which suggests that the density modulations describing the structures are changing from the 10 type of the 2D hexagonal structure to the 211 type of the cubic structure. The meso-structure of these different shaped crystals was investigated by tilting the crystals along the [100], [110], and [111] zone axes, Fig. 4.27a, corroborating the *Ia*-3*d* symmetry (20 h).

As time increases, the crystals start to break; however, perfectly ordered and symmetric [100], [311], and [111] SAED patterns can be easily observed in the microscope for the 30 h sample (Fig. 4.27b). Apparently, such SAED patterns can be indexed as *Ia*-3*d* but slight deviations toward orthorhombic symmetry can be found. It is well known that the cubic MCM-48 structure contains a 3D rodlike system with channels running along the <110> direction. Furthermore, the [100]

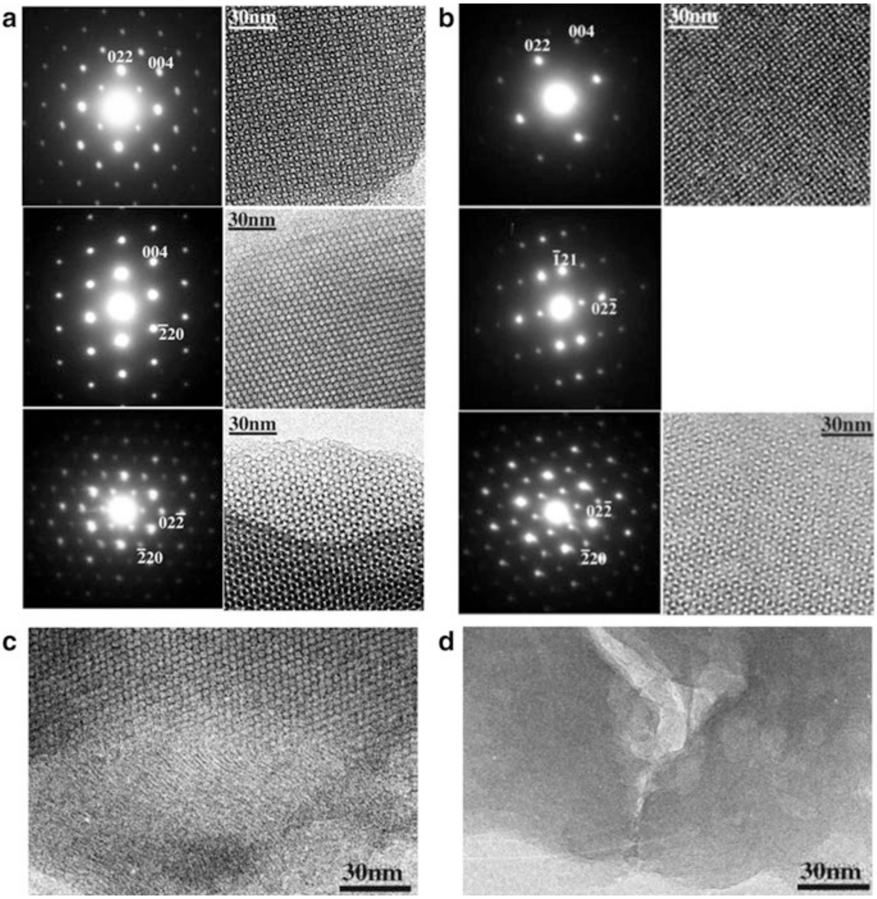

Fig. 4.27 (**a**) High-resolution images and selected area electron diffraction (SAED) patterns of a crystal of the 20 h as-made sample. The crystal was tilted until the incident electron was parallel with the [100], [110], and [111] axes. (**b**) HRTEM images and SAED patterns of a crystal of the 30 h as-made sample. The crystal was tilted until the incident electron was parallel with the [100], [311], and [111] axes. (**c**) [110] orientation of the 30 h as-made sample. (**d**) Image of a typical lamellar structure at the edges of the crystals of the 48 h as-made sample

and [111] orientations are the most favored for any structural crystallographic modification to orthorhombic symmetry to be observed. Thus, a given phase transformation would be expected to come from either of these two orientations. Conversely, a loss of symmetry is only observed in the [110] zone axis of the 30 h crystals. As an example, Fig. 4.27c shows an image of a crystal of the 30 h as-made sample, along the [110] orientation. In this image, the transition from 2D crystalline along the [110] face to a 1D lamellar structure can be seen due to the leaching of the material. This leaching, initially seen at the edges of the highly ordered crystals, developed with time, leading to the lamellar structure shown by the 48 h sample

(Fig. 4.27d). As is evidenced from the HRTEM images, the array of layers in this sample corresponds to a *d*-spacing of ca. 23 Å, in agreement with the occurrence of a rearrangement of the surfactant–silica system.

More recently, Che et al. [117, 118] found a new silica mesoporous family using anionic surfactant as a structure directors together with CSDA such as 3-aminopropyltrimethoxysilane (APS), which is composed of two moieties. The alkoxysilane is co-condensed in the silica framework providing an ammonium cation as a counter ion for the anionic surfactant. The AMS family shows a great variety of structures such as cage-type cubic *Fd*-3*m* (AMS-8) [103], cage-type tetragonal *P*42/*mnm* (AMS-9) [105], bicontinuous cubic *Pn*-3*m* (AMS-10) [106], and also a chiral structure [119]. It is worth mentioning here that these systems also show interesting structural modulations. For instance, these systems showed structural transformations by changing the composition and interestingly time and order of reagents addition [117, 118]. However, these transformations require further studies in order to understand the structural relationship involved.

The main advantage of TEM relies on the direct information in real space, that is, the observation of structural details localized in ordered mesoporous material arrays. Based on TEM images, it is possible to suggest crystal growth mechanisms and structural relationships between different structures.

4.6 Ordered Mesoporous Materials and Spherical Aberration-Corrected Electron Microscopy

One of the widely accepted uses of OMMs is as supports of enzymes for biotechnological applications. Enzymes have been trapped, anchored, or encapsulated in organized porous networks of the mesoporous range. The incorporation of functional groups into OMMs for catalytic applications has yielded optimum materials in the past [120]. The porous space engineering however brings OMMs to a scenario in which material science, biotechnology, and engineering bind together in a multidisciplinary field [121]. In particular, the good connectivity of the porous network and the unique porosity of these solids make them very suitable materials for enzyme carriers [122–124]. A good example of these enzymes is lipases, which are industrially interesting due to their applications in stereoselective processes in the pharmaceutical industry or regioselective nutraceutical synthesis enhancing the relevance of the process of immobilization within mesoporous matrixes. Lipase dimensions (4 nm diameter) fit well with the majority of ordered mesoporous materials, and different methods have been taken for the confinement of this enzyme within the pores of mesoporous silica [125, 126]. To these interesting applications, the immobilization in ordered mesoporous materials adds a series of advantages provided by the nature of these novel supports. Good connectivity enables better diffusion of substrates and products than the one obtained with amorphous materials. Confinement of the enzyme prevents protein unfolding providing better stabilization than achieved with macroporous supports. However, the location of enzymes inside the pores is not easy to be confirmed, and commonly a combination of indirect techniques has been used for the characterization of these materials such as N_2 adsorption or thermogravimetry. The only direct and the most complete method for the characterization of mesoporous solids is TEM [100] combined with electron crystallography (EC) [127] which, as already mentioned, has allowed solving all kinds of structures. When the subject of interest is low scattered guest materials, such as C-based materials, STEM combined with a high-angle annular dark-field detector (HAADF) is more suitable as the contrast is related to the atomic number Z. With the modern electron microscopes, which incorporate spherical aberration (C_s) correctors, probes down to sub-ängstrom resolution with a high current can be achieved, facilitating for the case of ordered mesoporous materials a detailed analysis of the pores [128].

4.6.1 Hybrid Cage-Like Materials: Lipase-SBA-12

In the present example, a detailed and conclusive analysis is performed on three-dimensional mesoporous structure SBA-12, formed by a cavity connected system [101], loaded with lipase. Based on ultrahigh-resolution images of perfectly orientated thin crystals combined with electron energy loss spectroscopy (EELS), which measures the energy that electrons lose when they pass thorough the sample and it is a characteristic of each element, the determination of the enzyme within the pores has been corroborated. All analyses were carried out at an accelerating voltage of 80 kV proving a good stability of the mesoporous materials at this beam energy.

The enzyme used was lipase from *Candida antarctica* B (CaLB) used in crude extract as kindly provided from Novozymes. Lipase-SBA-12 was prepared in situ using the lipase together with the Pluronic F127 as template, tetraethoxysilane (TEOS) as silica source, and mild conditions (pH 3.5 and room temperature) as described elsewhere [129].

A complete characterization of these solids has been carried out by electron microscopy and other different techniques which are explained in full detail elsewhere [123, 130]. Spherical aberration (C_s)-corrected STEM combined with a high-angle annular dark-field detector (HAADF) and electron energy loss spectroscopy (EELS) were the solely methods for the location and the structural determination of the enzyme and mesoporous solids.

Figure 4.28 displays the C_s-corrected STEM-HAADF images of the lipase-SBA-12 material. This figure shows two main crystallographic orientations in which the enzyme can be better identified. Figure 4.28a shows a crystal orientated along the [100] direction indexed assuming $Fm3m$ symmetry obtaining a unit cell value of $a = 20.3$ nm. Another crystal orientated along the [110] projection also exhibits a very good crystallinity with the presence, in this case, of stacking faults in the structure.

The simultaneous [100] HAADF image coupled with the EELS signal in the range of 200–610 eV using dispersion energy of 0.2 eV/channel is shown in Fig. 4.29. The scanned area, in green in Fig. 4.29a, was set to 48 pixels × 48 pixels

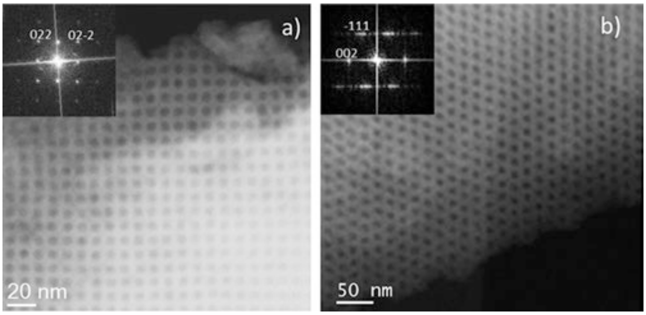

Fig. 4.28 C_s-corrected STEM-HAADF images of the lipase-SBA-12 recorded along the [100] and [110] orientations of the crystal. Adapted from [131]

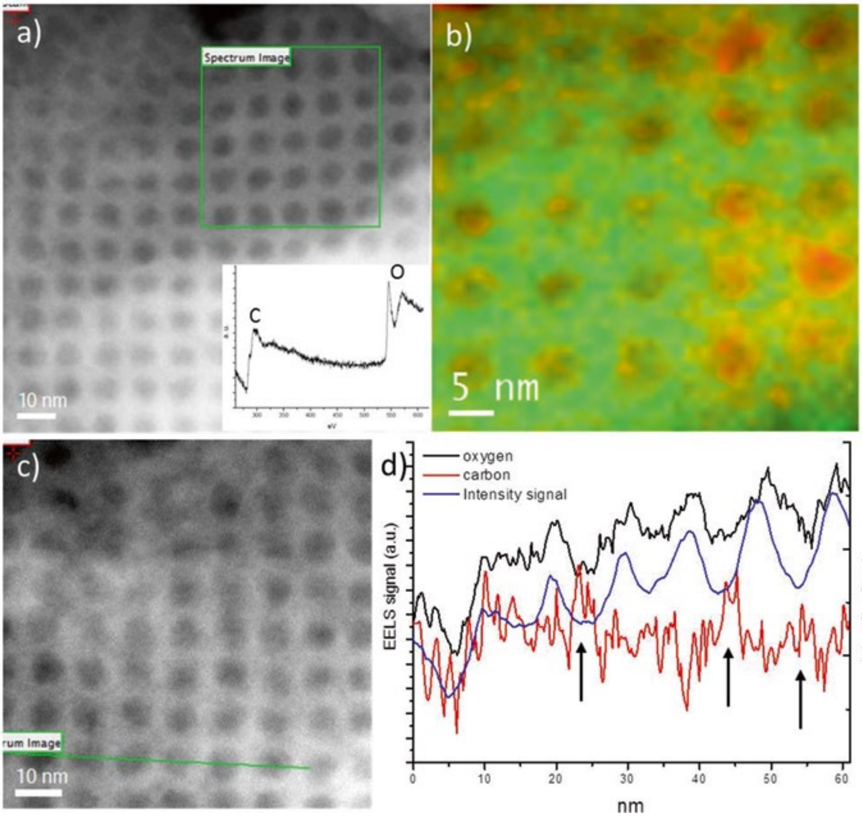

Fig. 4.29 Spectrum image and spectrum-line analysis performed on the [100] SBA-12. (**a**) C_s-*corrected* STEM-HAADF, where the EELS spectrum image has been recorded and marked by a green square. *Inset*, the total spectrum, after background subtraction, where the different signals (C–K and O–K edges) are observed. (**b**) Extracted spectrum image C–K edge (in *red*) and O–K edge (*green*), respectively. (**c**) C_s-corrected STEM-HAADF image with the spectrum line marked as a *green line*. (**d**) Extracted signals from the line profile, in *blue* is the intensity signal, in *red* is carbon, and oxygen is marked in *black*. Adapted from [131]

and the beam time per pixel was fixed to 0.15 s. Figure 4.29b displays the carbon (red) and oxygen (green) chemical maps extracted, after background subtraction, from the spectrum image of Fig. 4.29a. The total EEL spectrum of this spectrum image is shown in Fig. 4.29a (inset). The extracted O–K signal (Fig. 4.29b green) corresponds to the mesoporous framework (SiO_2) and, if present, to the enzyme inside the pores. However, the study of the C–K signal provides much richer information than this one obtained from the analysis of the O–K edge.

In fact, a more conclusive result is the presence of carbon inside the pores which, as the surfactant was removed, can be only attributed to the presence of the enzyme in those positions. Represented in red in Fig. 4.29b, it clearly proves a much higher concentration inside certain pores corroborating the uneven lipase loading. The extracted EELS signals from the spectrum-line profile analysis also reveal that certain pores present opposite intensity values in the pores where the carbon reaches maximums due to the presence of the enzyme (arrows in Fig. 4.29d). For this analysis, the beam was rastered over 213 pixels achieving a spatial resolution of 3 Å and pixel time of 0.3 s giving a total time of analysis of 64 s. It is quite remarkable that although a small structural distortion was appreciated after the analysis, the material appeared to be stable enough for the analyses at 80 kV.

In conclusion, high-resolution STEM-HAADF combined with EELS analysis can be used to unambiguously corroborate the presence of organic guest molecules inside the internal structure of three-dimensional ordered mesoporous silica.

4.6.2 Hybrid Channel-Like Materials: Lipase-PMO and Laccase-PMA

A very interesting group of materials for enzyme immobilization are the organosilica OMMs which contain hydrocarbon (HC) groups as part of their framework. Unfortunately, as already mentioned by conventional TEM imaging (using a parallel illumination inside the microscope), the identification and location of guest solids, such as enzymes or metals, is in the majority of the cases not possible.

Figure 4.30 corresponds to the [001] HAADF-STEM image, parallel to the mesopores of the lipase-PMO sample. Figure 4.30a shows the organosiliceous matrix where the cavities appear in black presenting a hexagonal array ($p6mm$ symmetry). The FFT (inset, upper left corner) proves the good crystallinity of the material; on the right corner, a perfectly orientated six pores (subject to analysis) with respect to the electron beam are shown; crystals perfectly aligned with respect to the electron beam are an indispensable requirement for a reliable analysis of the pores and the mesoporous walls. Figure 4.30b corresponds to the STEM-HAADF image of the area where a spectrum image was recorded. The dimensions used were 30 × 26 pixels giving a spatial resolution of 0.89 nm and the time for analysis was 0.6 s/pixel. Figure 4.30c represents the most crucial information for the enzyme location: the relative carbon/oxygen composition. As expected, the relationship between C and O

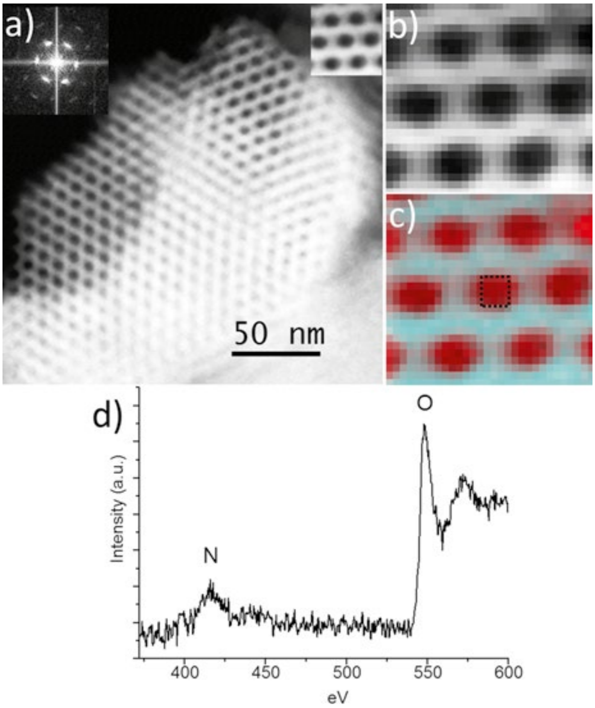

Fig. 4.30 (**a**) Aberration-corrected STEM-HAADF image of a PMO crystal along the [001] orientation showing the hexagonal array. The FFT, *left upper corner inset*, confirms the sixfold axis. On the *right upper corner*, a magnified image of the pores is presented. (**b**) STEM-HAADF signal of the area analyzed. (**c**) Map obtained from the EELS signal of the relative C/O composition (in *red*). (**d**) Sum of EEL spectra, after background subtraction, recorded in the *dashed square marked* in (**c**). Figure adapted [132]

is different whether the beam illuminates the pore within the enzyme or the walls which contain $SiO_2 + (-CH_2 - CH_2)$ groups; red areas correspond to the higher C content. Such a big difference makes it possible to distinguish the presence of lipase inside the pores. The fact that the nitrogen per molecule is so low made it not possible to construct a map based on the N signal; however, a punctual analysis (black dashed square in Fig. 4.30c) of 3 s allowed observing the nitrogen K edge at 401 eV. In Fig. 4.30d, the EELS analysis of the pore is shown after background subtraction where the oxygen and nitrogen edges are clearly identified.

As a result of different particle morphologies of PMO and PMA, the latter allowed a better tilting of larger crystals. Therefore, although the enzyme loading is similar in both cases, it was easier the location of pores with higher enzyme content. A low-magnification image is presented in Fig. 4.31a. A closer image of the pore system is shown in Fig. 4.31b, in which a spectrum image collection analysis was performed inside one of the pores (green square) analyzing 8×6 pixels with an exposure time of 2.5 s per pixel. The extracted spectrum profile (raw data),

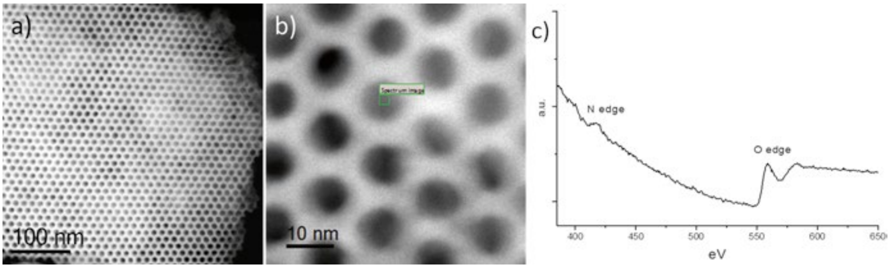

Fig. 4.31 (**a**) C_s-corrected STEM-HAADF image of the PMA loaded with laccase. (**b**) High-resolution image of the pores. The *green rectangle* represents the area where the EELS analysis was carried out. (**c**) EELS profile collected from (**b**) showing the three edges which confirm the presence of laccase [132]

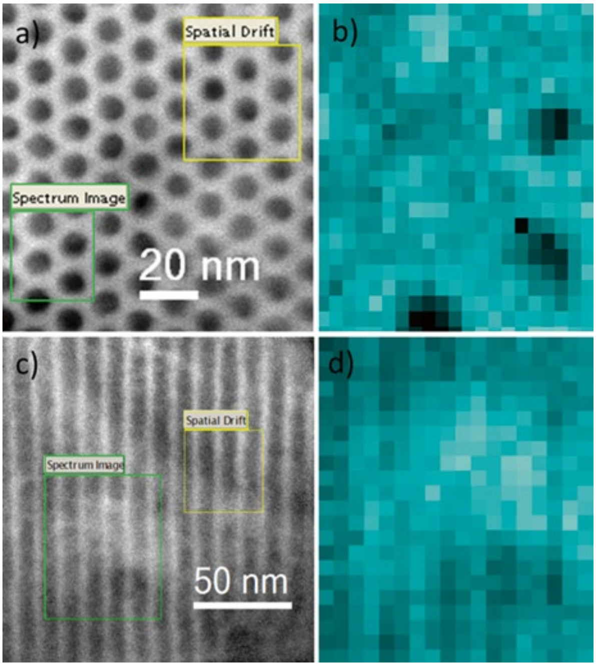

Fig. 4.32 C_s -corrected STEM-HAADF image of the pore system of PMA. (**b**) Nitrogen map extracted from (**a**) *green square*. (**c**) C_s-corrected STEM-HAADF image of the channels of PMA and (**d**) the corresponding nitrogen map [132]

Fig. 4.31c, exhibits the O and N edges corresponding to the enzyme. The nitrogen maps, extracted from spectrum images collected in areas perpendicular and parallel to the pores, are depicted in Fig. 4.32. The green square (Fig. 4.32a and c) represents the area where the map was acquired using 1.5 s per pixel in both cases. In light blue, the N maps (Fig. 4.32b and d) are shown. As a consequence of the amino functionalization, N was detected in the framework and in certain pores, where less contrast was observed (Fig. 4.32a and b) evidencing that some pores were not filled with laccase or that its content was too low to be detected. In Fig. 4.32c, a different contrast, much "whiter," appears for which the analysis indicates higher N content attributed to the enzyme immobilized within the pores as clearly observed in Fig. 4.32d.

A relatively strong electron beam was necessary in order to gain enough counts to identify the species. The total dose was 0.48 e/A^{2}s which stayed on each pixel during the data collection. The radiation damage has been related to radiolysis, when the energy from an electron of the beam is transferred to an electron of the specimen causing an increment of the energy of the electrons leading to bonds breakage [36, 53]. This effect is directly dependent on the beam energy making the materials more stable when higher accelerating voltages (kV) are applied as the cross section is decreased and the temperature in the sample is also kept to lower values. However, "knock-on" damage (which occurs when an incoming electron from the beam interacts with the core of an atom displacing it from its original position) cannot be completely discarded [35], especially in the current study where carbon chains are present in the structure. For both, PMO and PMA, knock-on damage may have raised its importance on the mesoporous decomposition as C–C bonds remained stable at 80 kV. On the contrary, working at this voltage may increase the temperature of the crystals analyzed which is an important contributor to specimen damage. For the case of analytical microscopes where the beam is "converted" into a very fine spot of about 1 Å (for the current case as a result of the C_s corrector present in the microscope), temperature heating may be significantly reduced with respect to conventional TEM observations which illuminates the entire crystal.

4.7 Concluding Remarks

The transmission electron microscopy area concerning the observation of ordered porous materials has been continuously growing since the pioneering works started in the 1970s. Due to the high importance of, in general, different porous structures and in particular zeolites and ordered Mesoporous Materials, diverse methods for their detailed characterization have been developed. TEM technology has played an important role in the evolution of the science of these materials allowing to extract unique information not achievable by any other technique, as it has been the observation of the fine structure, structural defects, intergrowths, or solving new structures. The tremendous beam sensitivity of zeolites and zeotypes has been associated to a radiolytic effect, and it has been the biggest drawback for the observation and analysis of these solids through transmission electron microscopy methods. Over the years, this issue has been at least partially overcome by controlling the electron dose, exposure time, and accelerating voltage obtaining fantastic images at high accelerating voltages. Due to this difficulty, the implementation of aberration-corrected electron microscopy has been delayed with respect to other nanomaterials; however, in the recent years, many results based on a careful control of the beam current have been reported from different groups. Even more, analytical spectroscopy has been performed within the pores of ordered meso-structures allowing the location of organic molecules.

The future perspective is exciting and promising as it has been shown along this chapter; all kinds of known and new zeolitic structures and similar materials can be imaged with an unprecedented resolution down to atomic level, which allow extracting new information on structural parameters of the framework or identifying single atoms responsible of many of the properties of zeolites and zeotypes.

Acknowledgments A.M. would like to acknowledge the European Union Seventh Framework Programme under Grant Agreement 312483—ESTEEM2 (Integrated Infrastructure Initiative – I3) and Transpyrenean Associated Laboratory for Electron Microscopy (TALEM) program. I.D. kindly acknowledges the Spanish Government (MAT 2012-31127). Y.S. acknowledges financial support from PRESTO, Japan Science and Technology Agency (JST).

References

1. A.F. Crønstedt, Kongl Svenska Vetenskaps Acadademiens Handlingar. **17**, 120 (1756)
2. Hd.S.C. Deville, Comptes. Rendus. Acad. Sci. **54**, 324 (1862)
3. G. Friedel, New experiments on zeolites. Bull. Soc. Fr. Minéral. Cristallogr. **19**, 363–390 (1896)
4. E.M. Flanigen, R.W. Broach, S.T. Wilson, *Zeolites in Industrial Separation and Catalysis* (Weinheim, Wiley, 2010)
5. G. Friedel, Zeolites and the substitution of various substances for the water which they contain. C. R. Acad. Sci. **122**, 948–951 (1896)
6. F. Grandjean, Optical study of the absorption of the heavy vapors by certain zeolites. C. R. Acad. Sci. **149**, 866–868 (1910)
7. O. Weigel, E. Steinhoff, Adsorption of organic liquid vapors by chabazite. Z. Kristallogr. **61**, 125–154 (1925)
8. W.H. Taylor, The crystal structure of analcite (NaAlSi2O6 • H2O). Z. Kristallogr. **74**, 1 (1930)
9. L. Pauling, The structure of sodalite and helvite. Z. Kristallogr. **74**, 213 (1930)
10. J.W. McBain, *The Sorption of Gases and Vapors by Solids* (Rutledge, London, 1932)
11. R.M. Barrer, Synthesis and reactions of mordenite. J. Chem. Soc. 2158–2163 (1948)
12. R.M. Barrer, Synthesis of a zeolitic mineral with chabazite—like sorptive properties. J. Chem. Soc. **127** (1948)
13. R.M. Barrer, D.W. Riley, Sorptive and molecular sieve properties of a new zeolitic mineral. J. Chem. Soc. 133–143 (1948)
14. W. Löwenstein, The distribution of Al in the tetrahedra of silicates and aluminates. Am. Mineral **39**, 92–96 (1954)
15. C. Baerlocher, L.B. McCusker, D.H. Olson, *Atlas of Zeolite Framework Types* (Elsevier, Amsterdam, 2007)
16. A. Corma, From microporous to mesoporous molecular sieve materials and their use in catalysis. Chem. Rev. **97**, 2373–2419 (1997)
17. J.M. Thomas, Design, synthesis, and in situ characterization of new solid catalysts. Angew. Chem. Int. Ed. **38**, 3588–3628 (1999)
18. J. Pluth, J. Smith, Silicoaluminophosphate with encapsulated methylbutylamine species: chabazite structure, charge coupling between framework and inferred ammonium species, and severe molecular disorder. J. Phys. Chem. **93**, 6516–6520 (1989)

19. R.M. Barrer, Chemical nomenclature and formulation of compositions of synthetic natural zeolites. Pure Appl. Chem. **51**, 1091–1100 (1979)
20. J.V. Smith, Topochemistry of zeolites and related materials. 1. Topology and geometry. Chem. Rev. **88**, 149–182 (1988)
21. T. Carey, C.C. Tang, J.A. Hriljac, P.A. Anderson, Chemical control of thermal expansion in cation-exchanged zeolite A. Chem. Mater. **26**, 1561–1566 (2014)
22. http://www.iza-online.org
23. S. Davis, Y. Inoguchi, CEH Marketing Research Report: Zeolites, (SRI Consulting, 2009)
24. D.E. Bryant, W.L. Kranich, Dehydration of alcohols over zeolite catalysts. J. Catal. **8**, 8–13 (1967)
25. P.B. Venuto, P.S. Landis, Organic catalysis over crystalline aluminosilicates. Adv. Catal. **18**, 259–371 (1968)
26. F. Degnan, Applications of zeolites in petroleum refining. Top. Catal. **13**, 349–256 (2000)
27. D. Chen, H.P. Rebo, A. Grønvold, K. Moljord, A. Holmen, Methanol conversion to light olefins over SAPO-34: kinetic modeling of coke formation. Microporous Mesoporous Mater. **35**, 121–135 (2000)
28. R.A.N. Bos, P.J.J. Tromp, H.N. Akse, Ind. Eng. Chem. Res. **34**, 3808 (1995)
29. M. Iwamoto, H. Yahiro, K. Tanada, Y. Mozino, S. Kagawa, J. Phys. Chem. **95**, 3727 (1991)
30. L. Scandella, G. Binder, T. Mezzacasa, J. Gobrecht, R. Berger, H.P. Lang, C. Gerber, J.K. Gimzewski, J.H. Koegler, J.C. Jansen, Combination of single crystal zeolites and microfabrication: two applications towards zeolite nanodevices. Microporous Mesoporous Mater. **21**, 403–409 (1998)
31. K.B. Yoon, Acc. Chem. Res. **40**, 29 (2007)
32. L.A. Bursill, E.A. Lodge, J.M. Thomas, Zeolitic structures as revealed by high-resolution electron microscopy. Nature **286**, 111–113 (1980)
33. L.A. Bursill, J.M. Thomas, K.J. Rao, Stability of zeolites under electron irradiation and imaging of heavy cations in silicates. Nature **289**, 157–158 (1981)
34. M.M.J. Treacey, J.M. Newsam, Electron beam sensitivity of zeolite L. Ultramicroscopy **23**, 411–420 (1987)
35. R. Csencsits, R. Gronsky, Damage of zeolite Y in the TEM and its effects on TEM images. Ultramicroscopy **23**, 421 (1987)
36. O. Terasaki, T. Ohsuna, V. Alfredson, J.-O. Bovin, D. Watanabe, K. Tsuno, The study of zeolites by HVREM. Ultramicroscopy **39**, 238–246 (1991)
37. V. Alfredson, O. Terasaki, J.O. Bovin, The conditions for detecting confined material in the channels/cavities of zeolites by using HREM. J. Solid State Chem. **105**, 223–233 (1993)
38. O. Terasaki, T. Ohsuna, What can we observe in zeolite related materials by HRTEM? Catal. Today **23**, 201–218 (1995)
39. V. Alfreson, O. Terasaki, J.O. Bovin, On crystal structure imaging of silicalite by HREM. J. Solid State Chem. **84**, 171–177 (1990)
40. J.W. Menter, The electron microscopy of crystal lattices. Adv. Phys. **7**, 299–348 (1958)
41. I.S. Kerr, J.A. Gard, R.M. Barrer, I.M. Galabova, Crystallographic aspects of the co-crystallization of zeolite-L, offretite and erionite. Am. Mineral. **57**, 439 (1970)
42. G.T. Kokotailo, S. Sawruk, S.L. Lawton, Direct observation of stacking faults in the zeolite erionite. Am. Mineral. **57** (1972)
43. J.G. Allpress, J.V. Sanders, The direct observation of the structure of real crystals by lattice imaging. J. Appl. Crystallogr. **6**, 165–190 (1973)
44. O. Terasaki, Electron microscopy studies in molecular sieve science. Struct. Struct. Determin. **2**, 71–112 (1999)
45. O. Terasaki, T. Ohsuna, TEM study on zeolite fine structures: homework from Cambridge days. Top. Catal. **24**, 13–18 (2003)
46. I. Díaz, E. Kokkoli, O. Terasaki, M. Tsapatsis, Surface structure of zeolite (MFI) crystals. Chem. Mater. **16**, 5226–5232 (2004)
47. A. Mayoral, P.A. Anderson, Production of bimetallic nanowires through electron beam irradiation of copper- and silver-containing zeolite A. Nanotechnology **18**, 165708 (2007)

48. A. Mayoral, Y. Sakamoto, P.A. Anderson, Synthesis of copper chloride nanowires by thermal treatment in the presence of zeolite X. CrystEngComm **12**, 3012–3018 (2010)
49. J. Ruan, P. Wu, B. Slater, Z. Zhao, L. Wu, O. Terasaki, Structural characterization of interlayer expanded zeolite prepared from ferrierite lamellar precursor. Chem. Mater. **21**, 2904–2911 (2009)
50. I. Díaz, A. Mayoral, TEM studies of zeolites and ordered mesoporous materials. Micron **42**, 512–527 (2011)
51. Y. Sakamoto, T. Kodaira, Effects of electron beam irradiation on aluminophosphate microporous material ALPO$_4$-5. Nucl. Instrum. Methods Phys. Res., Sect. B **315**, 197–200 (2013)
52. L. Hobbs, *Radiolysis and Defect Structure in Electron-Irradiated Alpha-Quartz* (Plenum, New York, 1979)
53. C.F. Blanford, C.B. Carter, Electron radiation damage of MCM-41 and related materials. Microsc. Microanal. **9**, 245–263 (2003)
54. L.W. Hobbs, Radiation effects in the electron microscope. EMSA Bull. **15**, 51–63 (1985)
55. J.E. Readman, P.D. Barker, I. Gameson, J.A. Hriljac, W. Zhou, P.P. Edwards, P.A. Anderson, An ordered array of cadmium clusters assembled in zeolite A. Chem. Commun. **6**, 736–737 (2004)
56. O. Terasaki, J.M. Thomas, G.R. Millward, Imaging the structures of zeolite L and synthetic mazzite. Proc. R. Soc. Lond. A **395**, 153–164 (1984)
57. O. Terasaki, Fine structures of zeolites. J. Electron. Microsc. **43**, 337–246 (1994)
58. G.R. Millward, S. Ramdas, J.M. Thomas, On the direct imaging of offretite, cancrinite, chabazite and other related ABC-6 zeolites and their intergrowths. Proc. R. Soc. Lond. A **399**, 57–71 (1985)
59. G.R. Millwar, J.M. Thomas, O. Terasaki, D. Watanabe, Direct imaging and characterization of intergrowth-defects in erionite. Zeolites **6**, 91–95 (1986)
60. M.W. Anderson, K.S. Pachis, F. Prébin, S.W. Carr, O. Terasaki, T. Ohsuna, V. Alfreddson, Intergrowths of cubic and hexagonal polytypes of faujasitic zeolites. J. Chem. Soc. Chem. Commun. **23**, 1660–1664 (1991)
61. O. Terasaki, T. Ohsuna, V. Alfredsson, J.O. Bovin, D. Watanabe, S.W. Carr, M.W. Anderson, Observation of spatially correlated intergrowths of faujasitic polytypes and the pure end members by high-resolution electron microscopy. Chem. Mater. **5**, 452–458 (1993)
62. M.W. Anderson, O. Terasaki, T. Oshuna, A. Philippou, S.P. Mackay, A. Ferreira, J. Rocha, S. Lidin, Structure of the microporous titanosilicate ETS-10. Nature **367**, 347–367 (1994)
63. J.M. Newsman, M.M.J. Treacy, W.T. Koetsier, C.B. Gruyter, Structural characterization of zeolite beta. Proc. R. Soc. Lond. A **420**, 375–405 (1988)
64. T. Ohsuna, O. Terasaki, V. Alfredsson, J.O. Bovin, D. Watanabe, S.W. Carr, M.W. Anderson, Observations on the role of crown ether templates in the formation of hexagonal and cubic polymorphs of zeolite Y. Proc. R. Soc. Lond. A **452**, 715–740 (1996)
65. V. Ortalan, A. Uzun, B.C. Gates, N.D. Browning, Direct imaging of single metal atoms and clusters in the pores of dealuminated HY zeolite. Nat. Nanotechnol. **5**, 506–510 (2010)
66. J. Lu, C. Aydin, N.D. Browning, B.C. Gates, Imaging isolated gold atom catalytic sites in zeolite NaY. Angew. Chem. Int. Ed. **51**, 5842–5846 (2012)
67. A. Mayoral, T. Carey, P.A. Anderson, A. Lubk, I. Diaz, Atomic resolution analysis of silver ion-exchanged zeolite A. Angew. Chem. Int. Ed. **50**, 11230–11233 (2011)
68. A. Mayoral, T. Carey, P.A. Anderson, I. Diaz, Atomic resolution analysis of porous solids: a detailed study of silver ion-exchanged zeolite A. Microporous Mesoporous Mater. **166**, 117–122 (2013). doi:10.1016/j.micromeso.2012.04.033
69. A. Mayoral, J.E. Readman, P.A. Anderson, Aberration-corrected STEM analysis of a cubic Cd array encapsulated in zeolite A. J. Phys. Chem. C **117**(46), 24485–24489 (2013)
70. T. Ohsuna, O. Terasaki, K. Hiraga, Mater. Sci. Eng. **A217/218**, 135–138 (1996)
71. O. Terasaki, HREM study of the fine structures of zeolites and materials confined in their spaces: are zeolites good enough as containers for confined materials? J. Solid State Chem. **106**, 190–200 (1993)

72. G. Bonilla, I. Díaz, H.K. Jeong, M. Tsapatsis, Y. Lee, D.G. Vlachos, Zeolite (MFI) crystal morphology control using organic structure-directing agents. Chem. Mater. **16**, 5697–5705 (2004)
73. L.A. Villaescusa, I. Díaz, P.A. Barrett, J.M. LLoris-Cormano, R. Martínez-Mañez, M. Tsapatsis, Z. Liu, O. Terasaki, M.A. Camblor, The pure silica large pore zeolite ITQ-7: synthetic strategies, structure-directing effects and control and nature of structural disorder. Chem. Mater. **19**, 1601–1612 (2007)
74. S. Qiu, W. Pang, H. Kessler, J.L. Guth, Synthesis and structure of the [AlPO4]12 Pr4NF molecular sieve with AFI structure. Zeolites **9**, 440–444 (1989)
75. T. Ikeda, K. Miyazawa, F. Izumi, Q. Huang, A. Santoro, Structural study of the aluminophosphate AlPO4-5 by neutron powder diffraction. J. Phys. Chem. Solid **60**, 1531–1535 (1999)
76. C. Aydin, J. Lu, A.J. Liang, C.-Y. Chen, N.D. Browing, B. Gates, Tracking iridium atoms with electron microscopy: first steps of metal nanocluster formation in one-dimensional zeolite channels. Nano Lett. **11**, 5537–5541 (2011)
77. A. Mayoral, J. Coronas, C. Casado, C. Tellez, I. Díaz, Atomic resolution analysis of microporous titanosilicate ETS-10 through aberration corrected STEM imaging. Chem. Cat. Chem. **5**, 2595–2598 (2013). doi:10.1002/cctc.201300045
78. K. Yoshida, K. Toyoura, K. Matsunaga, A. Nakahira, H. Kurata, Y.H. Ikuhara, Y. Sasaki, Atomic sites and stability of Cs+ captured within zeolitic nanocavities. Sci. Rep. **2**, 2457 (2013)
79. H. Robson, K.P. Lillerud, Syntheses of Zeolitic Materials, 2nd edn. (2001)
80. V. Gramlich, W.M. Meier, The crystal structure of hydrated NaA: a detailed refinement of a pseudosymmetric zeolite structure. Z. Kristallogr. **133**, 134–149 (1971)
81. A. Mayoral, P.A. Anderson, I. Diaz, Zeolites are no longer a challenge: atomic resolution data by aberration-corrected STEM. Micron (2014). doi:10.1016/j.micron.2014.05.009
82. Y. Kim, K. Seff, Structure of a very small piece of silver metal. The octahedral silver (Ag6) molecule. Two crystal structures of partially decomposed vacuum-dehydrated fully silver(1+) ion-exchanged zeolite A. J. Am. Chem. Soc. **99**, 7055–7057 (1977)
83. P.A. Jacobs, J.B. Uytterhoeven, H.K. Beyer, Some unusual properties of activated and reduced AgNaA zeolites. J. Chem. Soc. Faraday Trans. **75**, 56–64 (1979)
84. M. Tamarasso, G. Perego, B. Notari, U.S. Patent No. 4410501 (1983)
85. D.M. Chapman, A.L. Roe, Synthesis, characterization and crystal chemistry of microporous titanium-silicate materials. Zeolites **10**, 730–737 (1990)
86. R.C. Haushalter, L.A. Mundi, Reduced molybdenum phosphates: octahedral-tetrahedral framework solids with tunnels, cages, and micropores. Chem. Mater. **4**, 31–48 (1992)
87. J. Rocha, M.W. Anderson, Microporous titanosilicates and other novel mixed octahedral-tetrahedral framework oxides. Eur. J. Inorg. Chem. **5**, 801–818 (2000)
88. Z. Lin, J. Rocha, A. Navajas, C. Tellez, J. Coronas, J. Santamaria, Synthesis and characterisation of titanosilicate ETS-10 membranes. Microporous Mesoporous Mater. **67**, 79–86 (2004)
89. S. Uma, S. Rodrigues, I.N. Martyanov, K.J. Klabunde, Exploration of photocatalytic activities of titanosilicate ETS-10 and transition metal incorporated ETS-10. Microporous Mesoporous Mater. **67**, 181–187 (2004)
90. X. Wang, A.J. Jacobson, Crystal structure of the microporous titanosilicate ETS-10 refined from single crystal X-ray diffraction data. Chem. Commun. **11**, 973–974 (1999)
91. T. Kimura, T. Kamata, M. Fuziwara, Y. Takano, M. Kaneda, Y. Sakamoto, O. Terasaki, Y. Sugahara, K. Kuroda, Formation of novel ordered mesoporous silicas with square channels and their direct observation by transmission electron microscopy. Angew. Chem. Int. Ed. **39**, 3855–3859 (2000)
92. M.W. Anderson, J.R. Agger, N. Hanif, O. Terasaki, T. Ohsuna, Crystal growth in framework materials. Solid State Sci. **3**, 809–819 (2001)
93. M.W. Anderson, J.R. Agger, N. Hanif, O. Terasaki, Growth models in microporous materials. Microporous Mesoporous Mater. **48**, 1–9 (2001)
94. M.J. Hÿtch, E. Snoeck, R. Kilaas, Quantitative measurement of displacement and strain fields from HREM micrographs. Ultramicroscopy **74**, 131–146 (1998)

95. T. Yanagisawa, T. Shimizu, K. Kuroda, C. Kato, The preparation of alkyltriinethylaininonium–kaneinite complexes and their conversion to microporous materials. Bull. Chem. Soc. Jpn. **63**, 988–992 (1990)
96. C.T. Kresge, M.E. Leonowicz, W.J. Roth, J.C. Vartuli, J.S. Beck, Ordered mesoporous molecular-sieves synthesized by a liquid-crystal template mechanism. Nature **359**, 710–712 (1992)
97. J.S. Beck, J.C. Vartuli, W.J. Roth, M.E. Leonowicz, C.T. Kresge, K.D. Schmitt, C.T.W. Chu, D.H. Olson, E.W. Sheppard, A new family of mesoporous molecular sieves prepared with liquid crystal templates. J. Am. Chem. Soc. **114**, 10834–10843 (1992)
98. S. Inagaki, Y. Fukushima, K. Kuroda, Synthesis of highly ordered mesoporous materials from a layered polysilicate. J. Chem. Soc. Chem. Commun. **8**, 680–682 (1993)
99. A. Carlsson, M. Kaneda, Y. Sakamoto, O. Terasaki, R. Ryoo, S.H. Joo, The structure of MCM-48 determined by electron crystallography. J. Electron Microsc. **48**, 795–798 (1999)
100. Y. Sakamoto, M. Kaneda, O. Terasaki, Z.Y. Zhao, J.M. Kim, G.D. Stucky, H.J. Shin, R. Ryoo, Direct imaging of the pores and cages of three-dimensional mesoporous materials. Nature **408**, 449–453 (2000)
101. Y. Sakamoto, I. Diaz, O. Terasaki, D. Zhao, J. Perez-Pariente, J.M. Kim, G.D. Stucky, Three-dimensional cubic mesoporous structures of SBA-12 and related materials by electron crystallography. J. Phys. Chem. B **106**, 3118–3123 (2002)
102. M. Kaneda, T. Tsubakiyama, A. Carlsson, Y. Sakamoto, T. Ohsuna, O. Terasaki, S.H. Joo, R. Ryoo, Structural study of mesoporous MCM-48 and carbon networks synthesized in the spaces of MCM-48 by electron crystallography. J. Phys. Chem. B **106**, 1256–1266 (2002)
103. A.E. Garcia-Bennett, K. Miyasaka, O. Terasaki, S. Che, Structural solution of mesocaged material AMS-8. Chem. Mater. **16**, 3597–3605 (2004)
104. Y. Sakamoto, T.W. Kim, R. Ryoo, O. Terasaki, Three-dimensional structure of large-pore mesoporous cubic Ia-3d silica with complementary pores and its carbon replica by electron crystallography. Angew. Chem. Int. Ed. **43**, 5231–5234 (2004)
105. A.E. Garcia-Bennett, N. Kupferschmidt, Y. Sakamoto, S. Che, O. Terasaki, Synthesis of mesocage structures by kinetic control of self-assembly in anionic surfactants. Angew. Chem. Int. Ed. **14**, 5317–5322 (2005)
106. C.B. Gao, Y. Sakamoto, K. Sakamoto, O. Terasaki, S. Che, Synthesis and characterization of mesoporous silica AMS-10 with bicontinuous cubic Pn-3m symmetry. Angew. Chem. Int. Ed. **45**, 4295–4298 (2006)
107. Y. Han, D. Zhang, L.L. Chang, J. Sun, L. Zhao, X. Zou, J.Y. Ying, A tri-continuous mesoporous material with a silica pore wall following a hexagonal minimal surface. Nat. Chem. **1**, 123–127 (2009)
108. S. Inagaki, A. Koiwai, N. Suzuki, Y. Fukushima, K. Kuroda, Synthesis of highly ordered mesoporous materials, FSM-16. Bull. Chem. Soc. Jpn. **69**, 1449–1457 (1996)
109. Y. Sakamoto, S. Inagaki, T. Ohsuna, N. Ohnishi, Y. Fukushima, Y. Nozue, O. Terasaki, Structure analysis of mesoporous material "FSM-16" studies by electron microscopy and X-ray diffraction. Microporous Mesoporous Mater. **21**, 589–596 (1998)
110. F. Kleitz, T.W. Kim, R. Ryoo, Phase domain of the cubic Im3m mesoporous silica in the EO106PO70EO106-Butanol-H20 system. Langmuir **22**, 440–445 (2006)
111. D. Chen, Z. Li, Y. Wan, X. Tu, Y. Shi, Z. Chen, W. Shen, C. Yu, B. Tu, D. Zhao, Anionic surfactant induced mesophase transformation to synthesize highly ordered large-pore mesoporous silica structures. J. Mater. Chem. **16**, 1511–1519 (2006)
112. J.M. Kim, Y. Sakamoto, Y.K. Hwang, Y.U. Kwon, O. Terasaki, S.E. Park, G.D. Stucky, Structural design of mesoporous silica by micelle-packing control using blends of amphiphilic block copolymers. J. Phys. Chem. B **106**, 2552–2558 (2002)
113. C.C. Landry, S.H. Tolbert, K.W. Gallis, A. Monnier, G.D. Stucky, P. Norby, J.C. Hanson, Phase transformations in mesostructured silica/surfactant composites. Mechanisms for change and applications to materials synthesis. Chem. Mater. **13**, 1600–1608 (2001)
114. I. Diaz, J. Perez-Pariente, O. Terasaki, Structural study by transmission and scanning electron microscopy of the time-dependent structural change in M41S mesoporous silica (MCM-41 to MCM-48, and MCM-50). J. Mater. Chem. **14**, 48–53 (2004)

115. S. Che, S. Kamiya, O. Terasaki, T. Tatsumi, The formation of cubic Pm-3n mesostructure by an epitaxial phase transformation from hexagonal p6mm mesophase. J. Am. Chem. Soc. **123**, 12089–12090 (2001)
116. S. Kamiya, H. Tanaka, S. Che, T. Tatsumi, O. Terasaki, Electron microscopy study of structural evolutions of silica mesoporous crystals: crystal-growth and crystal-transformation from p6mm to Pm-3n with time. Solid State Sci. **5**, 197–204 (2003)
117. S. Che, A.E. Garcia-Bennett, T. Yokoi, K. Sakamoto, H. Kunieda, O. Terasaki, T. Tatsumi, A novel anionic surfactant templating route for synthesizing mesoporous silica with unique structure. Nat. Mater. **2**, 801–805 (2003)
118. A.E. Garcia-Bennett, O. Terasaki, Structural investigations of AMS-n mesoporous materials by transmission electron microscopy. Chem. Mater. **16**, 813–821 (2004)
119. S. Che, Z. Liu, T. Ohsuna, K. Sakamoto, O. Terasaki, T. Tatsumi, Synthesis and characterization of chiral mesoporous silica. Nature **429**, 281–284 (2004)
120. I. Diaz, C. Marquez-Alvarez, F. Mohino, J. Perez-Pariente, E. Sastre, Combined alkyl and sulfonic acid functionalization of MCM-41-type silica. Part I. Synthesis and characterization. J. Catal. **193**, 283–294 (2000)
121. X.S. Zhao, X.Y. Bao, W. Guo, F.Y. Lee, Immobilizing catalysts on porous materials. Mater. Today **9**, 32–39 (2006)
122. E. Serra, A. Mayoral, Y. Sakamoto, R.M. Blanco, I. Díaz, Immobilization of lipase in ordered mesoporous materials: effect of textural and structural parameters. Microporous Mesoporous Mater. **114**, 201–213 (2008)
123. E. Serra, E. Diez, I. Diaz, R.M. Blanco, A comparative study of periodic mesoporous organosilica and different hydrophobic mesoporous silicas for lipase immobilization. Microporous Mesoporous Mater. **132**, 487–493 (2010)
124. J.F. Diaz, J.J. Balkus Jr., Enzyme immobilization in MCM-4 1 molecular sieve. J. Mol. Catal. B Enzym. **2**, 115–126 (1996)
125. Y. Han, S.S. Lee, J.Y. Ying, Pressure-driven enzyme entrapment in siliceous mesocellular foam. Chem. Mater. **18**, 643–649 (2006)
126. E. Santalla, E. Serra, A. Mayoral, J. Losada, R.M. Blanco, I. Diaz, In-situ immobilization of enzymes in mesoporous silicas. Solid State Sci. **13**, 691–697 (2011)
127. M.W. Anderson, T. Ohsuna, Y. Sakamoto, Z. Liu, A. Carlsson, O. Terasaki, Modern microscopy methods for the structural study of porous materials. Chem. Commun. **21**, 907–915 (2004)
128. M. Vallet-Regi, M. Manzano, J.M. Gonzalez-Calbet, E. Okunishi, Evidence of drug confinement into silica mesoporous matrices by STEM spherical aberration corrected microscopy. Chem. Commun. **46**, 2956–2958 (2010)
129. S. Urrego, E. Serra, V. Alfredsson, R.M. Blanco, I. Diaz, Bottle-around-the-ship: a method to encapsulate enzymes in ordered mesoporous materials. Microporous Mesoporous Mater. **129**, 173–178 (2010)
130. D. Zhao, J. Feng, Q. Huo, N. Melosh, G.H. Fredrickson, B.F. Chmelka, G.D. Stucky, Triblock copolymer syntheses of mesoporous silica with periodic 50 to 300 angstrom pores. Science **279**, 548–552 (1998)
131. A. Mayoral, R.M. Blanco, I. Diaz, Location of enzyme in lipase-SBA-12 hybrid biocatalyst. J. Mol. Catal. B Enzym. **90**, 23–25 (2013)
132. A. Mayoral, R. Arenal, V. Gascon, C. Marquez-Alvarez, R.M. Blanco, I. Diaz, Designing functionalized mesoporous materials for enzyme immobilization: locating enzymes by using advanced TEM techniques. Chem. Cat. Chem. **5**, 903–909 (2013)

Chapter 5
Local TEM Spectroscopic Studies on Carbon- and Boron Nitride-Based Nanomaterials

Raul Arenal and Odile Stephan

5.1 Introduction to Carbon-Based and Related Nanomaterials

Nanostructured carbon-based materials, such as carbon nanotubes, nanodiamonds, fullerenes, nanofibers, and more recently graphene, are of increasing interest as potential building blocks for field emission, electronic and optoelectronic devices, gas and energy storage media, bio-sensing/bio-technology, and medicine [1–15]. In addition, other related nanomaterials, having similar crystalline structures to those based on carbon, can offer complementary properties. These counterpart nanomaterials are mainly based on boron and/or carbon and/or nitrogen, including pure phases, as in the case of boron nitride nanostructures [1–15]. In this first section, we will briefly describe these different nanostructures.

Nanocrystalline diamond (sometimes called nanodiamond) is a term encompassing a vast number of structures involving typical sizes smaller than 100 nm. These nanomaterials can be divided in two different kinds of morphologies: particles and films. Historically, nanocrystalline diamond particles were first synthesized in the 1960s using detonation techniques [4, 10]. However, they remained almost unknown until the beginning of the 1990s, when they rekindled a wider interest [4, 10]. In the case of crystalline nanodiamond films, two different kinds of nanostructures are classified: nanocrystal diamonds (NCD), which includes all these materials

---

R. Arenal (✉)
Advanced Microscopy Laboratory, Nanoscience Institute of Aragon,
University of Zaragoza, 50018 Zaragoza, Spain

ARAID Foundation, 50018 Zaragoza, Spain
e-mail: arenal@unizar.es

O. Stephan
Laboratoire de Physique des Solides (LPS), CNRS UMR 8502,
Université Paris Sud XI, Bâtiment 510, Orsay, 91405, France

F.L. Deepak et al. (eds.), *Advanced Transmission Electron Microscopy*,
DOI 10.1007/978-3-319-15177-9_5

<100 nm, and ultra-nanocrystalline diamonds (UNCD), in which the diamond grains, smaller than 10 nm, are bounded together by 1–2-nm-wide grain boundaries [4, 10, 12]. These nanomaterials exhibit superior mechanical, electronic, and optical properties (which are often related to the presence of sp^2-bonded carbon atoms) to diamond, and then, they are excellent candidates for various biomedical and electronic applications [4, 10, 12].

Also in the 1980s, another class of carbon-based nanostructures, the fullerenes, was discovered [8]. These cage-like molecules consist, in the simplest and best-known case, of 60 carbon (C_{60}) atoms joined together by single and double bonds to form a hollow sphere with 12 pentagonal and 20 hexagonal faces, in a soccer ball [8].

Soon after the fullerenes' discovery, Iijima identified another kind of carbon nanostructure, the multiwalled carbon nanotubes (C-NTs) [9], although the question of the first identification remains controversial [16]. It is worth mentioning that nanotubes can display two different morphologies: multiwalled (MW) or single-walled nanotubes (SWNTs). The latter were also identified by Iijima, via high-resolution TEM (HRTEM) imaging in 1993 [17]. Using a heuristic model, a SWNT is structurally equivalent to a sheet of graphene (or hexagonal BN layer) rolled into a tube [1–3]. For nearly 25 years, the research activity on these nanostructures has been (and still is) huge. This high interest on these materials is due to the extraordinary mechanical, thermal and transport properties of these C-NTs [1–3, 5–7, 15]. These unique properties make carbon NTs very good candidates for a large range of applications, from electronic to energetic and biological uses [1–3, 5–7, 15].

More recently, graphene (including graphene nanoribbons), a single-atom-thick sheet of carbon atoms bonded together in a hexagonal lattice, has also attracted enormous research interest [18]. Its structure directly determines its outstanding properties, such as high electrical and thermal conductivities, great mechanical strength, and large specific surface area [19]. It is a nanomaterial of fundamental importance, with applications in different areas from nanoelectronics to advanced composites [19].

All these carbon-based nanomaterials or nanostructures can be classified as a function of their molecular hybridization (sp^2, sp^3, sp^2 versus sp^3, and even sp^1 in the case of carbynes, not described in this review), which is intimately related to their structure and dimensionality. Indeed, upon bending, the molecular orbital hybridization of a graphene sheet can be regarded as being somewhere in between a pure sp^2 or sp^3 state. Referred to as a sp^2/sp^3 re-hybridization [4, 10, 14], this phenomenon occurs in polymorphs such as fullerenes and nanotubes [4, 10, 14] and is alternatively denoted as a spn hybridization, where $2<n<3$. Such a mixing of hybridization is found, for example, in amorphous and diamond-like carbons (DLCs) [10].

Counterpart materials to carbon, such as boron nitride (BN), can offer complementary properties. As a matter of fact, all the different allotropic structures of BN (cubic (c-BN), wurtzite (w-BN), hexagonal (h-BN), and rhombohedral (r-BN), which respectively correspond to diamond (zinc-blende form), hexagonal diamond (wurtzite form), hexagonal (graphite), and rhombohedral carbon) show a strong insulating character, leading to possible uses in optoelectronic devices [3, 5]. It is worth mentioning that these structural similarities between BN and carbon also exist in the case of nano-objects; thus, BN fullerenes, BN nanotubes, and BN flakes (even monolayers of h-BN) have been produced [3, 5].

Until now we have focused on pure carbon or pristine boron nitride nanomaterials and nanostructures. However, the presence of dopants and/or defects offers the opportunity to broaden their use in new emerging technologies [2, 3, 5–7, 10, 13, 14]. Indeed, it is well known that one route for modifying the solid-state properties of materials is the addition of electron acceptors or donors. In the case of carbon nanostructures, the use of boron, nitrogen, fluorine, lithium, phosphorous, etc. as dopants, which can introduce donor or acceptor states near the Fermi level, is thought to be a promising approach for tailoring their electrical, electronic, and optical properties [3, 5–7, 20–22]. In fact, as in semiconductor applications, the property optimization of a device depends on the control of the electronic states in the valence and conduction bands.

To sum up, in the last 25–30 years, a large variety of carbon-based and related nanomaterials (CB-RNM) have been synthesized. They possess unique properties, which, in most of the cases, depend on their atomic structure and composition. Particularly, in the aforementioned cases involving the presence of foreign atoms in low concentration rates, highly local (even atomic) analyses are required to unravel the details of the modification of the structural, electronic, optical, and chemical properties in these materials. As this will be presented below, several spectroscopic transmission electron microscopic (TEM) techniques (electron energy-loss spectroscopy (EELS), energy-filtered TEM (EFTEM), and cathodoluminescence) are employed in this regard.

5.2 Introduction to Analytical Spectroscopic TEM Techniques

Transmission electron microscopy (TEM) is a powerful tool, providing very rich information about the morphology, the microstructure, the elemental composition, and the physical properties of nanomaterials at the local (even atomic) scale. It thus plays a crucial role in the search for a deeper understanding of nanostructures' physics and chemistry.

Historically, image resolution was restricted by the unavoidable spherical aberration of the objective lens. In recent years, there has been significant activity in the area of aberration correction for both fixed-beam and scanning TEM leading to spectacular improvement in the spatial resolution [23–26]. Uncorrected microscopes only provide a point resolution of 0.15–0.2 nm, whereas resolutions below 0.1 nm can now be reached in aberration-corrected (scanning) TEM [23–26].

HRTEM can image crystallographic structures [23–26] making it invaluable in the study of nanostructures. In this context, carbon nanotubes were identified almost 25 years ago using this technique, which still remains the most widely employed method to study the morphology and structure [2, 3, 5, 9, 17].

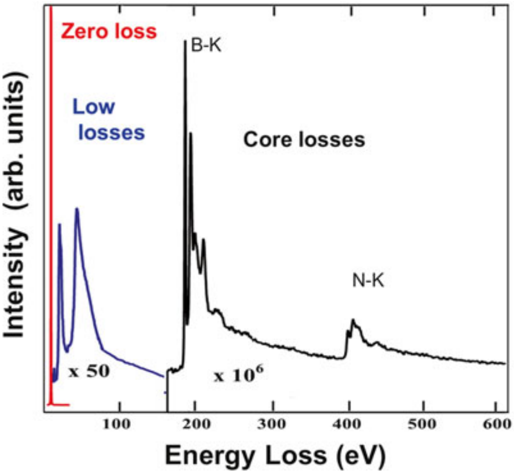

Fig. 5.1 Global EEL spectrum recorded on a BN-SWNT using a STEM. Low-loss (0–50 eV) and core-loss (>50 eV) regions are visible; see text. The low-loss region has been shifted vertically for clarity

EELS is the most powerful of the TEM-based analytical techniques for structural and chemical composition studies at the (sub)nanometer/atomic scale and is therefore well suited to the inspection of individual nanostructures. Basically, EELS consists in the measure of the energy losses of electrons resulting from the specific inelastic interactions of the electron beam with the specimen [27–29]. Two kinds of information can be extracted from EEL spectra, depending on the investigated energy-loss range: the core-loss region gives access to the chemical and electronic structure of the material, whereas the low-loss region (<50 eV) provides information on its optical, electronic, and (very recently) vibrational properties (Fig. 5.1) [27–29].

Characteristic elemental edges in the core-loss region correspond to excitations in the material associated with electronic transitions from a core level. Thus, EELS in the core-loss region provides information on the chemical species present in the samples and on their concentration and spatial distribution at a sub-nanometer/atomic scale [27–30]. The edges display near-edge absorption fine structures (ELNES), which are rich in information, similar to those of X-ray absorption (XAS) edges, about the electronic structure, the chemical environment, and the chemical bonding of the elements in question, at least qualitatively, from ELNES. In the present case, we will mainly focus on the K (we note that we will use the common spectroscopic notation) edges of B, C, O, and N, their onset energies being ~188 eV, ~284 eV, ~532 eV, and ~395 eV, respectively.

The study of EELS in the low-loss energy region (below 50 eV) provides direct access to the dielectric properties and lattice dynamics (most commonly when EELS is performed outside a TEM, as in reflection EELS) of a material. Inter-/intraband transitions, phonons, and collective oscillations of the electron gas (plasmons) have signals in this energy region and can be probed via this technique. Furthermore, when the experiments are performed in a TEM, sub-nanometer (atomic) spatial resolution can be simultaneously reached.

Spatially resolved (SR) spectroscopic information can be recorded using a scanning TEM (STEM) in particular acquisition modes called spectrum imaging (SPIM) or spectrum line (SPLI) [31–33]. These modes consist in the acquisition of one EEL spectrum for each position of the probe scanning over a 2D region (SPIM or SI) or a line (SPLI) at the surface of the nanotubes and nanoparticles. The spatial resolution of this technique is mainly limited by the probe size. From the collection of spectra recorded in a SPIM (SPLI), one can extract 2D elemental maps (1D elemental profiles) corresponding to the different elements present in the sample with a perfect spatial correlation. However, it is worth mentioning that such measurements must be done under particular illumination conditions to avoid any damage. In fact, the structure of heteroatomic carbon nanomaterials is, in general, very sensitive to the electron beam and can be modified and even become amorphous.

The energy-filtered TEM (EFTEM) mode is an alternative method for recording elemental maps based on EELS. For both techniques (EFTEM and SPIM-EELS), the energy-loss processes are identical; the only difference between them is how the information is acquired to obtain a 3D matrix containing an intensity value at each point (**x**, **y**, **E**), where **x** and **y** are two spatial coordinates and **E** is an energy coordinate [27, 34]. While a SPIM will be taken by filling the datacube at each spatial position (**x**, **y**) with a whole EEL spectrum, an EFTEM experiment will consist in acquiring the datacube by sampling the constant **E** planes (a large region of the specimen is then illuminated). In EFTEM an elemental map is obtained by subtracting several filtered images at different energies before and on a given core edge. If several elements are present in the sample, elemental maps should be captured serially.

Another technique, so-called electron dispersive spectrometry (EDS), can be employed for local analytical studies [25]. In this technique, hard X-rays emitted by a sample submitted to electron irradiation are detected. However, this X-ray technique is not always suitable for chemical analysis in our context. In fact, in our case, where we are dealing with materials composed of carbon and/or boron and/or nitrogen, their quantification is restricted, due to the detection limitation of this technique for light elements.

Finally, we mention that the traditional method for atomic-resolution analysis in STEM is high-angle annular dark-field (HAADF) imaging, often referred to as Z-contrast imaging as it involves collecting electrons which have, by interacting with the nuclei, been scattered through large angles and thus resembles in atomic number dependence the Rutherford scattering formula [35, 36]. This imaging mode will not be illustrated and described in the context of this book chapter dedicated to spectroscopic analysis techniques. For some recent applications, the reader may refer to [37, 38].

All these TEM capabilities have been extensively used to locally investigate the chemical structure of heteroatomic nanostructures. Several examples are presented below.

5.3 Local Composition Analysis of CB-RNM via TEM

Now we will illustrate, via a selection of examples, the contribution of spatially resolved EELS (SR-EELS) and EFTEM in (S)TEM microscopes to the compositional and atomic configuration analyses on these CB-RNM. We have selected examples that are representative of the different systems or that best highlight the capabilities of these local analytical techniques.

5.3.1 Single-Atom Spectroscopy on Carbon Nanostructures: From 0D to 1D and 2D Nanostructures

There are two very illustrative examples, showing the power of the techniques as well as the instrumental/technical advances developed in the last decade. The first example concerns the study of metallofullerene molecules (Gd@C_{82}) inside the single-walled carbon nanotubes (known as peapods). Suenaga et al. mapped the gadolinium atomic distribution showing that it was possible to identify individual atoms in these nanostructures; see Fig. 5.2 [39].

More recently, several further steps have been made, with the development of single-atom EEL spectroscopy on different metallofullerene-doped single-walled

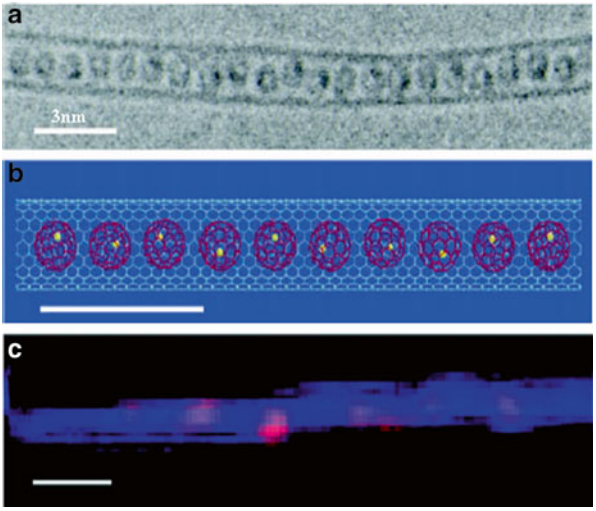

Fig. 5.2 (**a**) HRTEM micrograph showing a “peapod” (a nanotube filled with fullerenes: Gd@C_{82}@C-SWNT) system. (**b**) Schematic representation of the system containing doped fullerenes inside a C-SWNT. (**c**) Superposition of the elemental maps corresponding to Gd (*magenta*, $N_{4,5}$ edge) and C (*blue*, K edge) extracted from a SPIM-EELS recorded on one of these hybrid systems. Reprinted with permission of Suenaga et al. [39]

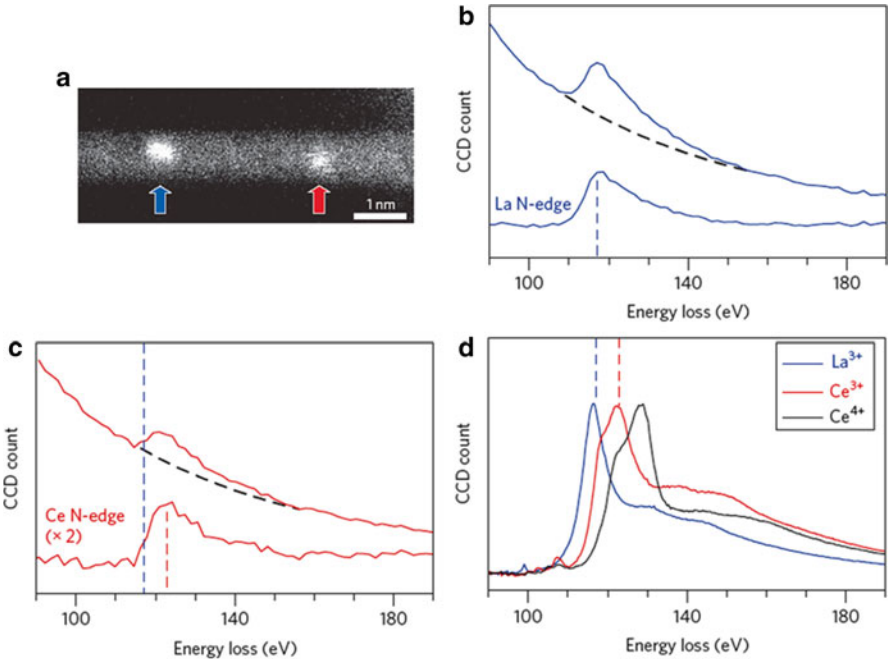

Fig. 5.3 Single-atom spectroscopy for La and Ce. (**a**) HAADF image of a peapod co-doped with La@C_{82} and Ce@C_{82}. La is indicated by the *blue arrow* and Ce by the *red arrow*. (**b**, **c**) EELS spectra taken from La@C_{82} (**b**) and Ce@C_{82} (**c**) shown in (**a**). (**d**) Reference EELS spectra of La^{3+} (in $LaCl_3$, *blue*), Ce^{3+} (in $CeCl_3$, *red*), and Ce^{4+} (in CeO_2, *black*). The atom on the *left* in (**a**) is assigned as La and the atom on the *right* in (**a**) as Ce in the trivalent state (Ce^{3+}). Reprinted with permission of Suenaga et al. [40]

nanotubes [40]. Indeed, single calcium atoms inside the peapods were unambiguously identified, and elemental analyses of lanthanum, cerium, and erbium atoms were also demonstrated. This is an important achievement as the onset energies of the La N and Ce N edges are very close (99 and 109 eV, respectively), so that the absorption edges overlap and make difficult the analysis. Suenaga et al., working at 60 kV to reduce knock-on damage, showed that these single atoms can be successfully distinguished with this technique; see Fig. 5.3 [40].

Following the latter of these examples, another very interesting work has been realized by Suenaga and Koshino on graphene boundaries [41]. They investigated, via atomically resolved EELS, the electronic and bonding structures of the graphene edge carbon atoms; see Fig. 5.4. Single-, double-, and triple-coordinated carbon atoms have been distinguished. These results have been achieved by overcoming the difficulties of this kind of single-atom spectroscopy on light atoms, which is limited by the extremely weak signals and by the specimen damage under the electron beam [41]. It is worth mentioning that another atomically resolved EELS experiment has been performed by Alem et al. on an h-BN bilayer [42].

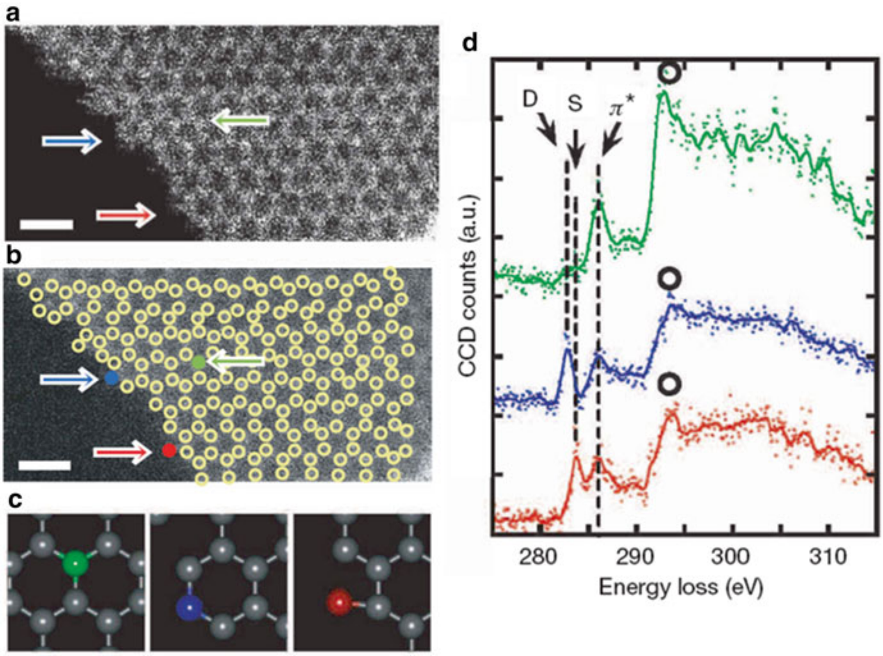

Fig. 5.4 Graphene edge spectroscopy. (**a**) ADF image of single graphene layer at the edge region. No image processing has been done. Atomic positions are marked by *circles* in a smoothed image (**b**). Scale bars, 0.5 nm. (**d**) ELNES of carbon K (1*s*) spectra taken at the color-coded atoms indicated in (**b**). *Green*, *blue*, and *red* spectra correspond to the normal sp^2 carbon atom, a double-coordinated atom, and a single-coordinated atom, respectively. These different states of atomic coordination are marked by *colored arrows* in (**a**, **b**) and illustrated in (**c**). Reprinted with permission of Suenaga et al. [41]

5.3.2 *Probing the Chemical Bond in BN Layered-Based Nanostructures*

A complementary approach to spatially resolved EELS (although much less employed) is angular-resolved EELS. There, the ELNES are recorded as a function of scattering angle (and therefore momentum transfer) at the expense of very high spatial resolution (an incident parallel beam is used to reduce the probe convergent angle). This is a very relevant approach in the case of anisotropic materials where the electronic orbitals are strongly directional. Hexagonal layered materials, like graphite or hexagonal boron nitride, possess such an anisotropic electronic structure in relation to their anisotropic (layered) structure. This anisotropy is visible in the variation of the relative weight of the π^* and σ^* features of the C (or B or N) K edges. Here we show the results of angular (momentum)-resolved EELS on highly pure h-BN microcrystals [43]. This work was performed in a FEI Tecnai F-20

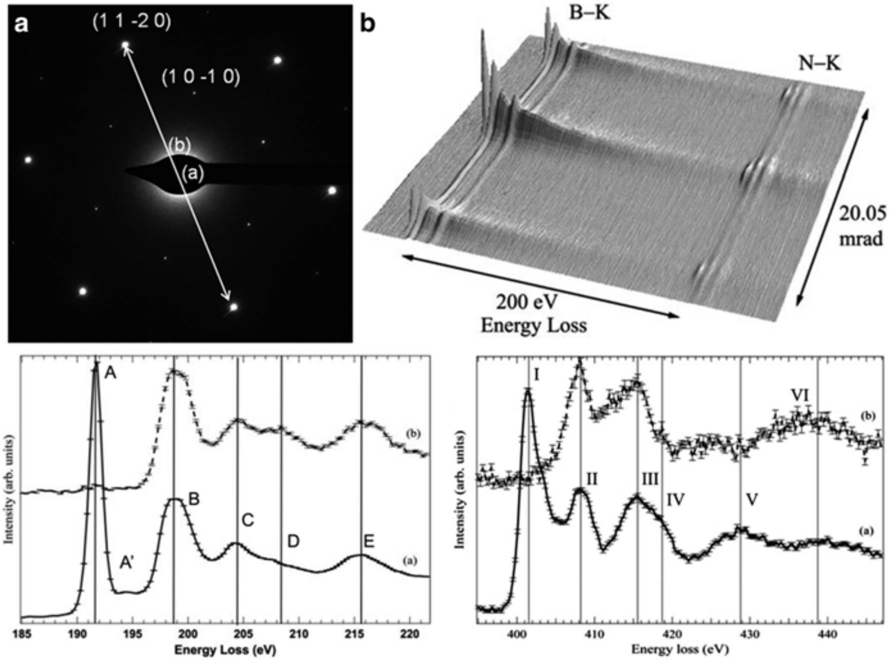

Fig. 5.5 (**a**) Selected area electron diffraction of a single crystal of h-BN (positions (**a**, **b**) indicate the *q* transfer directions studied). (**c**) B–K edge and (on the *right*, (**d**)) N–K edge for both scattering vectors marked in (**a**). Adapted from Arenal et al. [43]

electron microscope, equipped with a GIF and operating at 200 kV. The diameter of the near parallel probe used during these measurements was typically one micron defining the region of interest on a uniformly thick single crystal region of an oriented grain. Measurements were done on [position (a)] or near [position (b)] the {0001} axis (**c** axis) as can be seen in the selected area diffraction pattern shown in Fig. 5.5a. In order to access very high angular resolution, a small collection aperture (β of <0.3 mrad) and a highly coherent and nearly parallel probe ($\alpha < 0.05$ mrad) have been employed.

Examples of experimental B–K and N–K edges are shown in Fig. 5.5b–d for two different momentum transfer values when the collection aperture is set at two positions along the <11-2 0> crystallographic direction [position (a) at the center of the Brillouin zone and position (b), 1.49 mrad away from the center; see Fig. 5.5a]. These collection conditions correspond to two extreme kinematical conditions with the momentum transfer (**q**) parallel to the **c** axis [position (a)] and perpendicular to the **c** axis [position (b)]. The pairs of collected B–K and N–K edges are shown in Fig. 5.5c, d showing a large dependency on the orientation of the scattering vector with respect to the lattice. The first peak of the boron and nitrogen K edges disappears completely under the **q** perpendicular to **c** condition. This confirms that the origin of these peaks is the transition of a 1*s* electron to the B-2*pz* and the N-2 *pz* orbitals, in the boron and nitrogen edge, respectively. Nevertheless, we note that in the B–K edge the origin of this first peak is excitonic (as testified by the sharp and intense character of this peak at the onset of the edge), while this is not the case for N–K edge. The differences between the spectra due to the anisotropy of the h-BN are also visible in the set of peaks in the spectra after the π^* peak which correspond to the σ^* resonances. In the B–K edge, the principal differences are as follows: (1) the enhancement of the peak at 208 eV for the **q**//**c** orientation and (2) from 220 eV the different behavior (presence of a peak around 225 eV and absence of the broad peak centered at 230 eV) of the spectrum for the orientation **q** perpendicular to **c** comparing with the other. These differences are due to the influence of the different contributions, as a function of the orientation, of the core electron transitions to the B-2*pxy* and B-2*pz* orbitals. Since in the BN the bond between B and N atoms is rather strongly covalent, the shape of the N–K edge is similar to that of the B–K edge. The interpretation of the different peaks for the N–K edge is therefore similar to that of B–K [43].

Similarly to C nanostructures, spatially resolved ELNES analysis has also been employed to investigate the spatial distribution of various chemical states in BN-based nanostructures. One illustrative example concerns the study of boron-based nanoparticles produced during the synthesis of boron nitride nanotubes [44]. As boron was found to be present in various states—namely, B, B_2O_3, and h-BN—in these nanostructures, a statistical analysis technique has been developed to extract, from EELS-SPIM, the spatial distribution of this element according to the nature of its chemical bonding. Indeed, a nonnegative linear least square (NNLS) fitting method has been used to retrieve the information from large datasets acquired over inhomogeneous specimens with complex morphologies and compositions [33, 44]. This technique consists in reconstructing experimental EEL spectra as linear combinations of reference spectra. In the present case, the method has been used to map the spatial distribution of bond types for a given element. In practice, the boron bonds were mapped by fitting the EELS fine structures of the B–K edge in the specimen with reference spectra for well-defined boron compounds: B, B_2O_3, and h-BN; see Fig. 5.6c. Intensities in bonding maps (such as B–B, B–N, or B–O) were deduced from the weights of the different references in the total reconstructed spectrum.

Figure 5.6a shows an HAADF-STEM image acquired in parallel with a SPIM on a set of nanoparticles. A posteriori, several pixels (probe positions) were selected from the SPIM and the corresponding EEL spectra (B–K edges) are shown in Fig. 5.6b. The NNLS fitting procedure was then extended to all spectra within the SPIM to provide bonding maps (choosing an energy window of 18 eV from 187.5 eV). This is illustrated in Fig. 5.7a–d which show, for a set of nanoparticles, the spatial distribution of particles, which generally consist of a boron core covered by a boron oxide layer and encapsulated in an h-BN cage (Fig. 5.7). The results highlight the electronic anisotropy of h-BN, in accord with the momentum-resolved studies on h-BN presented above [42]. Thus, when the probe is scanned over the particles, it successively explores positions with the **c** axis of the h-BN layers parallel or perpendicular to the electron beam direction; see the h-BN NNLS maps (Fig. 5.7c, d).

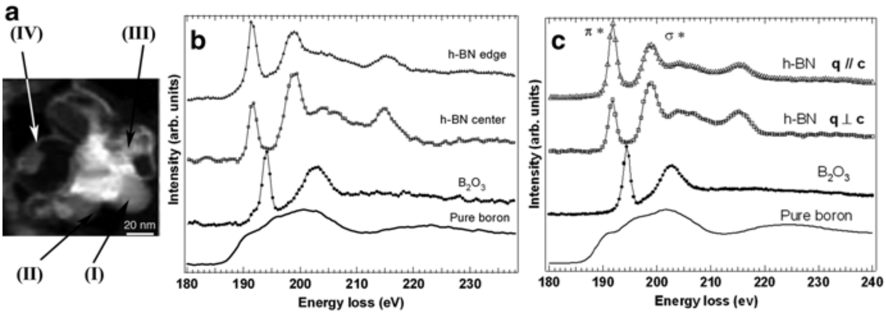

Fig. 5.6 (**a**) HAADF image associated with the SPIM recorded in parallel on a set of nanoparticles in a BNNT sample. (**b**) EEL spectra obtained from the different spots marked in (**a**). (**c**) EEL spectra recorded on highly purity samples of B, B_2O_3, and h-BN (the latter in two different orientations). Adapted from [33]

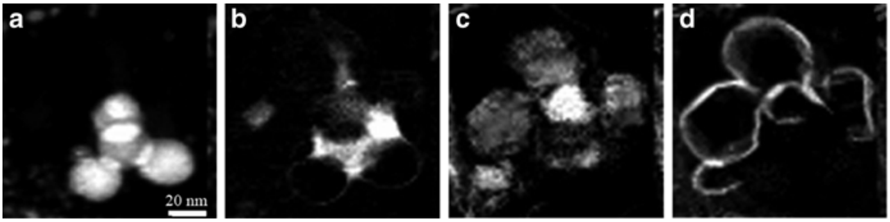

Fig. 5.7 (**a**–**d**) NNLS maps of B, B_2O_3, and h-BN (for two different **c** axis orientations), as extracted from the SPIM shown in Fig. 5.6a. Adapted from [33]

As mentioned above, one of the most important aspects to consider when studying heteroatomic nanostructures is the dopants' atomic arrangement. Several authors have investigated the distribution of boron or nitrogen atoms in different carbon-based nanostructures in this way. We have selected some examples illustrating the kind of information that spatially resolved EELS can offer.

5.3.3 Dopants in (Nano)Diamond Materials

Turner and coworkers have performed a comprehensive HR-EELS study of the B spatial distribution and chemical bonding in nanocrystalline diamond (NCD) films synthesized by microwave plasma-enhanced CVD [45, 46]. Their quantification at the sub-nanometer scale revealed embedding of B dopants in the diamond lattice and a preferential enrichment of boron at defective areas and twin boundaries [46]. From the EELS-SPIM acquired over the rectangle in Fig. 5.8a, they measured that the boron concentration in the diamond grains ranged from 1.1 at.% in the pristine diamond regions to a maximum of 4.6 at.%, in the defective regions. The authors

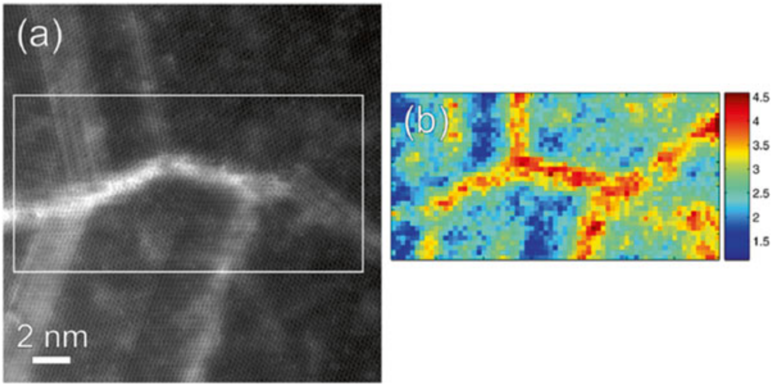

Fig. 5.8 High-magnification image of a diamond grain in a B:NCD film. (**a**) HAADF-STEM image of the area investigated by STEM-EELS. The region corresponding to the acquired 69 × 35 pixel spectrum image is indicated by the *white rectangle*. (**b**) *B*/*C* ratio map with color bar indicating the boron concentration ranges from 1.1 to 4.6 at.%. Adapted from [46]

found that the average B content was higher than the boron embedded at higher methane ratios during film growth. The authors attributed this effect to a higher density of defects and non-sp^3 carbon in these NCD films [46]. It is worth mentioning that the presence of other phases, such as B_4C or boron oxide, in these areas containing high amounts of boron cannot be excluded.

Coordination mapping reveals a distinct difference between the coordination of the B dopants in "pristine" diamond areas and that in defective regions. Figure 5.9a displays a typical EELS spectrum recorded in a diamond-rich region. B–K and C–K edges at 190 eV and 284 eV, respectively, are visible. The [B]:[C] concentration as measured from the spectrum is 2.2 at.%. They compare the B–K (this edge has been shifted over 94 eV for comparison) and C–K ELNES signatures for the diamond-rich region; see Fig. 5.9b. The C–K ELNES signatures are typical for diamond, with the addition of an sp^2-hybridized carbon contribution (pre-peak at 285 eV, corresponding to a $1s$-π^* transition). This sp^2 carbon is associated with amorphous carbon at the diamond grain boundaries. They also found, from this contribution, that the B–K ELNES signature is very similar to the carbon/diamond C–K fine structures. Thus, the excited boron atoms are embedded in a similar local environment to the excited carbon atoms implying that the main amount of boron dopants in the diamond-rich areas is present as substitutional impurities.

Another example involving these nanomaterials concerns the analysis of nitrogen-containing nanocrystalline particles, which have been also investigated via high-resolution (HR) STEM-EELS [47]. These EELS analyses were performed on isolated nanoparticles sticking out from aggregates. Figure 5.10 displays a bright-field (BF) STEM image of a single UDD particle of about 5 nm displaying a truncated octahedral morphology [47]. This is the typical size for classical nanodiamonds produced by detonation of TNT/RDX mixtures. An EEL spectrum line was

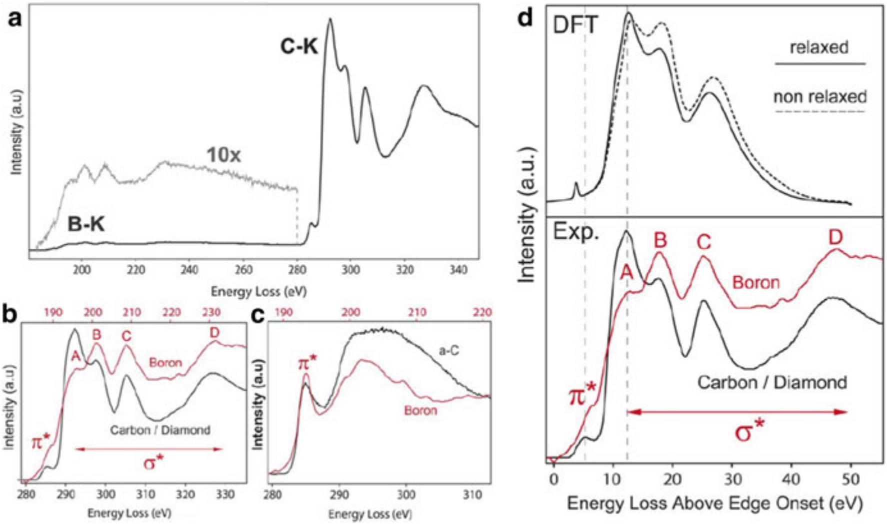

Fig. 5.9 (**a**) Typical EELS spectrum from a diamond grain region showing the boron K edge at 190 eV and the carbon K edge at 284 eV. (**b**) Comparison between a 2 eV smoothed boron ELNES with the simultaneously acquired carbon ELNES from a diamond region and (**c**) comparison between the smoothed boron ELNES with the simultaneously acquired carbon ELNES from an amorphous carbon-rich region, scaled to match the carbon K edge. The boron edges in (**b**, **c**) have been shifted to align with the carbon fine structure. (**d**) Comparison between the DFT-calculated ELNES and experimental data; *top*: DFT-calculated B–K edge ELNES for substitutional *B* in diamond with structure relaxation (*full line*) and without internal structure relaxation (*B* at ideal *C* position; *dotted line*). *Bottom*: Comparison between the 2 eV smoothed boron ELNES with the simultaneously acquired carbon ELNES from a diamond region. The carbon edge has been shifted to align with the boron fine structure. Adapted from Turner et al. [46]

performed horizontally across this particle. As pointed out in this work, the spectra from the surface of the particles have a significant contribution from the signature of sp^2 carbon bonding. However, the ELNES analyses at the core of the NP correspond to the characteristics of sp^3 carbon with only a very small contribution from the sp^2 surface layer. In addition, the signature of nitrogen (encircled N–K signal) has also been investigated, evidencing the presence of nitrogen at the core of the nanoparticle. Figure 5.10c shows several EEL spectra acquired from different NP associated with different samples: one large nanodiamond (20 nm in size) from sample ND2 (spectrum #2), one small nanodiamond (5 nm in size) in sample ND1 (spectrum #1), and one 40–50-nm nanodiamond from sample ND3 (spectrum #3). These spectra are compared to the N–K signal detected in cubic BN (spectrum #4) and in partly graphitized carbon nanoareas (spectrum #5). The N–K ELNES from spectrum #5 shows many similarities with those observed in thin CNx films [48], with a pre-peak at around 400 eV and a triangular σ* band, as this will be described below. However, in the cases where N is located at the core of the NP (spectra #1–3), the nature of the local chemical environment of these nitrogen atoms is similar to that of cubic BN [49].

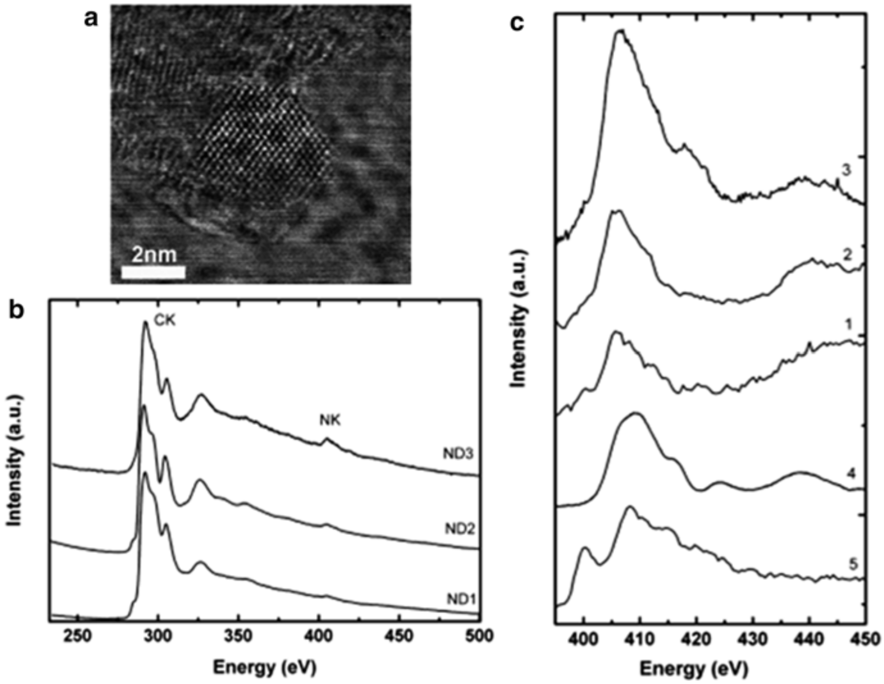

Fig. 5.10 (**a**) Aberration-corrected high-resolution bright-field STEM image of a typical 5 nm nitrogen-doped nanodiamond showing the truncated octahedral morphology. (**b**) EELS spectra of nanodiamonds in different samples. (**c**) Nitrogen signals extracted from EELS spectra obtained from sample ND1 (spectrum 1), sample ND2 (spectrum 2, nanodiamond; spectrum 5, *sp*^{2} structure), and sample ND3 (spectrum 3) nanodiamonds. Spectrum 4: profile observed for N in a cubic environment, such as c-BN. Adapted with permission from Pichot et al. [47]. Copyright American Chemical Society

Concerning *n*-type UNCD films, the nitrogen addition in the synthesis gas provokes drastic modifications in the morphology of the films, among other very significant effects related to their electronic properties. Indeed, there is a transformation from insulating to metallic conducting behaviors when nitrogen is added to the gas mixture during CH_4/Ar or C_{60}/Ar syntheses [50–52]. The addition of nitrogen increases the size of the diamond grains and the width of the grain boundaries (GB). In [51–53], it has been shown that the abrupt changes in the morphology of the films were related to a new configuration/arrangement of the diamond crystallites. As a matter of fact, elongated nanostructures were found to occur along with diamond nanograins, whereas a granular structure was typically found for the film grown without nitrogen. In order to fully characterize these differences, a detailed analysis of the *sp*^{2} and *sp*^{3} phase, the *N* concentration, the bonding environments of the *N* atoms, and their distribution was required. However, the small size of the crystal structures, the presence of disordered zones, and the inhomogeneity of the material made the characterization of these films highly difficult. Once more, STEM-EELS has proved to be the most appropriate technique to obtain this information. SR-EELS measurements were carried out on *n*-type UNCD films (Figs. 5.11 and 5.12) [53].

These EELS investigation confirmed the presence of elongated structures having a diamond core and a sp^2-bonded carbon sheath surrounding the core. In addition,

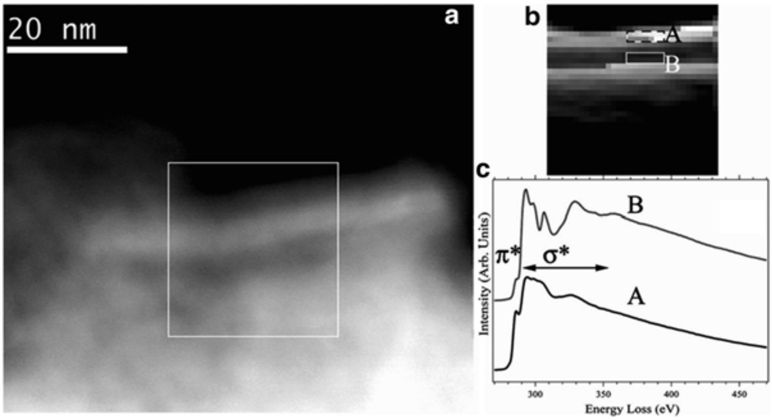

Fig. 5.11 (**a**) STEM–HAADF image of a UNCD film where several diamond nanowires can be observed. The *white box* shows the region from which an EELS spectrum image (SPIM) was acquired. (**b**) EELS C–K π peak intensity map extracted from the SPIM. (**c**) Two different EEL spectra showing the C–K edge, recorded in the areas *A* and *B* as marked in (**b**). Spectra from area *A* (*dotted area* in (**b**) at the edge of the NW) correspond to sp^2-bonded carbon. Spectrum from area *B* (*middle* of the NW) is assigned to sp^3 carbon with a small contribution of sp^2-bonded carbon from the surface of the NW. Reprinted from Arenal et al. [53]

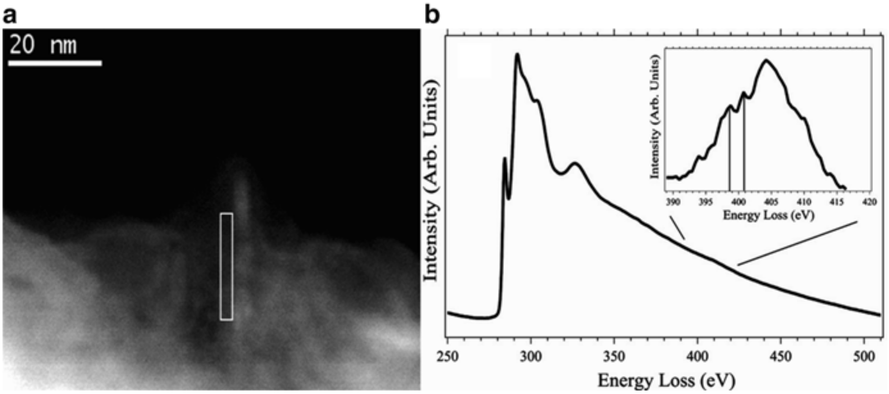

Fig. 5.12 (**a**) STEM–HAADF image of a different area of the sample. (**b**) EELS spectra recorded in the *white area* marked in (**a**). In this spectrum, C–K and N–K edges are visible at 284 eV and 397 eV, respectively. The inset is a magnification of the N–K edge, after background subtraction. Reprinted from Arenal et al. [53]

they showed that nitrogen was incorporated in the *sp*^{2} carbon sheath. The concentration of this nitrogen is approximately 1.5 at.%, and nitrogen atoms are situated in the so-called "pyridine-like" (twofold N-coordinated nitrogen) or "graphitic" (substitutional N) configurations; see Fig. 5.12. Nevertheless a pyrrole-like atomic arrangement (substitutional N atom sitting in a fivefold ring) cannot be excluded in less graphitized carbon sheaths. The assignments of the nitrogen configuration are often done comparing other works on *sp*^{2} nitrogen materials (films, multiwalled CNx-NT, etc.), which have been investigated by other macroscopic analytical techniques such as X-ray photoelectron spectroscopy (XPS), X-ray absorption spectroscopy (XAS), etc. [3, 5, 6, 13]. These results confirmed that the addition of large amounts of nitrogen to the synthesis gas is crucial for the formation of the diamond nanowires, as well as for the promotion of *sp*^{2} aromatic clustering, for the enhancement of the ordering of these clusters, and for increasing their size. All these aspects lead to the unusual *n*-type electrical conductivity exhibited by the UNCD films.

5.3.4 Heteroatoms Identification in sp^2*: Carbon-Based Nanostructures*

The number of analytical studies dealing with dopants in *sp*^{2} carbon-based nanostructures and nanomaterials is impressive and much larger than in the case of *sp*^{3} carbon. The largest fraction of these works concerns N incorporation in C-MWNTs and C-SWNTs. As already mentioned, these nanostructures have attracted much attention because of their interesting physical and chemical properties [2, 3, 5–7, 13, 14], which are significantly affected by the atomic arrangement of the dopant atoms within the nanostructures as has been demonstrated via EELS [5–7, 13, 43, 53–58]. Low dopant concentration measurements require precision experiments, combining high spatial resolution and high spectroscopic sensitivity. In nitrogen-doped single-walled carbon nanotubes (C-SWNTs), the amount of incorporated N atoms is usually below 1 at.%. Fortunately, atomically resolved EELS has been recently developed, allowing one to detect individual nitrogen dopants in single-walled carbon nanotubes and to compare to first principles calculations [58].

Figure 5.13a displays a HAADF image of a single-walled (SW) CNx-NT where an EELS-SPIM has been recorded in the red marked area of the image. Figure 5.13b shows three single EEL spectra, extracted from this SPIM (spectra labeled (i), (ii), and (iii)); the fourth spectrum is the sum of (i) and (ii). The carbon K edge is visible in the three spectra. In only two spectra from the whole dataset (1755 spectra) is the nitrogen signal also detectable. The nitrogen K ELNES, expanded in Fig. 5.13c, exhibit a strong peak at ~401 eV, with very little signal at energies above this. Comparing the spectra to density functional theory (DFT) ELNES calculations of possible single nitrogen defects, there is excellent agreement with the spectrum for substitutional nitrogen (Fig. 5.13c (iii) and atomic model, Fig. 5.13d) across the range of π^* and σ^* bands. This is the first time that such a combination of experimental and simulated EELS spectra has been obtained at this resolution for nitrogen

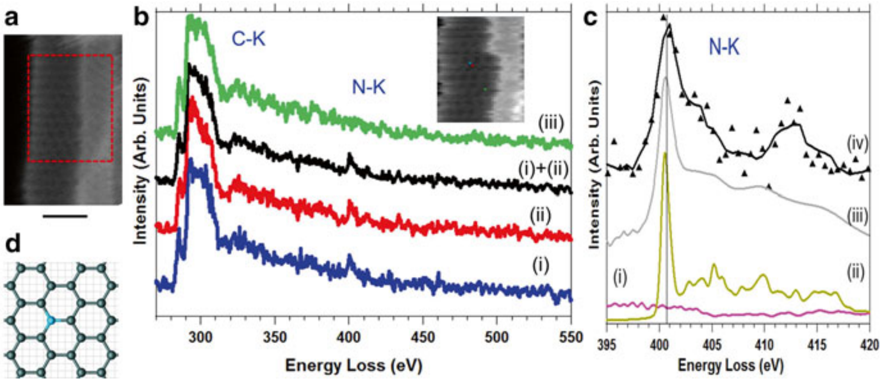

Fig. 5.13 (**a**) HAADF image displaying atomic resolution (scale bar: 1 nm). The *red dotted rectangle* marks out the scanned area during the acquisition of an EELS-SPIM. (**b**) Selection of EELS spectra extracted from the SPIM; *blue*, *red*, and *green* spectra correspond to the pixels outlined in *blue*, *red*, and *green* in the HAADF image acquired simultaneously with the SPIM and displayed in this figure. Each curve corresponds to a single spectrum from the SPIM, except the *black*, which is a sum of the *blue* and *red* spectra. (**c**) Simulated N–K ELNES (*gray*, (iii)) and nitrogen partial DOS calculations ((i) *purple*, p_z π^* states; (ii) *green*, p_{x-y} σ^* states) for substitutional nitrogen, compared to the experimental spectrum (iv), which is the same as spectra (i) + (ii) of (**b**). The EELS simulations allow unambiguous assignment of the peak at ~401 eV in the N–K edge to a substitutional configuration shown in the DFT-optimized structure of a substitutional nitrogen atom displayed in (**d**). Carbon and nitrogen atoms are respectively in *gray* and *blue*. Adapted with permission from [58]. Copyright American Chemical Society

dopants in SWNTs, demonstrating significant differences from earlier bulk studies. Thus, substitutional (graphitic) nitrogen was unambiguously identified, thanks to its relative stability under the 60 keV electron beam. The EELS spectroscopic signature showed a very weak π^* peak, a sharp "molecular-like" σ^* peak which is commonly misinterpreted as a π^* peak, and then almost no σ^* tail [58].

This work also revealed a second nitrogen defect resulting in a splitting of the N–K and C–K signals with additional peaks at 399.8 eV and 288.0 eV, respectively. Such splittings were interpreted as the signature of asymmetric C–N bonding and local distortion in the σ^* antibonding states for carbon (associated with bond dilation) in the environment of a "pyrrolic N atom," resolving previous literature ambiguities as to the structural origin of these peaks [2, 5–7, 13, 58].

This work also showed that another kind of nitrogen response associated with "pyridinic" nitrogen can be obtained from amorphous sheaths partially covering most of the CNx-SWNTs [58]. This sheath is associated with polyaromatic materials containing a larger amount of *N* than that incorporated within the C-SWNTs hexagonal lattice (typically at.1 % percent and less than 0.1 at.%, respectively). It is the case of the previously discussed *n*-type UNCD films, where the N is associated to a sp^2 sheath covering the sp^3 grains, which is probably associated with trans-polyacetylene chains [10, 14, 53]. The presence of this sheath emphasizes the need for ultrahigh spatial resolution measurements and questions the validity of previous results drawn from bulk or lower spatial resolution measurements [3, 5].

As in the case of nanotubes, the incorporation of dopants in graphene is a very important and fundamental problem—which has been widely studied over the last few years, in some cases via atomically resolved EELS [57, 59, 60]. Boron- and nitrogen-doped graphene, incorporated via low-energy ion-implantation technique, has been studied by Bangert et al. [59]. They found that the dopant atoms were predominantly substitutionally incorporated into the graphene lattice with a very small fraction residing in defect-related sites. Another very interesting example dealing with graphene doping is the work of Ramasse et al. on silicon-doped graphene [60]. Their findings reveal striking electronic structure differences between two distinct single substitutional silicon defect geometries in graphene; see Fig. 5.14. They optimized the acquisition conditions to obtain a good signal-to-noise ratio in the spectroscopic data, which allowed them to identify an *sp*^{3}-like configuration for a trivalent Si or a more complicated hybridized structure for a tetravalent Si impurity [60].

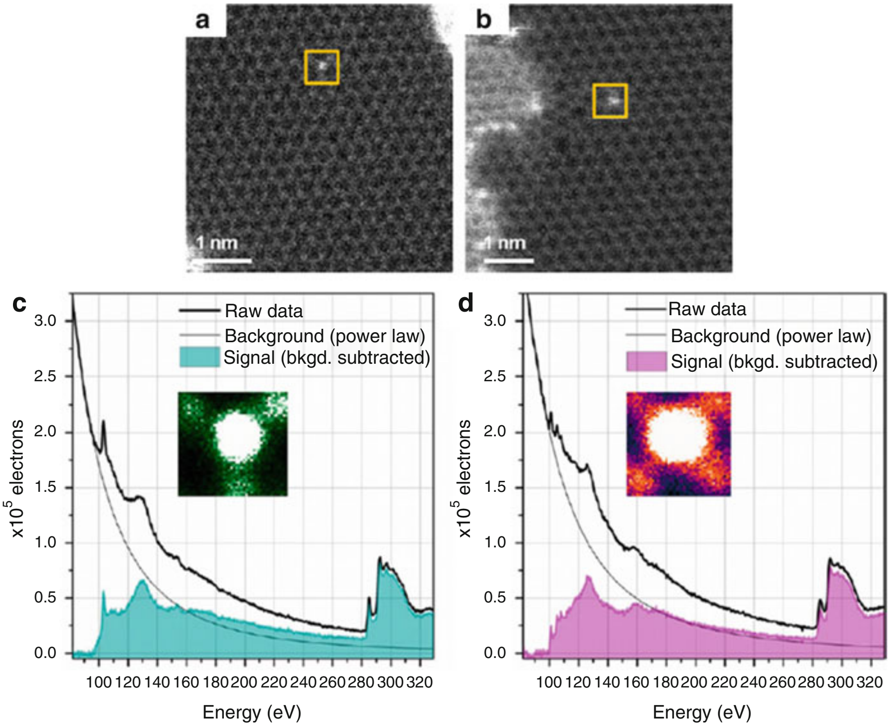

Fig. 5.14 (**a**) HAADF images (raw data) of Si atoms substituted within a single-layer graphene sheet. While the atom in (**a**) is in another wise pristine area of graphene, the atom in (**b**) is close to a highly defected region comprising 5- and 7-member C rings. The *yellow boxes* show the subregion over which the probe was scanned repeatedly to acquire high signal-to-noise EEL spectra displayed in (**c**, **d**). The *insets* of these figures (**c**, **d**) present a 50-frame average in false color from the stacks of images created during the acquisitions, showing clear threefold coordination (**c**) or fourfold coordination (**d**) of the Si atom. Adapted with permission from Ramasse et al. [60]. Copyright American Chemical Society

Another very interesting approach for obtaining rich information about the distribution of doping atoms in these nanostructures is analytical electron tomography. This technique is based on the use of energy-filtered transmission electron microscopy (EFTEM) in the tomographic mode (see the chapter devoted to tomography). This technique has been employed to investigate nitrogen-doped multi-walled carbon nanotubes [61]. Several tilt series of energy-filtered images were acquired on the K ionization edges of carbon and nitrogen on a multiwalled CNx-NT containing a large amount of nitrogen. Two tilt series of carbon and nitrogen 2D maps were then calculated from the corresponding energy-filtered images by using a careful extraction procedure for the chemical signals; see Fig. 5.15. Applying iterative reconstruction algorithms provided two spatially correlated C and N elemental-selective volumes. The 3D chemical maps show and explain the difference among the two different kinds of arches formed in these nanotubes (transversal or rounded ones depending on their morphology); the transversal arches contain more nitrogen than do the round ones. In addition, a detailed analysis of the reconstructed volume allowed the observation of an unexpected change in morphology along the tube axis: close to the round arches (with less N), the tube is roughly cylindrical, whereas near the transversal ones (with more N), its shape changes to a prism; see Fig. 5.15 [61].

These results indicate that the nitrogen is preferentially incorporated inside the transversal arches inside the nanotube structure, whereas the curled arches have relatively low nitrogen incorporation. Additionally, it has been shown that a high nitrogen density modifies the cross section of these nanotubes: indeed, in the nitrogen-rich areas, the circular shape of the tube is distorted into a prismatic structure.

We finally consider single-walled nanotubes comprising C, B, and N. Via the combination of HRTEM and STEM-EELS analysis, it has been shown that B–C–N nanotubes, synthesized by the laser vaporization technique, were indeed composed of carbon, boron, and nitrogen located at the vertices of a honeycomb lattice [62]. However, it was also demonstrated that the distribution of these elements was not uniform. Elemental maps extracted from EELS spectra (Fig. 5.16a, b) reveal that boron and nitrogen segregate from carbon to form small BN domains (1–2 nm long) embedded in the carbon network. Furthermore, the existence of BN sp^2 bonds is confirmed by the fine structure of the B–K and N–K edges (Fig. 5.16c), which are very similar to those encountered in pure BN tubes (Fig. 5.16). The BN entities measure a few square nanometer and replace not more than 5 at.% in average within a given rope, as attested by a close comparison of intensities of C–K edges in the pure carbon parts of the tube and in the BN-containing parts (Fig. 5.16). This particular microstructure is expected to result from the phase separation existing at equilibrium in bulk systems between h-BN and graphite. Furthermore, N was found to be in excess with respect to B, as a testimony to the fact that the C–B bond is energetically less favorable than the C–N bond. Therefore, BN domains are expected to be surrounded by a nitrogen shell in order to minimize C–B bond numbers [62]. This property of the bulk B–N–C system explains why the BN–C segregation is not restricted to the tubes obtained by the laser vaporization technique but has been also

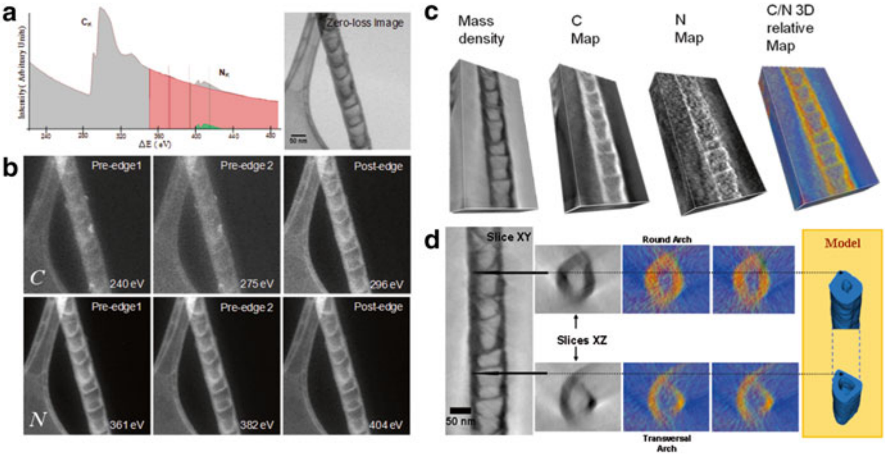

Fig. 5.15 (**a**) Mean EELS spectrum taken on the studied area of the N-doped carbon nanotube. The presence of two types of arches (i.e., transversal and rounded ones), which is typical for the highly nitrogen-doped C-NTs, can be observed. (**b**) The series of seven images acquired at the 0° tilt angle: zero-loss image, three energy-filtered images (generally called "pre-edge 1," "pre-edge 2," and "post-edge") at the C–K edge, and three corresponding to the N–K edge. (**c**) Typical longitudinal slices extracted at the same depth and orientation from the shape-sensitive reconstruction (*left*), C and N 3D elemental maps (*middle*), and C-to-N 3D relative map (*right*). The last one was obtained by superimposing the two elemental 3D maps with different colors, nitrogen in *green* and carbon in *red*. Note that the two types of arches are present within the analyzed area. (**d**) Combined morphological and chemical analysis of the highly doped N-CNT in cross section. *Left*: Longitudinal slice extracted from the mean-density (ZL) tomographic reconstruction, which contains the longitudinal axis of the tube. *Middle*: Two transversal sections through the 3D mean-density and chemical relative (C-to-N) reconstructions, extracted at the positions indicated by the two *arrows*. *Right*: Cross-sectional views by the 3D model of the analyzed tube, which illustrate better its morphology at the considered positions. Reproduced with permission of Florea et al. [61]. Copyright American Chemical Society

found in several (B–C–N)-MWNTs synthesized by different techniques. In addition, one cannot exclude the existence of segregation at a nanometer scale resembling that found in the laser-made tubes [62]. This example highlights the difficulty of faithfully identifying a heteroatomic tube structure. More recently, Ci et al. have synthesized large-area atomic layers of h-BNC material, consisting of hybridized, randomly distributed domains of h-BN and C phases with compositions ranging from pure BN to pure graphene [63]. However, there is not yet any atomically resolved experiment showing the atomic distribution.

In summary, these studies elucidated crucial questions concerning the nature of the boron/nitrogen atomic configuration of heteroatomic nanostructures. In fact, this detailed knowledge of how such atoms are incorporated into the carbon lattice as well as the precise control of their incorporation is required for the use of these nano-objects in future technological applications.

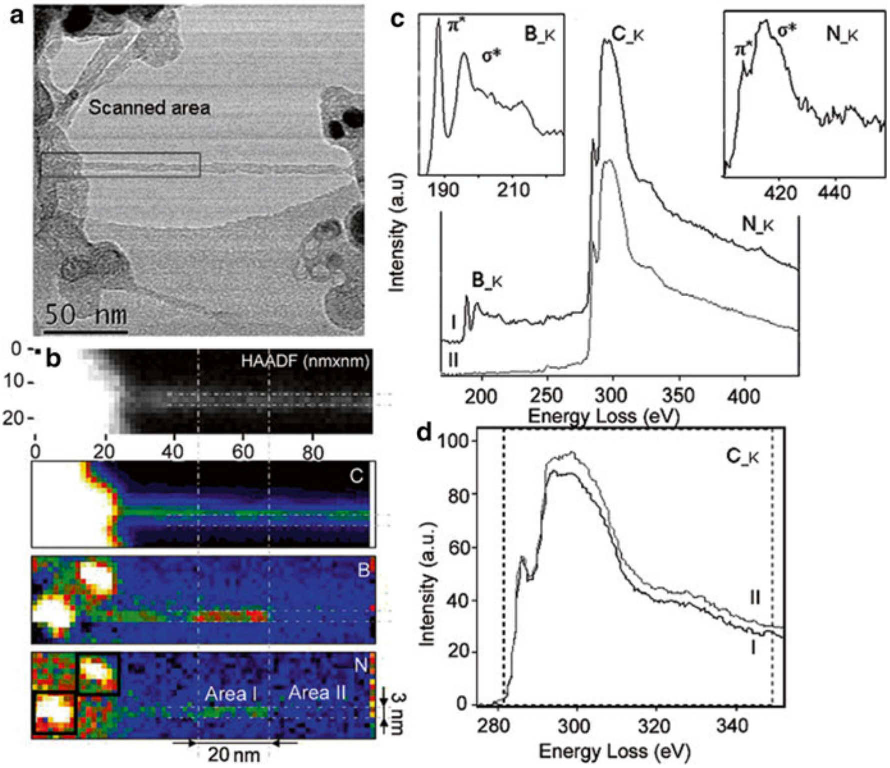

Fig. 5.16 (**a**) Bright-field image of nanotube rope of 4–5 nm. The *rectangle* shows the region analyzed by EELS. (**b**) HAADF image of the scanned area of 98 × 24 nm^2 and the relative intensity chemical maps of C, B, and N. The intensity of the signal varies from *dark/blue* (poor signal) to *white/red* (high signal) colors. (**c**) EEL spectra I and II are defined as the sum of the sum of areas I and II, respectively. Near-edge fine structures of B and N–K edges are shown in the *inset*. (**d**) Background-subtracted C–K edges of areas I and II. Reprinted from Enouz et al. [62], with permission from the American Chemical Society

5.4 Physical Properties of CB-RNM via TEM Techniques

The study of the local optical and electronic properties of materials can be developed via different techniques such as optical spectroscopy (emission or absorption), scanning tunneling spectroscopy (STS), cathodoluminescence, or EELS experiments. In this chapter we will focus on the techniques implemented in a TEM, namely, EELS and cathodoluminescence.

As mentioned above, the study of the low-loss energy region (below 50 eV) of an EELS spectrum provides direct access to the dielectric/optical/electronic properties of a material. In particular, intra-/inter-band transitions and collective oscillations of the electron gas (plasmons) can be probed. Furthermore, in the particular case where a TEM is used, sub-nanometer (even atomic) spatial resolution can be reached, which is a clear advantage as compared to optical techniques. In addition, there are two significant advantages in performing EELS measurements in comparison with the scanning transmission microscopy (STM) technique: (a) in EELS, the probed spectral region/range can spread over several hundreds of eV, and (b) if EELS measurements are developed in a TEM, no sample support is needed, avoiding any undesirable effect on the measurements.

5.4.1 Surface Plasmons in Carbon Nanotubes

Several studies have been developed on carbon nanotubes and carbon onions showing the response of the different plasmon modes as a function of the impact parameter (finite distance between the NT and the electron beam), the number of walls, the diameter value, etc. The classical continuum dielectric model was used for the interpretation of these results [64–66], taking into account the local anisotropic character of these nanostructures. This model is based on a strong hypothesis: locally the dielectric properties of a nano-object can be described by the macroscopic dielectric tensor of the related anisotropic bulk material (graphite (h-BN) in the case of C-(BN-)NTs). One of the main results is the evidence of surface-plasmon coupling between the internal and the external surfaces of these hollow nano-objects, also clearly identified in WS_2 analogs [67], and the dispersion of these surface-plasmon-mode energies as a function of the ratio of the external to the internal diameter. For thin C-MWNTs, two polarization modes have been identified at 15 and 19 eV, indexed as tangential and radial surface-plasmon modes, respectively, and resulting from this surface coupling [65]. Interestingly, the dielectric response of a C-SWNT, displaying a single energy mode at 15 eV, can be understood in the dielectric model as the thin layer limit of surface-plasmon excitation of C-MWNTs [65]. The spectroscopic signatures in the 4–25 eV range are gathered in Fig. 5.17 for several thin C-MWNTs down to the monolayer. The spectra were acquired in the so-called aloof (or near-field) geometry where the beam is focused outside the nano-object in order to isolate the surface-plasmon response of the nanotube. For thin nanotubes (typically six layers), a π plasmon is seen at 5 eV and both tangential and radial σ surface modes are clearly seen at 15 eV and 19 eV, respectively. Moreover, it has been shown [66] that the energy loss suffered by the incident electron is proportional to the imaginary part of the polarizability and can be written as a function of $\mathrm{Im}(\varepsilon(\perp) - 1/\varepsilon(//))$ where $\varepsilon(\perp)$ and $\varepsilon(//)$ are, respectively, the in-plane and out-of-plane components of the dielectric tensor of graphite. For a C-SWNT the 19 eV mode disappears, as a C-SWNT cannot sustain any radial mode. Therefore, the remaining spectral features coincide with resonances in the imaginary part of the in-plane component of the dielectric function of graphite $\mathrm{Im}(\varepsilon(\perp))$. Interestingly, strong similarities were later observed with the dielectric response of graphene [68, 69].

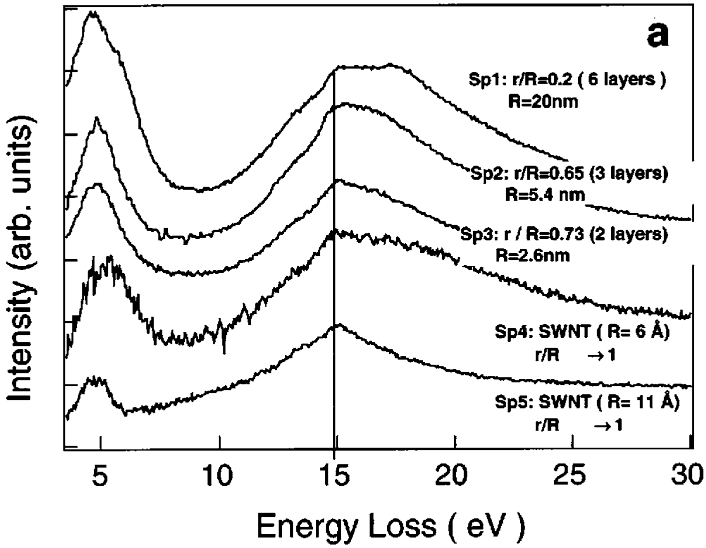

Fig. 5.17 Experimental EELS spectra recorded at grazing incidence on C nanotubes with different *r*/*R* ratios and number of layers [66]

5.4.2 *Optical Gap from Individual BN-SWNTs*

Since the discovery of BN-NTs, several groups have performed low-loss TEM-EELS measurements in these materials. Terauchi et al. [70] analyzed BN-MWNTs and a BN cone-structure material synthesized by arc discharge, as well as h-BN. These works were developed using a conventional TEM with a high-energy-resolution EELS spectrometer. They combined those studies with XES measurements. They found that the π and $\pi+\sigma$ plasmon energies of BN-NTs were smaller than those of h-BN. However, as they used a conventional TEM, the probe area was much larger than the investigated structure, precluding the discrimination between surface and bulk effects or identifying anisotropy effects. Kociak et al. also worked on BN-MWNTs produced by arc discharge using STEM [71]. As we have seen, this experimental technique provides the unique ability of disentangling and identifying the different excitation modes of a nano-object. These modes were accurately described by a classical continuum dielectric model and were directly related to the in-plane and out-of-plane components of the dielectric tensor. Moreau and Cheynet also studied bamboo-like BN-MWNTs (having diameters >40 nm) produced by CVD using a TEM [72]. The recorded spectra on these objects were compared to those of h-BN calculated using a full potential linearized augmented plane wave method (FLAPW) and within the LDA. More recently, the electromagnetic response of single-walled BN-NTs (individual tubes and ropes synthesized using the laser vaporization technique [44]) has been studied by spatially resolved

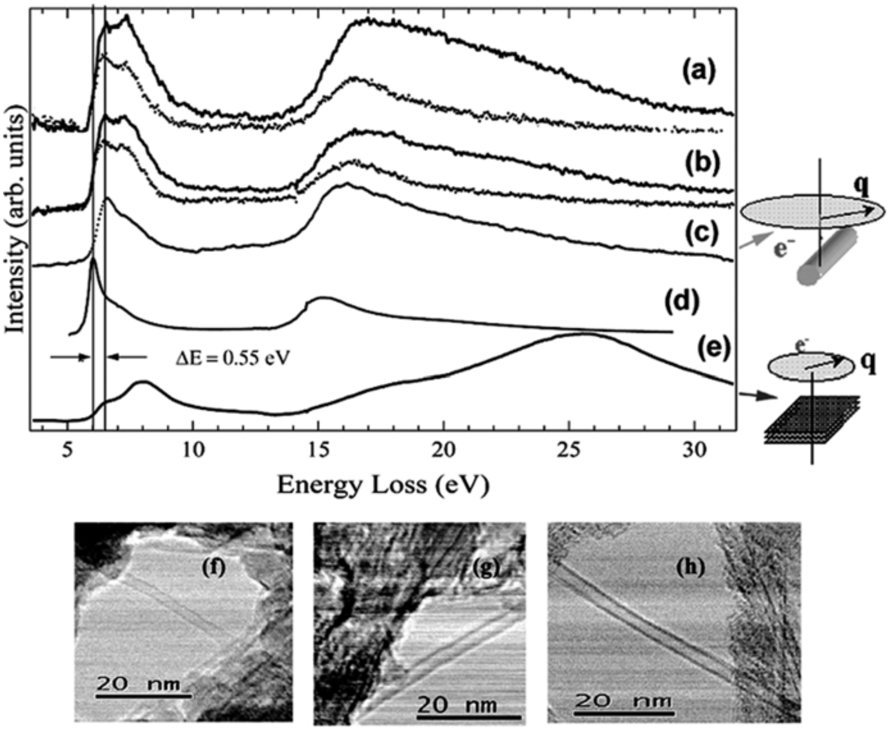

Fig. 5.18 (**a**) From *top* to *bottom*: Experimental deconvoluted spectra for (**a**) a TWNT inside the tube and at grazing incidence, (**b**) a DWNT inside the tube and at grazing incidence, (**c**) a SWNT in the rastered mode, and (**d**) Im($\varepsilon(\perp)$) as extracted from the bulk energy-loss spectra in (**e**). (**f**–**h**) Bright-field images of the tubes (**a**–**c**). Adapted from Arenal et al. [73]

EELS [73, 74]. In order to disentangle the inelastic signal at low energy from the tail of the very intense zero-loss peak (ZLP), a deconvolution procedure was applied in combination with a subtraction operation on the ZLP [74, 75]. All these results were interpreted using the classical continuum dielectric theory [66]. Figure 5.18 shows a collection of spectra acquired on different nanotubes, either in the rastered mode over a SWNT (2.2 nm in diameter) or using a probe fixed either at grazing incidence or over the tubes for a double-walled nanotube (DWNT) and a triple-walled NT (TWNT) (2.8 and 3 nm external diameter, respectively). As already mentioned for C nanotubes [66], at grazing incidence (in a geometry called "aloof geometry") and for a small number of layers, the energy loss suffered by the incident electron can be written as a function of Im($\varepsilon(\perp) - 1/\varepsilon(//)$) where $\varepsilon(\perp)$ and $\varepsilon(//)$ are, respectively, the in-plane and out-of-plane components of the dielectric tensor of a planar h-BN sheet [73, 74]. For comparison, Fig. 5.18d shows the imaginary part of the dielectric function of h-BN for an orientation in which the momentum transfer is perpendicular to the **c** axis. This was obtained after a Kramers–Kronig analysis of an EEL spectrum acquired in a high-purity thin foil of h-BN (Fig. 5.18e).

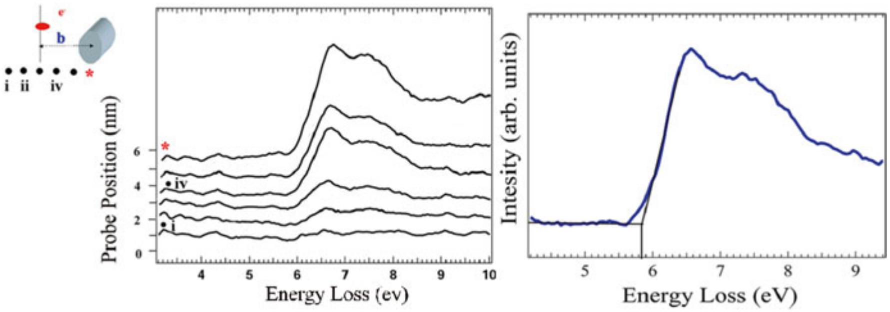

Fig. 5.19 (**a**) Spectrum line on a SW-BNNT. (**b**) Measurement of the optical gap of a BNNT from one of the spectra extracted the spectrum line of (**a**). Adapted from [73, 74]

This result is in agreement with the experimental dielectric constants obtained via EELS measurements by Tarrio and Schnatterly [76] and Vilanove [77]. We note the high similarity between the spectra corresponding to the NTs and $\mathrm{Im}(\varepsilon(\perp))$ of h-BN. This suggests that in the case of a vanishing number of layers, the different modes of the NTs' spectra can mainly be attributed to the $\mathrm{Im}(\varepsilon(\perp))$ contribution in the dielectric response of the tubes (confirming the previous results on C-SWNTs [66]).

Figure 5.19a displays a series of deconvoluted spectra going from the vacuum to the center of a BN-SWNT. As the onset of the spectrum mainly reflects the contribution of $\mathrm{Im}(\varepsilon(\perp))$, one can deduce the value of the optical gap (Fig. 5.19). A homogeneous value of around 5.80 ± 0.2 eV was found for all investigated BN-SWNTs, independent of the number of walls or tube diameters, as theoretically predicted by Blase et al. [78], and contrary to what is found for C-SWNTs where the optical gap depends on diameter and helicity (folding direction of the h-BN layer).

5.4.3 Excitonic Properties of Layered BN

The investigation of optical gaps and more specifically of excitonic energies can be performed much more accurately by cathodoluminescence. In this technique, the photons emitted by the sample primarily excited by an electron beam are collected and analyzed by an optical spectrometer. When performed in a STEM, the emission properties of a sample can be explored with unprecedented spatial resolution and compared with the absorption properties as measured by EELS. Very recently, the complex emission spectrum of h-BN flakes has been interpreted in relation with local changes in the layer-stacking order of h-BN. Together with the free excitonic emission at 5.75 eV (Frenkel exciton) for h-BN (observed at 5.80 ± 0.2 eV by EELS in BN nanotubes, see above), additional excitons were observed at individual folds occurring in the flakes. Figures 5.20a, b show bright-field and HAADF images synchronously acquired with a spectrum image (9×10^4 spectra obtained while

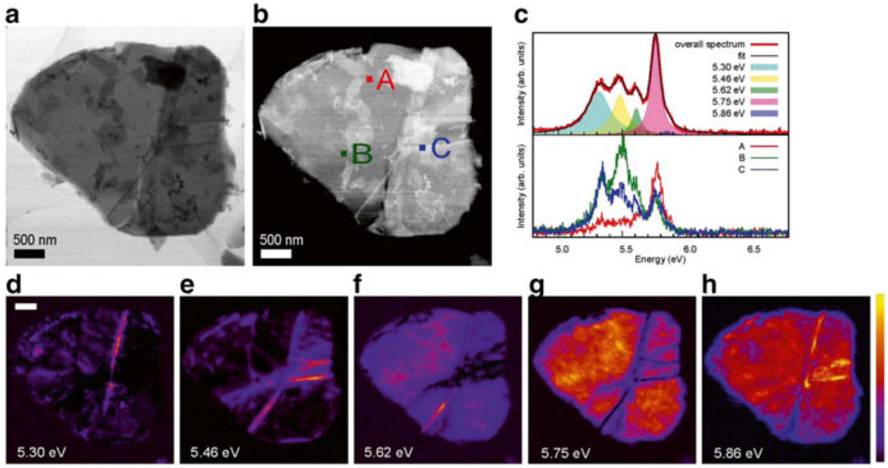

Fig. 5.20 (**a**) Bright-field and (**b**) dark-field images of an individual BN flake. (**c**) Overall emission spectrum of the flake and individual spectra taken at specific probe positions indicated in panel (**b**). (**d**–**h**) Emission maps for individual emission peak. Intensity is normalized independently within each individual map. Reproduced from R. Bourrellier et al. [84]. Copyright American Chemical Society

scanning the sample). A series of five emission lines at 5.30, 5.46, 5.62, 5.75, and 5.86 eV are clearly visible in the overall cathodoluminescence spectrum of the nanoparticle (Fig. 5.20c). These energies correspond to previously reported values for h-BN crystals and multiwalled BN nanotubes [79, 80]. As clearly observed in Fig. 5.20c, the emission maps associated with each of the excitonic energies are clearly not correlated with each other, and thus, all five emission features should be considered independent. The additional emissions can be interpreted as the consequence of the loss at the folds of the original AA′ stacking sequence of the perfect h-BN crystal. The characteristic energy values can be associated with specific stacking orders resulting from specific glides and rotations of the basal planes at the facets of the folds [80]. Such a faceting effect is similar to what is observed for large BN-MWNTs, which tend to display polygonal sections with facets of well-defined stacking, not necessarily AA′ [81–83].

5.4.4 Single-Photon Emitters in Nanodiamonds

Another very interesting STEM cathodoluminescence study is the recent work of Tizei and Kociak [85]. They have measured the response of N–V centers and reported on the experimental demonstration of single-photon state generation and characterization in an electron microscope. More specifically, they have used the fast electron beam of a STEM (operated at 60 and 100 keV) focused in a 1-nm-wide

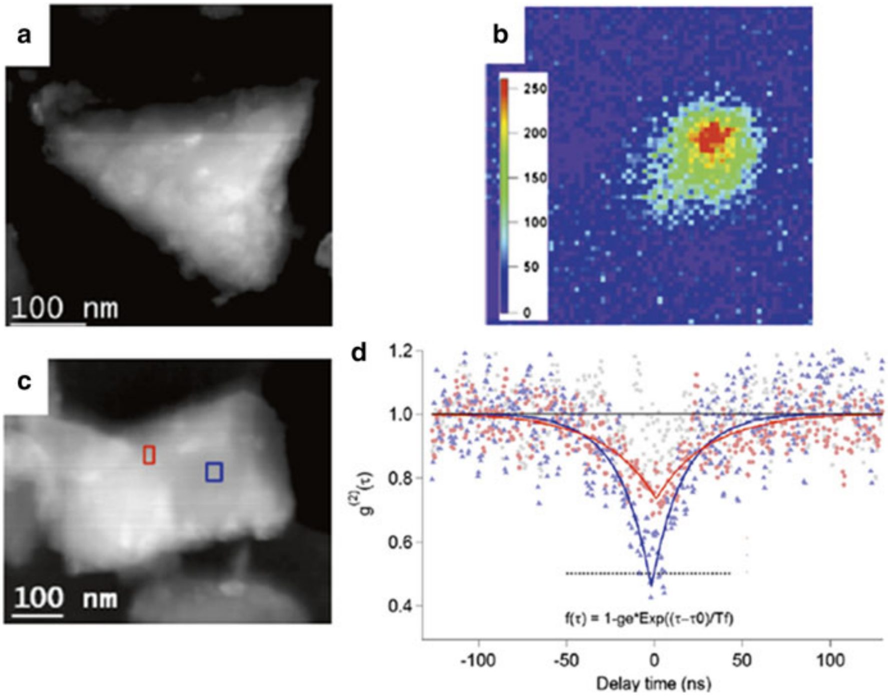

Fig. 5.21 (**a**) HAADF-STEM image of a NCD. (**b**) Cathodoluminescence intensity image extracted from a spectrum image acquired around the emission peak of the N–V^0 center emission of the same nanodiamond. (**c**) HAADF image of another ND particle. (**d**) Correlation functions of the emission of the two colored areas (*red* and *blue*) of (**c**) showing a change in the quantum state of the emitted light at sub-wavelength scale. For comparison, the data for classical light emission from another ND particle is shown in *gray*. Adapted from Tizei and Kociak [85, 87]

probe to excite neutral (NV^0) centers in diamond nanoparticles. This triggered the emission of photons which could be gathered and sent to a Hanbury Brown and Twiss (HBT) intensity interferometer [86]. Figure 5.21a shows an HAADF image of a diamond nanoparticle. The cathodoluminescence intensity map extracted from a SPIM acquired on the same nanodiamond in the spectral range of the N–V^0 center emission line is shown in Fig. 5.21b evidencing the presence of such defects. The emission characteristics of another nanodiamond are shown in Fig. 5.21d. The ad hoc correlation function (so-called g^2) of the emission from the two colored areas (red and blue) on this nanodiamond (see Fig. 5.21c) as obtained from the HBT interferometer is shown. The displayed correlation function clearly shows a dip for both colored areas, which was interpreted as the signature for the creation of non-classical light states at the sub-wavelength scale. Indeed, in the case of a nonclassical light source such as a single-photon emitter (SPS), the probability of detecting two simultaneous photon emissions is zero, independently of the exciting probe statistics. This quantum effect is called photon anti-bunching [87]. The detection of a dip in the g^2 correlation function at small time delays clearly demonstrates anti-bunching and therefore single-photon-state detection. The use of an extremely small electron probe size and the ability to monitor its position with sub-nanometer resolution represent a new approach to the generation of single-photon states, which could be applied to the study of electron-photon entanglement, as proposed recently [88].

5.4.5 *Prospects in Spatially Resolved Vibrational Spectroscopy with EELS*

Sub-20 meV resolution in spectra acquired for >1 s has recently been demonstrated in a newly designed monochromated EELS-dedicated STEM. Crucially, the extent of the ZLP tail has also been greatly reduced such that energy losses as small as 100 meV have been recorded, while permitting very high spatial resolution (a few Å) [89]. Thus, taken together, these capabilities promise that signals not accessible in electron microscopy so far are about to become available. In particular phonon spectroscopy becomes now possible. As an example, the optical phonons in h-BN and SiC at 175 meV and 106 meV, respectively, or vibrational peaks due to hydrogen in TiH_2 and in the epoxy resin at 147 meV and 360 meV, respectively, have been recorded [90]. The very rapid progress in this means that vibrational spectroscopy at the atomic scale may well become routine within a few years.

5.5 Conclusions and Prospects

Here we have presented a selection of works on carbon-based and related (pristine and heteroatomic) nanomaterials exploiting local spectroscopic TEM techniques. We have tried to illustrate how these spatially resolved techniques have become essential for investigating the chemical composition or the nature of the chemical bonding in these nanomaterials and for probing their optoelectronic properties at the nanometer scale and down to atomic scale. In particular, we have placed the emphasis on the new possibilities for single-atom detection by EELS, which nowadays cannot only map the spatial distribution of heteroatoms or dopants in nanostructures but also identify their electronic states and then their atomic configuration. This kind of analysis was not possible before, and it significantly helps to improve the knowledge of the growth, structure, and properties of these nanomaterials. EELS has also proved to be very powerful, when coupled with sophisticated data processing methods, for exploring the optical properties of nanostructures via the measurement of surface plasmons and optical gaps (and excitons) in C and BN nanostructures. With the democratization of monochromators in TEM, more developments are expected in the future in that direction. A major breakthrough has been the emergence of optical techniques in TEM. This convergence between photons and electrons provides an original and promising alternative to electron spectroscopies. In particular, we have shown here that cathodoluminescence has already demonstrated to be a powerful counterpart to photoluminescence for detecting point or extended defect signatures or to address new issues in quantum nano-optics in C and BN nanostructures. More instrumental progress is still to come. Recent developments in monochromators have yielded 10 meV energy resolution in EELS, with the promise of even better figures, suggesting that vibrational spectroscopy at the atomic scale will be available very soon. New horizons are also to be explored in the realm of time-resolved experiments. In particular, time resolution at the nanometer scale is yet to be performed routinely, following the impressive and encouraging first steps in this direction [91–93]. For sure, this extraordinary portfolio of techniques gathered within the same instrument for seeing individual atoms, identifying them, and measuring their electronic and optical spectra will lead in the near future to unique and exciting experiments on emerging new 2D materials and related nanostructures.

Acknowledgments We acknowledge the support received from the European Union Seventh Framework Programme under Grant Agreement 312483—ESTEEM2 (Integrated Infrastructure Initiative—I3). R.A. acknowledges funding from the Spanish Ministerio de Economia y Competitividad (FIS2013-46159-C3-3-P) and from the European Commission under Graphene Flagship (contract no. CNECT-ICT-604391). O.S. acknowledges the support from the National Agency for Research under the program of future investment TEMPOS–CHROMATEM with Reference No. ANR-10-EQPX-50.

References

1. M. Dresselhaus, G. Dresselhaus, P. Avouris, *Carbon Nanotubes: Synthesis, Structure, Properties, and Applications* (Springer, Berlin, 2001)
2. A. Loiseau et al., *Understanding Carbon Nanotubes*. Lectures Notes in Physics (Springer, Berlin, 2006)
3. Y.K. Yap (ed.), *B-C-N Nanotubes and Related Nanostructures* (Springer, New York, 2008)
4. O. Shenderova, D.M. Gruen, *Ultrananocrystalline Diamond: Synthesis, Properties, and Applications* (William Andrew, Norwich, 2006)
5. R. Arenal, X. Blase, A. Loiseau, Adv. Phys. **59**, 101 (2010)
6. P. Ayala, R. Arenal, A. Loiseau, A. Rubio, T. Pichler, Rev. Mod. Phys. **82**, 1843–1885 (2010)
7. P. Ayala, R. Arenal, M. Rummeli, A. Rubio, T. Pichler, Carbon **48**, 575 (2010)
8. H.W. Kroto, J.R. Heath, S.C. O'Brien, R.F. Curl, R.E. Smalley, Nature **318**, 162–163 (1985)
9. S. Iijima, Nature **354**, 56–58 (1991)
10. O. Shenderova, D.M. Gruen, *Ultrananocrystalline Diamond*, 2nd edn. (Elsevier, Amsterdam, 2012)
11. A.K. Geim, Science **324**, 1530 (2009)
12. O.A. Williams, Diam. Relat. Mater. **20**, 621–640 (2011)
13. C.P. Ewels, M. Glerup, J. Nanosci. Nanotechnol. **5**, 1345–1363 (2005)
14. R. Arenal, Adv. Phys. (2014)
15. S. Reich, C. Thomsen, J. Maultzsch, *Carbon Nanotubes: Basic Concepts and Physical Properties* (Wiley, Berlin, 2004)
16. M. Monthioux, V.L. Kuznetsov, Carbon **44**, 1621 (2006)
17. S. Iijima, T. Ichihashi, Nature **363**, 603–605 (1993)
18. K.S. Novoselov, A.K. Geim, S.V. Morozov, D. Jiang, Y. Zhang, S.V. Dubonos, I.V. Grigorieva, A.A. Firsov, Science **306**, 666–669 (2004)

19. A.K. Geim, K.S. Novoselov, Nat. Mater. **6**, 183–191 (2007)
20. P. Lammert, V. Crespi, A. Rubio, Phys. Rev. Lett. **87**, 136402 (2001)
21. S. Latil, S. Roche, D. Mayou, J.C. Charlier, Phys. Rev. Lett. **92**, 256805 (2004)
22. S. Latil, F. Triozon, S. Roche, Phys. Rev. Lett. **95**, 126802 (2005)
23. M. Haider, S. Uhlemann, E. Schwan, H. Rose, B. Kabius, K. Urban, Nature **392**, 768 (1998)
24. S.J. Pennycook, P.D. Nellist, *Scanning Transmission Electron Microscopy: Imaging and Analysis* (Springer, New York, 2011)
25. D.B. Williams, B. Carter, *Transmission Electron Microscopy*, 2nd edn. (Springer, New York, 2009)
26. L. Reimer, H. Kohl, *Transmission Electron Microscopy: Physics of Image Formation*, 5th edn. Series in Optical Sciences, vol 36 (Springer, New York, 2008)
27. R. Egerton, *Electron Energy-Loss Spectroscopy in the Electron Microscope*, 2nd edn. (Plenum, New York, 1996)
28. R. Brydson, *Aberration-Corrected Analytical Electron Microscopy* (Wiley, Chichester, 2011)
29. R.F. Egerton, Rep. Prog. Phys. **72**, 016502 (2009)
30. O.L. Krivanek, N. Dellby, A.R. Lupini, Ultramicroscopy **78**, 1–11 (1999)
31. C. Jeanguillaume, C. Colliex, Ultramicroscopy **28**, 252–257 (1989)
32. C. Colliex et al., Ultramicroscopy **123**, 80 (2012)
33. R. Arenal, F. de la Pena, O. Stephan, M. Walls, M. Tence, A. Loiseau, C. Colliex, Ultramicroscopy **109**, 32–38 (2008)
34. B. Schaffer, G. Kothleitner, W. Grogger, Ultramicroscopy **106**, 1129 (2006)
35. E.J. Kirkland, R.F. Loane, J. Silcox, Ultramicroscopy **23**, 77 (1987)
36. S.J. Pennycook, D.E. Jesson, Ultramicroscopy **37**, 14 (1991)
37. O.L. Krivanek, M.F. Chisholm, V. Nicolosi, T.J. Pennycook, G.J. Corbin, N. Dellby, M.F. Murfitt, C.S. Own, Z.S. Szilagyi, M.P. Oxley, S.T. Pantelides, S.J. Pennycook, Nature **464**, 571 (2010)
38. Z. He, K. He, A.W. Robertson, A.I. Kirkland, D. Kim, J. Ihm, E. Yoon, G.D. Lee, J.H. Warner, Nano Lett. **14**, 3766 (2014)
39. K. Suenaga, M. Tence, C. Mory, C. Colliex, H. Kato, H. Shinohara, K. Hirahara, S. Bandow, S. Iijima, Science **290**, 2280–2282 (2000)
40. K. Suenaga, Y. Sato, Z. Liu, H. Kataura, T. Okazaki, K. Kimoto, H. Sawada, T. Sasaki, K. Omoto, T. Tomita, T. Kaneyama, Y. Kondo, Nat. Chem. **1**, 415–418 (2009)
41. K. Suenaga, M. Koshino, Nature **468**, 1088 (2012)
42. N. Alem, Q.M. Ramasse, C.R. Seabourne, O.V. Yazyev, K. Erickson, M.C. Sarahan, C. Kisielowski, A.J. Scott, S.G. Louie, A. Zettl, Phys. Rev. Lett. **109**, 205502 (2012)
43. R. Arenal, M. Kociak, N.J. Zaluzec, Appl. Phys. Lett. **90**, 204105 (2007)
44. R. Arenal, O. Stephan, J.L. Cochon, A. Loiseau, J. Am. Chem. Soc. **129**, 16183 (2007)
45. S. Turner, Y.-G. Lu, S.D. Janssens, F. Da Pieve, D. Lamoen, J. Verbeeck, K. Haenen, P. Wagner, G. Van Tendeloo, Nanoscale **4**, 5960 (2012)
46. S. Turner, O.I. Lebedev, O.A. Shenderova, I.I. Vlasov, J. Verbeeck, G. Van Tendeloo, Adv. Funct. Mater. **19**, 2116–2124 (2009)
47. V. Pichot, O. Stephan, M. Comet, E. Fousson, J. Mory, K. March, D. Spitzer, J. Phys. Chem. C **114**, 10082–10087 (2010)
48. S. Trasobares, S.P. Gao, O. Stephan, A. Gloter, C. Colliex, J. Zhu, Chem. Phys. Lett. **352**, 12–19 (2002)
49. H.K. Schmid, Microsc. Microanal. Microstruct. **6**, 99 (1995)
50. J. Birrell, J.A. Carlisle, O. Auciello, D.M. Gruen, J.M. Gibson, Appl. Phys. Lett. **81**, 2235 (2002)
51. R. Arenal, P. Bruno, D.J. Miller, M. Bleuel, J. Lal, D.M. Gruen, Phys. Rev. B. **75**, 195431 (2007)
52. I.I. Vlasov, O. Lebedev, V.G. Ralchenko, E. Goovaerts, G. Bertoni, G. Van Tendeloo, V.I. Konov, Adv. Mater. **19**, 4058–4062 (2007)
53. R. Arenal, O. Stephan, P. Bruno, D.M. Gruen, Appl. Phys. Lett. **94**, 111905 (2009)

54. H. Lin, R. Arenal, S. Enouz, O. Stephan, A. Loiseau, J. Phys. Chem. C **113**, 9509 (2009)
55. H. Lin et al., C. R. Phys. **12**, 909–920 (2011)
56. T. Susi et al., ACS Nano **6**, 8837–8846 (2012)
57. C.P. Ewels, D. Erbahar, P. Wagner, X. Rocquefelte, R. Arenal, P. Pochet, M. Rayson, M. Scardamaglia, C. Bittencourt, P. Briddon, Faraday Discuss. (2014)
58. R. Arenal, K. March, C.P. Ewels, X. Rocquefelte, M. Kociak, A. Loiseau, O. Stephan, Nano Lett. **14**, 5509–5516 (2014)
59. U. Bangert, W. Pierce, D.M. Kepaptsoglou, Q.M. Ramasse, R. Zan, M. Gass, J.A. Van Den Berg, C. Boothroyd, J. Amani, H.C. Hofsaess, Nano Lett. **13**, 4902–4907 (2013)
60. Q.M. Ramasse, C.R. Seabourne, D.-M. Kepaptsoglou, R. Zan, U. Bangert, A.J. Scott, Nano Lett. **13**, 4989–4995 (2013)
61. I. Florea, O. Ersen, R. Arenal, D. Ihiawakrim, C. Messaoudi, K. Chizar, I. Janowska, C. Pham-Huu, J. Am. Chem. Soc. **134**, 9672–9680 (2012)
62. S. Enouz, O. Stephan, J.L. Cochon, C. Colliex, A. Loiseau, Nano Lett. **7**, 1856 (2007)
63. L. Ci, L. Song, C. Jin, D. Jariwala, D. Wu, Y. Li, A. Srivastava, Z.F. Wang, K. Storr, L. Balicas, F. Liu, P.M. Ajayan, Nat. Mater. **9**, 430 (2010)
64. T. Stockli, J.-M. Bonard, A. Chatelain, Z.L. Wang, P. Stadelmann, Phys. Rev. B **57**, 15599 (1998)
65. M. Kociak, L. Henrard, O. Stéphan, K. Suénaga, C. Colliex, Phys. Rev. B **61**, 13936 (2000)
66. O. Stéphan, D. Taverna, M. Kociak, L. Henrard, K. Suenaga, C. Colliex, Phys. Rev. B **66**, 155422 (2002)
67. M. Kociak, O. Stéphan, L. Henrard, V. Charbois, A. Rotschild, R. Tenne, C. Colliex, Phys. Rev. Lett. **87**, 075501 (2001)
68. T. Eberlein, U. Bangert, R.R. Nair, R. Jones, M. Gass, A.L. Bleloch, K.S. Novoselov, A. Geim, P.R. Briddon, Phys. Rev. B **77**, 233406 (2008)
69. M.H. Gass, U. Bangert, A.L. Bleloch, P. Wang, R.R. Nair, A.K. Geim, Nat. Nanotechnol. **3**, 676 (2008)
70. M. Terauchi, M. Tanaka, K. Suzuki, A. Ogino, K. Kimura, Chem. Phys. Lett. **324**, 359 (2000)
71. M. Kociak, L. Henrard, O. Stephan, K. Suenaga, C. Colliex, Phys. Rev. B **61**, 13936 (2001)
72. P. Moreau, M.C. Cheynet, Ultramicroscopy **94**, 293 (2003)
73. R. Arenal, O. Stephan, M. Kociak, D. Taverna, A. Loiseau, C. Colliex, Phys. Rev. Lett. **95**, 127601 (2005)
74. R. Arenal, O. Stephan, M. Kociak, D. Taverna, A. Loiseau, C. Colliex, Microsc. Microanal. **14**, 274 (2008)
75. A. Gloter, A. Douiri, M. Tence, C. Colliex, Ultramicroscopy **96**, 385 (2003)
76. C. Tarrio, S.E. Schnatterly, Phys. Rev. B **40**, 7852 (1989)
77. R. Vilanove, C. R. Acad. Sci. Paris **272**, 1066 (1971)
78. X. Blase, A. Rubio, S.G. Louie, M.L. Cohen, Europhys. Lett. **28**, 335 (1994)
79. P. Jaffrennou, J. Barjon, T. Schmid, L. Museur, A. Kanaev, J.-S. Lauret, C.Y. Zhi, C. Tang, Y. Bando, D. Golberg, B. Attal-Tretout, F. Ducastelle, A. Loiseau, Phys. Rev. B **77**, 235422 (2008)
80. K. Watanabe, T. Taniguchi, Phys. Rev. B **79**, 193104 (2009)
81. A. Celik-Aktas, J.-M. Zuo, J.F. Stubbins, C. Tang, Y. Bando, Acta Cryst. **A61**, 533–541 (2005)
82. K. Tibbetts, R. Doe, G. Ceder, Phys. Rev. B **80**, 014102 (2009)
83. D. Golberg, M. Mitome, Y. Bando, C. Tang, C. Zhi, Multi-walled boron nitride nanotubes composed of diverse cross-section and helix type shells. Appl. Phys. Mater. Sci. Process. **88**, 347–352 (2007)
84. R. Bourrellier, M. Amato, L.H.G. Tizei, C. Giorgetti, A. Gloter, M.I. Heggie, K. March, O. Stephan, L. Reining, M. Kociak, A. Zobelli, ACS Photonics **1**, 857–862 (2014)
85. L.H.G. Tizei, M. Kociak, Nanotechnology **23**, 175702 (2012)
86. B.R. Hanbury, R.Q. Twiss, Nature **178**, 1046 (1956)
87. L.H.G. Tizei, M. Kociak, Phys. Rev. Lett. **110**, 153604 (2013)
88. X. Bendaña, A. Polman, F.J. Garcia de Abajo, Nano Lett. **11**, 5099 (2011)

89. O. Krivanek et al., Microsc. Microanal. **20**, 66–67 (2014)
90. O.L. Krivanek, T.C. Lovejoy, N. Dellby, T. Aoki, R.W. Carpenter, P. Rez, E. Soignard, J. Zhu, P.E. Batson, M.J. Lagos, R.F. Egerton, P.A. Crozier, Nature **514**, 209 (2014)
91. M. Merano, S. Sonderegger, A. Crottini, S. Collin, P. Renucci, E. Pelucchi, A. Malko, M.H. Baier, E. Kapon, B. Deveaud, J.D. Ganiere, Nature **438**, 479–482 (2005)
92. F. Carbone, B. Barwick, O.-H. Kwon, H.S. Park, J.S. Baskin, A.H. Zewail, Chem. Phys. Lett. **468**, 107 (2009)
93. F. Carbone, O.-H. Kwon, A.H. Zewail, Science **325**, 181 (2009)

Chapter 6
3D Nanometric Analyses via Electron Tomography: Application to Nanomaterials

Simona Moldovan, Raul Arenal, and Ovidiu Ersen

6.1 Introduction to 3D Imaging

In the last few years, the 3D exploration of the nanoworld has gained growing attention in the field of material science research, as a full knowledge of the morphology, structure and composition of nano-objects requires to be acquired in three dimensions. Numerous scientific and technological efforts have been devoted to the synthesis of nano-objects and/or nanostructured materials for conceiving new systems and components making use of nanomaterials with characteristics adapted for applications in various fields: electronics, catalysis, biotechnology, medicine, etc. In addition, more fundamental developments in material science research such as spintronics or plasmonics should be taken into account as major points for the development of complex nano-systems and/or nanocomposites. One of the main interests of developing nanomaterials originates in the necessity of synthesising materials with enhanced surface areas with respect to the bulk, as demanded for various applications. Ultimately, the close control of the structural, morphological and chemical characteristics of nanomaterials is imperative as they define and control the final system properties. The continuous requirement for qualitative and quantitative analysis of complex nanomaterials has made the material research community turn its attention towards techniques allowing the investigation of small volumes. Obviously to reach all these goals, synergy between synthesis, characterisation and final

---

S. Moldovan • O. Ersen (✉)
Institut de Physique et Chimie des Matériaux de Strasbourg (IPCMS),
UMR 7504 CNRS, 23 Rue du Loess, Strasbourg 67037, France
e-mail: ersen@ipcms.unistra.fr

R. Arenal
Advanced Microscopy Laboratory, Nanoscience Institute of Aragon,
University of Zaragoza, 50018 Zaragoza, Spain

ARAID Foundation, 50018 Zaragoza, Spain

F.L. Deepak et al. (eds.), *Advanced Transmission Electron Microscopy*,
DOI 10.1007/978-3-319-15177-9_6

properties should be reached. In this general context, there is a need for state-of-the art techniques for assessing material characteristics at the nanoscale such as active specific areas or porosities and therefore qualifying structures and three-dimensional space relationship. We describe here the 3D characterisation methods based on electron tomography when developed in an electron transmission microscope, which allow the performance of qualitative and quantitative 3D analyses with a nanometric (even atomic) spatial resolution.

6.2 3D Characterisation Techniques: Electron Tomography, Atom Probe Tomography, FIB and Confocal Microscopy

Experimental techniques such as X-ray reflectivity, spectroscopic ellipsometry, small-angle X-ray scattering [SAXS or grazing incidence SAXS (GISAXS)] are widely employed to reveal the physical and chemical characteristics of materials in terms of structure, morphology and/or chemical composition. These techniques have the big disadvantage to furnish information only on the averaged volumes of the samples of interest and not on individual features. This drawback can be overcome by using near-field imaging techniques such as scanning tunnelling microscopy (STM), atomic force microscopy (AFM) or TEM, which are finely adapted for accessing information at the atomic level. The capabilities of probing very tiny surfaces with curvatures as small as possible situate the near-field and transmission electron microscopies on the other “extreme” of material characterisation. Another up-to-date technique for the 3D characterisation of materials is the atom probe tomography (APT). It allows for the achievement of the atomic resolution but can only explore very small volumes in a destructive manner and is not adapted for complex morphologies.

Before exploring deeper the electron tomography techniques, by highlighting their potentials, advantages and drawbacks, we will give a short overview of other methodologies currently available for the 3D analyses of materials, with resolutions ranging from micrometres down to nanometres. The X-rays attenuation when crossing a given material stands as the base principle of X-ray tomography. This attenuation strongly depends on the density of the material crossed by the incident ray and on the resolution attained of the order of micrometres or less when the experiments are carried out on synchrotrons. The confocal optical microscopy allows for the exploitation of volumes built up from slices acquired by optical microscopy with small depths of field. In the modern configurations, images are recorded by scanning the specimen using a laser beam and detecting the reflected or the fluorescence responses. After a scan, the next image is recorded deeper or higher from the specimen surface. This technique is well adapted for the 3D investigation of biological and/or soft materials, and it allows reaching a resolution down to 600 or even 200 nm. A more recent technique adapted for the study of hard materials is the APT. In principle, under the impact of a strong electric field, the atoms from the specimen surface evaporate one atomic layer after the other and their time of flight is measured. Finally, a mass-spectroscopy experiment is carried out allowing getting a chemically selective 3D mapping at the atom scale. As compared with electron tomography, the main advantage of the atom probe technique is that APT close to the atomic resolution, even for amorphous materials, can be obtained. However, the main drawback remains its permanent damaging character. In addition, the specimen preparation is not straightforward, owing to the geometry restrictions imposed by the technique itself: the samples need to be shaped needlelike and the regions to be analysed have to be representative of the whole sample.

The electron tomography-based techniques imply the use of the two different modes: the transmission and the scanning electron microscopies (SEM). In the scanning mode, there are two ways for acquiring 3D images: the acquisition of a "tilted" series of projections under a SEM and the SEM-focused ion beam (FIB) tomography. The "tilted" mode under SEM implies the use of a specific specimen holder and the analysis of a relative thick specimen, and one reaches resolutions ranging from a micrometre to several tens of nanometre. The SEM-FIB implies the use of a dual-beam machine: a SEM equipped with an FIB. In principle, an ion beam is used to cut the object slice by slice, and the series of micrographs are successively acquired under SEM either by using the signal of the secondary/backscattered electrons or the X-ray photons.

In transmission electron microscopy (TEM), one might use as well two different methodologies for the 3D analysis of objects: the first mode, single particle analysis, relies on the object observation by acquiring one or several images at a given orientation, without tilting the specimen. The assumption is made that on one micrograph alone one captures all the possible orientations of the object. A condition that needs to be imperatively fulfilled is that all objects must be identical and belong to specific morphological and structural classes. This type of tomography is well adapted for biological samples, when several copies of a biochemically homogenous specimen are available. It is thus frequently used for performing the reconstruction of specific molecules and viruses. Another possibility of 3D imaging by TEM tomography adaptable to all classes of nanomaterials and nano-objects implies acquiring a series of micrographs at different tilting angles, of a single specimen, and subsequent volume reconstruction and analysis.

In the present chapter, we will show that the electron tomography (or 3D-TEM) is an ideal tool that gives access to qualitative and quantitative information at the nanometre or even at the atomic level. When looking at a transparent and structured object, an observer does spontaneously rotate it in order to get a complete picture of the object. This idea stands as the principle of tomography: recording images at various given angles by employing the signal of some wave transmitted through the object of interest with a wavelength that limits the ultimate reachable resolution. Tomography generally uses light, sounds, neutrons, X-rays, etc. as probes as function of the size and the nature of the objects under investigation and information to inquest. In electron microscopy, the incident electrons with wavelengths in the picometre range are used as probe. They are therefore suitable for performing 3D imaging using the tomographic technique, with a nanometric resolution. When combined with chemical imaging (energy-filtered TEM), it gives access to the 3D chemical composition of nano-objects, which is a key issue for the subsequent analysis of the properties of interest.

6.3 Electron Tomography

Electron tomography is based on the recording of a series of projection images of an object rotated in the electron microscope for a well-defined number of incidence angles, in the range ±80° (or even 360º when a particular TEM holder is used). Each recorded image collects a projection in the observation plane of the quantity of interest: the mass or the chemical composition. In a second step, the Radon transformation [1] permits the construction of a 3D matrix, describing the sample in the real space. This is performed by the back-projection of the intensity of each corresponding pixel from the projections into a unique voxel of the matrix being constructed (Fig. 6.1).

Using the 3D voxel matrix constructed in this manner then allows to perform the quantitative or chemical analysis. A 3D imaging of the object of interest can be extracted from the matrix by recognising, through contrast measurements, the interface delimiting the vacuum and the matter in the case of shape-sensitive volumes. From this image, porosity, for example, can be quantitatively estimated with a nanometre-scale resolution as well as its distribution within the entire solid volume.

6.3.1 State of the Art

Electron tomography has been largely used in the second half of the last century as a powerful instrument for assessing the details of the morphology and the inner structures of living cells and molecular structures. The pioneering works of DeRosier and Klug [2] can be considered as the real starting points for the 3D imaging in electron microscopy. A brief history of the origin and the development of 3D

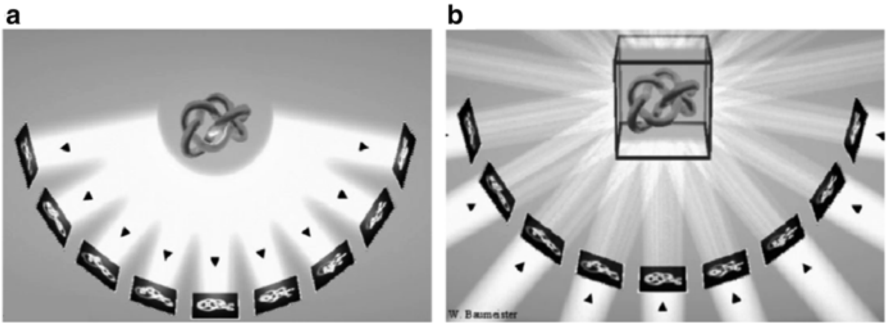

Fig. 6.1 Principle of electron tomography. (**a**) The projection: a set of projections recorded for a wide range of angles of rotation. (**b**) The back-projection: the intensity of each pixel from the projections is distributed along segments orthogonal to the recording plane. The summed intensity at the crossing point defines the intensity of one voxel within the reconstructed 3D object. Reprinted from Medalia et al. [4]

reconstruction methods is given in the Nobel Lecture of Klug in 1983 [3]. The work published by Medalia et al. [4] is still a reference as long as biological studies are referred to. The electron tomography has recently been more and more employed as an investigation method in the field of materials as the result of the high technological maturity of the electron microscopy techniques since the very beginning of the last century. Since soft materials and polymeric nanostructures are three-dimensional structures, electron tomography has been successfully applied in a quantitative manner at the mesoscale or with a sub-nanometric resolution as an ideal tool for their 3D characterisation. A large variety of polymeric structures such as block copolymers [5] or nanocomposite material [6] have been thus studied. From the inorganic material perspective, the teams conducted by de Jong (Utrecht University) and Midgley (Cambridge University) furnished pioneering works in the field of tomography at the nanoscale. In the early 2000s, the group of de Jong has performed for the first time a complete 3D investigation of a porous zeolite using TEM in the bright field (BF) mode [7]. More recently, even in the material field, the development and optimisation of experimental approaches based on the cryo-electron tomography have gained more and more attention [8]. By reducing the irradiation damages induced by the electron beam and thus the shrinkage effect of the analysed objects, these techniques allow for the 3D analysis of frozen-hydrated, vitrified biological materials and organic or hybrid materials with nanometric resolution [9]. In the case of hybrid organic–inorganic materials, a proper acquisition of tilt series can be performed either at low temperature on non-vitrified specimens or by using a low-dose mode for preserving the specimen structure during the total duration of the acquisition. However, as compared to the biological specimens, the method of single particle reconstruction (several digitised images of similar particles) does not seem to be appropriate for nanomaterials owing to the unicity of their geometrical and compositional characteristics.

Addressing the atomic structure of crystalline nanomaterials in three dimensions has been for long a challenge for electron tomography. While the detection performances have met the atomic resolution requirements in the latest years, probing nanoparticles under three dimentions and with atomic resolution has been possible only recently when new alignment protocols and reconstruction algorithms were developed. The very first testimony in this sense is brought forward by the work of Scott et al. [10], who proposed the mass-centre algorithm for the alignment of series resolved at the atom scale that were acquired on an Au nanoparticle having a diameter of 2 nm. The approach proposed for the volume reconstruction implies the use of a Fourier transform-based algorithm that allows for the achievement of atomic resolutions in 3D. The very same target but using different methods has been addressed to by using the combination of aberration-corrected TEM and of advanced reconstruction algorithms like simultaneous iterative reconstruction technique (SIRT), discrete algebraic reconstruction technique (DART), or the total variation minimisation (TVM) method. As we will see later, a high-level characterisation has been also achieved by combining analytical techniques as electron energy loss spectroscopy (EELS)-STEM [11, 12] and energy dispersive X-ray spectroscopy (EDS)-STEM [13] with electron tilt-series tomographic acquisitions.

6.3.2 Various Working Modes

Electron tomography (ET) under bright field transmission electron microscopy (BFTEM) is fast and easy to implement. Tomographic recording requires the image intensity to be characterised by a monotonic variation as a function of the signal of interest integrated along the thickness of the sample in each point. Signals of interest can be the mean density, the atomic number, the chemical nature or the plasmon resonances. This requirement is not fulfilled with crystalline materials, due to electron Bragg diffraction at specific recording angles of incidence. As a consequence, the use of BF-TEM in the field of materials has long been restricted to the study of amorphous materials at the atomic level, such as polymers or mesoporous structures [14–17].

For the 3D analysis of crystalline materials, the use of the annular dark field (ADF) imaging technique in the scanning TEM mode (STEM) constitutes an attractive alternative. For high collection angles in the ADF mode (HAADF), the contribution of Bragg-diffracted electrons diminishes strongly, and therefore, the recorded signal is predominantly incoherent, improving in this way the projection requirement for the tomography. This STEM-HAADF incoherent mode is also known as the Z-contrast 3D mode, since the contrast in the initial images depends mainly on the specimen thickness and scales with the local atomic number [18, 19]. For many situations, the 3D analytical information can indirectly be obtained through the dependence on the atomic number within the tomographic signal. However, the STEM-HAADF tomography is not efficient for materials with elements having close mean atomic numbers owing to the low contrast between them.

One of the most valuable methods to perform 3D chemical analytical mapping over a few hundred nanometres is to perform tomography in the energy-filtered TEM (EFTEM) mode [20]. This technique is one of the three different analytical techniques that can be implemented in a TEM. It is worth mentioning that the "analytical tomography" has an impressive potential since it combines the ability of conventional electron tomography to get 3D information at the nanoscale and the chemical selectivity of the EFTEM imaging. More specifically, it combines the tilt-series approach with the image acquisition in energy-filtered imaging mode. In principle, by carefully choosing the energy windows corresponding to the ionisation edges of the elements of interest, we are able to record chemically selective 2D images. This modus operandi is repeated for each tilt angle, and projection series of the spatial distribution of the elements are obtained in this way. They are further used to build up the 3D elemental map. Being rather difficult to operate under the tomography methodology [21, 22], this powerful method did not receive much attention in the field of material science up to now.

More recently another analytical TEM technique, EELS-SPIM tomography, has been developed [11, 12]. This technique consists of reconstructing the information extracted from EELS spectrum images (SPIM, images on which every pixel contains a full EEL spectrum, which has been recorded by scanning the electron beam at the surface of the nano-object) [23, 24] in 3D, by acquiring a series of EELS-SPIM at different tilt angles [12, 23].

Almost all electron microscopy modes that have been developed for the 2D imaging of samples can be adapted for the 3D investigation of nanomaterials. Obviously each mode—electron holography [23], EDS spectroscopy [11], EELS spectroscopy [12, 13, 23, 25], etc.—brings up its own advantages in terms of the signals acquired and the information accessed. However, adding the third dimension to the 2D imaging is not straightforward as specific requirements need to be fulfilled: large magnifications, large amounts of data to be rapidly collected and processed and new processes necessary to combine various bits of information collected on a single sample. In this context, the combination of recordings under various modes might be mandatory for the study of complex structures [23, 24].

6.3.3 Methodologies: Experiment and Calculation

From a practical point of view, electron tomography is developed in several steps: the acquisition which consists in acquiring a series of projected images by tilting the specimen with respect to the incident beam for the largest possible angular range. Afterwards, the raw images are stacked and carefully aligned, and then in a second step, the volume reconstruction is carried out. After volume rendering, data segmentation and modelling are the next steps for accessing the quantitative analyses of the investigated volumes. These steps are separately detailed in the next sections, by highlighting the role of each step, its specificities and obviously the difficulties encountered in practice.

Acquisition of a Tilt Series

The acquisition of tilt series can be carried out in any microscope equipped with a high-tilt specimen holder and data acquisition software. The latter ideally provide an automated recording of tilt series over a predefined angular range and a close control of both the defocusing and specimen drift at each tilt angle. The recorded images need to be real projections of the whole sample; in other words, the imaging depth of field must always be larger than the sample thickness. The maximum tilting angle and implicitly the number of projections do define the spatial resolution in the two directions perpendicular to the tilt axis, whereas along the tilt axis, the resolution remains the same as that of the initial 2D images. The corresponding spatial resolution/direction relationships have been detailed by Frank and McEvan [25] in their pioneering work edited in the early 1990s.

The use of an EFTEM tomography mode for obtaining reliable 3D chemical elemental mapping implies the acquisition of multiple series of images as a function of the number of elements to be explored. Basically, three energy-filtered TEM images are recorded, for each tilt angle and for each element, in addition to the zero-loss series that can be recorded twice. This methodology, e.g. known as the three-window method, allows for a proper extrapolation of the background for the quantitative extraction of the chemical signals [26, 27]. This approach lengthens the duration of the recording sessions but offers a good assessment of the background and elemental projections. This full set of recordings is carried out for every element of interest within the specimen.

As mentioned above EELS-SPIM or EDS-SPIM tomography techniques require the acquisition, in parallel to the HAADF signal, of the corresponding spectroscopic signal. However, it is worth mentioning that these analytical tomographic techniques present the drawback of high acquisition times and therefore high-energy doses. Thus, this aspect should always be taken into account in order to limit the sample possible degradation.

HAADF-/EELS-STEM, EDS-STEM EFTEM Specificities

As previously stated, the use of the parallel beam bright field mode for the 3D analysis is not well adapted for the study of crystalline materials owing to the Bragg-diffracted electrons which make it difficult to correct the observation of the object at various tilting angles. To overcome this difficulty, the signal is improved by using the high-angle annular dark field (HAADF) detectors under scanning (STEM) mode because the recorded signal is predominantly incoherent and the projection requirement for the tomography is satisfied in this way. The acquisition of scanning TEM tilt series involves the simultaneous acquisition of a BF and DF series by using a circular centred detector for the BF and an annular detector for the HAADF. In addition, as aforementioned, STEM tilt-series acquisition allows for the simultaneous recording of other spectroscopic signals, as it is the case for EDS and EELS tomography. The focusing depth of the electron beam is commonly of the order of a few tenths of nm, which ascertains the position of the investigated nano-system to be in the focal volume. Ideally, the acquisition software automatically modifies the tilt angle of the specimen holder according to the input scheme, i.e. in Saxton or continuous modes. At the same time, a close control of the defocusing and specimen drift is automatically performed for each tilt angle. Moreover, the software developments actually allow for the automatic tuning of the beam focus for keeping the focal point onto the tilted specimen. The main advantage of simultaneously acquired BF and DF series relies on the one hand on the signal complementarity and on the other hand on the achievement of spatially correlated volumes. It is well known that in the HAADF mode, the signal intensity scales with the Z atomic number, and therefore, this methodology is well adapted to the detection of heavy elements. The nano-systems analysed by HAADF comprise both single element nanoparticles with specific geometries or complex nanostructures and nanocomposites constituted by elements with significantly different atomic numbers. Under BF-STEM, one is able to access the system porosity. The information complementarity is totally ensured as the DF, and BF volumes are spatially correlated, and a precise direct comparison of the two volumes can be successfully performed. The STEM tomography remains a technique rather difficult to perform, and lots of undesired events might occur, like the specimen contamination or beam damage during long acquisition duration. However, this approach remains interesting not only for the investigation of crystalline materials but for the 3D exploitation of beam-sensitive materials, situations for which low-intensity currents and short exposures need to be used during the scanning step.

When the nano-systems to be analysed are constituted by elements with close atomic numbers, a possible solution for the 3D analysis is the "analytical tomography", the EDS or EELS tomography. EDS tomography is very difficult to implement as it requires up-to-date X-ray detectors able to cover high angular solid angles that became commercially available only in the last 2–3 years, and the approach requires huge hardware resources for the data acquisition and analysis. Still in an early stage, many efforts will be most probably done for the development of the EDS methodology as an alternative to the analytical tomography. Indeed, it is important to point out that one of the main advantages of this technique is that it allows for the simultaneous detection of a large range of elements (including those with a high atomic number). The EFTEM tomography requires the recording of multiple images for each tilt angle: a zero-loss (ZL) image that filters the elastic electrons and, for each element of interest, three energy-filtered images taken nearby its ionisation edge. In practice, once the zero-loss tilt images exhibiting good signal-to-noise ratio (SNR) are properly aligned, the alignment of the elemental projections can be done by using the very same alignment parameters. As a result, spatially correlated series of projections are obtained. In analytical tomography the prior knowledge of the external morphology and porous structure of the object is particularly beneficial as it allows for the extraction of the elemental volumes considering only the voxels corresponding to the material. The last step consists in a quantitative combined analysis of the elemental volumes and will be developed in the next sections. The spatial resolution of the 3D elemental maps depends on (1) the recording parameters (pixel size, maximum tilt angle, number of projections) and the data processing (accuracy of the image alignment, algorithm used for the reconstruction) and (2) the resolution in the 2D elemental projections [28]. Roughly, this leads to a theoretical 3D resolution of about 1–2 nm. In practice, the actual resolution strongly depends on the SNR [29]. Deeper insight on the methodology developed for analytical tomography is given in the Sect. 4.4, by analysing the case of nanomaterials constituted by an intimate mixture of silica and alumina, systems largely used for industrial applications.

Principal Reconstruction Algorithms: WBP, SIRT, ART, DART and New Algorithmic Approaches

Two main routes are usually considered for the specimen reconstruction from its recorded projections. The first one relies on the fact that the recorded intensity values can be used to calculate the 3D representation of the sample reciprocal space. Basically, each projection of the sample is univocally related to a Fourier central slice orthogonal to the projection direction, and therefore, the Fourier transform of this reciprocal space uniquely yields a reconstruction of the real space of the sample. Since the reciprocal space recorded through electron tomography is made out of non-evenly and non-periodically distributed point values, the Fourier calculations even in the fast Fourier transform (FFT) mode are complicated; it becomes more convenient to perform the reconstruction calculations in the direct space. Here, the intensity of one pixel on one projection image lays on a straight-line segment orthogonal to the image at the position of the pixel. By repeating this operation for each equivalent pixel in the full set of images and at the point where the segments intersect in space, the sum of the intensity values on each segment, one accesses the voxel that envelops this intersection in the real 3D space. This technique is named weighted back-projection [30].

The quality of the object reconstruction strongly improves when the number of recording angular steps is increased; it can be further enhanced by correcting the angular cosine dependence of the projection of the object and by varying the tilt angle of the sample according to a cosine function [31]. As the number of recorded projections is limited, the “star” artefacts occur, and consequently, the quality of the reconstructed matrix of the object is degraded [32]. In addition, the tomographic tilt series have a wedge of missing data corresponding to the angular range uncovered due to the limited value of the maximum angular rotation of the specimen holder, where no images are recorded. This TEM-specific limitation causes distortions in the 3D reconstructions. Furthermore, the spatial resolution is degraded in the direction of the incident electron beam at 0° tilt. All these artefacts can be significantly attenuated applying iterative algorithms that improve as well the signal-to-noise ratio within the reconstructed volumes. After each calculation of the reconstructed matrix, projected images are calculated and compared with the original ones. A least squares comparison technique allows reaching a stable matrix in a convergent process. The most popular algorithms are implemented in the SIRT and the algebraic reconstruction technique (ART). Their reliability and stability are discussed in Refs. [33] and [34].

The development of electron tomography for the material science research has led to the development of even more powerful reconstruction algorithms, which take advantage of the discrete nature of the reconstructed volume. The DART quotes with the association between the number of grey levels used for the reconstruction and the exact number of component known to be present in the sample under study [29].

More recently other alternative approaches based on compressive sensing (CS) or TVM have been developed [35]. The compressive sensing considers that a small number of well-chosen measurements can suffice to reconstruct signals that are amenable to sparse or compressible representation. In addition, the CS significantly reduces artefacts present in conventional electron tomography reconstruction (blurring of object boundaries, elongation, etc.) even if far fewer projections are employed.

Qualitative and Quantitative Volume Analyses

Several aspects can hamper the qualitative and quantitative interpretation and analysis of tomograms: the artefacts due to the missing wedge and to the limited number of projections, the low SNR and the low contrast between the various parts of the analysed object. The artefacts commonly lead to volume distortions and might mask the information along the incident beam direction. The most tedious step, which can induce considerable errors in the quantification, is the data segmentation process. It consists in decomposing the tomogram into its structural components by identifying the sets of constitutive voxels. Although several automatic or semiautomatic approaches have been developed based on simple density thresholds or more sophisticated threshold approaches, manual segmentation is sometimes the most reliable approach: the user assigns the structural features using visualisation tools. Once the parts of interest have been extracted from the volume, most of the 2D image analysis processes can be easily generalised to 3D allowing one to calculate the parameters of interest, as described in the next sections by considering suggestive and representative examples.

6.4 Application to Nanomaterials and Nanostructures

The nano-science demands nowadays the continuous development of specific tools aiming at first exploring and then controlling the materials structures, morphologies and chemistry and their subsequent properties at the atomic level. As a function of the applications envisioned, one assists at the building up of more and more complex three-dimensional nanostructures and nano-architectures with complex morphologies that dictate their specific responses. In the catalysis field, for instance, the active phase localisation, accessibility and the surface-active area are parameters of huge impact for the catalytic activity. Exploring the morphology and chemistry of complex systems would most probably open new routes for understanding their behaviour under operational conditions. Another example concerns the metal nanoparticles widely used in the fields of photonics, optoelectronics, photocatalysis and bio-sensing applications. Their optical response is dominated by the localised surface plasmon resonances (SPRs), whose spatial distribution strongly depends on the NP morphology [36–40]. The correlation between the morphology and the properties of complex nanostructures is a key issue for the comprehension of their characteristics. Electron tomography will furnish valuable information on the 3D characteristics of structured nanomaterials with the nanometre resolution.

6.4.1 Morphological Analyses of Nanostructures and Nano-objects

In the following section, we will illustrate the quality of the information gained when using electron tomography as well as the technique applicability to various types of nanomaterials and nano-objects.

Tailoring Few Layer Graphene Structures by Fe-Based NPs

Controlling the size of graphene nano-sheets and nano-ribbons has presently become a hot topic in the field of material science. Owing to their outstanding physical and chemical properties, graphene nano-ribbons with well-defined dimensions are ideal candidates for the production of nanocomposites that can find applications in many fields such as energy storage, electronics, catalysis, etc. The production of graphene nano-ribbons with a well-defined geometry remains a technological challenge, and in this sense, several routes have been considered: the mechanical and/or chemical exfoliation of graphite [41, 42] and subsequent selection of nano-ribbons as a function of their size and thickness, the catalytic unzipping of carbon nanotubes (CNTs) [43] or a combined approach.

In principle, under well-controlled atmosphere, a supported active nanoparticle does react with its support, and as a result, the system morphology changes drastically. When Fe-based NPs are deposited onto carbon-based supports, one assists to significant changes of the support morphology as, for instance, from CNT to GNR or the creation of trenches on the surface of few layer graphene (FLG) supports. A complete investigation of the morphology changes as induced by the catalytic cutting of FLG sheets has been carried out by electron tomography [44]. Initially the Fe-oxide NPs locate on both sides of the supports at the FLG steps and edges with different heights or on the terraces (Fig. 6.2a). After thermal treatment under

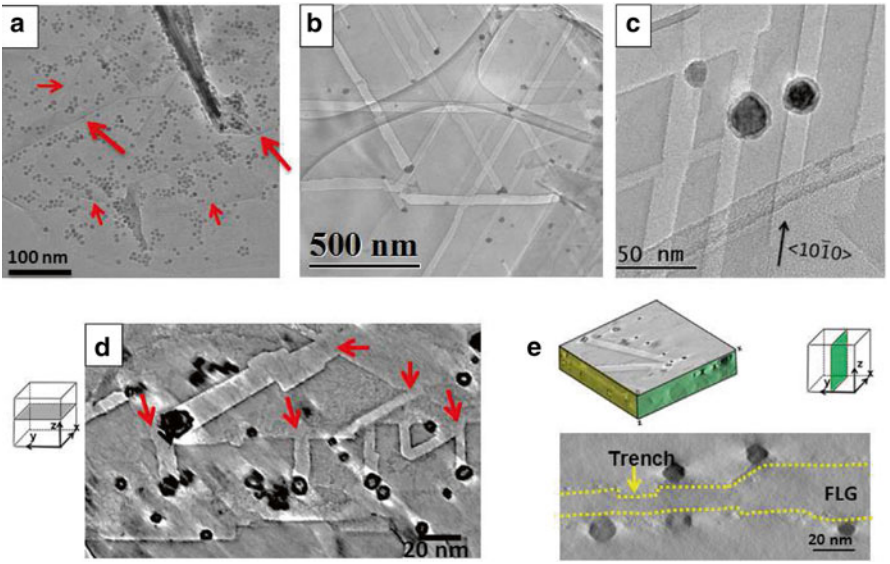

Fig. 6.2 Global view of the nanostructured few layer graphene. 2D TEM micrographs of typical Fe-based NPOs onto FLG (**a**) before and (**b**) after catalytic cutting accompanied by (**c**) the change of NP morphology. 3D overview of the cut system with (**d**) the *arrows* pointing to the initial location of NPs (*xy* slice) and (**d**) the volume representation showing roughly the system topography. Reprinted from Melinte et al. [44]

hydrogen flow, the NPs dig the surface of the supports forming trenches on its surface (Fig. 6.2b) along well-defined crystallographic directions (Fig. 6.2c). The NP morphology changes from homogenous to core-shell or hollow structures, accompanied by a change of the NP chemical composition (see in more detail supplementary information in ref. [44]).

From a statistical analysis, it has been shown that the only NPs located initially at the FLG steps and/or edges can cut trenches and that the cutting activity of Fe NPs is significantly higher than that of Fe_3O_4 or Fe-rich regions exist on the cutting front direction. From a 2D analysis, using different contrasts, one identifies the presence of sharp superimposed long morphological features within the support with possible various thicknesses. Their exact depth and location can be explored only by means of 3D imaging. Indeed, ET identified the presence of NPs and trenches on both sides of the FLG support. The role of FLG topography on the cutting phenomenon is also identified. During its motion, a cutting NP can encounter support defects, such as steps and edges. If the NP crosses a step-up defect with the height smaller than its diameter, the NP continues its path by creating a trench (Fig. 6.3a), whereas when the step-height is higher than the NP diameter, the NP digs a tunnel (Fig. 6.3b) in the same direction as before it encountered the step. It is however interesting that for both situations, the basal plane of the trench or channel remains flat and constant. When the NP meets a step-down defect, it either stops or changes its moving direction; see Fig. 6.3c, d, respectively. With all these elements, we are free now to turn our attention to the synthesis of graphene nano-ribbons, by considering a chemical exfoliation procedure as the one described by Ihiawakrim et al. [45] for isolating individual features with well-defined geometries and thicknesses.

Porosity of Mesoporous Hollow-Shell Mixed Oxide Nanoparticles

Silica-based meso-structured nano-systems, used as drug delivery agents, have been largely investigated during the last years. They allow a high flexibility of integration of multiple properties needed for efficient imaging diagnosis and/or therapeutic treatments. Lots of efforts have been spent in designing new silica-based nano-carriers with mesoporous architecture able to carry and release progressively important amount of drugs [46, 47]. One of the strategies consisted in doping the silica matrix with a few percent of zirconium. This methodology allows a very good dispersion and co-condensation of zirconium atoms within the silica network, producing spherical nanoparticles with meso-structured core and a dense shell. The zirconium-oxide surfaces are expected to catalyse the fast condensation of silicate species directly onto the cargo, and this would in principle promote a progressive rearrangement of both the meso-structured core and the shell. The raised questions focused on the pore connectivity within both the core and the shell and whether the shell is uniform and continuous around the core, or we deal with the presence of pores that would provide high accessibility to the nano-carrier. Since the BET experiments furnished no conclusive information on the pore connectivity and core accessibility, a very precise 3D morphological investigation of the cargo after drug

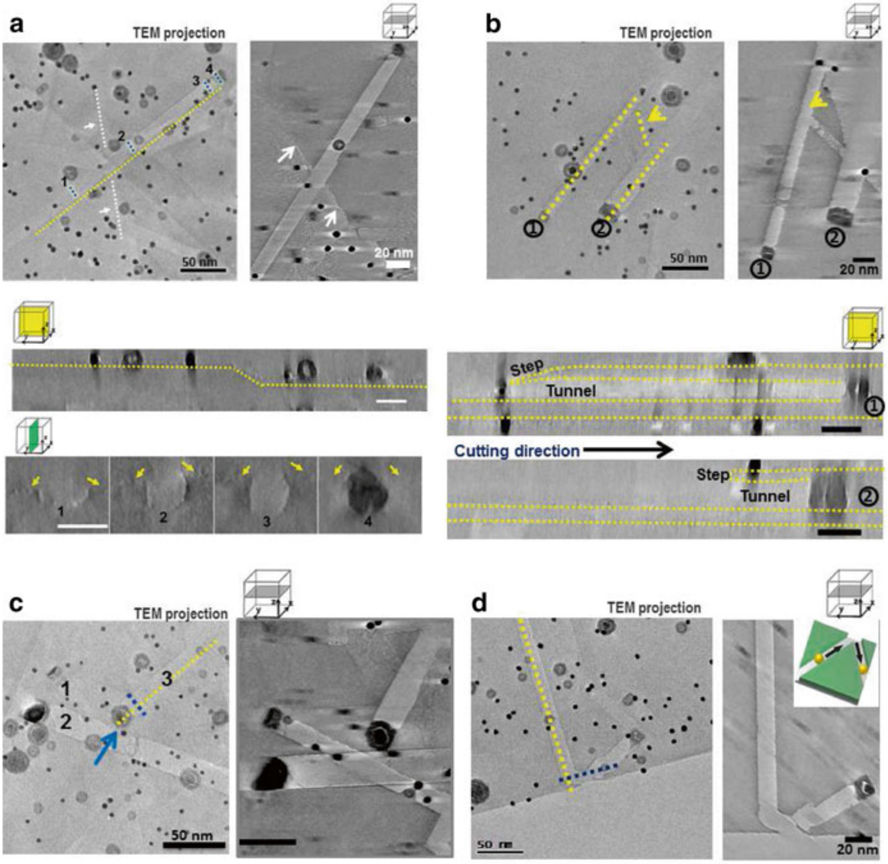

Fig. 6.3 The role of support tomography on the cutting process. 2D projections and slices redrawn from the reconstructed volume showing the impact of step-up and step-down defects encountered by the NPs. As a result, the NPs encountering a step-up defect (**a**) create trenches with the walls geometry defined by the NP shape when the step-height is less than the NP diameter and (**b**) dig tunnels within the support when the step-height is larger than the NP size. At the intersection with a step-down defect, the NPs either (**c**) stop or (**d**) change their cutting direction. Reprinted from Melinte et al. [44]

release was needed, by means of electron microscopy. Firstly, one emphasises the porous structure, and secondly, one concentrates on the zirconia location within the porous core.

As anticipated by the 2D analysis, interconnected meso-pores with irregular shapes and mean diameters of 8 nm do cross the silica core, whereas the shell appears to be a “continuous” coating with homogenous thickness. It is however marked by the presence of micro-pores with sub-nanometre size that go across the shell’s complete thickness. In the STEM HAADF mode, the intensity scales with the Z atomic number and therefore one may associate the highest intensity with the

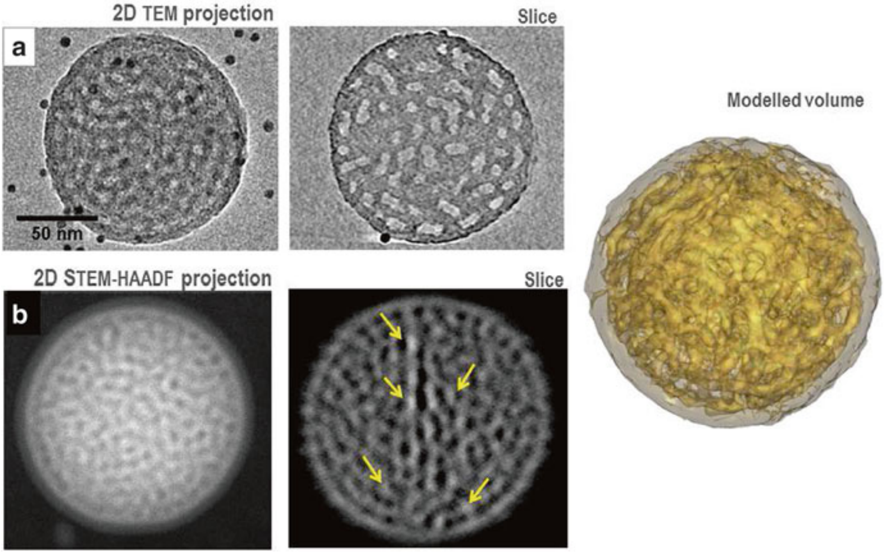

Fig. 6.4 Electron tomography of a silica structure embedded into a denser Zr-enriched silica layer. (**a**) The homogenous distribution of the mesoporous volume is marked by (**b**) the presence of Zr-rich areas within the meso-pore rims (*arrows*). (**c**) Volume modelling allowing for the achievement of valuable 3D quantitative information. Reprinted from et al. [to be published]

presence of Zr. It is surprising though that it can be identified not only within the shell but also within the core-silica as well into silica-meso-pore rims (arrows in Fig. 6.4b). Even if ET remains a local technique of investigation, one of its advantages is to give access to quantitative parameters. In our case, the analysis of several volumes showed that 40 % of the volume is porous, whereas the specific surface is six times larger than the external surface of the volume.

Au and Au/Ag Nano-bipyramids: Shape and Plasmon Response

Owing to their optical properties, the structure and morphology of noble metal-based nanoparticles with homogeneous or core-shell structures have been widely explored, for their optical response depends strongly on their shape and surface topography. Let us consider the case of core-shell Au–Ag bipyramids (BP). By exploring for the first time the Z-contrast within the STEM-HAADF tomography, it was possible to identify the bipyramidal shape of these nanoparticles constituted by a homogenous core embedded in an Ag matrix with a thickness of several nm. Secondly, we have identified and quantified the shape and structural defects within the NPs: transverse atomic steps perpendicular to the bipyramid long axis about everywhere on the particle surface (see the model in Fig. 6.5). The main advantage of this approach is its reliability for quantitative exploitation, which allows one to assess the inhomogeneous

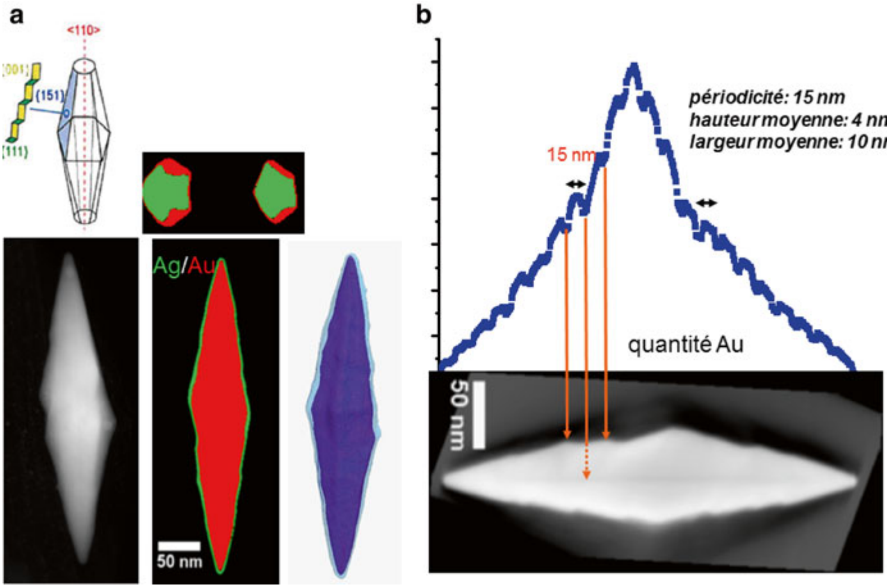

Fig. 6.5 Electron tomography (STEM-HAADF) of an Au–Ag core-shell bipyramid. (**a**) The distribution of Ag shell on the surface of Au nano-bipyramid filling the surface defects of the Au core. (**b**) Representation of the Au amount as assigned from a numerical cut within the volume

character of the steps occurrence. It is important to mention here that the proper quantification of the steps requires a perfect alignment of the BP, e.g. along its long axis. Even so, no complete access to all steps is ensured due to the random orientation of the steps against the BP long axis. From a quantitative perspective, performing a numerical cutting operation within the volume and subsequent calculation of the Au amount for each slice can search a solution. Since the variation of the Au amount along the axis exhibits a singularity at the location of a step, this type of representation identified the steps characteristics of mean periodicity, width and height, as being 15 nm, 10 nm and 4 nm, respectively. From a fundamental point of view, the presence of steps on the NP surface can strongly modify its optical responses as such defects act as hotspots, with a high concentration on the electric field lines [48].

CoPt Nanoparticle Grown on a NaCl Substrate

The 3D morphology of particles always has a huge impact on their physical and chemical characteristics. Therefore, the strict control of the particles' size, shape and crystallography has become a real challenge in the field of catalysts. Whilst the surface's energies properly describe the shape of macroscopic particles, in the case of NPs, many other structures as edges, vortices, surface state and atomic relaxation derive from the atoms disposed in small clusters [49]. From a statistical viewpoint, the NP faceting, shapes and morphologies vary significantly and differ from the

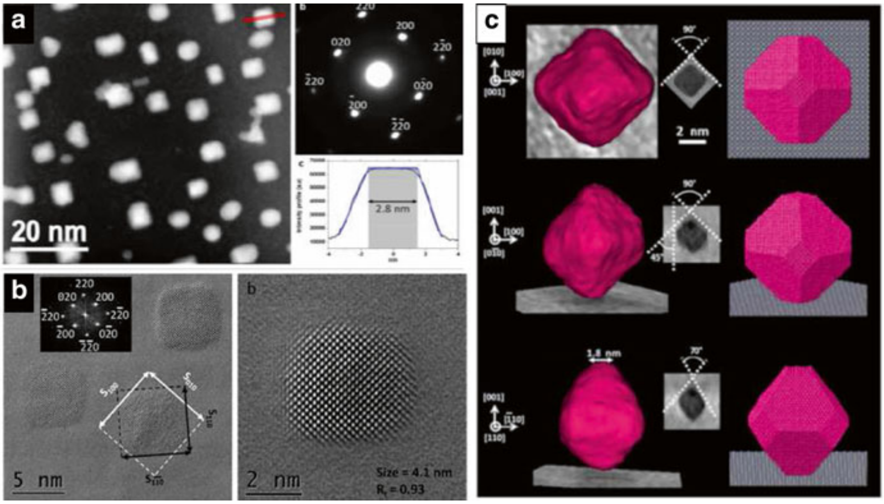

Fig. 6.6 Distribution and shape of chemically disordered CoPt NPs epitaxially grown onto NaCl substrate. (**a**) NPs' homogenous distribution after transfer on a carbon membrane. (**b**) HR images of NPs exhibiting ⟨110⟩ edges and truncated facets along the (100) and (010) directions. (**c**) Volume truncations as explored by STEM-HAADF electron tomography and molecular dynamics simulations (after system relaxation) along the [001], [0-10] and [110] directions (from *top* to *bottom*). Reprinted from Florea et al. [22]

energetically stable nanostructures even when the synthesis parameters are closely controlled. This is mainly due to the synthesis kinetics and to the NPs interaction with their environment. All these aspects have been checked with monometallic NPs [22]. Adding a second component introduces a new source of instability. Let us consider an intensively studied bimetallic system: CoPt NPs. These NPs have been epitaxially grown onto a NaCl substrate and subsequently investigated by HR-TEM, STEM and electron tomography, and the results were checked through molecular dynamics calculations (Fig. 6.6).

Slightly different-sized CoPt NPs exhibit high faceting within the chemically disordered FCC structure. The NPs are truncated octahedrons with different truncation ratios as a function of the NP size, in a way such that the larger the particle, the rounder its shape. In addition, up-down symmetry has been identified for all NPs, no matter their size. More specifically, the (001) support-interface facet is similar to the (001) vacuum facet, suggesting a negligible contribution of the fcc-CoPt/NaCl adhesion energy to the interface energy.

6.4.2 3D Distribution of Nanoparticles on Supports

The 3D distribution of NPs on supports and their behaviour under well-defined conditions are key issues for material implementation in applications. For example, the attrition of electron transport properties of semiconductive nanowires grown by chemical vapour deposition is mainly attributed to the presence of residual NPs on their surface (see Sect. 4.3.2), or in catalysis, the catalytic activity is closely related to the spatial and chemical distribution of the active phase, etc. During these working processes, the materials are submitted to more or less extreme conditions, such as high temperatures/pressures, gas flows or high electric fields. In this context, controlling the size, dispersion and shape of nanoparticles (NPs) in the high-temperature range and under specific conditions is a key topic for the development of new technologies. This section highlights the potential of electron tomography as combined with the in situ TEM, high-resolution imaging and spectroscopy for assessing the behaviour of complex nano-systems.

Co-Based Nanoparticles (NPs) Confined by CNTs

The confinement of magnetic Co-based NPs by inert and stable matrixes such as CNTs can be considered as an appropriate solution against NPs oxidation and therefore for the conservation of their magnetic and/or catalytic properties. Co-based NPs with mean sizes of 50 nm were casted inside multiwall CNTs by solvothermal synthesis, generating nano-peapod-like nanostructures. They exhibit specific morphologies marked by the NP faceting and the presence of voids and pseudo-fractures, i.e. closed fractures oriented along well-defined crystallographic directions within the same CoO monocrystalline grain [50]. The oxygen concentration in one NP is inhomogeneous, such that the oxygen concentration appears to be higher at the NP edges and the pseudo-fracture rims. For the initial system, the lengths of the pseudo-cracks are inferior to the grain dimensions, and their disposal is predominantly radial being surrounded by randomly disposed voids.

The hydrogen-assisted thermal treatment leads to the opening of the pseudo-fractures, as shown schematically in Fig. 6.7d, e. It is however interesting to note that the pseudo-fractures are practically confined within the same mono-crystal for the initial oxidised Co NPs, whereas after reduction one observes fracture opening, but the grain geometry is roughly confined due to NP encapsulation. The behaviour of such structures in the high-temperature range can furnish insights on the most probable morphology changes under operational conditions. The in situ thermal treatment identified a temperature two times higher necessary for the change of NP shape and subsequent coalescence in the case of reduced system as compared with the as-prepared specimen.

Au Nanoparticles (NPs) on Silicon Nanowires (NWs)

Semiconducting silicon nanowires (NWs) synthesised by chemical vapour deposition are promising candidates for building up complex structures such as biosensors or programmable nanowire circuits. One of the most employed methods for their synthesis is the vapour–liquid–solid (VLS) growth technique. This method very often implies the use of Au as catalyst and leads to the production of NWs with the

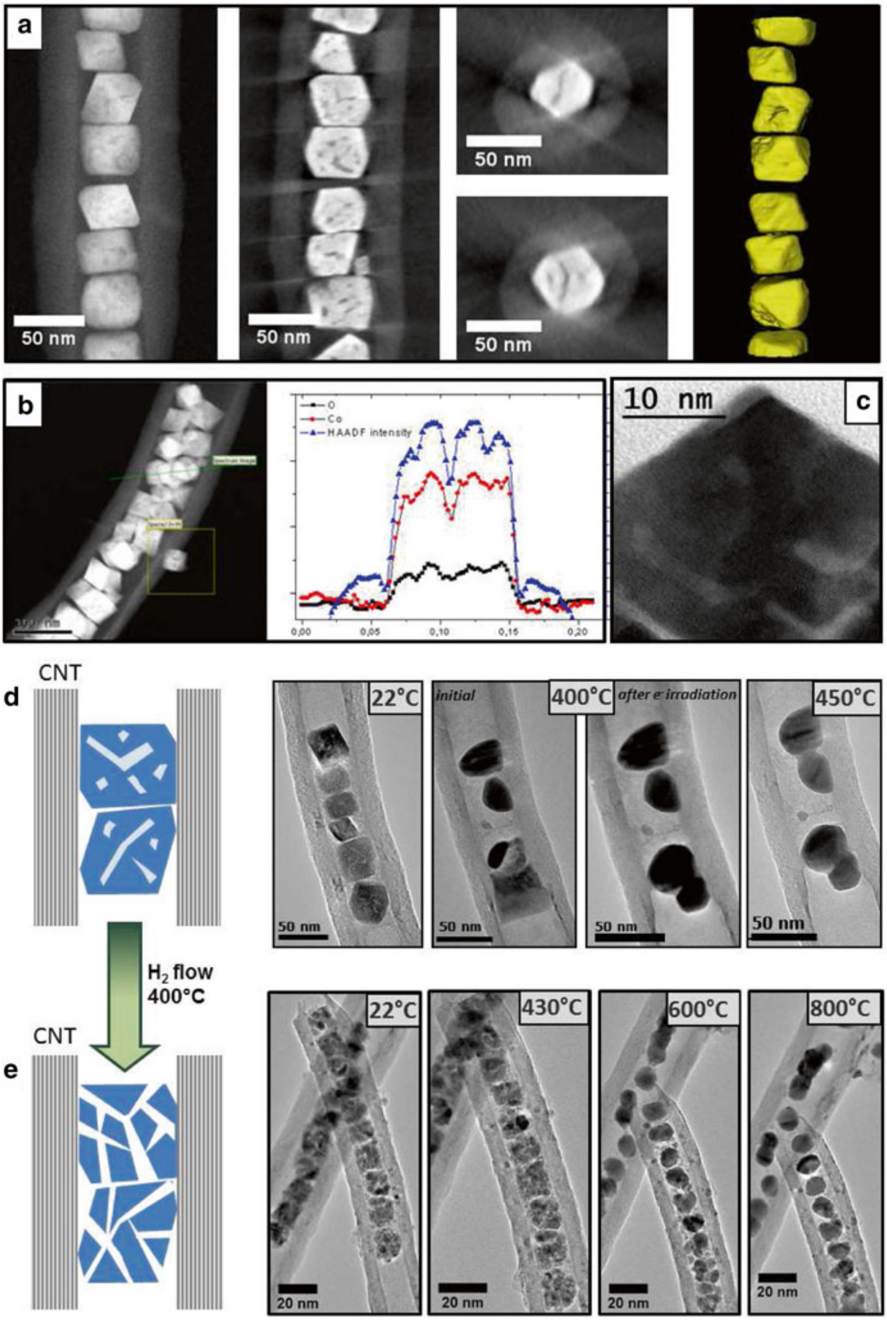

Fig. 6.7 Morphology and annealing behaviour of Co-based NPs casted in carbon nanotubes. Monocrystalline faceted Co-based NPs (**a**) randomly distributed within the tubes exhibit inner voids and pseudo-fractures that (**c**) do not cross the NPs. (**b**) The NPs' outer surface as well as the voids and the pseudo-fractures' rims are rich in oxygen. The hydrogen-assisted reduction leads to crack opening. The porous defects within the nonreduced and reduced Co NPs disappear through thermal annealing at (**d**) 400 °C and (**e**) from 600 °C, respectively. Reprinted from Baaziz et al. [50]

surface contaminated by the presence of Au residuals. These residues have a key role on the transport properties of NWs, an issue that is not completely covered up to now. Parameters like residues' size and their scattering on the nanowire's surface are obviously of huge importance. The measure of the transport properties carried out by AFM tip work function has revealed the strong interplay between Schottky interface junctions, surface conduction along the Au-rich nanowire sidewalls and intrinsic conduction of the NW. In order to get a deeper insight on the role on the transport properties of Au on the sidewalls, the question of system morphology needs to be addressed [40]. Indeed, spherical Au NPs with mean diameter of 2 nm are uniformly distributed on the NW surface, and they coalesce when heated at 750 °C. It is highly interesting to note that a longer duration of the thermal treatment leads to the formation of a thin layer. This layer grows along the NWs' length, whereas the NW end changes completely the morphology in a club-like structure. Certainly, questions like the presence of a pure Au coating or of the AuSi alloy remain opened. However, this particular thermally induced behaviour cannot be neglected as it is equivalent to the Joule effect that takes place upon application of an intense electric field, inducing a subsequent attrition of the transport properties of the system (Fig. 6.8).

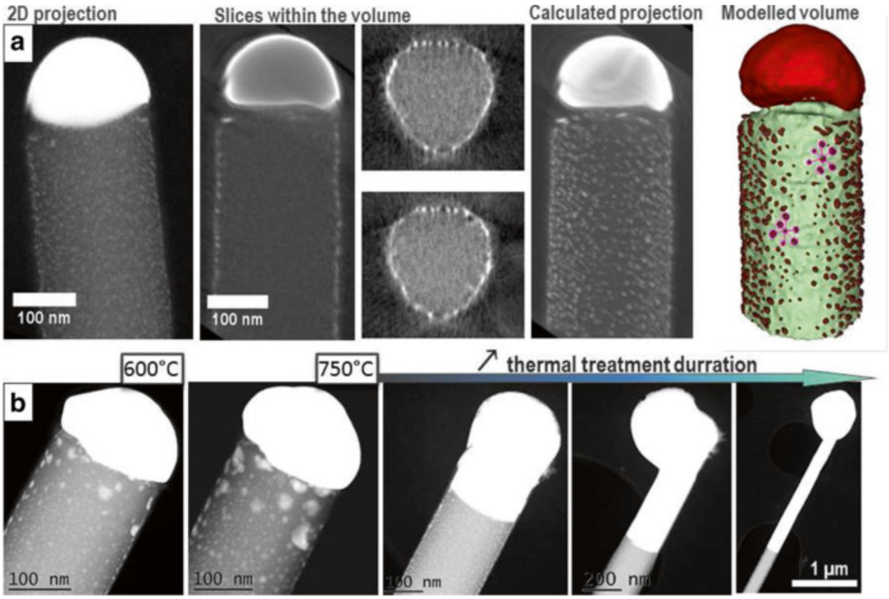

Fig. 6.8 Morphology and thermally induced evolution of Au/Si nanowires. (**a**) Au catalyst NPs are uniformly distributed on the outer surface of the Si nanowires, whereas a big catalyst particle sticks to the Si NW end. The surface NPs coalesce (**b**) at 600 °C, such that at 750 °C the Au from the tip melts, embedding the wire and completely changing the system morphology

Pt Nanoparticles (NPs) onto FLG

The perspective of using graphene as a support for Pt nanoparticles with enhanced catalytic activity is very attractive, opening a new way in the development of durable and efficient proton exchange membranes (PEM) for fuel cells. Since the major part of the catalytic reactions takes place in the high-temperature range, the stability of Pt NPs onto FLG supports is a key issue for the applications. If one considers a system made of Pt NPs with mean diameters of 2 nm, the in situ TEM approach revealed that upon heating the size distribution of the Pt NPs shifts towards two maxima centred at 3.5 and 5.5 nm [51]. In addition, questions on Pt NP faceting and sintering by coalescence and/or Ostwald ripening were addressed by considering the interaction with the FLG support (Fig. 6.9).

The NP/support interaction is the parameter controlling the behaviour of the system in the high-temperature range. This parameter strongly depends on the support topography, which is marked by the presence of edges, steps, and terraces, as shown in Fig. 6.10. Since the FLG edges and steps are marked by the presence of dangling bonds, the NPs have a strong tendency to fix there rather than onto the terraces. This latter configuration requires the presence of defect within the FLG sheet, which can be seen as traps for the metallic atoms and/or NPs. Upon heating, the NPs and atoms diffuse and coalesce being located exclusively on the steps and edges. Those from the terraces moved from the FLG surface towards the steps. From a phenomenological point of view, one assists most probably at the defect reconstruction within the FLG surface upon heating, leading to metal NPs and/or atoms dislodging and subsequent diffusion on the surface. When their diffusion paths intersect an obstacle

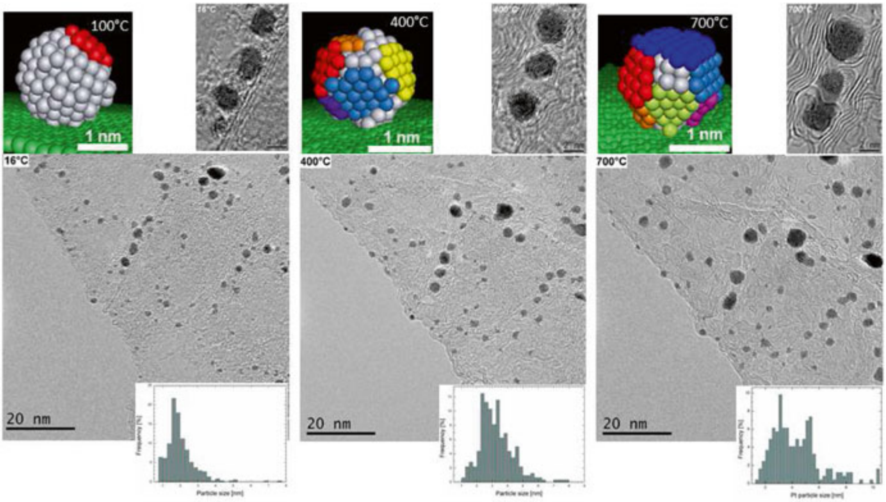

Fig. 6.9 Thermal evolution of Pt NPs deposited onto few layer graphene supports. Pt NPs with mean size of 2 nm coalesce under the impact of thermal constraints leading to NP faceting and subsequent NP size increasing. Reprinted from Moldovan et al. [51]

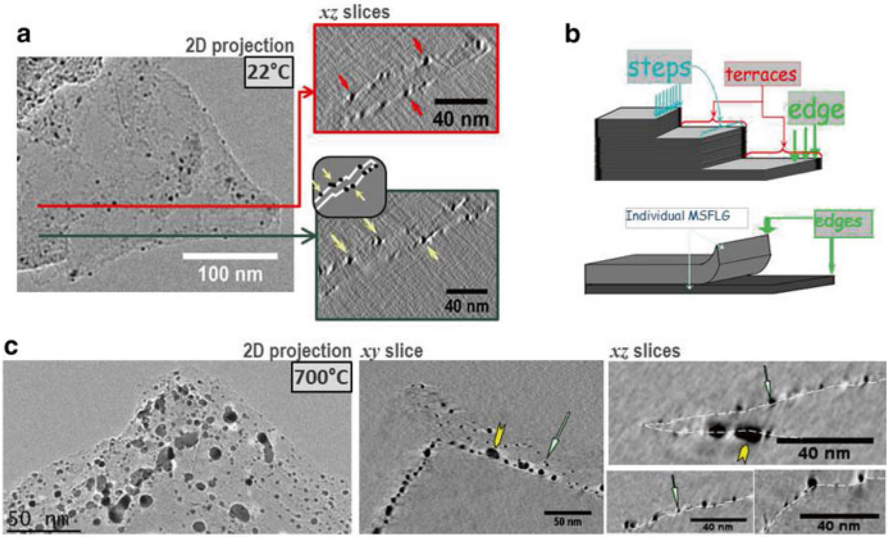

Fig. 6.10 Three-dimensional investigation of Pt NPs onto FLG supports (**a**) prior and (**c**) after in situ thermal treatment. Initially, (**a**) the Pt NPs and atomic clusters locate preferentially at the supports' steps and edges as well as on the terraces for typical support configurations schematised in (**b**). After thermal treatment (**c**), the NPs locate exclusively at the steps and edges. Reprinted from Moldovan et al. [51]

such as a step or an edge, they stop, and if more thermal energy is furnished to the system, they diffuse along the steps and then coalesce with other NPs placed on their path. The information gained by the electron tomography experiments allowed one to access the topography of the FLG support by bringing together the elements missing for the comprehension of the 3D structure of metallic NPs deposited on the FLG supports.

6.4.3 Long-Range Ordering of Core-Shell Co-Pt NPs

Understanding magnetisation dynamics of nanostructures is an important topic in nano-science as it opens potential new routes for various applications in optics, data storage, nano-electronics or biology. The Co-Pt-based nanoparticles have well-known magnetic properties. If they are gathered in compact assemblies or they are simply compressed into pellets, apart from their crystallography, structure and morphology, the NP spatial arrangement is expected to impact their magnetic response. After electron tomography analysis, the positions of each NP in a pellet allowed one to determine their arrangement. The distance distribution between pairs of NPs show a short-range order, with the distances of the first-, second- and third-range neighbours of 6.5, 11.5 and 16 nm, respectively.

Super-paramagnetic Co-Pt nanoparticles assembled into pellets change their spatial arrangement through mild laser annealing, such that a local super crystalline order appears at the surface of the pellet within a penetration depth of about 20 nm for a 400 nm laser wavelength [52]. Therefore, the approach of in situ heating has been carried out in order to establish the changes induced during annealing. Indeed, the NP morphology changes drastically from core-shell into a homogenous structure, whereas in terms of structure, the initial structure consisting a Co 5 nm core surrounded by a 2 nm thick Pt layer changes into a crystalline CoPt phase (see Fig. 6.11c).

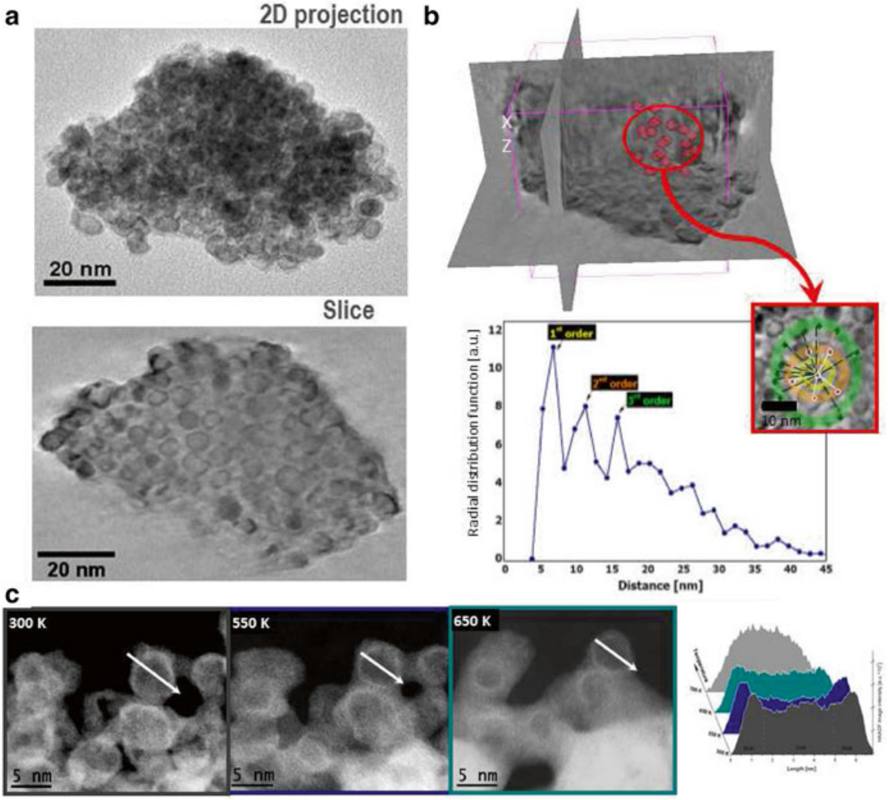

Fig. 6.11 Combined electron tomography and in situ thermal treatment study of CoPt core-shell pellets. (**a**) Two-dimensional projection and slices redrawn from the reconstructed volume that has been used to calculate (**b**) the radial distribution of NPs as function of the distances between the NPs in the pellet. (**c**) The evolution from a core-shell morphology towards homogenous structures as induced by the in situ thermal treatment. Reprinted from Bigot et al. [52]

6.4.4 3D Chemical Composition: Analytical Spectroscopic Tomography

EFTEM Tomography for the Study of Silica/Alumina Industrial Catalysers

Analytical tomography combines chemical mapping through EFTEM with electron tomography showing the route to 3D chemical selectivity. The experimental set-up is heavy to develop as it implies on the one hand the use of adapted materials, i.e. resistant to beam damage, and the close control of the experimental set-up itself on the other hand. This implies the prior knowledge of the specimen chemistry, which needs to be explored by EELS in order to properly define and select the corresponding energy windows. Afterwards, the acquisition, reconstruction and visualisation/quantification steps are very delicate to carry out as the signal-to-noise ratio is rather low for this kind of working mode.

We will consider as an example the case of a heterogeneous industrial catalyser made out of a mixture of silica and alumina. This kind of support is often used in the oil industry as the mix-up of the two phases generates Al–O–Si surface chemical bonds generally associated with increased acidic sites. In this way, the analytical tomography experiment has been considered for assessing the spatial distribution of Si and Al within the volume, emphasising the exploration of the surface concentration of the two elements. Figure 6.12a, b displays the zero-loss micrograph and the corresponding energy loss spectra acquired at 0° tilting. The windows marked by W1, W2 and W2 and W5 were chosen for the background extraction of the Al and Si signal, respectively. The windows W3 and W6 were used for the calculation of the signal by using the $L_{3,2}$ lines of the Al and Si. The corresponding micrographs are shown in Fig. 6.12c, together with the images after image filtering (on the right side). Once the images are acquired at each tilt angle, one obtains three series of projections corresponding to the mean mass density and Al and Si signals, which are used to calculate the three spatially correlated corresponding volumes [21]. Afterwards, one can differentiate the elements from every volume and then superimpose them to reach the "relative" chemical volume. By comparing the intensities of the elemental volumes, one can split the volume into two contributions from the Al and Si, generating in this manner an analytical model of the volume. Finally, a quantitative analysis of the volumes has been carried out. It identified that among the 50 % of silica contained in a grain, 30 % is located on the grain surface in the case of a sample prepared by liquid–solid mixture [21], as shown in Fig. 6.13a. For the materials prepared by mechanical mixture, one identifies a core-shell-like morphology with the alumina surrounding the silica core and only 15 % of silica on the grains surface; see Fig. 6.13b. Although this kind of analysis is pretentious in terms of time and resources demanded, it remains one of the most convenient resolutions for the assessment of chemical composition of nanostructures made out of elements with close Z in a three-dimensional structure at the nanometre scale.

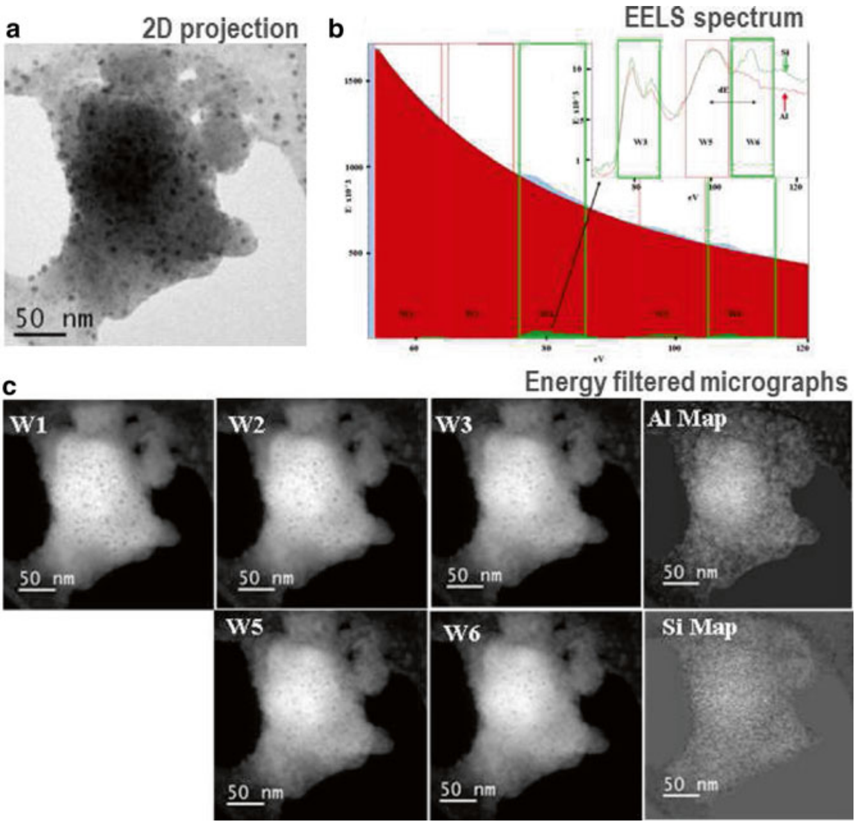

Fig. 6.12 Illustration of the acquisition series in analytical tomography; if two elements are searched for, a complete series comprises three image series, spatially correlated: (**a**) the zero-loss image series, which offers a high-quality contrast, and the filtered image series corresponding to the two elements. The latter are acquired by fixing the energy windows in (**b**) the corresponding EELS spectra and by (**c**) recording three micrographs for each element of interest and using the well-known three-window method. Reprinted from Roiban et al. [21]

EELS-STEM Tomography: Application to $Fe_xCo_{(3-x)}O_4@Co_3O_4$ Mesoporous Materials

In this work the feasibility of EEL spectroscopic tomography at low voltages (80 kV) and short acquisition times was probed. This was made possible by the recent advances in TEM and the use of multivariate analysis (MVA), which were applied to mesoporous antiferromagnetic Co_3O_4 nanocast replicas of SiO_2 KIT-6 templates filled with $Fe_xCo_{(3-x)}O_4$Co3O4. It is worth mentioning that mesoporous silica have recently attracted much interest as hard templates for nanostructures, as the size and shape of the pores can be tailored by the choice of surfactants and synthesis paths.

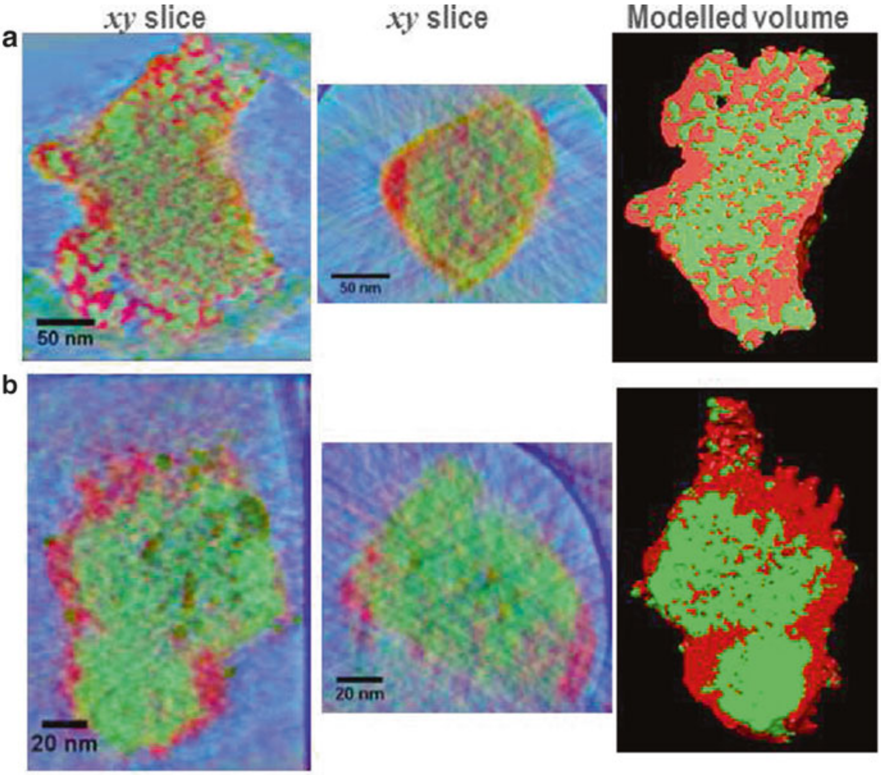

Fig. 6.13 3D analytical study of the Si (*green*) and Al (*red*) distribution within industrial catalysts made out of a mixture of silica and alumina. The Si/Al distribution (**a**) is rather homogenous for a specimen prepared through a liquid–solid mixture, whereas a silica–alumina core-shell-like structure is identified for a sample prepared through mechanical mixture. Reprinted from Roiban et al. [21]

Data acquisition was carried out on a probe C_s-corrected FEI Titan operated at an 80 kV acceleration voltage. The whole data set consisted of 48 SPIM ranging from 68.99° to –64.74° following a Saxton scheme angle step with 55 × 55 spectra each, acquired during 0.1 s. High-angle annular dark field (HAADF) signal was simultaneously recorded. For data treatment, MVA methods were applied, namely, the principal component analysis (PCA) and the independent component analysis (ICA) [53]. From the noisy raw spectra, enhanced O_K, Fe ($L_{3,2}$) and Co ($L_{3,2}$) edges were retrieved after PCA analysis (Fig. 6.14).

ICA successfully retrieved the Fe-oxide and Co-oxide signals of the sample as well as the background signal before the oxygen K edge (Fig. 6.15). Structural and chemical information has been obtained from the reconstruction of these signals (Fig. 6.15). Concerning the chemical information, an interesting result was revealed: the comparison between iron and cobalt signals showed that some of the iron which was intended to penetrate the structure remained on the outer surface (Fig. 6.15), whilst the rest of the iron content is uniformly distributed inside the particle.

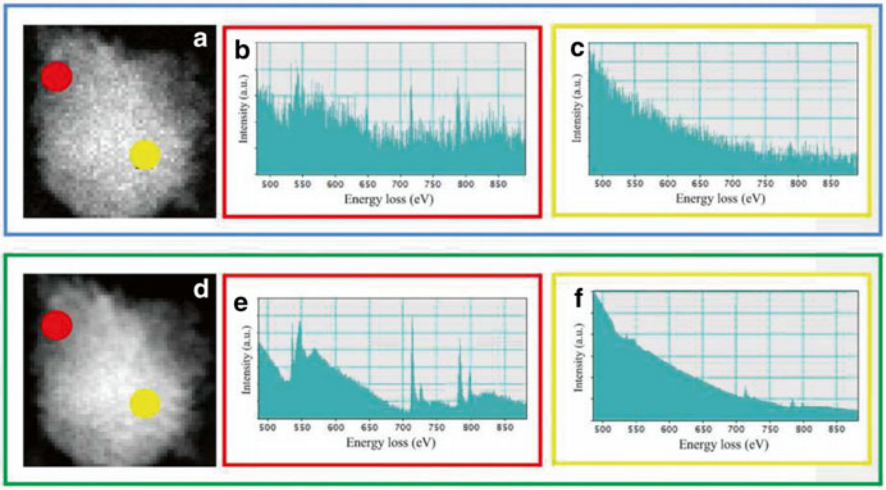

Fig. 6.14 (**a**, **d**) Spectrum images at 68.99° before (framed in *blue*) and after (framed in *green*) PCA-assisted noise reduction. Individual spectra from the edge of the particle [(**b**) and (**e**), in *red*] and the thicker part [(**c**) and (**f**), in *yellow*] are shown. Adapted from Yedra et al. [12]

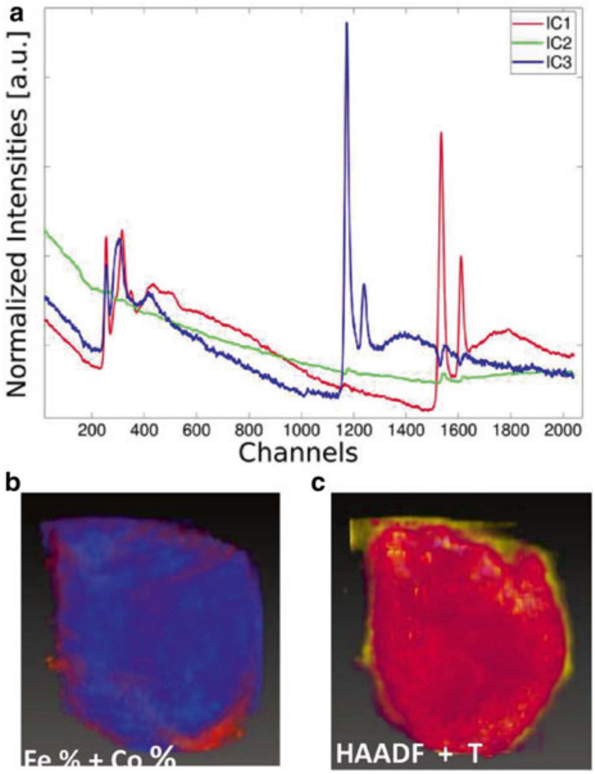

Fig. 6.15 (**a**) Independent components used for the reconstruction. (**b**) Superposition of the vortex with the Co (*blue*) and Fe (*orange*) signals as obtained from quantification. (**c**) Superposition of the vortex with the HAADF signal (*yellow*) and the corresponding thickness maps from ICA (*violet*). Adapted from Yedra et al. [12]

The particles are richer in iron at the edge, and therefore, iron-related chemical signals give a sharp interface between the particle and the background, where HAADF signal is very low and has fallen to background levels due to the small thickness of the sample. These results show that iron signals more precisely reconstruct the edge of the particles than HAADF. On the other hand, the thickness signal has the drawback of underestimating the border more than the HAADF signal (Fig. 6.15). However, the most interesting feature of this signal is that it is insensitive to the chemistry of the sample and independent of multiple scattering, a characteristic not found in any other signal used for electron tomography.

To sum up, EELS-STEM tomography is shown to be able to reconstruct chemical information of a sample in the three spatial dimensions.

6.4.5 Morphology of Sensitive Materials: Cryo-electron Low-Dose Tomography of Phospholipids-Silica Nanocapsules

Owing to the mild conditions required (low temperatures and pressures), the multi-enzyme cascade catalysis is an attractive alternative to chemical catalysis for the production of fine chemicals and to carry out specific reactions. For instance, the use of encapsulated enzymatic systems into silica nanoparticles has been proven to be efficient for the generation of in situ H_2O_2 and for the oxidation of polycyclic aromatic hydrocarbon pollutants in water using O_2 as oxidant (ref. [54] and reference therein). The proof of concept for the encapsulation of polyenzymatic systems in inorganic matrices and its increased efficiency for several reactions has been verified for the last 15 years. However, no direct observation by using microscopy tools has been performed because such systems are very sensitive under the impact of all kinds of radiation.

In electron microscopy, these systems exhibit important electron beam-induced damage similar to the situation of biologic specimens. Performing EM observations on such systems is not straightforward as one needs nanometre resolution within a tomography set-up for treating a complex 3D system and the system is highly sensitive to beam damage. Therefore, the approach considered combines the cryo-TEM and the low-dose electron tomography. A careful analysis of the reconstructed volume has confirmed the presence of nanocapsules with a mean size of 25 nm, made of silica cases with shell thickness of the order of 2–5 nm embedding the polyenzymes. Their shape is rounded and generally the silica shells are continuous, only a few nanocapsules exhibiting opened shells with horseshoe-like shapes (Fig. 6.16).

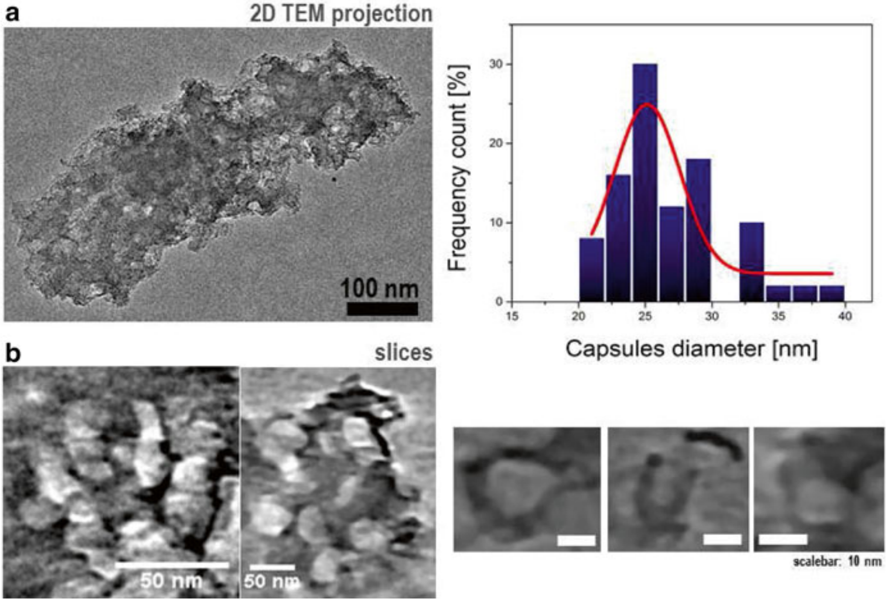

Fig. 6.16 Electron tomography investigation of phospholipids–silica nanocapsules by cryo-TEM low-dose tomography. The arrangement and morphology of nanocapsule assemblies is difficult to explore by (**a**) 2D cryo-TEM, whereas (**b**) volume slicing allowed the direct visualisation of nanocapsule size, shape and spatial arrangement. Reprinted from Cazelles et al. [54]

6.4.6 3D Studies of Physical Properties: Advanced Tomography

Atomically Resolved Tomography: Gold Nanorods

Significant progress has recently been achieved to obtain atomic resolution in 3D. As a matter of fact, the electron tomography at the atom scale offers the possibility not only to probe crystallographic details but to explore other physical properties such as the strains within 3D nano-objects [10, 55–57]. For instance, the group of Antwerp carried out these kinds of experiments on free-standing gold nanorods [55]. They deeply analysed these nanoparticles in 3D, collecting four different high-resolution HAADF-STEM images along different zone axes ([100], [110], [010] and [1-10]) and applying a compressive-sensing-based 3D reconstruction algorithm. Thus, the surface facets of the nanorods, as well as the surface relaxation, were investigated with high precision. From these analyses the authors concluded that these nanorods are mainly composed of {110} and {100} facets (Fig. 6.17a, b), and they also observed the presence of an atomic surface step (Fig. 6.17c), which can have an influence in the properties (catalytic, optical/electronic, mechanical) of these nanoparticles. In addition, they applied the

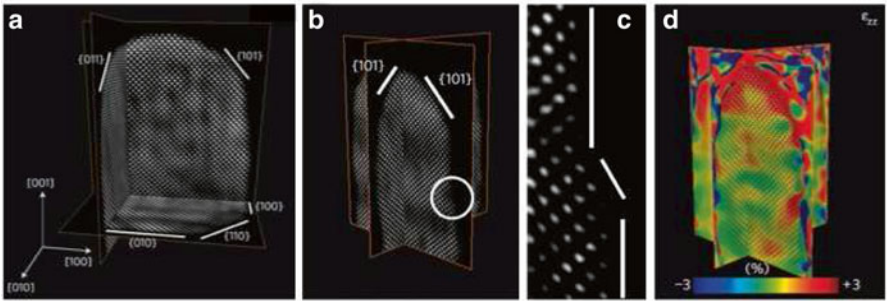

Fig. 6.17 (**a**) Three orthogonal slices through the reconstruction of a nanorod, showing individual atom positions. It can be seen that {110} and {100} facets compose the morphology of the rod. The tip is rounded, with clear terraces at the {101} planes. (**b**) The tip of another nanorod is composed of {101} facets. A region with an atomic surface step is indicated. (**c**) A more detailed view of the region encircled in (**b**). In this region, a surface step with a thickness of two atoms is observed in the tomographic reconstruction. (**d**) Slices through the 3D ε_{zz} strain measurement indicating an outward relaxation of the atoms at the tip of the nanorod. Adapted from Goris et al. [55]

geometrical phase analysis (GPA) to the 3D reconstruction, and they obtained the full 3D ε_{zz} strain field (Fig. 6.17d). The colour code in Fig. 6.17d corresponds to the strain in the nanorod and is scaled between −3 % and +3 %. This map revealed the anisotropy present in the ε_{zz} strain, which again, as also the authors pointed out, could have a significant impact on the optical response of these nanomaterials.

Plasmonic 3D Studies via STEM-EELS Tomography: Silver Nanocubes

In the recent years significant attention has been devoted to the study of noble metallic nanoparticles due to their optical response, which is related to the SPRs. It is well known that particle size, shape and composition, as well as the local dielectric environment of these nanoparticles, have strong impact on these SPRs [36–39, 48]. The combination of a precise 3D morphology and the distribution, at the nanoscale, of each SPR, provides very significant knowledge about the optical response of nanomaterials. In order to get this kind of information, the group of Cambridge developed monochromated STEM-EELS spectrum-imaging (SPIM) with a novel combination of non-negative matrix factorisation (NMF), compressed sensing and electron tomography [39]. Thus, they reconstructed a 3D image of the dominant SPR modes for an individual silver nanocube. These authors acquired STEM-EELS SPIMs at 5 different tilt angles (ranging from −60° to 0°, with 15° step, as they took advantage of the 4 mm symmetry of the Ag nanocube), tilting about a ⟨100⟩ cube axis perpendicular to the electron beam. Using NMF, they performed a blind separation between the different peaks in the STEM-EELS SPIMs and obtained five dominant SPRs for the Ag nanocube and their corresponding 2D maps at each tilt angle. Finally, they employed an iterative compressed sensing tomographic algorithm for obtaining the 3D reconstruction of the distribution of the SPRs (see Fig. 6.18).

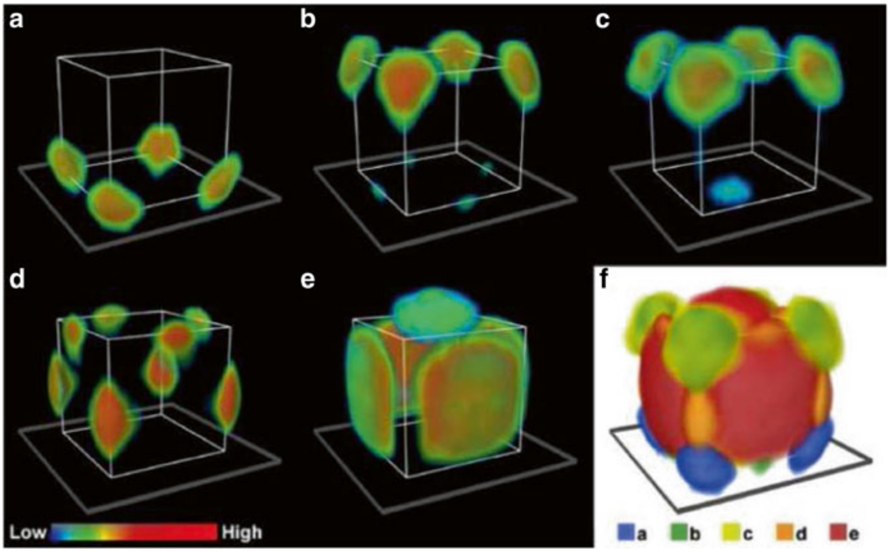

Fig. 6.18 3D visualisation of the SPR modes of an Ag nanocube. The 3D images displayed in (**a**–**e**) were obtained by tomographic reconstruction of the EELS maps of the respective five SPR modes identified by NMF. The visualisations are voxel projections of the reconstructed 3D volumes. The colour bar indicates the SPR intensity. (**f**) Combined 3D rendering of all the modes. Reprinted from Nicoletti et al. [39]

6.5 Conclusions and Perspectives

During the last decades, the material research community has paid increasing attention to the synthesis and the development of nanomaterials, leaving aside the development of means, methods and tools for the complete characterisation, including in 3D, of such objects and structures. We have shown in this review that full characterisation of nanomaterials, nano-objects and complex hybrid nano-systems can be achieved by means of electron microscopy. The electron tomography is the appropriate tool for a complete three-dimensional characterisation, whereas the in situ microscopy can provide key answers on questions relating the material structure and morphology to their behaviour under specific functioning conditions. The methods and approaches described herein are becoming more and more popular for they provide the direct relationship between material characteristics and their performances.

Owing to the variety of recording modes available in a TEM, modes experimentally adaptable to tomography, the 3D information gained covers key issues from nanomaterial morphology to elemental mapping. For instance, the quantitative tomography allows to carry out both qualitative and quantitative evaluations of nano-object porosity, e.g. to ascertain whether we deal with micro- or mesoporous objects, to explore the pores connectivity, to estimate the porous volumes and/or surface areas and so on. It is the only technique capable to check whether nano-objects lie inside or outside hollow structures or to explore the location and distribution of nanoparticles and/or atomic clusters relative to a support. In addition, it is well adapted to accurate morphological studies like nano-crystal faceting, and to a larger extent, it describes quantitatively short- and long-range orders. Certainly, different recording modes can be successfully combined to optimise the quality/quantity of data necessary to access the specific information.

By combining the electron energy loss spectroscopy with the 3D tomography, one accede the three-dimensional chemical information at the nanometre scale: analytical tomography. Two representative examples have been given in this review: (1) the study of industrial silica/alumina catalysers prepared by different methods and (2) assessment of Fe and Co distribution within mesoporous antiferromagnetic Co_3O_4 nanocast replicas of SiO_2 KIT-6 templates filled with $Fe_xCo_{(3-x)}O_4$Co3O4. These approaches have been used to establish the correlation between the morphology of the object, the 3D relative distribution of the elements and its catalytic performance. Although the analytical tomography is a rather volume-selective technique, it gives a clear representation of nanocomposite surface properties as correlated with the surface chemical selectivity. The close correspondence between morphology and chemical composition provides a powerful tool for the analysis of materials at the forefront in catalysis, nano-electronics, therapy or imaging. The analytical tomography is hence expected to have a strong impact in these fields' research in the very next future.

The recent progress in electron microscopy instrumentation and the development of new methodologies pave the path for the development of routine electron tomography with atomic resolution. Only a visionary project in the early 2000s, this vision is becoming more and more realistic, and it will certainly become a reality in the very next future. Further improvements are still needed though, as one first challenge will be to reduce the number of projections needed for obtaining reliable results. In principle, one should be able to increase the SNR in the acquired projections or to access more fragile materials by diminishing the total irradiation dose during the acquisition. A reliable solution to this problem can be the hardware implementation of compressed sensing. There's however one more provocative task to perform, maybe the most challenging one: the implementation of all characterisation techniques on the production chain of nanomaterials, no matter the applications envisioned.

Acknowledgements S.M. and O.E. acknowledge the French electron microscopy and atom probe network METSA. Prof. Clement Sanchez and his research group at Collige de France are acknowledged. We acknowledge the support received from the European Union Seventh Framework Program under Grant Agreement 312483—ESTEEM2 (Integrated Infrastructure Initiative—I3). R.A. acknowledges funding from the Spanish Ministerio de Economia y Competitividad (FIS2013-46159-C3-3-P).

References

1. J. Radon, Ben. Vehr. K. Sächs. Ges. Wiss. Leipzig Math-Phys. Kl. **69**, 262 (1917)
2. D. DeRosier, A. Klug, Reconstruction of three dimensional structures from electron micrographs. Nature **217**, 130 (1968)
3. A. Klug, From macromolecules to biological assemblies (Nobel lecture). Angew. Chem. Int. Ed. **22**, 565 (1983)
4. O. Medalia, I. Weber, A.S. Frangakis, D. Nicastro, G. Gerisch, W. Baumeister, Macromolecular architecture in eukaryotic cells visualized by cryoelectron tomography. Science **298**, 1209 (2002)
5. H. Jinnai, Y. Nishikawa, R.J. Spontak, S.D. Smith, D.A. Agard, T. Hashimoto, Direct measurement of interfacial curvature distributions in a bicontinuous block copolymer morphology. Phys. Rev. Lett. **84**, 518 (2000)
6. Y. Zhao et al., Small-molecule-directed nanoparticle assembly towards stimuli-responsive nanocomposites. Nat. Mater. **8**, 979 (2009)
7. A.J. Kloster et al., Three-dimensional transmission electron microscopy: a novel imaging and characterization technique with nanometer scale resolution for materials science. J. Phys. Chem. B **104**, 9368 (2000)
8. W.L. Ling et al., J. Nanopart. Res. **14**, 806 (2011)
9. D. Vanhecke et al., Cryo-electron tomography: methodology, developments and biological applications. J. Microsc. **242**, 221 (2011)
10. M.C. Scott, C.C. Chen, M. Mecklenburg, C. Zhu, R. Xu, P. Ercius, U. Dahmen, B.C. Regan, J. Miao, Electron tomography at 2.4 angstrom resolution. Nature **483**, 444 (2012)
11. K. Jarausch et al., Four-dimensional STEM-EELS: enabling nano-scale chemical tomography. Ultramicroscopy **109**, 326 (2009)
12. L. Yedra et al., EEL spectroscopic tomography: towards a new dimension in materials analysis. Ultramicroscopy **122**, 12 (2012)
13. S. Goris et al., Monitoring galvanic replacement through three-dimensional morphological and chemical mapping. Nano Lett. **14**, 3220 (2014)
14. A.H. Janssen, A.J. Koster, K.P. de Jong, Three-dimensional transmission electron microscopic observations of mesopores in dealuminated zeolite Y. Angew. Chem. Int. Ed. **40**, 1102 (2001)
15. O. Ersen, J. Werckmann, M. Houllé, M.-J. Ledoux, C. Pham-Huu, 3D electron microscopy study of metal particles inside multiwalled carbon nanotubes. Nano Lett. **7**, 1898 (2007)
16. O. Ersen, C. Hirlimann, M. Drillon, J. Werckmann, F. Tihay, C. Pham-Huu, C. Crucifix, P. Schultz, 3D-TEM characterization of nanometric objects. Solid State Sci. **9**, 1088 (2007)
17. H. Friedrich, J.R.A. Sietsma, P.E. de Jongh, A.J. Verkleij, K.P. de Jong, Measuring location, size, distribution, and loading of NiO crystallites in individual SBA-15 pores by electron tomography. J. Am. Chem. Soc. **129**, 10249 (2007)
18. P.A. Midgley, M. Weyland, J.M. Thomas, B.F.G. Johnson, Z-Contrast tomography: a technique in three-dimensional nanostructural analysis based on Rutherford scattering. Chem. Commun. **10**, 907 (2001)
19. P.A. Midgley, M. Weyland, 3D electron microscopy in the physical sciences: the development of Z-contrast and EFTEM tomography. Ultramicroscopy **96**, 413 (2003)
20. G. Mobus, R.C. Doole, B.J. Inkson, Spectroscopic electron tomography. Ultramicroscopy **96**, 433 (2003)
21. L. Roiban, L. Sorbier, C. Pichon, P. Bayle-Guillemaud, J. Werckmann, M. Drillon, O. Ersen, Three-dimensional chemistry of multiphase nanomaterials by energy-filtered transmission electron microscopy tomography. Microsc. Microanal. **18**, 1118 (2012)
22. I. Florea, A. Demortière, C. Petit, H. Bulou, C. Hirlimann, O. Ersen, Electron tomography and 3D molecular simulations of platinum nanocrystals. Nanoscale **2**, 2668 (2010)
23. P.A. Midgley, E.P.W. Ward, A.B. Hungría, J.M. Thomas, Nanotomography in the chemical, biological and materials sciences. Chem. Soc. Rev. **36**, 1477 (2007)
24. P.A. Midgley, C. Durkan, The frontiers of microscopy. Mater. Today **11**, 8 (2008)

25. J. Frank, B.F. McEwan (eds.), (Plenum, New York, 1992), p. 91
26. M.H. Gass, K.K.K. Koziol, A.H. Windle, P.A. Midgley, Four-dimensional spectral tomography of carbonaceous nanocomposites. Nano Lett. **6**(3), 376 (2006)
27. G. Möbus, B.J. Inkson, Three-dimensional reconstruction of buried nanoparticles by element-sensitive tomography based on in elastically scattered electrons. Appl. Phys. Lett. **79**, 1369 (2001)
28. M. Radermacher, Radon transform techniques for alignment and three-dimensional reconstruction. Scanning Microsc. **11**, 171 (1997)
29. K.J. Batenburg, S. Bals, J. Sijbers, C. Kübel, P.A. Midgley, J.C. Hernandez, U. Kaiser, E.R. Encina, E.A. Coronado, G. Van Tendeloo, 3D imaging of nanomaterials by discrete tomography. Ultramicroscopy **109**, 730 (2009)
30. G.L. Zeng, Image reconstruction—a tutorial. Comput. Med. Imaging Graph. **25**, 97 (2001)
31. W.O. Saxton, What is the focus variation method—is it new—is it direct. Ultramicroscopy **13**, 57 (1984)
32. R.A. Crowther, D.J. DeRosier, A. Klug, The reconstruction of a three-dimensional structure from projections and its application to electron microscopy. Proc. R. Soc. Lond. A **317**, 319 (1970)
33. R. Gordon, R. Bender, G.T. Herman, Algebraic reconstruction techniques (ART) for three-dimensional electron microscopy and x-ray photography. J. Theor. Biol. **24**, 471 (1970)
34. P. Gilbert, Iterative methods for the three-dimensional reconstruction of an object from projections. J. Theor. Biol. **36**, 105 (1972)
35. Z. Saghi, D.J. Holland, R. Leary, A. Falqui, G. Bertoni, A.J. Sederman, L.F. Gladden, P.A. Midgley, Three-dimensional morphology of iron oxide nanoparticles with reactive concave surfaces. A compressed sensing-electron tomography (CS-ET) approach. Nano Lett. **11**, 4666 (2011)
36. L. Novotny, B. Hecht, *Principles of Nano-Optics* (Cambridge University Press, Cambridge, 2006)
37. S.A. Maier, *Plasmonics: Fundamentals and Applications* (Springer, Berlin, 2007)
38. L.M. Liz-Marzan, Langmuir **22**, 32–41 (2006)
39. O. Nicoletti, F. de la Peña, R.K. Leary, D.J. Holland, C. Ducati, P.A. Midgley, Three-dimensional imaging of localized surface plasmon resonances of metal nanoparticles. Nature **502**, 80–84 (2013)
40. L. Borowik, I. Florea, D. Deresmes, O. Ersen, D. Hourlier, T. Mélin, Surface and intrinsic conduction properties of Au-catalyzed Si nanowires. J. Phys. Chem. C **116**, 6601–6607 (2012)
41. I. Janowska, F. Vigneron, D. Bégin, O. Ersen, P. Bernhardt, T. Romero, M.J. Ledoux, C. Pham-Huu, Mechanical thinning to make few-layer graphene from pencil lead. Carbon **50**, 3092 (2012)
42. A. Ciesielski, S. Haar, M. El Gemayel, H. Yang, J. Clough, G. Melinte, M. Gobbi, E. Orgiu, M.V. Nardi, G. Ligorio, V. Palermo, N. Koch, O. Ersen, C. Casiraghi, P. Samori, Harnessing the liquid-phase exfoliation of graphene using aliphatic compounds: a supramolecular approach. Angew. Chem. Int. Ed. **53**(39), 10355 (2014)
43. I. Janowska, O. Ersen, T. Jacob, P. Vennegues, D. Begin, M.J. Ledoux, C. Pham-Huu, Catalytic unzipping of carbon nanotubes to few-layer graphene sheets under microwaves irradiation. Appl. Catal. A **371**, 22 (2009)
44. G. Melinte, I. Florea, S. Moldovan, I. Janowska, W. Baaziz, R. Arenal, A. Wisnet, C. Scheu, S. Begin-Colin, D. Begin, C. Pham-Huu, O. Ersen, A 3D insight on the catalytic nanostructuration of few-layer graphene. Nat. Commun. **5**, 4109 (2014)
45. D. Ihiawakrim, O. Ersen, F. Melin, P. Hellwig, I. Janowska, D. Begin, W. Baaziz, S. Begin, C. Pham-Huu, R. Baati, Non-covalent functionalization of graphene with hexahistidine-pyrene amphiphiles in water: stepwise construction of 2D-nanostructured composites with iron oxide nanoparticles. Nanoscale **5**, 9073 (2013)
46. T. Fontecave, C. Sanchez, T. Azais, C. Boissiere, Chemical modification as a versatile tool for tuning stability of silica based mesoporous carriers in biologically relevant conditions. Chem. Mater. **24**, 4326 (2012)

47. T. Fontecave, C. Boissiere, N. Baccile, F.J. Plou, C. Sanchez, Using evaporation-induced self-assembly for the direct drug templating of therapeutic vectors with high loading fractions, tunable drug release, and controlled degradation. Chem. Mater. **25**, 4671 (2013)
48. R. Arenal, L. Henrard, L. Roiban, O. Ersen, J. Burgin, M. Treguer-Delapierre, Local plasmonic studies on individual core-shell gold–silver and pure gold nano-bipyramids. J. Phys. Chem. C **118**, 25643–25650 (2014)
49. V. Pierron-Bohnes, I. Florea, O. Ersen, C. Ulhaq-Bouillet, C. Goyhenex, N. Braidy, C. Ricolleau, Y. Le Bouar, D. Alloyeau, Atomic-scale faceting in CoPt nanoparticles epitaxially grown on NaCl. Cryst. Growth Des. **14**(5), 2201 (2014)
50. Baaziz, I. Florea, S. Moldovan, V. Papaefthimiou, S. Zafeiratos, S. Begin-Colin, D. Begin, O. Ersen, C. Pham-Huu, Microscopy investigations of the microstructural change and thermal response of cobalt-based nanoparticles confined inside a carbon nanotube medium. J. Mater. Chem. A. (2015). doi:10.1039/C5TA00283D
51. M.S. Moldovan, H. Bulou, Y.J. Dappe, I. Janowska, D. Begin, C. Pham-Huu, O. Ersen, On the evolution of Pt nanoparticles on few-layer graphene supports in the high-temperature range. J. Phys. Chem. C **116**, 9274 (2012)
52. J.-Y. Bigot, H. Kesserwan, V. Halté, O. Ersen, M.S. Moldovan, T.H. Kim, J.-t. Jang, J. Cheon, Magnetic properties of annealed core-shell CoPt nanoparticles. Nano Lett. **12**, 1189 (2012)
53. R. Arenal, F. de la Pena, O. Stephan, M. Walls, M. Tence, A. Loiseau, C. Colliex, Extending the analysis of EELS spectrum-imaging data, from elemental to bond mapping in complex nanostructures. Ultramicroscopy **109**, 32 (2008)
54. R. Cazelles, J. Drone, F. Fajula, O. Ersen, S. Moldovan, A. Galarneau, Reduction of CO_2 to methanol by a polyenzymatic system encapsulated in phospholipids–silica nanocapsules. New J. Chem. **37**, 3721 (2013)
55. B. Goris, S. Bals, W. Van den Broek, E. Carbó-Argibay, S. Gómez-Graña, L.M. Liz-Marzán, G. Van Tendeloo, Atomic-scale determination of surface facets in gold nanorods. Nat. Mater. **11**, 930 (2012)
56. S. Van Aert, K.J. Batenburg, M.D. Rossell, R. Erni, G. Van Tendeloo, Three-dimensional atomic imaging of crystalline nanoparticles. Nature **470**, 374–377 (2011)
57. S. Bals et al., Three-dimensional atomic imaging of colloidal core-shell nanocrystals. Nano Lett. **11**, 3420–3424 (2011)

Chapter 7
In Situ TEM of Carbon Nanotubes

Pedro M.F.J. Costa and Paulo J. Ferreira

7.1 Introduction

The recognition that in situ TEM can be used as a powerful tool for the dynamic characterization of materials has been widely established. However, with the advent of CCD and direct detection cameras, and the development in electron optics, stage design and fabrication, and recording media, scientists and engineers are now being able to further enhance the capabilities of previous TEM analysis through novel in situ experiments, by observing and recording the behavior of materials in different conditions, such as heating, cooling, stress, light, electric fields, as well as liquid and gas environments. This technique has been critical in understanding and characterizing the relationship between properties and the nano/microstructure of materials and has been important in validating the information contained in previous single static TEM experiments with a series of dynamic sequential images. In addition, the emerging development of nanomaterials, a field which has become one of the most promising fields of science and technology today, has brought an exciting resurgence of interest in in situ TEM, as the previous issue of thinning bulk specimens is no longer present.

Currently, the development of aberration-corrected TEM/STEMs, direct detection cameras, and the miniaturization of specimen holders have created new opportunities for in situ TEM. In the case of aberration-corrected TEM/STEMs, the

---

P.M.F.J. Costa (✉)
Physical Sciences and Engineering Division, King Abdullah University
for Science and Technology, Thuwal 23955-6900, Saudi Arabia
e-mail: pedro.dacosta@kaust.edu.sa

P.J. Ferreira
Materials Science and Engineering Program, University of Texas at Austin,
Austin, TX 78712, USA

F.L. Deepak et al. (eds.), *Advanced Transmission Electron Microscopy*,
DOI 10.1007/978-3-319-15177-9_7

incorporation of additional lenses to reduce and/or eliminate the spherical aberration (C_s) of the objective lenses allows for wider pole-piece gaps and consequently more experimental flexibility, despite the fact that higher chromatic aberration (C_c) coefficients of lenses are expected. The new detection cameras, where electrons in the TEM image are detected directly in the image sensor, eliminating the use of scintillators with fiber optics or lenses, provide 1,600 frames per second, a major improvement from the common TV rates of 30 frames per second. This permits the design of novel experiments, capable of monitoring a broad hierarchy of length and time scales. In other words, the behavior at each scale can be captured in real time, from atomistic to microscale (grain level) to mesoscale (multigrain) and finally to macroscale. The miniaturization in the manufacturing of specimen holders has facilitated the variety of experiments that can be performed, as it does not require specially designed columns (as for gas experiments), exhibits less restrictions with respect to narrow pole-piece gaps, and, in some cases, is capable of exposing or stimulating a sample to a diverse number of stimuli.

For the selection of the in situ specimen holder, the first consideration goes into assessing which pole-piece gap is installed in the TEM, as it determines the type of holders that will fit the instrument and the image resolution. High resolution requires short focal lengths in conventional TEM lenses, which inevitably restrict specimen tilting and limit access to the specimen. Modern TEM/STEMs (uncorrected and aberration-corrected) are typically equipped with a URP ultrahigh resolution pole piece (gap = 2 mm) or an ARP analytical pole piece (gap = 4.5 mm). The ARP pole piece can accommodate any commercial specimen holder, whereas the URP pole piece cannot. Although not capable of achieving the highest resolution, the ARP provides adequate resolution, especially in aberration-corrected TEM/STEMs. In addition, it allows considerable more sample tilting, which is crucial for some types of material analysis. Secondly, it is important to decide whether to use a single-tilt or double-tilt holder. In particular, most of the commercial dedicated holders, as, for example, heating, cooling, and others, are equipped with single-tilt capability. Double-tilt holders are less frequent and more expensive but sometimes critical in providing the ability to reach specific zone axes. Another major consideration concerning the choice of a holder is the issue of sample drift. This is particularly true for the case of in situ heating, electrical and light holders, where heat is transferred from the sample region to the rest of the holder, leading to significant drift.

Having in mind these issues, there are a wide variety of commercial in situ specimen holders readily available, including heating, electrical, cooling, liquid, gas, tomography, electrochemical, straining, and nanoindentation holders. However, most of these holders allow only one external stimulus to be applied to the sample. Thus, to combine various stimuli in a single holder as, for example, temperature and straining, is still a major challenge. The use of MEMS-based and piezo-actuated in situ holders allows the integration of devices with a suitable size to be accommodated within narrow pole-piece gaps and permits a wide range of experiments to be performed where real-time TEM observations under combined external stimuli can be made.

7.2 Experimental Requirements and Challenges for In Situ TEM of CNTs

Carbon nanotubes have been extensively studied driven by interests at different levels which range from basic science phenomena (ballistic conduction [1], quantum dot behavior [2], etc.) to technological applications (electromechanical resonators [3], nanoelectronics components [4], chemical sensors [5], etc.). Among these materials, a one-dimensional heterostructure of two different materials harbors immense potential for applications of nanomaterials [6, 7]. This is because of two reasons: firstly, it provides a single system of two different materials. Secondly, such systems are rich in properties due to contributions from different constituents along with that from the interfacial region having a markedly different behavior, which is not negligible at this length scale (tens of nanometer range).

Starting with the selection of the microscope, as CNTs are 1D nanostructures, it is best to use instruments with high spatial resolution, in particular aberration-corrected TEMs. Besides the fact that these TEMs can achieve the best possible spatial resolution (as high as 0.5 Å), delocalization effects are minimized, which facilitates imaging of the CNT's surfaces or interfaces. Second, still due to the morphology of CNTs, it is challenging to observe these structures parallel to the long axis. This requires dedicated sample preparation, where the CNTs are mounted, sectioned perpendicular to the long axis, and finally observed.

Possibly, the most important is to ensure that the effect of the electron beam is well characterized or, at least, minimized. Knock-on radiation damage is a known effect that may significantly influence the outcome of CNT observations, in particular when probing specific physical properties of these nanostructures. Given the generally accepted damage threshold of 86 kV for carbon, in situ TEM studies of CNTs should be performed below this value. Yet, the sputtering threshold voltage, which is about half of the displacement threshold for bulk solids but differs for all-surface nanostructures, should be taken into account. Particularly for single-walled CNTs (and graphene), all atoms reside on the surface which implies they can be more easily knocked away (more so for the edge and corner atoms) [8].

Another thing to bear in mind is the two-dimensional nature of TEM imaging. Images are projected and therefore real dimensions of the nanotubes may not be exactly as measured from the micrographs. It is possible to minimize the projecting effect by tilting the freestanding nanotubes until the maximum projected length is obtained. Other issues are more specific to each technique such as ensuring robust contacts in mechanical probing of CNTs. One recent article highlights these issues for environmental TEM but constitutes a good starting point also for other in situ experiments [9].

In the following, we have divided the chapter according to the predominant applied stimulus. Each section is then subdivided by categorizing the CNTs in raw or modified (hybrid) structures. Given the ubiquitous presence of the electron beam, we consider the irradiation stimulus as a first level of in situ TEM experiments and therefore it is described first. Higher levels of sample stimulation follow and include

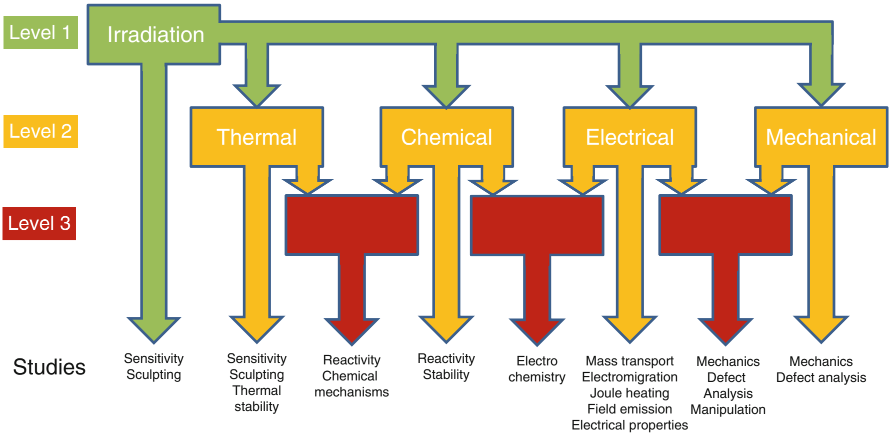

Fig. 7.1 Diagram summarizing the different stimuli and types of experiments available for CNT in situ TEM analysis. Level 1 is common to all techniques and does not require a specialized holder or column configuration. Level 2 usually requires purpose-built instrumentation and may be used in tandem with level 1 methods (irradiation). Level 3 combines two different methods from the level(s) above

thermal, chemical, electrical, and mechanical experiments. In all cases, these higher order stimuli may be used isolated (e.g., mechanical) or combined (e.g., irradiation-thermal) (Fig. 7.1).

7.3 Irradiation

Electron beam irradiation is the basic tool that should be first considered in in situ TEM studies. The same beam that is used to image the specimen can be utilized as a shaping tool to engineer nanotubes with nm precision. Over the years, using the electron beam to tailor the shape and function of carbon nanotubes has been very commonly employed, as it will be shown below. The key immediate issue is effectively, for most in situ TEM experiments, on how to dissociate the influence of the ever-present electron beam from the effect of other stimuli applied to nanotube samples within the column. Over the next paragraphs, we will discuss the major areas in which this tool has been used on its own to alter specimens or study their resilience to irradiation damage.

Carbon Nanotubes

An early report on the systematic study of the effect of the electron beam irradiation on CNTs was written by Crespi et al. in 1996 [10]. The authors used a beam of 800 kV (at 2×10^5 e/nm^{2}s dose rate) to promote the collapse of arc-made multiwalled carbon nanotube (MWCNT) structures. These are known for their well-ordered graphitic structure and clearly defined inner tubular void. In addition to the time-resolved micrographs, molecular dynamics simulations were carried out, which helped understanding anisotropic damage distribution, as well as the collapse of the inner tubule. Different displacement energies were seen to be dependent on the direction of the beam to the nanotube's major axis. In fact, the damage is mostly induced at the front and back of the nanotube when the electron beam is normal to the CNT's main axis. At this orientation, electron channeling effects are minimal.

Two years later, another team explored the subject of structural stability of CNTs with a lower energy beam (200 kV) and using single-walled carbon nanotubes (SWCNTs) [11]. Working at current densities of 0.1–1 A/cm^2, the CNTs were seen to undergo diameter reductions from 1.4 to 0.4 nm. Necking preceding the total nanotube rupture was monitored and imaged. Molecular dynamics simulations sustained the nonuniform atomic displacement and subsequent surface reconstruction into a nonhomogenous structure. The reconstruction mechanism proposed, which continued down to diameters of 0.4 nm, was based on dangling bond saturation and the Stone-Wales process. The authors further speculated that the final stage before complete rupture would be the generation of linear atomic C chains.

In these early days, besides the study of structural degradation, beam irradiation was used to study the mechanical properties of SWCNTs [12]. Young's modulus of discrete, freestanding nanotubes was extracted from the analysis of their vibration amplitude upon the incidence of a 100 kV electron beam (dose rate of 800 e/nm^{2}s). The structures selected were less than 100 nm long, 1–1.5 nm in diameter, and assumed to behave as a clamped cantilever. Working at room temperature, the average modulus obtained from 27 nanotubes was 1.25 TPa, thus 25 % higher than the accepted in-plane modulus of graphite.

It is interesting to notice that some groups were already imaging and studying CNTs at relatively low accelerating voltages for in situ studies from as early as 1996 [13]. However, up until 2001, some doubts persisted on the necessity to lower the beam energy (200 kV and 300 kV observations were the most common then). Smith and Luzzi wrote what became a classic article on how the electron irradiation inherent to the TEM observation of nanotubes may influence their structure, in particular for SWCNTs [14]. In agreement with previous work [10], the surfaces lying normal to beam direction were the most affected. In these cases, a carbon atom could be displaced from its position when employing beams of 86 kV or more. For higher energies (>139 kV), any atom in a SWCNT was susceptible to be knocked out (irrespective of its position or orientation of the beam). More than a decade later, it is fair to say that the realization of this low voltage threshold was one of the main drivers for TEM manufacturers to seriously consider the production of instruments working at less than 100 kV. In fact, current TEMs can already work at 60 kV, while 40 kV instruments will be available soon (Fig. 7.2).

Given the direct relation between spatial resolution and beam energy, lowering the working voltage had immediate consequences on the quality of high-resolution micrographs. Fortunately, aberration-corrected microscopes were then becoming more common. In 2004, Hashimoto et al. presented an electron irradiation study

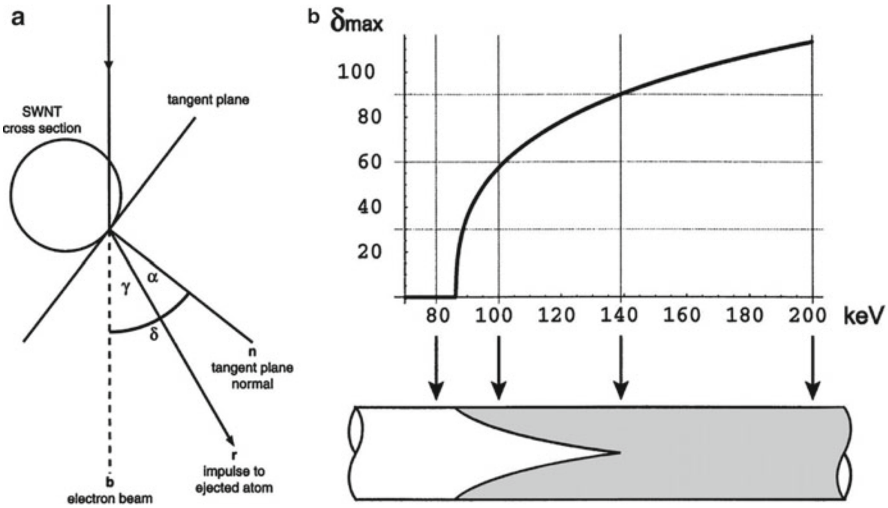

Fig. 7.2 (**a**) Cross-sectional illustration of the displacement of a carbon atom by primary knock-on, where $\delta = \alpha + \gamma$. (**b**) At ~140 kV, $\delta_{\max} = 90°$, which implies that all carbon atoms can be ejected ballistically. The *shaded* area corresponds to the locations where knock-on takes place. Adapted from [14] with permission

providing the first evidence for the formation of atomic defects in SWCNTs [15]. Working at 120 kV and a total electron dose of 60,000 e/nm^2, the team tuned the microscope's contrast transfer function to certify that voids or lattice vacancies would be observed as bright spots. Besides identifying point defects expressively induced in the CNT, adatoms in the carbon lattice were also imaged.

Recently, one interesting study of high-energy particle irradiation of SWCNT was described where the active beam was composed not of electrons but of Kr cations [16]. These 30 kV particles were directed to the carbon nanostructures and observed at 100 kV (imaging beam of electrons) using a unique facility available at the Argonne National Laboratory (USA). At Kr$^+$ dose rates of up to 1×10^{14} cm^{-2} s^{-1}, the nanotubes look largely unchanged at low magnification. However, raising the rate will lead to the accumulation of defects and then eventual amorphization and finally followed by total disintegration of the nanotubes.

Hybrid Carbon Nanotubes

Mixing carbon nanotubes with other materials, thereby forming composite (or hybrid) structures, has been a subject of study almost since the 1991 groundbreaking work of Iijima [17]. In this respect, an investigation of hybrid CNTs using in situ TEM methods was reported in 1998 [18]. This work also constituted a milestone on the topic of C$_{60}$ encapsulated SWCNTs, also known as peapods. Prolonged exposure to a 100 kV beam led to the observation of coalescence of the confined C_{60} molecules into dimers and elongated fullerene capsules. This merging behavior and other dynamical phenomena were further studied in a subsequent report by the same team [19]. Coaxial (or double-walled) nanotubes wherein the inner nanotube was roughly half the diameter of the outer one were fabricated in situ, and a remarkable translation movement of C_{60} clusters in the tubular channels was reported and explained to be the result of beam-specimen interactions. Some closely related in situ TEM studies (using heating holders) on this material followed but these will be described further on.

In 2007, a pyrrolidine-functionalized C_{60} molecule was imaged attached to the external surface of a SWCNT [20]. The decorating fullerene was seen to gradually degrade under the incidence of the 120 kV electron beam, particularly at doses higher than 100,000 e/nm^2. The images taken with an aberration-corrected microscope showed that it was possible to visualize a single molecule and that the pyrrolidine chain did not break up during the observations. The latter is particularly interesting given the short length of the hydrocarbon chain. The same team reported another study where the beam-induced dynamics of C_{80} and $Er_3N@C_{80}$ were described [21]. Orientation shifts and translation motion of individual molecules were clearly visualized and the respective images simulated.

Besides fullerenes, other substances can be confined in CNTs. Similar to the case of peapods, chemical reactions, ionization, and atomic displacements can also take place in the tubular channel. The first reported case of such transformations in an encapsulated inorganic crystal was for the photolytic reduction of AgBr to metallic Ag [22]. The beam sensitive halide was difficult to image due to the beam irradiation action. This work was, moreover, one of the first articles detailing the filling of SWCNTs with different types of inorganic materials.

In 2001, another encapsulated metal halide ($ZrCl_4$) was seen to progressively lose chlorine under continued 300 kV beam irradiation (dose rate of 5×10^5 e/nm^{2}s) [23]. The originally one-dimensional crystal underwent a structural change, which resulted in the formation of zirconium chloride clusters. The authors suspected that the segregation, if continued until complete depletion of the chlorine, would eventually produce chains of metallic Zr clusters.

A later report from the same team delved into the dynamical behavior of a metal oxide encapsulated in SWCNTs [24]. Subjected to the irradiation of a 300 kV electron beam (dose rate of 5×10^5 e/nm^{2}s), clusters of rhenium oxide were seen to rotate inside the minute channel of the host nanotube. This movement was attributed to the concomitant loss of oxygen. Interestingly, the oxide clusters could be reduced in tubulo to metallic Re when exposed (ex situ) to a hydrogen flow. While some of the particles sintered, forming structures akin to rods, the remaining discrete Re clusters were more stable under the beam.

Albeit not so common, in situ TEM studies have also looked into the interaction of water with the internal CNT channel. MWCNTs with narrow 2–5 nm channels retained small volumes of water that were locally heated using the electron beam [25]. The fluid dynamics of the aqueous filling was followed and wet-dry transitions along with disordered gas/liquid interfaces were dissimilar to the observations made for larger bore (>10 nm) nanotubes containing water [26]. For these narrower systems, a slower than expected response of the aqueous fluid was reported which suggests that large and efficient transport of liquids within CNTs may be difficult to realize.

Polymer composites with CNT fillers were another type of material studied with beam irradiation in TEM [27]. Using a 200 kV microscope, cracks were initiated and propagated along the composite films. The area most prone to fail was the one with lower density of CNTs. The results clearly show the CNTs aligning across the crack as bridges and eventually breaking or pulling out from the matrix. This was an elegant way to show how the tensile load transferred to the CNTs and explained the increments of the mechanical properties of the polymer with just 1 % filler loading.

While by no means exhaustive of all that has been done over the past two decades, the previous paragraphs demonstrate that it is possible to perform a wealth of different in situ TEM studies having as object of interest CNT-based materials and without resorting to dedicated instrumentation.

7.4 Thermal

The structural and thermal stability of nanostructures can be studied under a microscope in vacuum by heating them with a specialized holder. The range of temperatures for experiments that can be performed in the TEM is indeed vast going from liquid helium to 1,473 K. Furthermore, processes can today be recorded at rates of milliseconds or faster with the most recent direct detection cameras. Using the thermal stimulus in tandem with the high-energy electrons provides further capabilities to analyze and tailor CNTs, as written below. In this respect, reference [28] provides a useful overview of how one may combine the dual action of irradiation heating applied to carbon nanostructures.

Carbon Nanotubes

The use of TEM heating holders for the study of dynamical events related to CNTs was described by Treacy and colleagues in 1996 [13]. This team calculated the Young's modulus of individual structures based on their intrinsic thermal vibrations (300–600 K) at 100 kV and under vacuum. Interestingly, temperature was the dominating stimuli to control the vibrations, as the authors refer that altering the electron beam density would affect the motion considerably. The nanotubes were freestanding, acting as clamped cantilevers and assumed as a homogenous cylindrical body. The method shows some limitations as it is best suited for short and small-diameter structures while measuring the maximum displacement can be challenging, particularly at 600 K. Still, the figures extracted for the modulus ranged from 0.4 to 4.2 TPa, which agreed with the known in-plane modulus of graphite (1 TPa).

Combining high temperatures with very high voltages to observe the response of SWCNTs was an idea explored a few years later [29]. At 1,073 K and 1.25 MV irradiation, adjoining nanotubes with equivalent chirality rearranged and coalesced along their length in a zipper-like fashion. Molecular dynamics simulations helped explaining this phenomenon. Following the generation of vacancies in the carbon lattice (by knock-on), reconstruction of the surface takes place followed by thermal annealing. Given the large number of rearrangements that would be necessary for different chirality CNT pairs, the coalescence of these was found unlikely (Fig. 7.3).

A follow-up on this study was published in 2002 [30]. Working at 1.25 MV, 1,073 K, and a beam intensity of 10 A/cm^2, molecular junctions were fabricated from two crossing, superposed SWCNTs. Several types of connections were achieved, namely, *T*, *X*, and *Y* shapes. Molecular dynamics simulations provided a mechanism based on the generation of dangling bonds followed by intertube cross-linking. The reconstructed interface involved the presence of seven and eight membered rings supposedly to provide negative curvature and increase the energetic stability of the joint. The work paved way to the possibility of constructing tailored networks of carbon nanotubes using the tandem action of the sculpting electron beam and the heat-induced structural annealing.

The combination of irradiation-heat was used in 2004 to engineer both bundles and discrete CNTs [31]. Instead of an almost parallel beam, a converged probe

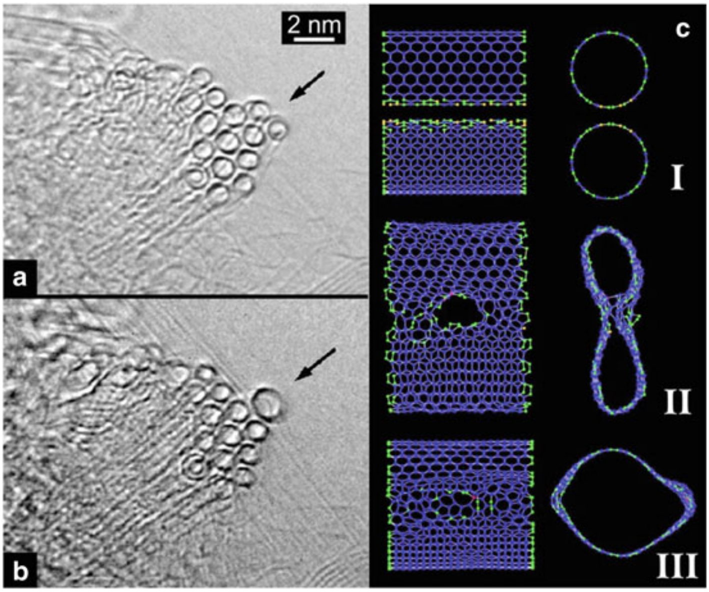

Fig. 7.3 (**a**) Bundle of SWCNTs viewed end-on. (**b**) The bundle in (**a**) after irradiation at 1.25 MV and 1,073 K for some seconds; the coalesced nanotube (*arrowed*) is almost 2 nm in diameter. (**c**) Molecular dynamics simulation of the coalescence between two (10, 10) SWCNTs (I). After 100 ps (II), the lattices are being connected by a zipping mechanism which is completed at 150 ps, leading to a 2.6 nm nanotube (III). Adapted from [29] with permission

(at 1×10^4 A/cm^2) was employed to modify and cut through the nanotubes. Single- and multi-walled CNTs were sculpted at 873 K with a 300 kV beam. Depending on the size of the probe, sections from individual layers of MWCNTs could be eliminated or bending of the nanotubes induced. Bundles of SWCNTs were continuously irradiated for 28 min at 50 A/cm^2 to undergo a coherent transition to a multiwalled structure. Up to this point, this change had only been achieved by thermal annealing. The possibility of performing this type of work was explained by the higher mobility of interstitials at elevated temperatures. While these become mobile and dominate the structural annealing process, vacancies, on the other hand, remain mostly steady, thus prompting the increased curvature of the irradiated nanotubes.

The production and migration of the interstitials under the conditions mentioned were further analyzed by Banhart et al. [32]. Arc-made MWCNTs and bundles of SWCNTs were irradiated with converged 300 kV beams (60–500 A/cm^2) at 873 K and their structural changes recorded. Shrinkage of the nanotubes invariably took place at the probed area with the rate of carbon atoms displacement being dependent on the diameter of the nanotubes. Due to the smaller curvature, the carbon atoms from the inner shells are primarily knocked out of their positions and diffusion of the interstitials takes place along the inner cavity.

The concept of nanotubes acting as pipes for the transport of interstitials was further developed 3 years later [33]. For this work, bundles of SWCNTs were used and modified at 673–1,173 K under a 300 kV beam (converged probe current density of 2,000–4,000 A/cm^2). Sustained by Monte Carlo simulations, it was shown that the migration barrier for C interstitials trapped inside SWCNTs was 0.25 eV. The mobility, however, was dependent on the temperature of the system and the speed at which the probe cut through the nanotube.

The topic of defect formation, particularly interlayer ones, was studied using double-walled CNTs (DWCNTs) irradiated at 120 kV (estimated dose rate of 60,000 e/nm^{2}s) and temperatures ranging from 90 to more than 900 K [34]. Defects bridging adjacent layers were identified and interpreted as clusters of interstitial-vacancy pairs. At higher temperatures these were fairly transient due to the fast recombination of the interstitial-vacancy pairs. However, at temperatures below 450 K, the rate of formation-annihilation was slow enough to allow imaging by TEM. Notably, the authors were able to identify the presence of a temperature threshold (450–500 K) for the deactivation of the recombination barrier which concurred with the expected annealing temperature for the Wigner energy release.

In addition to the study of beam-induced defects and sculpting of carbon nanostructures, novel designs of heating stages were developed and used to test the ultimate thermal stability of MWCNTs [35]. Temperatures of up to 3,200 K were reached that did not seem to affect the atomic integrity of these nanostructures which furthermore could still withstand electrical current densities on the order of 10^8 A/cm^2. Finite element analysis was employed to estimate the temperature distribution on the electrically heated membrane containing the CNT. To read experimentally the temperature, Au nanoparticles were used as local markers (given their well-defined melting temperature and immediately subsequent evaporation). To date, this remains one of the unique in situ TEM studies confirming the extreme thermal stability of arc-made MWCNTs (which surpassed all other known carbon allotropes).

Hybrid Carbon Nanotubes

Likely, the first report of in situ TEM observations with a heating holder loaded with hybrid carbon nanotubes was published in 2000, when Luzzi and Smith followed the diffusion and coalescence processes in peapods [36]. The exposure to the 100 kV beam (dose rate of 3.4×10^{19} e/cm^{2}s) was complemented by a temperature window of 498–723 K, from which it was possible to observe the onset of C_{60} molecules momentary adsorption on the surface of SWCNTs. By further performing in situ annealing experiments of fullerene-SWCNT mixtures (at 723 K), the authors were able to confirm that the C_{60} inclusion synthesized ex situ took place not during acid purification or thermal cleaning (at 498 K) but instead at the final annealing step.

The observation of dynamical behavior in peapods went a step further when atomic-resolved motion was studied [37]. Starting from a metalofullerene system imaged at 117 kV and temperatures down to 100 K, time-resolved series of micrographs showed that the cage confined Gd atoms ($Gd_2@C_{92}$) were highly mobile. Its motion could be slowed by decreasing the temperature allowing clearer definition of the single atoms position and their amplitude of movement. Interestingly, the metallofullerene poles and respective Gd^{3+} cations are preferentially aligned with the SWCNT major axis.

Around the same time, the concept of a nano-thermometer based on filled CNTs was introduced [38]. Ga was used as a thermal indicator due to the large interval of temperatures at which it remains liquid (from 303 to 2,676 K). Employing a TEM heating holder, the temperature was repeatedly varied between 323 and 773 K. This resulted in linear thermal expansion/contraction of the filling as measured by the translation of the meniscus along the nanotube capsule. To date, this system remains the certified Guinness World Records holder for the smallest thermometer ever produced by mankind.

In 2006, various metal-filled CNT systems, derived from metallocene-based pyrolytic growth, were studied under intense 300 kV beam irradiation (100–600 A/cm^2) and 873 K [39]. The encapsulated wires of the transition metals Fe, Co, and the carbide Fe_3C were continuously exposed to stringent conditions that led to their deformation, supposedly due to pressure buildup as the host nanotube collapsed on them. A direct reading of the pressure was not possible to obtain but theoretical calculations point to values in the order of 4×10^5 bar or higher. While the collapse of MWCNT under irradiation-heating conditions had been previously acknowledged, using this phenomenon as a compressive chamber to force confined materials to restructure and extrude from the CNT tubular channel was a novel endeavor. The extruding process is all the more remarkable as it consists of a purely physical event despite the presence of the catalytically active metals.

In contrast, using similar conditions (300 kV, 50–200 A/cm^2 and 873 K) and a range of metal-filled CNT systems (Fe, Co, Ni, FeCo), it was possible to follow the growth of internal nanotubes via a solid-state catalytic process [40]. Note that these experiments were performed under vacuum and the electron beam irradiation effectively promoted the displacement and subsequent ingestion of carbon from the nanotube host to the confined transition metal particles. The authors further claimed the existence of chemical bonding between the metal particle and emergent CNTs justified by the bulk diffusion of carbon (as opposed to surface diffusion on the catalytic particles).

In 2009, Rodriguez-Manzo and collaborators published two reports on the fabrication of metal-nanotube junctions using the binomial irradiation-heat [41, 42]. In the first of these, MWCNTs containing encapsulated particles of Fe, Co, Ni, and FeCo were irradiated with a 200 kV converged beam (10^3 to 10^5 A/cm^2 for a 2–20 nm probe) at temperatures ranging from 723 to 973 K. Linear CNT-metal-CNT junctions were formed upon the probe-induced disintegration of the carbon lattice enveloping the discrete particles. In parallel to the sputtering action of the beam, restructuring at the metal-nanotube interfaces took place leading to their covalent bonding, as supported by density functional theory calculations. Besides making the junctions mechanically robust, the strong bonding contributed in considerably decreasing the metal-carbon contact resistance. The same type of hetero-junctions was obtained for 300 kV irradiated specimens subjected to joule heating via a two-terminal electrical probing holder. Transport measurements were performed, which confirmed the fabrication of metal-nanotube ohmic contacts and low-resistance systems (<80 kΩ). In the follow-up study [42], the team focused their attention on junctions fabricated between Co and MWCNTs. An important point was the possibility of linking efficiently different types of CNTs (diameter, chirality, etc.) [30]. However, the aim was now to obtain a multibranched system with a single-particle Co node. Besides producing the structures in situ, Rodriguez-Manzo et al. also studied their electrical and mechanical properties inside the microscope's column. Three different types of holders were used namely, heating, two-terminal electrical probing and force sensing, the latter two also known as STM and AFM holders (from Nanofactory Instruments). The cross-joined nanotubes were produced at 873 K with a 200 kV converged beam (10^4 A/cm^2) or under joule heating at 300 kV. Together with the restructuring of the CNT region containing the Co particle, as previously demonstrated [41], a second CNT was welded in a perpendicular orientation. From these four-branched structures, three- and two-terminal junctions could subsequently be obtained by selectively beam cutting one or two branches, respectively. The Co-linked multibranched junctions showed low electrical resistance (ca. 50 kΩ) and high tensile strength (1–5 GPa). Overall, the toolbox available to design and create in situ various types of CNT networks (without or without metal nodes) has expanded considerably. Still, taking this work outside the TEM column remains a goal not yet completed.

Heating of filled CNTs has been investigated as a means to extract the encapsulated materials. Undoubtedly, the drive for controllably removing the nanotube contents is to enact the concept of nanopipettes. Extraction of CuI from MWCNTs using an in situ TEM heating approach was mentioned in 2009 (cf. supporting information of [43]). Other reports followed, such as those by Toimil-Molares [44] and Hayashi [45]. In the first case, Cu fillings were subjected to prolonged heating (up to 80 min) at 773 K [44]. Driven by surface diffusion, the solid-state metal is sequentially drained from the nanotube accumulating at the tip as a monocrystalline faceted Cu particle. Monte Carlo simulations explain that removal of the confined

Cu minimizes the total free energy of the system. In a related work [45], exposure of Pd_4Si/Pd and Co/Pd fillings to temperatures above 1,773 K and 300 kV resulted in the extraction of Pd and Co. The authors proposed that, upon heating, pressure built up internally and forced both the CNT tip rupture and diffusion of the confined molten metal (which accumulated, still in the molten state, at the nanotube's end). More recently, the structural stability of a doped ZnS alloy confined in MWCNTs was followed when exposed to beam irradiation at different temperatures [46]. Remarkably, whereas a 300 kV converged probe (room temperature) would lead to complete and localized drilling of the ca. 100 nm thick nanotubes after 5 min, raising the temperature to 773 K led, under the same irradiation conditions, to a much more extended volume of material extracted/sublimed. While interesting, the thermal approach does not appear to be a viable means to construct a nanopipette out of CNTs. Among other factors, the dispensing rates are slow and the applicability will always be limited given the high temperatures involved [43].

7.5 Chemical

Understanding the mechanisms of reactions is one of the ultimate aims of chemists and chemical engineers. Likewise, correlation of growth conditions and structure has been one of the most pressing topics of the CNT field since its inception. Collecting direct evidence of reaction paths is a daunting task that may only be partially achieved due to the transient nature of intermediate states. For the major part, simulations are necessary to complete a meaningful pathway from reactants to products. Given that chemical vapor deposition (CVD) is presently the most widely used method to grow CNTs, most efforts for in situ TEM chemical processes have been directed towards the observation, in real time, of gas-solid interactions. Working in environmental TEM (E-TEM) mode allows one to emulate analogous conditions to those employed in thermal CVD growth of CNTs [47].

Carbon Nanotubes

The gas-solid interactions between a mixture of CH_4/H_2 and metallic Ni were studied with near atomic detail in 2004 using a 300 kV beam (0.2–2 A/cm^2) [48]. NiO nanoparticles were supported on $MgAl_2O_4$ and exposed to a 1×10^{-3} bar flow of H_2 at 773 K for 1 h. After the metallic Ni (5–20 nm) was obtained, the carbon feedstock was added (CH_4) resulting in a 1:1 mixture of CH_4:H_2 at 2×10^{-3} bar. During the in situ growth runs, while the temperature was varied, other variables were kept constant, enabling thereby the observation of shape changes in the Ni particles and extrusion of the concentric carbon shells, typical of nanotubes. The high-resolution images showed that, upon elongation, the catalytic Ni particles developed monoatomic steps where the graphene sheets terminated. This level of detail, coupled to

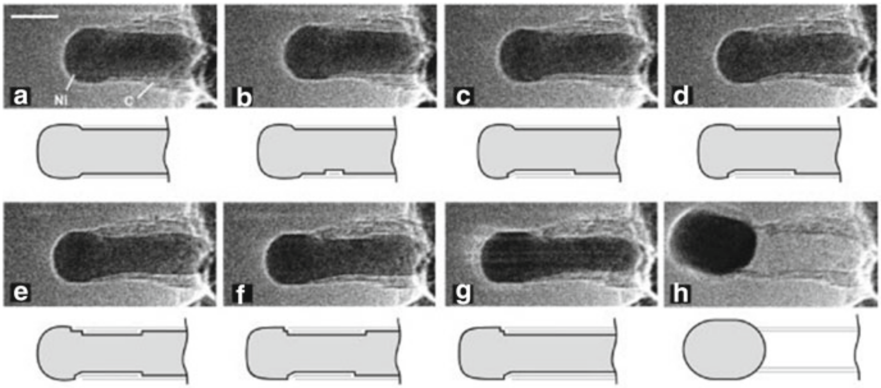

Fig. 7.4 Sequence of time-resolved images (**a**–**h**) showing the elongation-contraction process behind the growth of a CVD-made CNT. The drawings help localize the surface steps on the catalytic Ni particle which drive the formation of graphene layers. Scale bar: 5 nm. Reproduced from [48] with permission

the information extracted from theoretical calculations, placed the step edges of the particles as the active centers for the graphene shell growth. Indeed, carbon was found to bind more strongly to the step sites than the facets of Ni. The work of Helveg et al. supported a growth mechanism where the migration and extrusion of carbon take place on the surface of the catalyst particle as opposed to the competing bulk diffusion model (Fig. 7.4).

While the work of the Danish team was remarkable, other groups were also investigating the reaction conditions for growth of CNTs with E-TEM. Less than 2 weeks after the publication of [48], Sharma and Iqbal demonstrated a CVD process to produce CNTs using three catalyst/precursor systems: Ni-SiO_2/propylene, Ni-SiO_2/acetylene and Co, Mo-MgO/acetylene [49]. The gas pressure was kept in the range 1.3×10^{-4} to 2×10^{-3} bar, the temperature kept at either 723 or 1,023 K, and the microscope operated at 200 kV. At the lower temperature, the growth of MWCNTs is dominant whereas, under similar conditions, the double- and single-walled varieties were obtained for runs at 1,023 K. In both cases, acetylene was employed as the propylene feedstock resulted in nontubular, Baker-like filaments [50]. Interestingly, for MWCNTs, catalyst particle remainders were seen at the center or ends of the nanotubes but none was identified in the SWCNT case. In 2005, Sharma published another report using the system Ni-SiO_2/acetylene [51]. This turn, the pressure window was lower, from ~10^{-6} to 10^{-4} bar, but the temperature was kept constant at 753 K. The 200 kV experiments were supported by analogous ex situ CVD growth. Two different regimes were observed depending on the pressure used. For $<1.3 \times 10^{-5}$ bar, SWCNTs were produced (3.5 nm diameter) at rates of 6–9 nm/s. For $>2.7 \times 10^{-5}$ bar, MWCNTs with varied morphologies (serpentine or zigzag) were grown at 35–40 nm/s rates to lengths in excess to 300 nm. The nanotubes contained bends of 60° and 120°, which the authors attribute to particle orientation changes during the carbon extrusion process. Taken together, the two articles corroborate that, for the same catalyst/precursor system, the type and quality of the CNTs produced by CVD are very much dependent on the reaction variables, temperature and pressure.

Two other reports followed that also used the Ni-SiO$_x$/acetylene system. The first of these, out in 2007, combined two different in situ characterization methods (TEM and X-ray photoelectron spectroscopy (XPS)) to follow the CVD growth of SWCNTs and carbon nanofibers [52]. Thermally induced restructuring of a 1 nm film of Ni originated the ~5 nm catalyst particles to be used. For the 200 kV E-TEM study, promotion of CNF growth required a 3:1 gas mix of NH_3:C_2H_2 at 1.3×10^{-3} bar and 753 K; for SWCNTs, undiluted C_2H_2 at 8×10^{-6} bar and 888 K was employed. Similar to the observation of Helveg [48], the catalyst particles were seen to remain crystalline and change frequently their shape and orientation during growth. The E-TEM results focused only on the Ni catalyst. In the case of CNFs, the particles' elongation-contraction cycles drive the growth via a tip-growth mode. On the other hand, the SWCNTs nucleate by a cap liftoff mechanism which is followed by cap stabilization and nanotube extrusion. Further mechanistic considerations are made to explain how variations in the particle reshaping may account for the production of different CNFs (including CNTs). In a related report, the team used in situ TEM and XPS again but expanded the range of metal catalysts to include also Pd and Au [53]. In regard to the electron microscopy work, the results support the conclusions of the preceding article and find the 4d metals fairly unreactive towards the production of CNTs. Taken together, complementing the E-TEM investigation with other in situ analytical methods (particularly those not relying in electron imaging) can open a new window for the interpretation of gas-solid interactions.

The dynamics of SWCNT growth inside a TEM was further studied using a Ni-MgO/acetylene system [54]. The temperature used was 923 K and the gas pressure was 5.3×10^{-9} bar. The main variable in this study was the catalyst particle size. The team observed that Ni particles with <6 nm would lead to the formation of 0.6–3.5 nm diameter SWCNTs and maximum growth rates of 0.31 nm/s. Contrastingly, larger ones poison the growth process and result in filled carbon onions. Moreover, nonfaceted, spherical particles manifestly favored the production of SWCNTs. No carbide phase formation (Ni_3C) was identified. Concerning the mechanisms, three distinct steps were identified: (1) hemispherical cap nucleation with an activation energy of 2.7 eV, (2) tubular growth subsequent to a strain relaxation catalyst shape transition, and (3) passivation of the Ni particle. In all cases, the catalyst particle remained at the bottom of the nanostructure (base-growth mode). Lin et al. published a second E-TEM study where they followed the growth of bamboo-shaped MWCNTs [55]. The system used was again the Ni-MgO/acetylene, exposed to 923 K, 1.07×10^{-8} bar of gas pressure and a beam current density of 0.1–0.3 A/cm^2. The presence of small (<6 nm) Ni particles resulted in the formation of SWCNTs, whereas 7–30 nm particles originated filled carbon onions and a few MWCNTs (these were not mentioned in [54]). The authors mentioned that the generation of full/partial transversal knots on the bamboo-shaped structures is due to the pace at which restoration of cohesive forces results in the Ni particle contraction (also mentioned in [52]). Unlike their previous SWCNT study [54], the growth mechanism for the bamboo-MWCNTs follows a tip-mode.

An additional system used for CNT growth in E-TEM is Co-SiO_2/ethanol [56]. In a microscope operating at 120 kV, temperature of 923 K and gas pressure of 0.1 mbar, MWCNTs were grown. Again a cap liftoff is mentioned followed by a growth stage where the metal catalyst undergoes shape changes (it was not possible to confirm that the Co remained solid throughout). Upon further high-temperature irradiation exposure, the CNTs appear to transform into filled carbon onions. Soon after, Yoshida et al. published another study, this time working with a Fe-SiO_2/C_2H_2:H_2 system, under 873 K and 1×10^{-4} bar [57]. Both SWCNTs and MWCNTs were reported, dependent on the catalyst particle size. The authors claim that the catalyst particle of Fe changes to the carbide and remains solid during the growth of the CNTs. Furthermore, the Fe_3C particles fluctuate and undergo shape changes, while C diffuses through the bulk (as opposed to surface diffusion).

A more recent study communicated a mixture series system covering from the pure Ni to the pure Au extremes, Au_xNi_y-SiO_2/acetylene [58]. The E-TEM growth of CNFs (including MWCNTs and SWCNTs) was carried out at 200 kV, a constant gas pressure of 4×10^{-6} bar and temperatures ranging from 793 to 1,073 K. They observe that adding fractional amounts of Au to Ni results in an increased linear growth rate and higher number of CNFs. This is explained by theoretical calculations which point to a volume diffusion of C in the Au_xNi_y particles with a much lower energy barrier (0.07 eV at 0.06 M Au) compared to that of pure Ni (1.62 eV). In fact, for pure Ni particles, Ni_3C seems to be the active species for growth (instead of fcc-Ni). The addition of Au to Ni also affects the growth mechanism and structure of the carbonaceous products. Accordingly, depending on the growth temperature and fraction of Au chosen, one may grow from herringbone-like fibers to SWCNTs.

Apart from the growth experiments, few other types of E-TEM studies have been reported. An example of an alternative gas-solid interaction is the analysis of CNT oxidation mechanisms, as recently described by Koh et al. [59]. Using an aberration-corrected TEM operated at 80 kV (dose rate of 1,195 electrons/$Å^2$s), an atmosphere of oxygen at 1.5×10^{-3} bar and temperatures in the range 573–793 K, the CVD- and arc-made MWCNT resilience to oxidation was imaged. Steps were taken to avoid ionized gaseous species in the column during the reaction period. Given the high-resolution imaging available, it was possible to pinpoint the initial locations for carbon removal and, surprisingly, these were not necessarily the ends of the nanotubes. In fact, the outside walls start to degrade first, despite the higher energy of the strained carbon atoms at the ends. Infiltration of gas into the nanotubes with subsequent first burning of the inner layers was also observed.

Hybrid Carbon Nanotubes

Concerning this family of CNTs, we have not been able to identify reports in the literature apart from one study [60]. In 2010, the in situ oxidation of individual MWCNTs filled with a ternary semiconductor alloy was followed at 300 kV.

Under reactive conditions, the dose was reduced to $<1\times10^3$ electrons/nm^{2}s. Oxygen was introduced inside the column at pressures ranging from 4×10^{-3} to 12×10^{-3} bar and temperatures varied between 773 and 873 K. The reaction path followed the well-known Kirkendall mechanism with the initial step consisting in the oxidation of the protective carbon shell. Oxidation of the doped II–VI wire followed with the final product consisting of a larger polycrystalline ZnO tubular structure. On further heating, sintering of the oxide crystals took place. These observations confirmed the mechanistic interpretation that had previously been put forward for equivalent ex situ experiments (Fig. 7.5) [61].

The discussions above illustrate the work that has been carried out over the past 20 years on chemical reactions within a TEM using CNTs as the object of study. It is evident that the major part of this effort has focused on mimicking the CVD growth process and particularly trying to understand the role of the catalyst particles. Additional work on hybrid CNTs would be of interest as real-life applications of these nanostructures will likely require the production of composites or interaction of the carbon materials with other substances.

Naturally, it is difficult to extrapolate the findings from the TEM column to real-life reactor chambers where a variety of variables have completely different values (e.g., pressure and flow of the gaseous species). For this reason, equivalent ex situ analysis should always accompany E-TEM experiments [9].

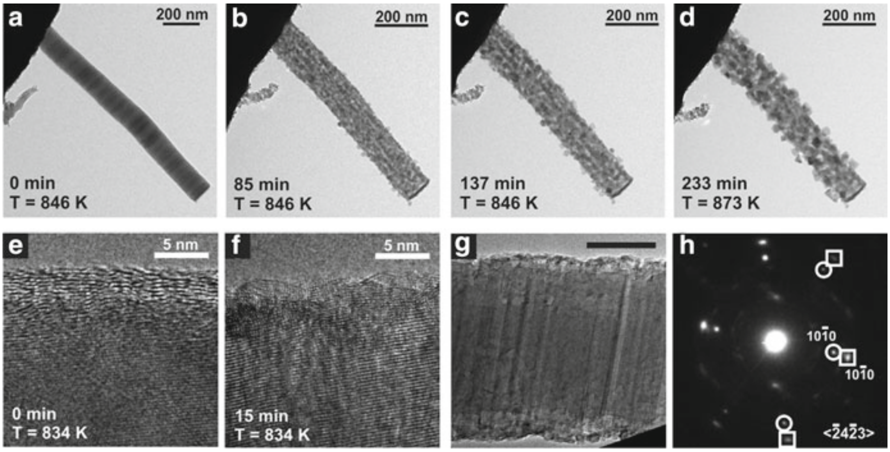

Fig. 7.5 (**a**–**d**) Time-resolved sequence of images of the oxidation and sintering processes for a single Ga-doped ZnS-filled CNT. (**e**) Detail of the semiconductor-CNT interface. (**f**) The region in (**e**) after the combustion of the carbon shell and subsequent oxidation of the surface layers of the sulfide wire. (**c**) Intermediate stage in the reaction where the formation of voids is noticeable. (**h**) Electron diffractogram of (**g**) showing the epitaxial coexistence of the zinc sulfide and zinc oxide structures. *Circles*: sulfide; *squares*: oxide. Adapted from [60] with permission

7.6 Electrical

Probing the electrical properties of nanotubes and using electrical currents to modify their structure or manipulate associated substances (e.g., fillings) is, by far, the most popular type of in situ TEM experiments done with CNTs. For this, the widespread availability of two-terminal electrical probing holders was determinant. The design is simple and has been reproduced by various labs and manufacturers. It consists of two opposite metal electrodes, usually in the form of sharp wires with a diameter of around 250 nm, where one can be biased. In addition, one of the wires is mounted on a movable piezo-actuated rod with which it is possible to manipulate and electrically contact samples as small as a single CNT. Given the profusion of articles, we opted to divide this section into subtopics according to the type of experiment done.

7.6.1 Electrical Properties

Carbon Nanotubes

One of the first studies to investigate the electrical behavior of discrete CNTs inside a TEM was published in 1998 [62]. Here, instead of two wires, one of the electrodes was a pool of liquid metal (Ga, Hg and a Cerrolow alloy). A discrete arc-made MWCNT, mounted on the oppositely positioned and movable electrode, was selected and its freestanding tip brought into contact with the Hg metal. As the biased nanotube was repeatedly dipped and retracted from the pool, the conductance as a function of time/displacement was measured. For some of the nanotubes, currents were up to 1 mA before electrical breakdown. Others, however, had resistances of 13 kΩ and did not undergo structural failure even at current densities $>1\times10^{7}$ A/cm^{2}. On the basis of their observations of conductance plateaus at $1G_0$, the authors concluded that the ballistic response of these CNTs could only be explained if they were acting as quantized conductors.

Two years later, another report came out that used the hypothesis of ballistic transport of arc-made MWCNTs to explain novel observations [63]. In this, high current densities were used as a tool to control the electrically driven vaporization of CNTs tips. Repeated exposure to currents of 200 μA led the set of walls from a 12.6 nm diameter to less than 3 nm. By sequentially stripping portions of the outermost layers from the nanotubes, it was possible to gradually sharpen them. This, according to the authors, is indicative that current flow takes place mainly at the outer walls.

In 2005, Huang et al. described how an arc-made MWCNT interconnect underwent sequential wall breakdown with increasing electrical current density [64]. Various failure sequences were identified (e.g. from the outermost wall inward), but they were all consistent with the view that every wall was conductive as a current drop was clearly observed each time one was broken. Crucially, the breakdown is not initiated randomly, at a wall defect or the ends, but precisely at mid-length of the nanotubes. This is in sharp contrast to the conclusions of Frank et al. [62], as it implies a diffusive transport regime (Fig. 7.6).

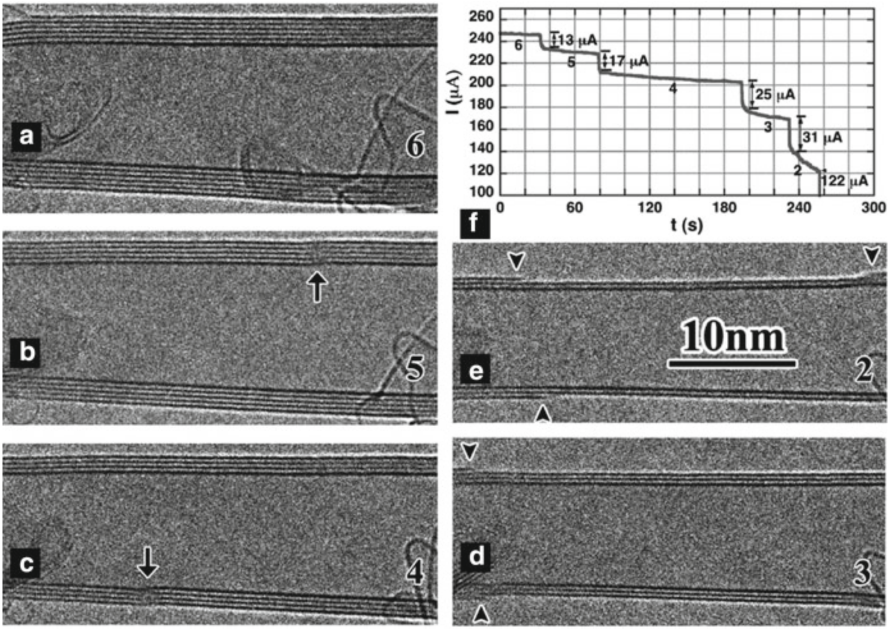

Fig. 7.6 Sequence of images demonstrating the electrical breakdown in arc-made MWCNTs. The wall-by-wall rupture proceeds from the outermost wall to the innermost wall (**a**–**e**). (**f**) Corresponding current-time plot where the current steps clearly indicate the removal of a wall (from 6 to 2 walls). Adapted from [64] with permission

Other studies followed that probed the stability and electrostatics interactions of CNTs subjected to high densities of electrical current in a TEM [65]. One interesting observation was that the failure mode for arc-made and CVD-made CNTs was different with the latter leading mostly to fiber thinning and necking (as opposed to gradual burning of its layers).

Very recently, a novel platform for multiterminal electrical probing of CNTs was demonstrated [66]. Using a holder that can host a 3×3 mm Si-based chip, four-terminal electrical measurements were carried out in discrete nanotubes previously mounted ex situ with the aid of a SEM. In addition to the four suspended metal electrodes in the Si chip, a piezo-controlled wire electrode can be contacted to the CNT and used to form a field effect transistor (FET) with a movable gate.

Hybrid Carbon Nanotubes

Apart from the investigations with empty CNTs, others have been performed using hybrid systems—in particular, where the tubular interior is filled or the external wall coated with a foreign substance. Invariably, these have had, as main purpose, the manipulation of the associated material for which reason they will only be described further on.

7.6.2 Field Emission

Carbon Nanotubes

One of the proposed applications for CNTs is in field emission tips (e.g., for electron microscopes). Given the manipulation and probing capabilities of two-terminal electrical holders, it is possible to study the local work function, turn-on field and threshold field of a single nanotube with much higher confidence than with other characterization setups.

The first report on this topic was communicated in 2001 [67], when the local work function of arc-made MWCNTs tips was measured at 100 kV. The method used relies on the mechanical resonance response of the CNTs induced by an externally applied oscillating voltage with tunable frequency. It also requires that a true fundamental resonance frequency be examined and the resonance stability and frequency drift analyzed before and after each measurement. For the window of diameters analyzed, 14–55 nm, the work function values extracted were practically constant at 4.6–4.8 eV. Some 25 % of the nanotubes showed higher values, 5.6 eV, possibly due to the semiconductor nature of their electronic structure. Overall, for metallic CNTs, there was no observed dependence of the work function on diameter.

Shortly afterward, Cummings et al. used electron holography at 200 kV to understand the magnitude and spatial distribution of the electric field in discrete arc-made MWCNTs field emitters [68]. Observing that both magnitude and spatial distribution are mostly unchanged over time, the highest field was recorded at the CNT freestanding tip. Eventual wall imperfections do not contribute significantly to field concentration. The authors suggest that time-dependent changes in emission current may occur due to tip adsorbates more than those derived from overall electric field distribution variations.

At the same time the work by Cummings et al. [68] was published, Wang et al. provided an alternative justification for the emission current fluctuations [69]. When carrying out real-time imaging at 100 kV of the field emission process, they found that visible structural damage to the nanotubes occurred along with vibrations of the freestanding tip (“head shaking”). The authors explain that electrons are likely to be emitted as bunches in a ballistic way when the electrostatic attraction between the CNT tip and counter electrode is maximum. After the emission, the high-aspect-ratio nanotubes relax, accounting therefore for the body swings observed as well as the fluctuations and blinking in the emission current. During the field emission, and given the strong electric field at the CNT tip, the local temperature may increase considerably which will result in higher probability to induce structural damage. As the applied bias is increased, the likelihood of damage to the nanotube also increases. The authors mention a stripping-layer process and the sequential vaporization of the nanotubes. A third contributive factor, not mentioned by the authors, could be derived from electron beam irradiation. At high temperatures and electric fields, a much lower critical voltage for damage to the carbon lattice would be expected [70].

The possibility of using the field emission process to controllably modify the freestanding tip of a CNT was again picked up in 2008 [71]. Previously, sharpening of the CNT had been reported but this required direct contact of the tip to another CNT [63]. Here, the ends could be opened and grinded using applied voltages of 140 V, field emission current densities on the order of 10^8 A/cm^2 and an imaging beam at 200 kV. To ensure physical stability, correct orientation and the individuality of the emitter, a selected CVD-made nanotube was manipulated and glued to a sharp W wire using in situ electron beam deposition of amorphous carbon. The vaporization process was promoted by the sculpting action of the electron beam and could be controlled in grinding speed and length. In fact, the onset of the vaporization was reduced by 4 V/nm in the presence of the beam.

Hybrid Carbon Nanotubes

Not many publications on field emission exist where CNTs were mixed with other substances. In 2012, Fe_3C-filled nanotubes were evaluated [72]. Besides their electrical response, the evolution of discrete carbide particles under joule heating was described as well as the field emission capabilities of discrete nanotubes. As regards the latter, Su et al. mention a 61.1 V onset voltage and that the effective emission area is smaller than the total available area of the MWCNT cap. In fact, less than 10 % of the tip is active as a field emitter.

About the same time, a similar report on Fe-filled CNFs was published [73]. Interestingly, the authors did not just measure the field emission but also followed it over time, recording alongside structural and electrical property changes. A field enhancement factor of 73.6 was extracted from a field of 83 V/μm. Also, various events took place under the high electrical current densities applied. Apart from graphitization of the walls, which leads to the change from CNFs to CNTs, the improvement in the electrical conduction and field emission by three orders of magnitude, sintering and removal of the Fe content were observed. In addition, cross-sectional inner walls were formed in the CNTs, turning them into bamboo-like nanotubes.

7.6.3 Mass Transport

The study of mass transport activated by electrical currents in CNTs is specific to hybrid nanotube systems. The nanotube acts as a medium through which matter is directed from points A to B usually taking advantage of strong directional electric fields and charge carriers.

Hybrid Carbon Nanotubes

In 2004, two reports were communicated on the use of MWCNTs either as a conveyor belt for metal transport [74] or a container for delivery and manipulation of metal nanoparticles [75]. In the first case, a two-terminal electrical probing holder was used to contact a sample of arc-made MWCNTs that were previously coated with thermally evaporated indium [74]. When a voltage was applied to the system, the interconnecting nanotube underwent joule heating. The amount of thermal energy injected was enough to melt the In nanoparticles decorating the external surface of the CNTs. On further voltage increments, the metal could be evaporated and transported controllably between different points on the outer wall of the nanotube. Each particle acts as a mass reservoir that can be sequentially and reversibly depleted. Other particles along the nanotube will collect the indium transported. To explain their observations, the authors recall that electron transfer from the In particle to the interconnecting nanotube, under an electromigration-based mechanism, would account for the direction of mass transport. Here, the so-called “direct” force (electric field) dominates over the opposite “wind” force (charge carriers). Other effects such as Ostwald ripening and thermal gradients are supposedly secondary. In the second paper, instead of mass transport taking place on the outer wall, the Fe metal was flowed via the inner tubule of arc-made MWCNTs [75]. High electrical current densities (typically $>10^6$ A/cm^2) were used to promote the electromigration of Fe particles confined in the nanotubes and to deliver them onto substrates. This phenomenon effectively turned the CNTs into nanoscale pipettes for storage, transport and delivery of transition metals. The deposited Fe nanoparticles were further manipulated, being individually picked up and taken to different locations in the substrate. Notably, a threshold for the current density guiding the Fe migration was mentioned which suggested a limiting value for the electromigration process. In contrast to the work by Regan et al. [74], the team suggests a mechanism of thermally assisted electromigration as the “direct” force does not necessarily dominate the “wind” force (Fig. 7.7).

Another CNT-encapsulated transition metal that was manipulated using electrical currents, for purposes of mass transport and delivery, was Cu. Two independent studies on this topic were published in 2007 [76, 77]. Working with a 300 kV electron beam (1–2 A/cm^2), Golberg et al. placed individual turbostratic CNTs filled with Cu (either as wires or particles) between two Au wire electrodes and varied the applied bias up to 10 V [76]. For some of the nanotubes, full length fillings were manipulated. Accordingly, not only mass transport along the same CNT was seen but also across different CNTs (at rates of <1 fg/s). Further to this, the filled nanotubes behaved like switches where the electrical resistance was dependent on the Cu filling ratio. Welding of filled nanotubes was also mentioned. Electrical plumbing of Cu-filled nanotubes was a topic also covered by Dong et al. [77]. In this work, conical bamboo-type CNTs were used where the sectional fillings were preferentially located at the tips. Upon injecting a high current density (at fairly low voltages of 1.5–2.5 V), melting of the confined Cu occurred (via joule heating) and this flowed, via electromigration, outside the nanotubes at average flow rates of 120 ag/s. Interestingly, the resistance of the system increased as the Cu was continuously extracted from the interior of the CNT.

Apart from metals, giant fullerenes encapsulated in MWCNTs have been subjected to joule heating inside a TEM [78]. These structures were the result from electrical breakdown experiments previously carried out by the same authors [64].

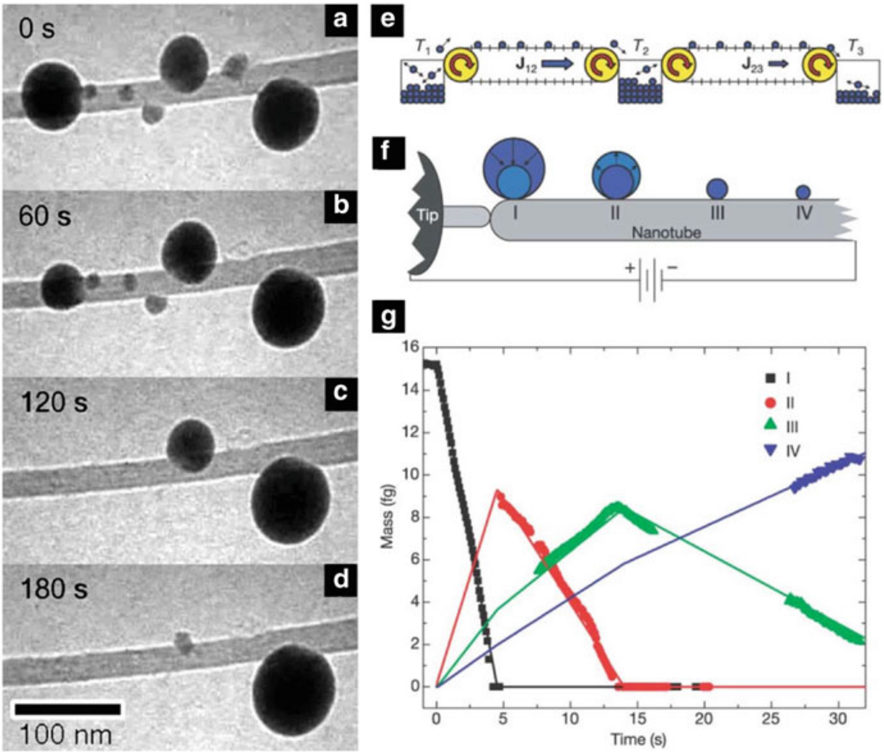

Fig. 7.7 (**a**–**d**) Time-resolved images showing the transport of In from the shrinking particles on the left to the one on the right. (**e**) Diagram illustrating the conveyor-like transport of In between reservoirs at different temperatures, $T_1 > T_2 > T_3$. (**f**) Diagram depicting the process shown in (**a**–**d**). (**g**) Particles masses as a function of time. The numbering follows what is portrayed in (**f**). Adapted from [74] with permission

Here, the nanotubes acted as a furnace from where the molecules were gradually sublimed. From Monte Carlo simulations, carbon atoms appear to be sequentially removed from the fullerene in C_2 units. This takes place when gliding 5|7 pairs encounter a pentagon-type defect. Molecules as large as C_{1300} could be shrunk to C_{60} which would then fully disintegrate. Although mass transport is not referred to in the article, it is likely that the carbon dimers diffuse inside the nanotubes, as suggested elsewhere [33].

Meanwhile, electrically driven mass transport of more complex fillings was studied by one of us. In 2008, chains of CuI nanograins were released in a stepwise fashion from the interior of MWCNTs exposed to pulses of electrical current [43]. At each pulse, a few ag of the halide were extracted with a concomitant effect on the overall electrical response of the interconnector. Conductance increments were observed up to the point where the full length of the nanotube channel was empty. This is in sharp contrast to the observations made for metallic Cu-filled nanotubes, where depletion of the confined metal led to lower overall conductances [76, 77].

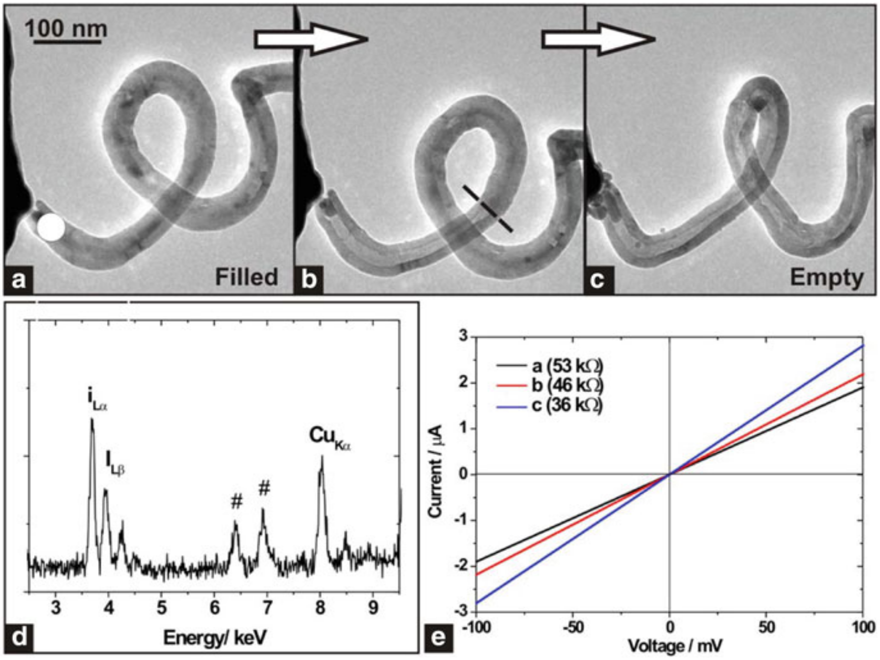

Fig. 7.8 (**a**–**c**) Sequence of images showing the stepwise electrical extraction of CuI from the interior of a CVD-made MWCNT. In (**c**) nanoparticles accumulated outside the nanotube's open end. (**d**) EDX spectrum of the region *circled* in (**a**). (**e**) Current–voltage curves for (**a**–**c**). Adapted from [43] with permission

Some of the extracted material ended up deposited on the Au wire electrodes but the quantities delivered were markedly smaller than those extracted. To complement the electrical pulsing approach, irradiation and heating experiments were also carried out. Upon the incidence of a converged 300 kV beam, depletion of iodine took place and the Cu material was flown out leading to the formation of faceted particles on the TEM grid. Furthermore, it was found that the CuI could be released from the internal CNT cavity at 723 K, a lower figure than the tabled 873 K for its melting under standard conditions. Likely, this was the first time that the response of a hybrid CNT to a variety of externally applied stimuli was followed in situ (Fig. 7.8).

In 2011, three reports were communicated on the behavior of doped ZnS-filled MWCNTs undergoing electrical heating. The importance of this material is reflected in its chemical complexity (a ternary system as opposed to the elemental Fe and Cu studied before) and its quantitative filling rate (i.e., all nanotubes filled in their entire extension). First, the dynamics of the joule heating process taking place inside the nanotube channel was followed [79]. Using the sublimation temperature of the confined semiconductor alloy as a temperature marker (ex and in situ heating experiments were also performed), it was possible to identify the location of hot spots in the interconnector and estimate the gradient of temperatures in it as the material was gradually depleted. Besides longitudinal thermal gradients, cross-sectional ones were also observed. The full extension of the carbon shell could be voided from its contents as further shown in a companion article [80]. Here various extraction methods were compared together with two types of delivery substrates. The pulsed-current approach and the use of carbon substrates were seen to be particularly favorable as they allowed more efficient delivery with full view of the deposited particles. The "missing matter" issue was also discussed [77]. It was suggested that not only surface migration but also vapor losses should be considered to explain the disparity of volumes extracted to those delivered. On the third paper of the series, the chemical stability of the sulfide materials was compared before and after being expelled from the MWCNTs [81]. Working within the electrical-pulse approach, the substrate containing the delivered particles was left in air for 30 days. These were observed to undergo oxidation, changing into core-shell nanoparticles with an oxygen-rich skin. Throughout this time, an adjoining particle that was left encapsulated remained unaltered.

The use of Sn- and Cu-filled CNTs as optical antennae was explored with a 200 kV TEM [82]. Two methods, namely, irradiation- and current-based, were employed to drive the metal contents from the interior of the nanotubes. The converged beam irradiation led to melting, pressure buildup and thermal expansion of the fillings with consequent destruction of the carbon shell and extraction of the materials. On the other hand, the substrate heat-sinking effect on the electrical current approach was studied. According to the authors, large electrodes provide better heat dissipation which helps the recrystallization of the extracted particle. If a smaller sink is used, such as a section of another nanotube, the delivered Cu particles will retain a spherical shape.

The TEM is particularly well placed to study mass transport in individual CNTs. This type of experiments requires high-resolution imaging and spectroscopic analysis coupled to the option of recording, in real time, the dynamical phenomena that occur on or inside the nanotubes. Further to this, the fact that various stimuli may be applied to the nanotubes (irradiation, heat, current) opens up the possibility of comparing separately what the effect of each is in the mechanism of transport under vacuum.

7.6.4 Contacts and Junctions

The integration of CNTs into devices or other types of technological applications will depend highly on how these materials are contacted with their surroundings. Contacts are also crucial when measuring CNT electrical properties. To construct electrical circuits bearing nanotubes as interconnects, it is almost unavoidable to resort to metal-nanotube junctions. Optimizing these is therefore a matter of importance to better take advantage of the unique CNT properties. Another possibility is to have all-carbon circuits where, for instance, metal-like nanotubes could be fused to semiconducting ones.

Carbon Nanotubes

The group of Lian-Mao Peng in Beijing was an early developer of electrical soldering of CNTs inside a TEM [83]. Selected MWCNTs, contacted to opposite wire electrodes, were first cut using the electrical breakdown method. Next, the CNT segments were reattached by depositing amorphous carbon on the junctions. The soldering method was promoted by the electron beam and allowed end-to-end, side-to-side and end-to-side connections. This flexibility permitted the fabrication of CNT networks at room temperature that, up until then, had only been constructed under high temperatures [30]. Upon electrical annealing, the amorphous carbon of the junctions was seen to graphitize and consequently, the overall resistance of the soldered nanotubes decreased. Loads were also applied demonstrating that the contacts were surprisingly robust and could even withstand the tensile rupture of the nanotube.

Joining single- and double-walled CNTs by means of electrical currents in a TEM operated at 120 kV (18 A/cm^2) was communicated in 2008 by Jin et al. [84]. Two very distinct situations were explored. In the first scenario, no metal particle intermediates were employed. Nanotubes could then be electrically connected only if they were end-to-end and had the same or very similar diameters. By contrast, in the second scenario, encapsulated W particles (produced in situ under conditions analogous to those of field emission studies) catalyzed the structural rearrangements of the contacted tips, even in the case of nanotubes with very dissimilar diameters. End-to-side junctions were also fabricated. As it does not require irradiation or high-temperature environments, the process reported could be very useful in CNT-based electronic devices as it would allow electrically driven self-repair of sectioned nanotubes.

A two-terminal electrical holder was used to follow the dynamics of a MWCNT-W electrode wire contact interface when exposed to a high current density [85]. The end-to-end contact established was considerably changed as chemical reactions promoted by joule heating took place between the C and W. The formation of the hexagonal phase α-WC was aided further by electromigration leading to visible extensions of mixing and eventual extrusion of excess carbon from the top of the WC segments. The chemically connected junctions of CNT-WC-W represented fully annealed ohmic contacts and showed drops in electrical resistance of one order of magnitude when compared to the initial configuration. The team reported beam current densities of 1–2 A/cm^2 at 300 kV, so it is unlikely that irradiation contributed significantly for this joining process.

The electrical and mechanical responses of the CNT-WC-W junctions were described in a second communication [86]. Currents in the order of 100–200 μA were injected in the CNT-W contact to produce the merged junction. The authors assume the formation of covalent bonds of the metal to all the carbon shells in the nanotube. All-shell bonding explains the very high tensile strengths measured, 5–15 GPa, and low resistance values of less than 1 kΩ. The comparison of these carbide junctions to the analogous CNT-Co ones (constructed via irradiation and thermal annealing [42]) demonstrated that the first were almost 3 times stronger. Another evidence for the contact robustness was the field emission experiments which saw the nanotubes disintegrating while the contact remained stable.

Karita et al. also investigated the structural evolution of CNT-metal contacts with in situ TEM electrical annealing [87, 88]. In a microscope operating at 120 kV, two metals were studied, namely, Ni and Au, along with arc-made MWCNTs with two different types of tips, open and closed. Current densities in the order of 10^8 A/cm^2 were reportedly needed to induce melting of the Ni surface at the contact region [87]. This annealing process led to a marked decrease of the overall electrical resistance, particularly for the open-end nanotubes. For the case of Au contacts, the melting threshold was similarly at 10^8 A/cm^2 and the open-end CNTs again led to less resistive contacts [88]. The authors do not discuss chemical mixing of the materials [85] or hot-spot migration upon annealing [79].

Hybrid Carbon Nanotubes

Besides the above, another type of contact has been fabricated that involves irradiation and electrical heating performed, in parallel, in metal-filled CNTs.

On a follow-up work of [42], Wang et al. demonstrated how electrical heating may assist in establishing CNT-metal-CNT junctions from Co-filled MWCNTs [89]. A 300 kV converged electron beam was used to displace the carbon shell where a Co particle was located. This was done with the interconnecting nanotube biased and led to CNT-m-CNT heterojunctions. However, these extracted Co particles could be used to promote the junction with other nanotubes. First, one of the CNT segments was separated and then, the CNT-Co section was electrically soldered to a different CNT. Even CNTs to *N*-doped CNTs connections could be fabricated in this way. In some cases, the reconnection of the CNTs led to the electrical removal of the soldering Co. The mechanical resilience of the joints was tested using tensile stress with a force-sensing and electrically conductive holder. These showed strengths up to 31 GPa, particularly for the systems where the Co particle had been removed from the soldering location.

Analogous work was carried out in metal atomic chains connecting two segments of CNTs, generating therefore CNT-metal-CNT junctions [90]. This went beyond the previous example as the metal section is effectively sculpted into a very thin wire with quantized electrical conductance. Starting from a metal-filled nanotube (Fe, Fe alloy or Pt), the fabrication of the atomic metal chains is done by irradiating the areas with encapsulated particles (100–300 A/cm^2) while, simultaneously, applying a tensile strength to the system under bias. When the carbon had been sputtered off and the metal section reached thicknesses of 6 nm, the etching rate was slowed by decreasing the irradiating beam density (10–30 A/cm^2). The electrical response could be examined showing that the CNT-m-CNT interconnect remained metallic throughout. However, upon tensile stressing at constant bias, reduction of conductance with step heights at multiples of $0.5G_0$ was observed for the magnetic metal sections. Thinning of the metal chains proceeded down to thickness of less than 1 nm for the case of Fe (calculated conductance of $1.5G_0$). The TEM observations were supported with first-principles calculations.

7.6.5 *Growth*

Given the possibility of growing CNTs within a TEM resorting to irradiation and heat [40], it would be logical to expect that the binomial irradiation—electrical heating may also be capable to promote CNT formation. As shown below, this has in fact been observed by various groups using the classical two-terminal electrical probing holder.

Carbon Nanotubes

While it was not the first study on electrically driven growth of CNTs in vacuum, Jin et al. communicated in 2008 a demonstration of how this could be carried out in catalyst-free conditions [91]. Working at 120 kV (6×10^4 electrons/nm^2), the cap of a confined CNT (acceptor) was reshaped and extended inside a parent double-walled CNT in parallel to the shrinkage of an oppositely confined nanotube (donor). The authors proposed that carbon clusters are extracted from the shrinking nanotube, are diffused by electromigration, and finally are incorporated into the expanding and oppositely positioned cap of the growing structure. Throughout, the caps of the internal shrinking/growing nanotubes were closed and evolved differently. Here, the DWCNT has multiple roles: it acts as a reaction vessel, a medium for heat dissipation, a channel for mass transport and a template for the nanotube growth.

In their study of CNT-W junctions [85], Wang et al. saw that under high electrical current density, the formation of WC takes place. As more carbon is depleted from the nanotube, leading to the expansion of the carbide section along the W wire electrode, a carbon concentration gradient is generated. Eventually, supersaturation is reached at which point extrusion of graphitic shells is observed on the carbide section. On further precipitation of the carbon, the first layers are pushed outward and along the tip, effectively generating a short section of a WC-filled CNT. Put together, the nanotube is used as the carbon source first for the reactive production of the carbide and next for the segregation of graphitic tubular shells that envelope the W wire. Given that this work was performed at a beam density of 1–2 A/cm^2 (300 kV), it is unlikely that irradiation was a major driver in the solid-state reaction and subsequent carbon precipitation.

Hybrid Carbon Nanotubes

In 2005, a report came out on how one could use electrical current to control the growth of a discrete CNT [92] within a Co-particle-filled MWCNT. The process took place inside another (parent) nanotube that acted as a reaction chamber and effectively limited the growth direction. Remainders of the parent CNT synthesis, encapsulated Co particles were reactivated in their catalytic role when sufficient joule heating was provided. The authors mentioned that about 20 μA would be flowing through the particle. Apart from heating, the high density of current forced the electromigration of carbon ingested in the catalyst, subsequently also forcing its extrusion as an internal nanotube. Remarkably, the reaction rate could be controlled or stopped altogether followed by an on-demand restart. In addition to this, structural annealing of the parent nanotube could be promoted by electrical currents and the confined catalyst particles. No mention was made on possible effects from beam irradiation.

The growth of SWCNTs from silicon oxide particles encapsulated within MWCNTs was described in 2011 [93]. In this work, the carbon source is the parent CNT from where atoms are displaced via the electron beam. Electrically induced diffusion of the carbon occurs inside the tubular channels, resulting in their inclusion in the SiO_x particles and subsequent formation of the single-walled nanotube under joule heating. The magnitude of the current injected and the size of the silicon oxide particles determined the propensity for nucleation of the internal nanotubes. At currents higher than 200 μA, the particles were first reduced to Si and would subsequently melt, forming SiC. In addition to the in situ TEM observations, the authors performed related CVD experiments and theoretical calculations which supported the view that oxygen atoms can help capturing carbon species and facilitate the growth of nanotubes. Overall, the active catalyst in SiO_x growth of CNTs appears to be the oxide rather than the carbide or Si.

The use of the internal cavity of MWCNTs as a reaction vessel was again illustrated with the study of CNTs nucleation in encapsulated Fe_2O_3 and Au particles [94]. While a high density of electrical current induced heating of the nanotube, beam irradiation on the parent MWCNT supplied the carbon necessary to initiate the nucleation. In the first case, the oxide particles were first reduced to the carbide which then catalyzed the formation of the nanotube. The Fe_3C particle turned into metallic Fe when the growth was stopped. For Au, no chemical reactions took place either promoted by heat or irradiation. Still, the authors observe that carbon shells partially coat the surface of the particles and, in some cases, form lifted caps. Analogous ex situ CVD growth was also carried out.

From the above, the use of a parent CNT acting as a nanoscaled tubular furnace is a concept that has become an interesting alternative to follow the first steps of CNT formation. However, in contrast to experiments done with heating holders, electrical heating is unavoidably associated with the possibility of mass transport. This likely complicates the full understanding of the mechanism that rules reactions within the nanotubes as observed with in situ TEM.

7.6.6 Electrochemical

Of late, the common two-terminal electrical probing holder has been adapted for other purposes besides electrical measurements and CNT manipulation. Its use in electrochemical studies is one good example. Given the restrains of using volatile electrolytes inside TEMs, some groups have been exploring an electrochemical "open-cell" design for battery studies [95]. For purposes of investigating the structural and chemical changes in anode materials, an electron-transparent nanostructure is employed such as CNTs. The second component is an electrolyte that can withstand the vacuum in the microscope's column (e.g., an ionic liquid). Finally, a source of the mobile cations is needed which may be a discharged cathode.

Carbon Nanotubes

In the first work of this kind where MWCNTs were employed [96], lithiation of the nanotube anodes was carried out at 100 kV via a solid electrolyte in the form of lithium oxide. Expansion of the interwall distance was noticed along with overall structural distortion. The process also rendered the MWCNTs' brittle leading to fracture upon compression or tension. Brittleness is not a failure mode normally associated with MWCNTs. Internal stress derived from radial expansion contributes highly for this as the outermost shell was estimated to be at 50 GPa of tensile hoop stress. Arc- and CVD-made CNTs were studied and found to react the same way.

Hybrid Carbon Nanotubes

Recently, two reports by Su et al. used Co_9S_8-filled CNTs to directly study the electrochemical response of these structures as anodes for ionic batteries [97, 98]. First, lithiation-delithiation cycles were followed in tip-closed and tip-open CNT [97]. The filled nanotubes were produced by CVD and contained, besides Co_9S_8, particles of Co. The cathode/electrolyte ensemble was Li/Li_2O and cycling the applied bias in the two-terminal holder from negative to positive values led to the insertion and removal of Li from the CNT anode, respectively. The carbon lattice of the CVD-made nanotubes had a high density of defects which facilitated the insertion and migration of the Li^+. For the tip-closed structures, axial and radial elongations of 4.5 % and 32.4 %, respectively, were seen. This was in sharp contrast to the tip-open structures were the lithiated sulfide nanowire was extruded reaching axial elongation of more than 94 %. Interestingly, the extrusion is accompanied by the telescopic expansion of the host CNT as its innermost layer is subjected to sliding forces. An analogous report was published soon after where instead of Li^+ the cation was Na^+ [98]. The same sulfide-filled nanotubes, with either open or closed tips, were used but the cathode/electrolyte ensemble was $Na/(Na_2O + NaOH)$. Sodiation in the open-tip structures resulted in the extrusion of the nanowire with a 121 % axial elongation. For the closed-tip structures, the largest changes were in the radial expansion of almost 41 % and the conversion of the Co_9S_8 to Co nanograins in a Na_2S matrix. Multiple-shell fracture was also observed for the closed-tip structures as a result of extreme tensile hop stress on the CNT at higher charging voltages.

7.6.7 Mechanics

The electrical holder has been used also to probe the mechanical behavior and properties of CNTs. In fact, some of the pioneering mechanical essays for individual arc-made MWCNTs were carried out resorting to a two-terminal electrical holder [99] (another in situ TEM preceded this, as mentioned above [13]). Needless to say, these holders do not integrate a force sensor meaning that moduli figures obtained were, in reality, estimates extracted from indirect methods such as resonance frequency analysis. Studies where direct readings of force have been performed will be described in the next section.

Carbon Nanotubes

In 1999, the electrostatic deflections and electromechanical resonances of freestanding MWCNTs were followed inside a 100 kV TEM [99]. To induce deflection or resonance, a constant or alternating voltage was applied to the electrodes when an appropriately positioned nanotube was found suspended in vacuum (i.e., adopting a similar configuration to that used in field emission in situ TEM experiments). In the electrostatic regime, the nanotubes could be reversibly bent over many cycles, with their on-off deflection solely controlled by the action of the applied bias (at ±40 V limits). The mechanical resonance originated from tuning the alternating voltage, which led to correspondingly alternating oscillations of the nanotubes, to the natural resonance frequency of the suspended structures. As the arc-made MWCNTs were electrically excited to their fundamental frequency and higher harmonics, the elastic bending modulus could be estimated and correlated to the diameter of the nanotubes. With increasing diameter, the modulus decreased and a shift in the mechanical response was observed, i.e., from a uniform to a rippled bending elastic mode. The bending modulus extracted was as high as 1.2 TPa for MWCNTs with a diameter of less than 8 nm. In this article, the authors also briefly mention that the method is suitable to measure the mass of nanoparticles attached to the freestanding end of the nanotube. In a follow-up work [100], the resonance frequency of mass-loaded nanotubes was seen to drop by more than 40 % in comparison to free ones. Masses down to 22 fg could be measured (Fig. 7.9).

Low-friction nanoscaled linear bearings based on CNTs is a concept described by Cummings and Zetl who showed a peculiar property of arc-made MWCNTs: their capability to extend telescopically [101]. Working within a 100 kV TEM, the ends of the nanotubes were welded to metal wire electrodes of the holder. As a tensile load was applied, some of the nanotube's internal shells could be selectively extracted, sliding out in a sword-in-sheath way. When one of the contacts was broken, the nanotube relaxed by retracting the protruding shells to their original position. This reversible phenomena underpins a very low-friction force between the shells and is further characterized by the absence of observed fatigue upon cycling.

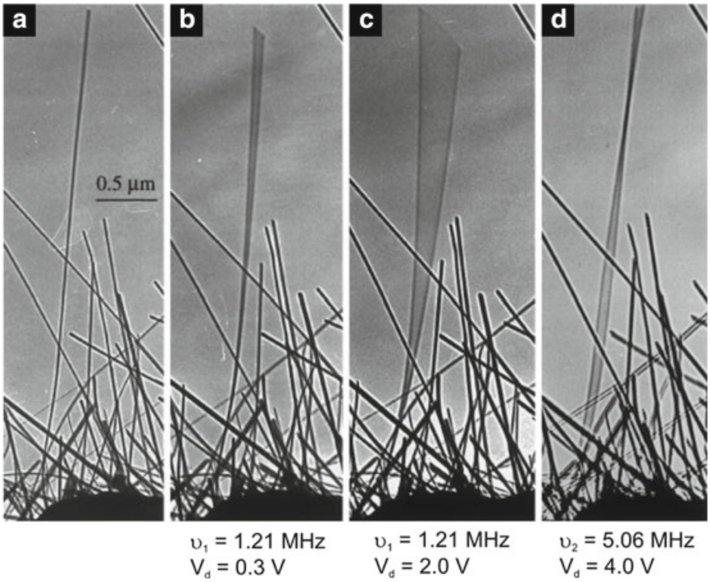

Fig. 7.9 Freestanding nanotube subjected to an oscillating applied voltage (V_d) and undergoing electromechanical resonance. (**a**) Initial configuration. (**b**) and (**c**) First harmonic resonance. (**d**) Second harmonic resonance. Adapted from [100] with permission

Hybrid Carbon Nanotubes

One of the few, if not the only, study to use the electrical holder as a tool for the mechanical analysis of filled CNTs was written by Loeffler et al. [102]. Starting from a Fe-filled MWCNT connected between the electrodes of the holder, the deflection of the nanotube was induced resorting to a quasi-static current-driven Lorentz force. The adapted resonance method is claimed to be independent of inhomogeneous mass distributions (such as particles decorating the external surface of the nanotube) and contamination by amorphous carbon can be subtracted. Young's moduli of 312 GPa and 698 GPa were estimated from the Euler-Bernoulli's model employed.

7.7 Mechanical

It is understood that the main advantages of probing physical properties (mechanical, electrical or others) of nanostructures with in situ TEM are access to discrete particles analysis and the simultaneous real-time imaging/measurement of structural and chemical changes of those. This multidimensional data set collection capability is the reason why the study of CNTs mechanics has advanced significantly over the years. Historically, for the measurement of mechanical properties of individual CNTs, two TEM-based methods have been used: resonance (either thermally or electrically induced) and force sensing. In this section, we are solely concerned with the latter, i.e., those studies that have employed a force-sensing holder capable of directly providing force–displacement data.

Carbon Nanotubes

To our knowledge, the first studies using a force-sensing holder inside a 200 kV TEM for the purpose of measuring mechanical properties of CNTs were reported by two Japanese teams [103, 104]. The Young's modulus was estimated for individual MWCNTs after subjecting these structures to uniaxial compressive loads measured with the help of a commercial atomic force microscopy (AFM) cantilever [103]. Moduli figures as high as 3.3 TPa (for arc-made nanotubes) were extracted. From the analysis of different sets of carbon fibers (which included arc- and CDV-made nanotubes besides non-tubular species), Young's modulus values were very much dependent on the degree of structural order of the carbon lattice. The authors further give an honest account of the limitations of the technique, namely, issues related to measurement of projected displacements and uncertainty of absolute force readings. The buckling mechanics of individual arc-made MWCNTs and their local plastic deformation were studied in a companion report [104]. At 200 kV (25 pA/cm^2), the nanotubes showed flexibility with shape recovery on load release, but when repeatedly compressed beyond their elastic limit, structural fatigue settled in and deformation took place at the vicinity of the defects generated. Inducing fatigue had a clear effect on the original stiffness; therefore a correlation between the mechanical properties and structural defects could be made.

Two years later, Kuzumaki and Mitsuda used the same force-sensing holder to perform tensile deformation on arc-made MWCNTs, reporting two different telescopic shell-sliding modes [105]. While for an inner shell of 5.8 nm diameter the sliding force was constant at 70 nN, multiwalled structures showed varied figures. To generate single-layered nanotubes, sequential electrical breakdown of MWCNT walls was undertaken in situ at 200 kV (60 nA/cm^2). In addition to the number of walls, structural defects and distortion also affect the sliding forces measured. Interestingly, the authors do not refer to the retraction phenomenon previously observed by Cummings and Zettl [101].

In 2008, Peng et al. used a custom-made force-sensing MEMS device to test the tensile strength of arc-made MWCNTs [106]. The nanotubes were probed at 100 kV but higher voltages were used to purposely irradiate and introduce wall-linking defects in some of the structures observed. For as-produced MWCNTs, mean fracture strengths >100 GPa were measured, validating previously calculated theoretical values. Importantly, direct imaging of the failure process allowed precise counting of the fractured shells and, consequently, determination of the failure cross section. For those MWCNTs subjected to beam irradiation, failure loads were maximized with increasing exposure time and led to multishell fracture. This was explained by the load-sharing effect derived from the introduction of interlayer defects (i.e., various layers are stressed as opposed to just the external one). Still, it should be noted that both Young's modulus and failure strains were not decreased considerably. The authors suggest that interlayer load transfer could be maximized with a surprisingly low density of linking defects. The subject of correlating defect density to tensile strength was also studied for the case of SWCNTs [107]. In a 300 kV instrument and using a conductive force-sensing cantilever, clamped arc-made MWCNTs were electrically stripped from the outer layers until one remaining layer was left. By displacing one of the clamps, the nanotube could be stretched, and, in contrast to other reports [101, 105], sliding of the inner shell did not take place. Sliding was prevented due to the welding of the MWCNT ends to the clamps using electron beam irradiation. Fracture strengths of up to 100 GPa were obtained for well-ordered structures. Lower figures predominated in the cases where the end configuration of the single section was not ideal or structural defects abounded (e.g., atomic steps). Electrical annealing of irradiation-induced defects was also demonstrated. More recently, Tsai et al. reported an analysis of buckling deformation for discrete MWCNTs where the probe was a nanoindentation diamond tip and the microscope was operated at 400 kV (1–2 A/cm^2) [108]. The authors make an analysis of how different boundary conditions may affect the critical buckling characteristics of CNT-based systems.

Hybrid Carbon Nanotubes

The few reports available delving into the mechanics of hybrid CNTs (probed with force-sensing holders) relate to the same material, nanotubes filled with doped ZnS [109–111]. The first communication in this series demonstrated that the semiconductor filling had a considerable effect on the mechanical response of the nanocomposite [109]. Accordingly, the same MWCNT was uniaxially compressed when entirely filled and after being voided of the semiconductor nanowire (via electrical heating). The variables and pitfalls behind the operation of the force-sensing holder were shortly after extensively described [110] along with the influence of boundary conditions and aspect ratio of the nanostructures [111]. As regards the latter, it was reported that an optimum window existed to perform the compressive essays for these holders. These in situ TEM investigations were recently complemented by a finite element analysis study that reproduced the differentiated buckling behavior in the filled versus empty states of the MWCNTs (Fig. 7.10) [112].

In contrast to other stimuli, mechanical loads have not been used much in the study of CNTs by in situ TEM. The studies that exist have invariably been performed in MWCNTs (whether electrically stripped or not) and, for the most part, the

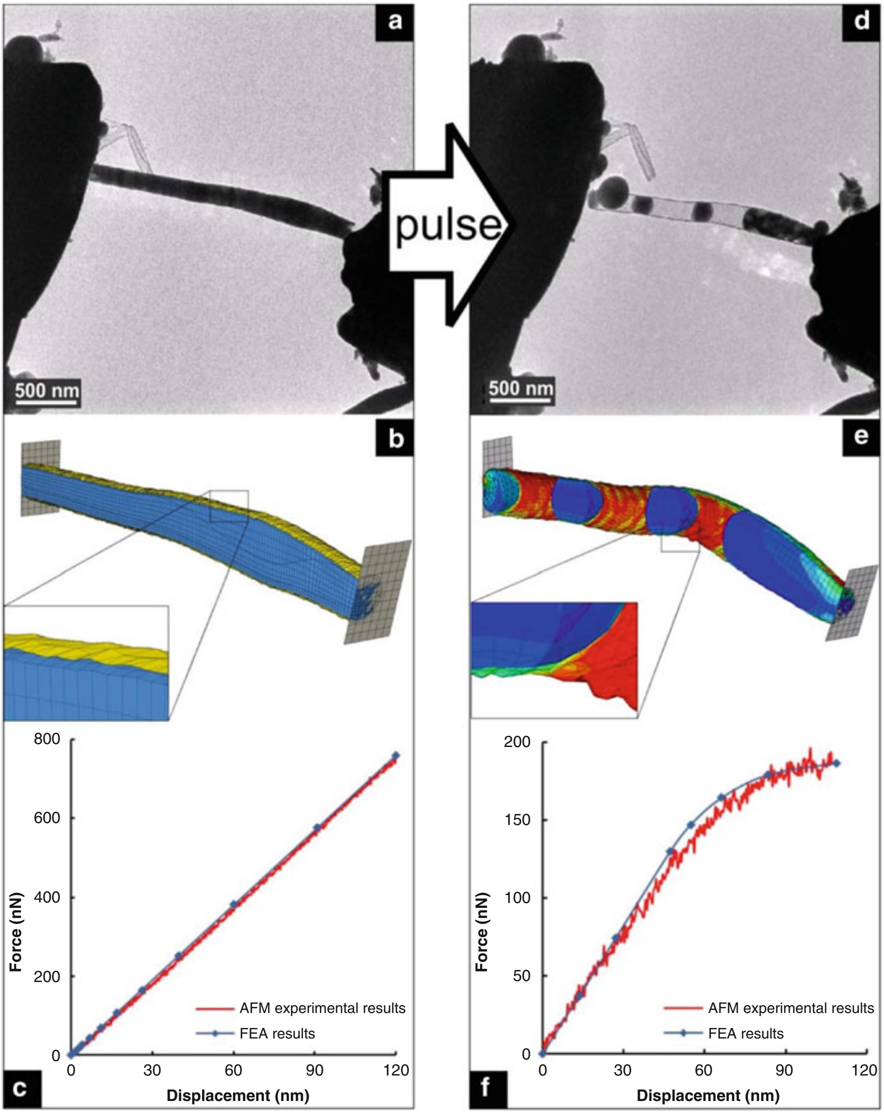

Fig. 7.10 (**a**) Ga-doped ZnS-filled CNT placed between two mechanical clamps. (**b**) Finite element model of the nanotube in (**a**). (**c**) Force–displacement curves (experimental and modeled) of the uniaxial compressive essay performed on the nanotube in (**a**). (**d**) The nanotube in (**a**) after passing an electrical pulse through it. (**b**) Finite element model of the structure in (**d**) under compressive stress. (**f**) Force–displacement curves (experimental and modeled) of the uniaxial compressive essay performed on the nanotube in (**d**). Adapted from [112] with permission

only topic of interest has been on how the density of structural defects will influence the mechanics. With one system studied, the work on hybrid nanotubes is very limited. Finally, for all studies identified, matching ex situ analysis is nonexistent although some of the works have been complemented by numerical analysis.

7.8 Final Remarks

The breadth of the studies described is certainly remarkable. The application of isolated or combined stimulus at a discrete nanostructure level coupled to simultaneous imaging and spectroscopic analysis is a clear advantage of TEM over other characterization methods. From various approaches to study the catalyzed nucleation and growth of CNTs such as gas-solid reactions and high-temperature irradiation to mechanical properties measured using direct- or indirect-force reading techniques, the use of in situ TEM has helped understanding the response of (hybrid) nanotubes exposed to diverse stimuli.

From the studies presented above, it is clear that the community's effort has been laudable but certain issues still need to be looked into. In particular, the disclosure of information concerning experimental procedures is inconsistent and, at instances, even lacks the voltage at which the TEM was operated (not to mention dose rates or beam current density). Where possible, the realization of the proper control experiments such as analogous ex situ essays is also advisable. In all cases, it is important to recall that due to its flexibility and usefulness, in situ TEM studies provide great insight to real-life situations.

We believe that, with further advances in instrumentation, the TEM will soon become one of the main tools to perform all sorts of physical and chemical studies in individual nanostructures such as CNTs. Coupled to the appropriate control and modeling experiments, in situ TEM has the potential to provide atomically resolved insight of reactions and physical responses converting it into a fully fledged laboratory at the nanoscale.

Acknowledgments PMFJC is grateful for the financial support from KAUST. PJF acknowledges the support from KAUST for a 2-week research collaboration visit to this institution.

References

1. C.T. White, T.N. Todorov, Carbon nanotubes as long ballistic conductors. Nature **393**(6682), 240–242 (1998)
2. N. Mason, M.J. Biercuk, C.M. Marcus, Local gate control of a carbon nanotube double quantum dot. Science **303**(5658), 655–658 (2004)
3. V. Sazonova et al., A tunable carbon nanotube electromechanical oscillator. Nature **431**(7006), 284–287 (2004)
4. S.J. Tans, A.R.M. Verschueren, C. Dekker, Room-temperature transistor based on a single carbon nanotube. Nature **393**(6680), 49–52 (1998)
5. E.S. Snow et al., Chemical detection with a single-walled carbon nanotube capacitor. Science **307**(5717), 1942–1945 (2005)
6. W.Q. Han et al., Synthesis of gallium nitride nanorods through a carbon nanotube-confined reaction. Science **277**(5330), 1287–1289 (1997)
7. L.J. Lauhon et al., Epitaxial core-shell and core-multishell nanowire heterostructures. Nature **420**(6911), 57–61 (2002)
8. R.F. Egerton et al., Basic questions related to electron-induced sputtering in the TEM. Ultramicroscopy **110**(8), 991–997 (2010)

9. R. Sharma, Experimental set up for in situ transmission electron microscopy observations of chemical processes. Micron **43**(11), 1147–1155 (2012)
10. V.H. Crespi et al., Anisotropic electron-beam damage and the collapse of carbon nanotubes. Phys. Rev. B. Condens. Matter **54**(8), 5927–5931 (1996)
11. P.M. Ajayan, V. Ravikumar, J.C. Charlier, Surface reconstructions and dimensional changes in single-walled carbon nanotubes. Phys. Rev. Lett. **81**(7), 1437–1440 (1998)
12. A. Krishnan et al., Young's modulus of single-walled nanotubes. Phys. Rev. B **58**(20), 14013–14019 (1998)
13. M.M.J. Treacy, T.W. Ebbesen, J.M. Gibson, Exceptionally high Young's modulus observed for individual carbon nanotubes. Nature **381**(6584), 678–680 (1996)
14. B.W. Smith, D.E. Luzzi, Electron irradiation effects in single wall carbon nanotubes. J. Appl. Phys. **90**(7), 3509–3515 (2001)
15. A. Hashimoto et al., Direct evidence for atomic defects in graphene layers. Nature **430**(7002), 870–873 (2004)
16. A.C.Y. Liu, R. Arenal, G. Montagnac, In situ transmission electron microscopy observation of keV-ion irradiation of single-walled carbon and boron nitride nanotubes. Carbon **62**, 248–255 (2013)
17. S. Iijima, Helical microtubules of graphitic carbon. Nature **354**(6348), 56–58 (1991)
18. B.W. Smith, M. Monthioux, D.E. Luzzi, Encapsulated C-60 in carbon nanotubes. Nature **396**(6709), 323–324 (1998)
19. B.W. Smith, M. Monthioux, D.E. Luzzi, Carbon nanotube encapsulated fullerenes: a unique class of hybrid materials. Chem. Phys. Lett. **315**(1–2), 31–36 (1999)
20. Z. Liu, K. Suenaga, S. Iijima, Imaging the structure of an individual C-60 fullerene molecule and its deformation process using HRTEM with atomic sensitivity. J. Am. Chem. Soc. **129**(21), 6666–6667 (2007)
21. Y. Sato et al., Structures of D-5d-C-80 and I-h-Er3N@C-80 fullerenes and their rotation inside carbon nanotubes demonstrated by aberration-corrected electron microscopy. Nano Lett. **7**(12), 3704–3708 (2007)
22. J. Sloan et al., Capillarity and silver nanowire formation observed in single walled carbon nanotubes. Chem. Commun. **8**, 699–700 (1999)
23. G. Brown et al., Electron beam induced in situ clusterisation of 1D ZrCl4 chains within single-walled carbon nanotubes. Chem. Commun. **9**, 845–846 (2001)
24. P.M.F.J. Costa et al., Encapsulation of RexOy clusters within single-walled carbon nanotubes and their in tubulo reduction and sintering to Re metal. Chem. Mater. **17**(26), 6579–6582 (2005)
25. N. Naguib et al., Observation of water confined in nanometer channels of closed carbon nanotubes. Nano Lett. **4**(11), 2237–2243 (2004)
26. Y. Gogotsi, J.A. Libera, M. Yoshimura, Hydrothermal synthesis of multiwall carbon nanotubes. J. Mater. Res. **15**(12), 2591–2594 (2000)
27. D. Qian et al., Load transfer and deformation mechanisms in carbon nanotube-polystyrene composites. Appl. Phys. Lett. **76**(20), 2868–2870 (2000)
28. F. Banhart, *In-situ electron microscopy at high resolution*, vol. vi (World Scientific, Hackensack, 2008). p. 311
29. M. Terrones et al., Coalescence of single-walled carbon nanotubes. Science **288**(5469), 1226–1229 (2000)
30. M. Terrones, F. Banhart, N. Grobert et al., Molecular junctions by joining single-walled carbon nanotubes. Phys. Rev. Lett **89**(7), 075505 (2002)
31. J.X. Li, F. Banhart, The engineering of hot carbon nanotubes with a focused electron beam. Nano Lett. **4**(6), 1143–1146 (2004)
32. F. Banhart, J.X. Li, A.V. Krasheninnikov, Carbon nanotubes under electron irradiation: stability of the tubes and their action as pipes for atom transport. Phys. Rev. B **71**(24), 241408(R) (2005)
33. Y.J. Gan et al., The diffusion of carbon atoms inside carbon nanotubes. New J. Phys. **10** (2008)
34. K. Urita, K. Suenaga, T. Sugai et al., In situ observation of thermal relaxation of interstitial-vacancy pair defects in a graphite gap. Phys. Rev. Lett **94**(15), 155502 (2005)

35. G.E. Begtrup, K.G. Ray, B.M. Kessler et al., Probing nanoscale solids at thermal extremes. Phys. Rev. Lett **99**(15), 155901 (2007)
36. D.E. Luzzi, B.W. Smith, Carbon cage structures in single wall carbon nanotubes: a new class of materials. Carbon **38**(11–12), 1751–1756 (2000)
37. K. Suenaga et al., Evidence for the intramolecular motion of Gd atoms in a Gd-2@C-92 nanopeapod. Nano Lett. **3**(10), 1395–1398 (2003)
38. Y.H. Gao, Y. Bando, Carbon nanothermometer containing gallium—Gallium's macroscopic properties are retained on a miniature scale in this nanodevice. Nature **415**(6872), 599–599 (2002)
39. L. Sun et al., Carbon nanotubes as high-pressure cylinders and nanoextruders. Science **312**(5777), 1199–1202 (2006)
40. J.A. Rodriguez-Manzo et al., In situ nucleation of carbon nanotubes by the injection of carbon atoms into metal particles. Nat. Nanotechnol. **2**(5), 307–311 (2007)
41. J.A. Rodriguez-Manzo et al., Heterojunctions between metals and carbon nanotubes as ultimate nanocontacts. Proc. Natl. Acad. Sci. U. S. A. **106**(12), 4591–4595 (2009)
42. J.A. Rodriguez-Manzo, M.S. Wang, F. Banhart et al., Multibranched junctions of carbon nanotubes via cobalt particles. Adv. Mater **21**(44), 4477 (2009)
43. P.M.F.J. Costa et al., Stepwise current-driven release of attogram quantities of copper iodide encapsulated in carbon nanotubes. Nano Lett. **8**(10), 3120–3125 (2008)
44. M.E. Toimil-Molares et al., Pipetting nanowires: in situ visualization of solid-state nanowire-to-nanoparticle transformation driven by surface diffusion-mediated capillarity. Adv. Funct. Mater. **22**(4), 695–701 (2012)
45. Y. Hayashi et al., High temperature in-situ observations of multi-segmented metal nanowires encapsulated within carbon nanotubes by in-situ filling technique. Nanoscale Res. Lett. **7**, 1–4 (2012)
46. P.M.F.J. Costa et al., Effect of electron beam irradiation and heating on the structural stability of sulphide-filled carbon nanotubes. Microsc. Microanal. **18**, 77–78 (2012)
47. J.R. Jinschek, Advances in the environmental transmission electron microscope (ETEM) for nanoscale in situ studies of gas-solid interactions. Chem. Commun. **50**(21), 2696–2706 (2014)
48. S. Helveg et al., Atomic-scale imaging of carbon nanofibre growth. Nature **427**(6973), 426–429 (2004)
49. R. Sharma, Z. Iqbal, In situ observations of carbon nanotube formation using environmental transmission electron microscopy. Appl. Phys. Lett. **84**(6), 990–992 (2004)
50. R.T.K. Baker, J.J. Chludzinski Jr., Filamentous carbon growth on nickel-iron surfaces: the effect of various oxide additives. J. Catal. **64**(2), 464–478 (1980)
51. R. Sharma et al., In situ observation of the growth mechanisms of carbon nanotubes under diverse reaction conditions. J. Electron Microsc. (Tokyo) **54**(3), 231–237 (2005)
52. S. Hofmann et al., In situ observations of catalyst dynamics during surface-bound carbon nanotube nucleation. Nano Lett. **7**(3), 602–608 (2007)
53. S. Hofmann et al., State of transition metal catalysts during carbon nanotube growth. J. Phys. Chem. C **113**(5), 1648–1656 (2009)
54. M. Lin et al., Direct observation of single-walled carbon nanotube growth at the atomistic scale. Nano Lett. **6**(3), 449–452 (2006)
55. M. Lin et al., Dynamical observation of bamboo-like carbon nanotube growth. Nano Lett. **7**(8), 2234–2238 (2007)
56. H. Yoshida, T. Uchiyama, S. Takeda, Direct observation of carbon nanotube growth by environmental transmission electron microscopy. Microsc. Semicond. Mater. 2007 **120**, 209–212 (2008)
57. H. Yoshida et al., Atomic-scale in-situ observation of carbon nanotube growth from solid state iron carbide nanoparticles. Nano Lett. **8**(7), 2082–2086 (2008)
58. R. Sharma et al., Evaluation of the role of Au in improving catalytic activity of Ni nanoparticles for the formation of one-dimensional carbon nanostructures. Nano Lett. **11**(6), 2464–2471 (2011)

59. A.L. Koh et al., Observations of carbon nanotube oxidation in an aberration-corrected environmental transmission electron microscope. ACS Nano **7**(3), 2566–2572 (2013)
60. P.M.F.J. Costa et al., Imaging the oxidation of ZnS encapsulated in carbon nanotubes. Chemistry **16**(39), 11809–11812 (2010)
61. U.K. Gautam et al., Ga-doped ZnS nanowires as precursors for ZnO/ZnGa2O4 nanotubes. Adv. Mater **20**(4), 810 (2008)
62. S. Frank et al., Carbon nanotube quantum resistors. Science **280**(5370), 1744–1746 (1998)
63. J. Cumings, P.G. Collins, A. Zettl, Materials—peeling and sharpening multiwall nanotubes. Nature **406**(6796), 586–586 (2000)
64. J.Y. Huang et al., Atomic-scale imaging of wall-by-wall breakdown and concurrent transport measurements in multiwall carbon nanotubes. Phys. Rev. Lett. **94**(23), 236802 (2005)
65. D. Golberg et al., Nanotubes in a gradient electric field as revealed by STM-TEM technique. Nano Rese. **1**(2), 166–175 (2008)
66. T.T. Xu, Z.Y. Ning, T.W. Shi et al., A platform for in-situ multi-probe electronic measurements and modification of nanodevices inside a transmission electron microscope. Nanotechnology **25**(22), 225702 (2014)
67. R.P. Gao, Z.W. Pan, Z.L. Wang, Work function at the tips of multiwalled carbon nanotubes. Appl. Phys. Lett. **78**(12), 1757–1759 (2001)
68. J. Cumings, A. Zettl, M.R. McCartney et al., Electron holography of field-emitting carbon nanotubes. Phys. Rev. Lett **88**(5), 056804 (2002)
69. Z.L. Wang et al., In situ imaging of field emission from individual carbon nanotubes and their structural damage. Appl. Phys. Lett. **80**(5), 856–858 (2002)
70. Z.L. Wang, In situ electron microscopy for nanomeasurements, in *Handbook of microscopy for nanotechnology*, ed. by N. Yao, Z.L. Wang (Springer, New York, 2005), p. 731
71. M.S. Wang, Q. Chen, L.M. Peng, Grinding a nanotube. Adv. Mater **20**(4), 724 (2008)
72. Q.M. Su et al., In situ TEM study on the electrical and field-emission properties of individual Fe3C-filled carbon nanotubes. J. Phys. Chem. C **116**(43), 23175–23179 (2012)
73. M.Z.M. Yusop et al., In situ TEM observation of Fe-included carbon nanofiber: evolution of structural and electrical properties in field emission process. ACS Nano **6**(11), 9567–9573 (2012)
74. B.C. Regan et al., Carbon nanotubes as nanoscale mass conveyors. Nature **428**(6986), 924–927 (2004)
75. K. Svensson, H. Olin, E. Olsson, Nanopipettes for metal transport. Phys. Rev. Lett **93**(14), 145901 (2004)
76. D. Golberg et al., Copper-filled carbon nanotubes: rheostat like behavior and femtogram copper mass transport. Adv. Mater **19**(15), 1937 (2007)
77. L.X. Dong et al., Nanorobotic spot welding: Controlled metal deposition with attogram precision from copper-filled carbon nanotubes. Nano Lett. **7**(1), 58–63 (2007)
78. J.Y. Huang, F. Ding, K. Jiao et al., Real time microscopy, kinetics, and mechanism of giant fullerene evaporation. Phys. Rev. Lett **99**(17), 175503 (2007)
79. P.M.F.J. Costa et al., Direct imaging of Joule heating dynamics and temperature profiling inside a carbon nanotube interconnect. Nat. Commun. **2**, 421 (2011)
80. P.M.F.J. Costa et al., The electrical delivery of a sublimable II-VI compound by vapor transport in carbon nanotubes. Carbon **49**(12), 3747–3754 (2011)
81. P.M.F.J. Costa et al., Comparative study of the stability of sulfide materials encapsulated in and expelled from multi-walled carbon nanotube capsules. Carbon **49**(1), 342–346 (2011)
82. Z. Fan et al., Metal-filled carbon nanotube based optical nanoantennas: bubbling, reshaping, and in situ characterization. Nanoscale **4**(18), 5673–5679 (2012)
83. M.S. Wang et al., Fabrication and electrical and mechanical properties of carbon nanotube interconnections. Adv. Funct. Mater. **15**(11), 1825–1831 (2005)
84. C.H. Jin, K. Suenaga, S. Iijima, Plumbing carbon nanotubes. Nat. Nanotechnol. **3**(1), 17–21 (2008)
85. M.S. Wang, D. Golberg, Y. Bando, Interface dynamic behavior between a carbon nanotube and metal electrode. Adv. Mater **22**(1), 93 (2010)

86. M.S. Wang, D. Golberg, Y. Bando, Superstrong low-resistant carbon nanotube-carbide-metal nanocontacts. Adv. Mater **22**(47), 5350 (2010)
87. M. Karita et al., In situ TEM study on the improvement of contact resistance between a carbon nanotube and metal electrodes by local melting. Surf. Interface Anal. **44**(6), 674–677 (2012)
88. M. Karita et al., In situ TEM study on changes in structure and electrical conductance of carbon nanotube-gold contact induced by local joule heating. J. Mater. Sci. **48**(2), 936–940 (2013)
89. M.S. Wang et al., Cobalt nanoparticle-assisted engineering of multiwall carbon nanotubes. ACS Nano **3**(9), 2632–2638 (2009)
90. D.M. Tang et al., Carbon nanotube-clamped metal atomic chain. Proc. Natl. Acad. Sci. U. S. A. **107**(20), 9055–9059 (2010)
91. C. Jin, K. Suenaga, S. Iijima, How does a carbon nanotube grow? An in situ investigation on the cap evolution. ACS Nano **2**(6), 1275–1279 (2008)
92. K. Jensen, W. Mickelson, W. Han et al., Current-controlled nanotube growth and zone refinement. Appl. Phys. Lett **86**(17), 173107 (2005)
93. B.L. Liu et al., Importance of oxygen in the metal-free catalytic growth of single-walled carbon nanotubes from SiOx by a vapor-solid-solid mechanism. J. Am. Chem. Soc. **133**(2), 197–199 (2011)
94. D.M. Tang et al., Structural changes in iron oxide and gold catalysts during nucleation of carbon nanotubes studied by in situ transmission electron microscopy. ACS Nano **8**(1), 292–301 (2014)
95. X.H. Liu et al., In situ TEM experiments of electrochemical lithiation and delithiation of individual nanostructures. Adv. Energy Mater. **2**(7), 722–741 (2012)
96. Y. Liu et al., Lithiation-induced embrittlement of multiwalled carbon nanotubes. ACS Nano **5**(9), 7245–7253 (2011)
97. Q.M. Su et al., In situ transmission electron microscopy investigation of the electrochemical lithiation-delithiation of individual Co9S8/co-filled carbon nanotubes. ACS Nano **7**(12), 11379–11387 (2013)
98. Q.M. Su et al., In situ transmission electron microscopy observation of electrochemical sodiation of individual Co9S8-filled carbon nanotubes. ACS Nano **8**(4), 3620–3627 (2014)
99. P. Poncharal et al., Electrostatic deflections and electromechanical resonances of carbon nanotubes. Science **283**(5407), 1513–1516 (1999)
100. Z.L. Wang, P. Poncharal, W.A. de Heer, Measuring physical and mechanical properties of individual carbon nanotubes by in situ TEM. J. Phys. Chem. Solid **61**(7), 1025–1030 (2000)
101. J. Cumings, A. Zettl, Low-friction nanoscale linear bearing realized from multiwall carbon nanotubes. Science **289**(5479), 602–604 (2000)
102. M. Loffler et al., Robust determination of Young's modulus of individual carbon nanotubes by quasi-static interaction with Lorentz forces. Ultramicroscopy **111**(2), 155–158 (2011)
103. K. Enomoto et al., Measurement of Young's modulus of carbon nanotubes by nanoprobe manipulation in a transmission electron microscope. Appl. Phys. Lett **88**(15), 153115 (2006)
104. T. Kuzumaki, Y. Mitsuda, Nanoscale mechanics of carbon nanotube evaluated by nanoprobe manipulation in transmission electron microscope. Jpn. J. Appl. Phys. Part 1-Regular Papers Brief Communications & Review Papers. **45**(1A), 364–368 (2006).
105. T. Kuzumaki, Y. Mitsuda, Characterization of carbon nanotubes by nanoprobe manipulation in transmission electron microscope. Diamond Relat. Mater. **17**(4–5), 615–619 (2008)
106. B. Peng et al., Measurements of near-ultimate strength for multiwalled carbon nanotubes and irradiation-induced crosslinking improvements. Nat. Nanotechnol. **3**(10), 626–631 (2008)
107. M.S. Wang, D. Golberg, Y. Bando, Tensile tests on individual single-walled carbon nanotubes: linking nanotube strength with its defects. Adv. Mater. **22**(36), 4071–4075 (2010)
108. P.C. Tsai et al., Buckling characterizations of an individual multi-walled carbon nanotube: insights from quantitative in situ transmission electron microscope nanoindentation and molecular dynamics. Appl. Phys. Lett **103**(5), 053119 (2013)

109. P.M.F.J. Costa et al., Effect of crystalline filling on the mechanical response of carbon nanotubes. Carbon **47**(2), 541–544 (2009)
110. P.M. Costa, P.B. Cachim, U.K. Gautam et al., The mechanical response of turbostratic carbon nanotubes filled with Ga-doped ZnS: I. Data processing for the extraction of the elastic modulus. Nanotechnology **20**(40), 405706 (2009)
111. P.M. Costa, P.B. Cachim, U.K. Gautam et al., The mechanical response of turbostratic carbon nanotubes filled with Ga-doped ZnS: II. Slenderness ratio and crystalline filling effects. Nanotechnology **20**(40), 405707 (2009)
112. A.O. Monteiro, P.M.F.J. Costa, P.B. Cachim, Finite element modelling of the mechanics of discrete carbon nanotubes filled with ZnS and comparison with experimental observations. J. Mater. Sci. **49**(2), 648–653 (2014)

Chapter 8
Physical Characterization of Nanomaterials in Dispersion by Transmission Electron Microscopy in a Regulatory Framework

Jan Mast, Eveline Verleysen, and Pieter-Jan De Temmerman

8.1 Introduction

The combination of transmission electron microscopy (TEM) imaging with image analysis is one of the few methods that allow obtaining the number-based size distribution of nanoparticles in powders and liquids [1]. TEM remains a key technique to identify the presence of nanomaterials in consumer products [2–4]. It is one of the few methods that allow characterizing a material as a nanomaterial and measure the size distribution in particle numbers [5]. In addition, TEM imaging allows attaining a very high resolution, which reliably covers the entire size range from 1 to 100 nm specified in the various definitions of nanomaterial [6, 7].

TEM analyses are useful to describe the physical characteristics of a nanomaterial qualitatively [8–10]. In such analyses, nanomaterial properties essential for analyzing the risks of using nanomaterials in food and consumer products [2, 11] are determined through information extracted from representative and selected TEM images.

If the particles can be brought on an electron microscopy (EM) grid and if their distribution is homogeneous and representative for the sample, a semiautomatic analysis of TEM micrographs can be applied to estimate the distributions of the particle size and shape, describing the sample quantitatively [12–14]. This analysis can be complemented by results of electron diffraction to determine the crystallographic phase [15, 16] and of energy dispersive X-ray spectroscopy (EDX) and electron energy-loss spectroscopy (EELS) to determine the chemical composition or electronic structure of the particles [17–21].

Disadvantages of EM analysis of nanomaterials include the bias from suboptimal sampling and sample preparation, the measurement of 3D objects from 2D

J. Mast (✉) • E. Verleysen • P.-J. De Temmerman
Service Electron Microscopy, Veterinary and Agrochemical Research Centre (CODA-CERVA), Groeselenberg 99, Brussels 1180, Belgium
e-mail: Jan.Mast@coda-cerva.be

F.L. Deepak et al. (eds.), *Advanced Transmission Electron Microscopy*,
DOI 10.1007/978-3-319-15177-9_8

projections, the interpretation of the size of primary particles in aggregates or agglomerates, the relatively high number of particles required for measurement, and the need to develop algorithms for automated image analysis for each separate type of nanomaterial. In many cases, technical solutions that can overcome these disadvantages are available or under development, e.g., more advanced EM techniques such as electron tomography and cryo-EM can be used to obtain information about the third dimension of the particles and to avoid artifacts [22–26].

Quantitative TEM analyses can play an important role in the implementation of the newly established regulatory framework of the European Commission (EC) regulating the use of nanomaterials in consumer products [6, 27–32]. The implementation of the EC definition of a nanomaterial [29] across various regulatory fields requires a detailed detection and characterization of manufactured nanomaterials by appropriate, validated testing methods [1, 33]. TEM seems to be a well-suited technique because of its high resolution, ability to obtain number-based size distributions, and ability to visualize colloidal nanomaterials as well as primary particles in aggregates in 2D.

The specimen preparation and characterization techniques applied in conventional material science, such as focused ion beam (FIB), atomic force microscopy (AFM), Rutherford backscattering spectrometry (RBS), and secondary ion-mass spectrometry (SIMS), are most relevant to characterize solids. However, to perform toxicity testing of nanomaterials, which typically includes in vitro and in vivo experiments, nanomaterials have to be characterized when they are in dispersion in a specific medium. To realize this, OECD [4, 34, 35] recommends that ensemble techniques based on light scattering, such as dynamic light scattering (DLS), and density-based methods, such as centrifugal liquid sedimentation (CLS) and the Brunauer-Emmett-Teller (BET) method, are complemented with TEM analyses [1]. Currently, particle separation techniques such as field-flow fractionation (FFF) are combined with inductively coupled plasma-mass spectrometry (ICP-MS) [36], and new techniques, such as particle tracking analysis (PTA), are developed for the measurement of particle size [1]. However, these techniques do not yet have the spatial resolution required to cover the complete nano-range, have difficulties in distinguishing primary particles from aggregates, and only measure size in one dimension.

Only if the specimen preparation results in placing the dispersed nanomaterials on a suitable support representatively, microscopy-based techniques such as AFM and TEM are well suited to characterize nanomaterials. For this reason, this chapter will focus not only on nanomaterial characterization but also on the preparation of TEM specimens of dispersed nanomaterials. Furthermore, different methodologies to obtain homogeneous and stable dispersions of colloidal nanomaterial and powders are reviewed. The different steps required to analyze dispersed nanomaterials by TEM are treated sequentially, from the sample preparation to the validation of the results. A typical TEM analysis of a nanomaterial includes bringing the nanomaterial in dispersion and preparing an EM grid; recording representative and selected EM images; performing a descriptive, qualitative analysis; performing a quantitative analysis which includes detection, classification, and measurement of primary particles; and validating the measurement results.

8.2 Preparing Samples for TEM Analysis

To be able to interpret the results of in vivo and in vitro tests, a physicochemical characterization of the nanomaterial samples in the stock dispersion and in the administration medium prior to and during administration is considered indispensable [4, 37, 38]. These guidelines consider quantitative and qualitative TEM analyses instrumental to determine the properties of as-produced, nanoparticle powders and nanoparticles in dispersion. It is required that the examined dispersions are stable enough such that a representative specimen can be prepared. To achieve a homogeneous and stable dispersion of particles, nanomaterials that are already dispersed in liquid, as well as powdered nanomaterials, need to undergo specific treatments, such as dilution, drying, and dispersion [1]. These treatments allow obtaining a sample in a state of dispersion which is fit for analysis.

For colloidal solutions, sample preparation does not tend to introduce a significant bias in the size measurement of the particles [39]: the solutions are stable and their particles do not sediment permanently when kept in bottles under ordinary laboratory conditions. For colloidal gold and silica reference materials, NIST [40–42] and IRMM [43, 44] instruct to gently invert the sample vial several times to assure homogeneity and resuspension of any settled particles. Other producers like Thermo Scientific suggest to prepare their 3000 Series Nanosphere Size Standards with a vortex mixer [45].

In the case of powdered nanomaterials, finely dispersed and stable dispersions are more difficult to prepare [46]. Specific protocols proposed by Guiot and Spalla [46], De Temmerman et al. [14], and Bihari et al. [47] systematically analyze the importance of sonication, selection of dispersion medium, and addition of stabilization agents and determine an optimized nanoparticle dispersion method specific for each type of nanomaterial. These protocols aim to prepare samples in their most disperse state, facilitating characterization of these materials. Typically, these nanomaterial-specific protocols are not limited to aqueous dispersion media, but also include dispersing the materials in apolar solvents.

For toxicity testing in a regulatory framework, dispersion of particles using a generic dispersion protocol eliminates some of the uncertainty factors, and development of generic protocols has been initiated [48–50]. These protocols combine prewetting of the material with electro-steric stabilization resulting in comparable, stabilized dispersions of various types of (powdered) nanomaterials. A compromise needs to be found between obtaining the material in its most disperse form and applicability of the protocols on different types of nanomaterials. Furthermore, it has to be considered that dispersion of particles may lead to partial dissolution of particles or to swelling [1]. The generic Nanogenotox [48], Prospect [49], and NIST [50, 51] protocols are tested on a variety of nanomaterials to optimize the protocol for dispersing a range of nanomaterials using stabilizing components such as serum and bovine serum albumin that are compatible with the medium and performance of the test. These protocols focus on bringing the material in a stable dispersion in water or buffer. The advantage is that the dispersions of various types of nanomaterials are prepared in the same way, reducing sample preparation bias when comparing test results of these nanomaterials. However, dispersing materials in complex media, such as buffers, cell or bacterial culture media, and biological fluids, can induce strong agglomeration and reduce the stability of the material. Verleysen et al. [13] and Guiot and Spalla [46] showed that among others the pH of the dispersion medium has a strong influence on the stability of the nanomaterials. Surfactant-stabilized preparations such as oligonucleotides and polyethylene glycols are proposed as an alternative to stabilize materials under higher salt concentrations [52].

As opposed to online sizing methods like PTA and DLS, TEM measurements require recovering particles from the dispersion, coating them on an appropriate support and drying them [1]. Recovering nanoparticles from suspension is generally done by floating the grid on a droplet of suspension (grid on drop) [13, 14] or placing a droplet of suspension on the grid (drop on grid) [40–42], followed by washing the grid and passively drying at room temperature. Using these approaches, a representative and homogeneous distribution of the particles on the grid can be obtained relatively easily and cheaply for many materials. Alternatively, ultracentrifugation allows to quantitatively recover nanoparticles from the liquid medium [53]. This has the advantage that the nanoparticles are actively concentrated and quantitatively centrifuged on the TEM grid. However, the amount of salts and debris that attach to the grid, and concomitant background, increases proportionally with the concentration of the particles. Dilution of the sample avoids such increased background but can influence the properties of agglomerates.

The above-described preparation methods profit from the use of a stable film on the EM grids. This stability can be assured by using TEM grids with a small mesh size (e.g., 400 mesh) combining a Formvar or Pioloform film with the depositing of carbon to reinforce the surface. To assure adhesion of a representative fraction of the particles to the grid, it is essential that the charge of the particles is compatible with the charge of the grid surface. The carbon layer makes, for example, the grids hydrophobic, reducing the recovery of charged particles from suspension [54]. Rendering the grids hydrophilic by pretreatment of the grids with BSA, bacitracin, Alcian blue, or glow discharge allows adapting the charge of the grids to the charge of the particles and generally increases the recovery of particles (Fig. 8.1) [54]. Alcian blue pretreatment of the EM grids results in positively charged grids, while glow discharging results in negatively charged grids. After glow discharging, positive charges can be introduced by performing an additional treatment with bivalent ions like Ca^{2+} and Mg^{2+}. Alternatively, functionalized “smart” hydrophobic, hydrophilic, positively and negatively charged grids are commercially available [55]. It has to be considered that the background can be reduced by avoiding multiple layers on the TEM grids (Formvar/Pioloform, carbon, Alcian blue, etc.). Another possibility is high vacuum baking, which has the extra benefit of reducing carbon contamination during acquisition.

Most samples for TEM must be “supported” by a thin electron transparent film, to hold the particles in place. Certain specific particles, such as carbon nanotubes, are “self-supporting” and have a length that can span the holes in holey grids [56]. For these types of nanomaterials, using holey grids can be beneficial because there is no background from the film on the images. Disadvantages of using holey grids

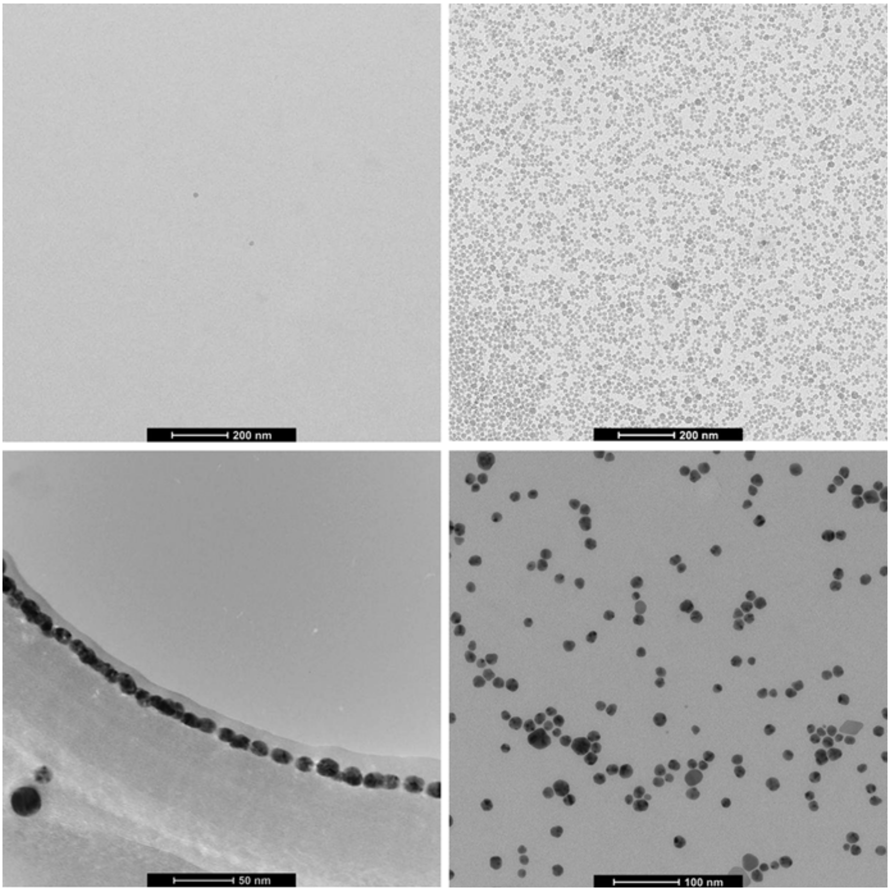

Fig. 8.1 Micrographs illustrating the effects of TEM specimen preparation conditions on the distribution of particles on the grid. Colloidal silica particles on an untreated grid (**a**) and on a grid coated with Alcian blue (**b**). Ag particles on a holey grid (**c**) and on a Pioloform and carbon-coated grid (**d**)

are that only a small amount of particles remains attached to the grid, that the specimen drift might be higher [56], and that the interaction of particles with the borders of the holes in the film selects subpopulations of nanoparticles (Fig. 8.1).

8.3 Imaging and Chemical Analysis of Nanoparticles by TEM

When a representative specimen of nanomaterial in dispersion can be prepared, different TEM imaging techniques can be applied and combined with image analysis to obtain complementary information on the size, morphology, crystallographic structure, and composition of the nanomaterial. Detailed information about TEM imaging and analysis can be found in excellent textbooks, for example, by M. De Graef [57] and by D. B. Williams and C. B. Carter [58]. In this section the TEM imaging techniques for the direct visualization and physical characterization of nanomaterials and the determination of the chemical composition of nanomaterials by analytical TEM are discussed in the scope of analysis of nanomaterials in dispersion.

8.3.1 TEM Bright-Field Imaging Mode

To characterize nanomaterials and to implement the EC nanomaterial definition on a larger scale, conventional bright-field TEM has the advantage over other, more advanced imaging modes in that it is cheap, widely available, and easy to use. In the bright-field imaging mode, contrast originates from the absorption and scattering of electrons in the specimen, due to the thickness and composition of the material (i.e., mass-thickness contrast). In addition, in crystalline materials, the crystallite orientation introduces diffraction contrast.

To perform a descriptive, qualitative analysis, all relevant features of the nanomaterial, including size and shape of the particles, surface structure, crystallinity, and distribution of particles on the grid, are visualized. Representative images are typically recorded at high (approximately ×400,000), medium (approximately ×40,000), and low magnifications (approximately ×1,000) to illustrate, respectively, the atomic structure and particle properties and to provide an overview of the specimen.

To perform a quantitative analysis, multiple images of different regions on the grid are usually recorded at one magnification only. To assure unbiased random image collection, a systematic micrograph selection procedure can be used. De Temmerman et al. [14] avoid, for example, subjectivity in the selection of particles by the microscopist, by recording micrographs randomly and systematically, at positions predefined by the microscope stage and evenly distributed over the entire grid area. When the field of view is obscured, e.g., by a grid bar or an artifact, the stage can be moved sideways to the nearest suitable field of view. The selected magnification has to allow measuring particle features with high enough accuracy and measuring enough particles to obtain sufficient precision and to limit the time needed for analysis. Therefore, a medium magnification is usually selected, depending on the size of the primary particles of the nanomaterial.

A disadvantage of characterizing nanomaterials by TEM might be that a statistically relevant number of particles cannot be analyzed in a time- and labor-efficient manner. As guidelines are still missing, reported particle numbers vary from a few particles to several thousands in reports characterizing nanomaterials. An estimate of the number of particles required for the estimation of the mean particle diameter with a certain confidence level can be calculated based on De Temmerman et al. [12, 59].

Expression of the measurement uncertainties of the size as a function of the number of measured particles demonstrated that no more than 200 particles have to be measured to obtain a relative laboratory uncertainty of 5 % for sizing colloidal silica reference nanomaterials [59]. This number is in agreement with the calculations proposed by Matsuda and Gotoh [60] but requires adjustment for nanomaterials with a more polydisperse size distribution.

The pixel size and the field of view determine the useful range, which is defined by the lower and upper size of the detection limit. Applying the criterion of Merkus [61] for the lower particle size detection limit, large systematic size deviations can be avoided if the smallest particle area is at least 100 pixels. The field of view restricts the upper size detection limit to one tenth of the image size [5].

In the case of crystalline materials, the orientation of the crystallites and the occurrence of crystal defects can be studied by increasing the magnification. At high magnification (HR-TEM mode), the specimen can be modeled as an object that modifies the phase of the incoming waves. In a crystalline material, elastic coherent scattering leads to diffraction of the incident electron beam. The diffracted electron waves interfere constructively or destructively with the undiffracted transmitted wave depending on defocus and phase shift of the waves in the specimen. The interference of transmitted and diffracted electrons gives rise to so-called phase contrast. As a consequence, the electrostatic potentials of the atom columns can be visualized and related to the crystal structure, but are not a direct projection of the atom positions. Examples of HR-TEM studies on nanoparticles are given in [16, 62–66]. For HR-TEM images to provide information on atomic arrangements in a material, comparison of the images with computer simulations based on atomic models is usually required.

8.3.2 Diffraction Mode

The fact that for a crystalline material the electron beam undergoes Bragg diffraction can be used to obtain information about the crystal structure of the crystalline nanoparticles [16, 18, 67–69]. Electron diffraction patterns of larger regions containing crystalline nanoparticles consist of ring patterns analogous to those from X-ray powder diffraction. Such a ring pattern originates from the different orientations of the particles (which can be mono- or polycrystalline) with respect to the electron beam and can besides obtaining crystallographic information be used to identify texture and discriminate crystalline from amorphous phases. The recorded diffraction patterns should be indexed using a diffraction database, which allows determining the possible structure and composition or phase of the material (e.g., AtomWork [70]).

8.3.3 High-Angle Annular Dark Field-Scanning Transmission Electron Microscopy

In STEM mode, the electron beam is focused into a (sub-)nanometer-sized probe. This illuminating electron probe scans over the specimen, and various signals produced by the scattering of the electrons can be detected and displayed as a function of the probe position. The interactions with the specimen give accurate localized chemical and physical information. High-angle annular dark-field (HAADF) imaging refers to the use of a geometrically large ring-shaped detector, placed below the specimen. Because of the detector geometry, only electrons that are scattered at high angle are detected. While electrons scattered to low angles are predominantly coherent (and as such conventional bright-field and dark-field images can give contrast reversals with changes in specimen thickness, orientation, or defocus), electrons scattered to high angles are predominantly incoherent. More information can be found in articles by Nellist and Pennycook (1999) [71], Shiojiri and Yamazaki [72], Pennycook and Jesson [73], and Hartel et al. [74].

Since high-angle incoherent scattering is associated with scattering from the atomic nuclei, it gives an intensity which is more or less proportional with the squared atomic number ($I \sim Z^{1.7-2}$), as expected on the basis of Rutherford scattering. This imaging mode is therefore also called Z-contrast imaging. One of the advantages of High-Angle Annular Dark Field-Scanning Transmission Electron Microscopy (HAADF-STEM) imaging is the possibility to visually distinguish materials of different compositions. Furthermore, if the elements contained in the specimen are known, an HAADF-STEM image gives directly a qualitative 2D distribution of the different materials in the specimen.

Since the annular detector is used to exclude Bragg scattering and eliminate the phase problem, a complete physical characterization of a nanomaterial can be performed in HAADF-STEM mode in a manner similar to TEM mode, with the advantage that there is almost no diffraction contrast visible in the images, allowing easier image analysis [24, 75–81]. Channeling effects, which take place when a crystal is oriented with a zone axis parallel to the electron beam, can disturb the intensity of HAADF-STEM images. The channeling effect corresponds to the tendency of the electron beam to stay close to the atomic columns when it crosses the specimen. This maximizes the scattered intensity and makes the crystal appear brighter than in an off-axis orientation. The spatial resolution that can be obtained is mainly controlled by the nanosized illuminating probe, down to 0.1 nm in high-resolution STEM mode, when a probe-corrected STEM is used.

8.3.4 Analytical Transmission Electron Microscopy

Chemical analysis of nanomaterials can be necessary, for instance, when nanoparticles are embedded in a complex matrix, and visual inspection does not allow distinguishing the nanoparticles from the background. Two analytical techniques that can be incorporated in the TEM system are energy dispersive X-ray spectroscopy (EDS) and electron energy-loss spectrometry (EELS). Both techniques allow both point measurements and elemental mapping and give qualitative (which elements are present) as well as quantitative (the chemical composition in atomic percent or in weight percent) information. To obtain high spatial resolution, these techniques are generally performed in HAADF-STEM mode. More information can be found in the textbooks by D. B. Williams and C. B. Carter [58] and by Egerton [82].

Energy dispersive X-ray spectroscopy (EDS) measures the X-rays that are emitted from the specimen during bombardment with the electron beam, to determine the elemental composition of the analyzed volume. Elements with atomic numbers ranging from that of boron to uranium can be detected. The minimum detection limits vary from approximately 0.01 to 0.1 wt%, depending on the element, the specimen, and the specimen thickness [58]. Examples of EDX analyses on nanoparticles are given in [18, 68, 69, 80, 83]

Electron energy-loss spectroscopy (EELS) measures the energy which is lost by the inelastically scattered beam electrons by interacting with the specimen, to obtain analytical information. EELS tends to work better for light elements than for heavy elements, making it complementary to EDS. Examples of EELS analyses on nanoparticles are given in [17, 20, 21, 80]

An advantage of EELS over EDS is the ability to "fingerprint" different forms of the same element (e.g., graphite vs. diamond) by comparing the plasmon peaks [17, 19, 67, 84] or by comparing the fine structure (termed energy-loss near-edge structure or ELNES) that can be visualized on the core-loss edges. The ELNES contains information about the electronic structure of the specimen and originates from excitations of core electrons to unoccupied states above the Fermi level. The ELNES thus depends on the number and energy of the unoccupied states at the excited atom. Even though interpretation is not straightforward, ELNES can be used as a fingerprint to identify a certain material or to study quantum effects due to the decrease in size of nanomaterials compared to the bulk [85–90]. The main reason why a fine structure can be detected in EELS and not in EDS is the difference in energy resolution between the two techniques (<1 eV for EELS, ~150 eV for EDS).

8.4 Qualitative Characterization of Nanomaterials in Dispersion in a Regulatory Framework

An increasing number of publications demonstrate that the particle size of a nanomaterial can strongly influence its toxicological properties [91–93], as well as its dosimetric fate in the entire organism, including the organ of uptake, circulation, and secondary organs of accumulation [4]. The characterization of nanomaterials is, however, not a trivial task. Often, nanomaterials show a distribution of sizes and shapes and their measurement is challenging, especially in dispersion [91, 92, 94–98].

Even though there is a general need for harmonization of the methodologies used for the characterization of nanomaterials, currently, no generally applicable guidelines for measurement of primary particle size and morphology are available. The parameters of interest with respect to nanoparticle safety testing are listed and described in detail in [2, 4, 37, 99].

A qualitative TEM analysis allows describing the key properties of the physical form of the nanomaterial under which it is exposed to in vitro and in vivo test systems based on TEM micrographs. Before nanomaterials are tested, a qualitative TEM analysis is instrumental to judge the relevance and suitability of a quantitative TEM analysis, which is more objective, and to avoid/evaluate possible measurement artifacts or bias in in vitro and in vivo systems. In these systems, the properties which need to be determined might be largely dependent on the surrounding media and the temporal evolution of the nanomaterials. Thus, a primary focus should be to assess the nanomaterials in exactly the form/composition they have as manufactured and in the formulation delivered to the end user or the environment if the formulation contains free nanoparticles [2].

To our knowledge no formal guidelines for the unambiguous and detailed description of a nanomaterial are available. Procedures can be based on methods described in the literature [10, 100, 101]. In addition to an estimate of the size (distribution) of the primary and aggregated/agglomerated particles, a qualitative description includes at least: (1) representative and calibrated micrographs, (2) the agglomeration and aggregation status, (3) the general morphology, (4) the surface topology, (5) the structure (crystalline, amorphous, etc.), and (6) the presence of contaminants and aberrant particles.

Examination of the EM grid to check whether the amount of particles is high enough and their distribution is homogeneous is important to assess the relevance of a quantitative TEM analysis.

A descriptive qualitative analysis contains representative images that give an overview of the sample and show all typical features. In addition, selected micrographs can highlight abnormal or rare features, such as impurities, large agglomerates, crystal defects, etc.

The primary particle size tends to be a relatively robust parameter as compared to the aggregate/agglomerate size, since it is less influenced by environmental conditions (pH, solvent, sonication, presence of proteins, etc.) [5, 10]. It is correlated with nano-specific properties such as the volume-specific surface area (VSSA) [12, 46, 102]. Broad application of sizing methods in particle characterization shows that particle size is often an important factor, but is not sufficient to allow particle phenomena such as powder flow, mixing, abrasion, or biological response to be understood. Particle shape and morphology play an important role in particle systems as well [10, 102].

Particle morphology represents the extension of a simple shape description to more complex descriptions including characteristics such as porosity, roughness, and texture [10]. Various glossaries of terms giving descriptions, in words, of particle shape and morphology already exist ([100, 103–108]). These descriptions may be useful for the classification and identification of particles, but, at the moment, there is insufficient consensus on the definition of particle shape and morphology in the quantitative terms necessary for them to be implemented in software routines. A future revision of this part of ISO 9276 may cover this [10]. ISO/TS 27687 defines specific nanoparticles based on their shape, such as nanofibers and nanoplatelets [9]. In addition to particle size, shape, and morphology, the crystallographic phase, texture, and crystallographic defects can be examined and reported.

An important characteristic of materials consisting of a collection (or "population") of particles is their polydispersity [1]. A monodisperse material consists only of particles of the same size and shape. A material consisting of particles is to a certain degree always polydisperse: it contains particles of various sizes and/or shapes. How the sizes and shapes of the individual particles vary is described by the particle size and shape distributions, which can be monomodal, bimodal, trimodal, or polymodal.

8.5 Quantitative Analysis

To objectify a descriptive qualitative TEM analysis, the particles in electron micrographs can be identified and measured by image analysis. Image analysis techniques allow detection of the nanomaterials and measurement of the properties of the nanomaterials such as the size, the elongation, the curvature of the particle corners, and the smoothness of the particle surface [107–111].

No generally accepted and validated procedure is available [4]. General approaches of quantitative image analysis methodology are proposed by NIST [101]. More specific imaging and image analysis guidelines are given in ISO publications [5, 10, 100, 112]. Data analysis and representation can be done in combination with the methods described in ISO publications [5, 10, 112, 113]. Basic principles are (1) the traceability of information, imaging, and results; (2) detection, measurement, classification, and representation of results on a per-particle level (number-based); and (3) (for practicality) automation of repetitive tasks.

To assure a maximum traceability of information, storage of micrographs in a dedicated database with their administrative and sample preparation information as well as the information related to their imaging conditions is recommended [4]. Both commercial [114, 115] and freely accessible software solutions [116–118] that integrate the database in the image analysis software are available. Modifications of the imaging and database software are reported to transfer the micrographs and their associated microscope data efficiently into the database while simultaneously calibrating the images [14].

For simple models, like colloidal materials, particles can relatively easily be detected using grayscale thresholding: they are relatively abundant and have a homogeneous size, density, shape, and surface topology [40–42, 59, 119, 120].

A major advantage of such grayscale thresholding is that all nanoparticles in a micrograph can be detected simultaneously, allowing a statistically relevant number of measurements avoiding the tedious repetitive task of manual measurement. This reduces operator-induced bias. Since this method contains no steps that are specific for a certain material, it can readily be adapted to detect aggregates and agglomerates of a variety of nanomaterials [121–123], provided that they can be coated quantitatively to the EM grid and distinguished from the background (Fig. 8.2). For most metal oxides and for metallic nanomaterials, the latter poses no problem.

When the background signal of the micrographs is not homogeneous and cannot be corrected sufficiently [124, 125], as illustrated in Fig. 8.1 for a holey grid, grayscale thresholding can be difficult. Particle detection approaches based on magic wand [126], Hough transform [127], and template matching [128] can be useful alternatives to manual detection. For automatically detected particles, multiple and arithmetically complex parameters, such as described in [10, 13, 14], can be measured simultaneously on high numbers of particles (Fig. 8.2).

Access to multiple parameters such as the aspect ratio, the mean diameter, and the convexity allows selecting the parameter in function of a specific material or purpose. Verleysen [13] and De Temmerman [14] illustrate this in the scope of definition and characterization of colloidal, aggregated, and agglomerated nanomaterials.

Principle-component analysis and correlation analyses allow grouping measurands in independent classes. Representation of the number-based distribution of one representative measurand of each class allows a detailed, quantitative characterization of a nanomaterial. For agglomerated/aggregated synthetic amorphous silica and TiO_2, three independent groups of measurands are observed; these basically consist of measures of the size, shape, and surface topology. This grouping is in line with the guidelines in [4, 28, 35, 129] that parameters of these classes are essential for the characterization and identification of a nanomaterial, e.g., in the context of the risk assessment of the application of nanomaterials in the food and feed chain. The findings of [130] corroborate this, showing that the size, physical form, and morphology parameters determine the access of nanomaterials to human cells and cell organelles. In this context, the properties of individual particles measured in two dimensions can be more meaningful. Subpopulations that cannot be distinguished based on one parameter can be distinguished based on combinations of parameters for size, shape, and surface.

Access to multiple parameters also allows post-analysis classification of the detected particles, avoiding the distortions in the shape and size of the detected particles introduced by a separator filter-based approach as suggested by [131] and [132]. Information of the size, shape, and surface topology can be used to classify particles as single primary particles or aggregates/agglomerates and erroneously detected particles like crystallized salts, precipitated proteins, and holes in the grid. Automation of this classification includes a learning step where a preliminary manual classification is used as reference and input in linear discriminant analysis or cluster analysis [59]. Alternatively, for particles with a homogeneous size, shape, and surface topology, template matching can be used to detect specific particles of interest [128]. A manual classification deleting artifacts from the images and excluding them from the dataset tends to be time-consuming, and the results may vary between operators.

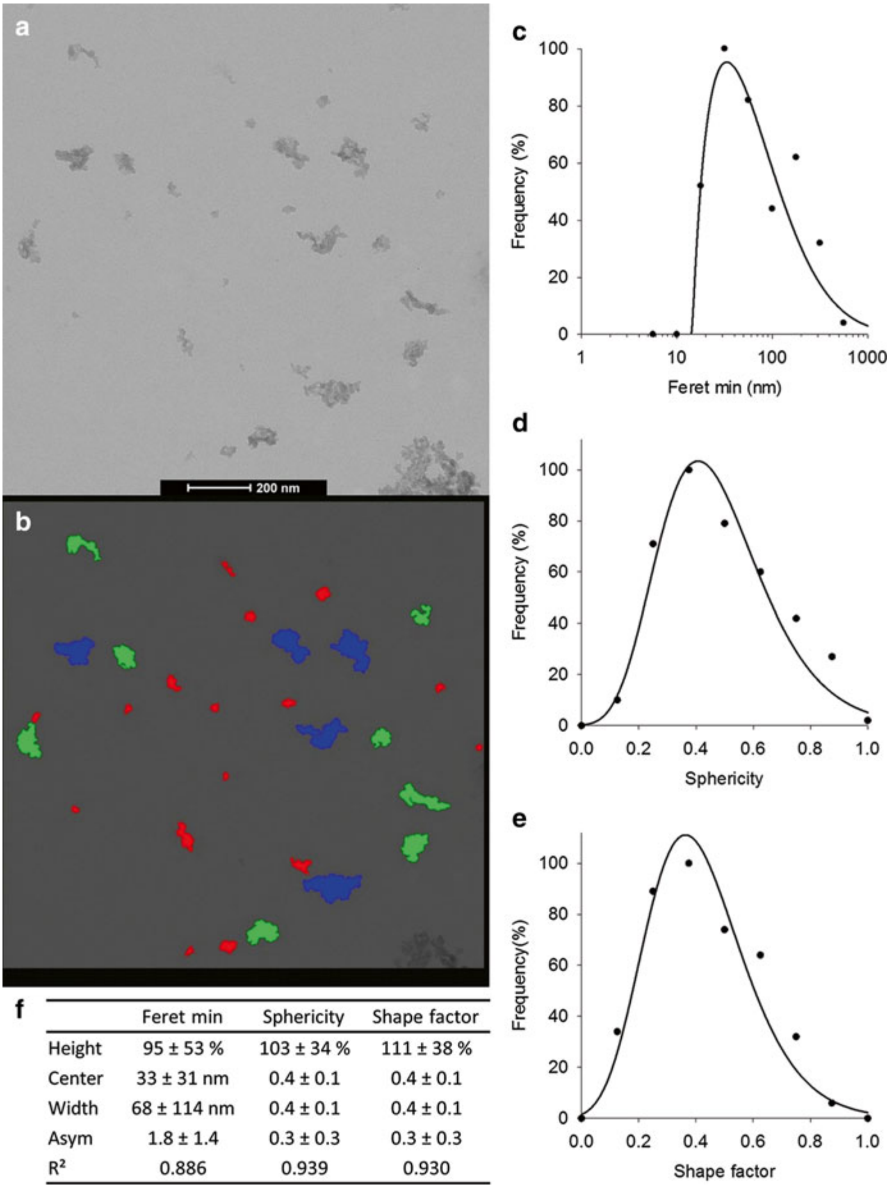

	Feret min	Sphericity	Shape factor
Height	95 ± 53 %	103 ± 34 %	111 ± 38 %
Center	33 ± 31 nm	0.4 ± 0.1	0.4 ± 0.1
Width	68 ± 114 nm	0.4 ± 0.1	0.4 ± 0.1
Asym	1.8 ± 1.4	0.3 ± 0.3	0.3 ± 0.3
R^2	0.886	0.939	0.930

Fig. 8.2 Illustration of the steps of a quantitative analysis of the physical properties of aggregates of the silica nanomaterial NM-200 in dispersion used in an in vivo test that combines TEM imaging with semiautomatic particle detection and analysis. The aggregates in randomly selected micrographs (**a**) are detected by setting the threshold to separate particles from the background based on their gray values (**b**). False coloring shows particles <50 nm in *red*, from 50 to 70 nm in *green*, and >70 nm in *blue*. Based on correlation analysis, the 23 measurands are grouped in three independent classes containing measurands of the size, the shape, and the surface properties. The number-based distributions of the Feret Min (**c**), the sphericity, (**d**) and the shape factor (**e**), selected as the representative measurands of these classes, are represented quantitatively based on the parameters and their uncertainties determined by iterative curve fitting (**f**)

The data collected for each characteristic parameter can be presented by its conventional descriptive statistics such as mean, median, and percentiles [101, 112]. ISO 9276-1 [113] and ISO 9276-3 [133] provide guidelines for representation of results of particle size analysis. Representation as a number-based distribution by binning the data over a selected range and fitting a (log)normal distribution allows a more precise estimation of the mode (Fig. 8.2). Weighing the number of nonempty bins to the number of measurements in the largest bin followed by lognormal fitting is suggested to balance the uncertainty of the measurement of the mode (bin width) and the number of particles supporting this measurement (bin height) for non-normal distributions. It is an alternative for the Freedman-Diaconis rule, Scott's rule, and the Sturges rule, designed for normal distributed data [134–136].

The three-dimensional structural and fractal properties of aggregates can be characterized from their projected images [137–140]. Starting from geometrical properties that are directly measured from the projected image—such as primary particle mean diameter, maximum projected length, projected area, and overlap coefficient—important three-dimensional properties of nanomaterials, including number of primary particles in an aggregate, radius of gyration, aggregate surface, or fractal dimensions, were inferred by [12, 141] for fractal-like materials including SiO_2, TiO_2, ZrO_2, Al_2O_3, Fe_2O_3, and Fe_3O_4.

One of the major difficulties in this fractal analysis is to reliably obtain the primary particle size, overlap coefficient, and center of mass. These characteristics can be estimated manually [141] or automatically [12].

For reliable and accurate quantitative analysis of nanoparticles present in representative TEM micrographs, validated methods are required. Without these validated technologies or applicable reference materials, meaningful and equivalent methodologies for classifying materials based on particle number would be very difficult to develop [142].

Obtaining reliably estimated measurement uncertainties is essential to validate a method and to interpret and compare the generated experimental results. To date, TEM methods have only been rarely validated: the majority of today's nanomaterial characterization studies lack information that reflects the quality (i.e., measurement uncertainties) of the presented data. Reliably estimated measurement uncertainties are essential to underpin the credibility of experimental data and to compare TEM measurement results. Results of several interlaboratory comparisons have been recently published [119, 120, 143, 144]. Only few studies are available where the precision and accuracy of the quantitative TEM method are measured by determining repeatability (within 1-day variability) and intermediate precision (day-to-day variability) for measurements on (certified) reference materials [59]. These studies remain limited to relatively easy models (near-spherical colloidal nanoparticles). For TEM analyses of aggregated/agglomerated nanoparticles and for particles with a more complex morphology, validation data are still lacking.

Setting up the uncertainty balance of shape measurands and many size measurands is hampered by the lack of certified values of reference materials such that only intra-laboratory uncertainties are available [59].

Only the silica nanomaterial ERM-FD100 [43] has certified values for its size and uncertainty, as determined by TEM. The silica nanomaterial ERM-FD304 [44], the polystyrene 3000 Series Nanosphere NIST Traceable Size Standards [45], and the Au nanoparticles from NIST RM 8011 [40], RM 8012 [41], and RM 8013 [42] have indicative size and uncertainty values. Inter- and intra-laboratory comparison studies for characterization of these reference materials are presented by Franks et al. [119], Braun et al. [120], Motzkus et al. [143], Rice et al. [144], Bell et al. [145], and Anderson et al. [146].

Acknowledgments This review was supported and partially funded by the European Union Seventh Framework Programme (FP7/2007–2013) under the projects NANoREG (a common European approach to the regulatory testing of nanomaterials), grant agreement 310584, and NanoDefine (development of an integrated approach based on validated and standardized methods to support the implementation of the EC recommendation for a definition of nanomaterial), grant agreement n°604347.

References

1. T.P.J. Linsinger, G. Roebben, D. Gilliland, L. Calzolai, F. Rossi, N. Gibson, C. Klein, *Requirements on Measurements for the Implementation of the European Commission Definition of the Term "Nanomaterial", EUR 25404 EN* (Publications Office of the European Union, Luxembourg, 2012)
2. SCENIHR, *Risk Assessment of Products of Nanotechnologies*. (Scientific Committee on Emerging and Newly Identified Health Risks, 2009)
3. ISO/TR 13014, *Nanotechnologies—Guidance on Physico-Chemical Characterization for the Detailed Identification of Manufactured Nanomaterials Subjected to Toxicological Testing*. (International Organization for Standardization, Geneva, 2009)
4. OECD, *Guidance on Sample Preparation and Dosimetry for the Safety Testing of Manufactured Nanomaterials, ENV/JM/MONO(2012)40* (Organisation for Economic Co-Operation and Development, Paris, 2012)
5. ISO 13322-1, *Particle Size Analysis—Image Analysis Methods, Part 1: Static Image Analysis Methods*. (International Organization for Standardization, Geneva, 2004)
6. E.A. Bleeker, W.H. de Jong, R.E. Geertsma, M. Groenewold, E.H. Heugens, M. Koers-Jacquemijns, D. van de Meent, J.R. Popma, A.G. Rietveld, S.W. Wijnhoven, Considerations on the EU definition of a nanomaterial: science to support policy making. Regul. Toxicol. Pharmacol. **65**, 119 (2013)
7. G. Lövestam, H. Rauscher, G. Roebben, B.S. Klüttgen, N. Gibson, J.-P. Putaud, H. Stamm, *Considerations on a Definition of Nanomaterial for Regulatory Purposes. JRC Reference Reports* (Publications Office of the European Union, Luxembourg, 2010)
8. ISO/TR 11360, *Nanotechnologies—Methodology for the Classification and Categorization of Nanomaterials*. (International Organization for Standardization, Geneva, 2010)
9. ISO/TS 27687, *Nanotechnologies—Terminology and Definitions for Nano-Objects—Nanoparticle, Nanofibre and Nanoplate*. (International Organization for Standardization, Geneva, 2008)
10. ISO 9276-6, *Representation of Results of Particle Size Analysis Part 6: Descriptive and Quantitative Representation of Particle Shape and Morphology*. (International Organization for Standardization, Geneva, 2008)
11. S. Barlow, A. Chesson, J.D. Collins, A. Flynn, A. Hardy, K.-D. Jany, A. Knaap, H. Kuiper, J.C. Larsen, P. Le Neindre, J. Schans, J. Schlatter, V. Silano, S. Skerfving, P. Vannier,

Scientific opinion of the scientific committee: the potential risks arising from nanoscience and nanotechnologies on food and feed safety, Question no EFSA-Q-2007-124a. EFSA J. **958**, 1–39 (2009)

12. P.-J. De Temmerman, E. Verleysen, J. Lammertyn, J. Mast, Semi-automatic size measurements of primary particles in aggregated nanomaterials by transmission electron microscopy. Powder Technol. **261**, 191 (2014)
13. E. Verleysen, P.-J. De Temmerman, E. Van Doren, M. Abi Daoud Francisco, J. Mast, Quantitative characterization of aggregated and agglomerated titanium oxide nanomaterials by transmission electron microscopy. Powder Technol. **258**, 180 (2014)
14. P.-J. De Temmerman, E. Van Doren, E. Verleysen, Y. Van der Stede, M. Francisco, J. Mast, Quantitative characterization of agglomerates and aggregates of pyrogenic and precipitated amorphous silica nanomaterials by transmission electron microscopy. J. Nanobiotechnol. **10**, 24 (2012)
15. Y. Sun, Y. Xia, Shape-controlled synthesis of gold and silver nanoparticles. Science **298**, 2176 (2002)
16. S. Sun, C. Murray, D. Weller, L. Folks, A. Moser, Monodisperse FePt nanoparticles and ferromagnetic FePt nanocrystal superlattices (2000). Science **287**, 1989–1992 (1989)
17. B. Schaffer, K. Riegler, G. Kothleitner, W. Grogger, F. Hofer, Monochromated, spatially resolved electron energy-loss spectroscopic measurements of gold nanoparticles in the plasmon range. Micron **40**, 269 (2009)
18. T. Klaus, R. Joerger, E. Olsson, C.-G. Granqvist, Silver-based crystalline nanoparticles, microbially fabricated. Proc. Natl. Acad. Sci. U. S. A. **96**, 13611 (1999)
19. A.L. Koh, K. Bao, I. Khan, W.E. Smith, G. Kothleitner, P. Nordlander, S.A. Maier, D.W. McComb, Electron energy-loss spectroscopy (EELS) of surface plasmons in single silver nanoparticles and dimers: influence of beam damage and mapping of dark modes. ACS Nano **3**, 3015 (2009)
20. S. Schamm, C. Bonafos, H. Coffin, N. Cherkashin, M. Carrada, G. Ben Assayag, A. Claverie, M. Tencé, C. Colliex, Imaging Si nanoparticles embedded in SiO_2 layers by (S) TEM-EELS. Ultramicroscopy **108**, 346 (2008)
21. T.C. Rojas, M.J. Sayagués, A. Caballero, Y. Koltypin, A. Gedanken, L. Ponsonnet, B. Vacher, J.M. Martin, A. Fernández, TEM, EELS and EFTEM characterization of nickel nanoparticles encapsulated in carbon. J. Mater. Chem. **10**, 715 (2000)
22. P.A. Midgley, M. Weyland, 3D electron microscopy in the physical sciences: the development of Z-contrast and EFTEM tomography. Ultramicroscopy **96**, 413 (2003)
23. S. Van Aert, K.J. Batenburg, M.D. Rossell, R. Erni, G. Van Tendeloo, Three-dimensional atomic imaging of crystalline nanoparticles. Nature **470**, 374 (2011)
24. S. Sueda, K. Yoshida, N. Tanaka, Quantification of metallic nanoparticle morphology on TiO2 using HAADF-STEM tomography. Ultramicroscopy **110**, 1120 (2010)
25. E.M. Pouget, P.H. Bomans, J.A. Goos, P.M. Frederik, N.A. Sommerdijk, The initial stages of template-controlled CaCO3 formation revealed by cryo-TEM. Science **323**, 1455 (2009)
26. E. Van Doren, P.-J. De Temmerman, M. Francisco, J. Mast, Determination of the volume-specific surface area by using transmission electron tomography for characterization and definition of nanomaterials. J. Nanobiotechnol. **9**, 17 (2011)
27. SCENIHR, *Opinion on the Scientific Aspects of the Existing and Proposed Definitions Relating to Products of Nanoscience and Nanotechnologies, scenihr_o_012* (Scientific committee on emerging and newly identified health risks, Brussels, 2007)
28. SCENIHR, *Scientific Basis for the Definition of the Term "Nanomaterial", scenihr_o_030* (Scientific Committee on Emerging and Newly Identified Health Risks, Brussels, 2010)
29. EC, Commission recommendation of 18 October 2011 on the definition of nanomaterial. 2011/696/EU. Off. J. Eur. Union **L275**, 30 (2011)
30. EC, Regulation (EC) No 1223/2009 of the European parliament and of the council of 30 November 2009 on cosmetic products. Off. J. Eur. Union **L342**, 59 (2009)
31. EC-1333/2008, Regulation (EC) no 1333/2008 of the European parliament and of the council of 16 December 2008 on food additives. Off. J. Eur. Union **L354**, 16 (2008)

32. EC-258/97, Regulation (EC) No 258/97 of the European parliament and of the council of 27 January 1997 concerning novel foods and novel food ingredients. Off. J. Eur. Communities. (1997)
33. H. Stamm, N. Gibson, E. Anklam, Detection of nanomaterials in food and consumer products: bridging the gap from legislation to enforcement. Food Addit. Contam. A Chem. Anal. Control Expo. Risk Assess. **29**, 1175–1182 (2012)
34. OECD, *Preliminary Guidance Notes on Sample Preparation and Dosimetry for the Safety Testing of Manufactured Nanomaterials, ENV/JM/MONO(2010)25* (Organisation for Economic Co-Operation and Development, Paris, 2010)
35. OECD, *Guidance Manual for the Testing of Manufactured Nanomaterials: OECD Sponsorship Programme: First Revision, ENV/JM/MONO(2009)20/REV* (Organisation for Economic Co-operation and Development, Paris, 2010)
36. E.K. Lesher, A.R. Poda, A.J. Bednar, J.F. Ranville, Field-Flow Fractionation Coupled to Inductively Coupled Plasma-Mass Spectrometry (FFF-ICP-MS): Methodology and Application to Environmental Nanoparticle Research, in *Field-Flow Fractionation in Biopolymer Analysis*, ed. by S. Kim, R. Williams, K.D. Caldwell (Springer, Vienna, 2012), pp. 277–299
37. EFSA, Scientific opinion: guidance on the risk assessment of the application of nanoscience and nanotechnologies in the food and feed chain. EFSA J. **9**, 2140 (2011)
38. Nanogenotox, *The final NANOGENOTOX Publishable Report*. (2013), http://www.nanogenotox.eu/files/PDF/nanogenotox_web.pdf
39. K.J. Mysels, Textbook errors: II. Brownian motion and the stability of colloids. J. Chem. Educ. **32**, 319 (1955)
40. D.L. Kaiser, R.L. Watters, *Reference Material 8011: Gold Nanoparticles, Nominal 10 nm Diameter*. (Report of Investigation, National Institute of Standards & Technology, Gaithersburg, 2007a)
41. D.L. Kaiser, R.L. Watters, *Reference Material 8012: Gold Nanoparticles, Nominal 30 nm Diameter*. (Report of Investigation, National Institute of Standards & Technology, Gaithersburg, 2007b)
42. D. L. Kaiser and R. L. Watters, Reference Material 8013: Gold Nanoparticles, Nominal 60 nm Diameter (2007c), Report of Investigation, National Institute of Standards & Technology, Gaithersburg, MD
43. IRMM, *Certificate of Analysis ERM®-FD100* (Institute for reference materials and measurements, Geel, 2011)
44. IRMM, *Certificate of Analysis ERM®-FD304* (Institute for reference materials and measurements, Geel, 2012)
45. T.F. Scientific, 3000 Series Nanosphere™ Size Standards. (2014) http://www.thermoscientific.com/en/product/3000-series-nanosphere-size-standards.html
46. C. Guiot, O. Spalla, Stabilization of TiO_2 nanoparticles in complex medium through a pH adjustment protocol. Environ. Sci. Technol. **47**, 1057 (2013)
47. P. Bihari, M. Vippola, S. Schultes, M. Praetner, A. Khandoga, C. Reichel, C. Coester, T. Tuomi, M. Rehberg, F. Krombach, Optimized dispersion of nanoparticles for biological in vitro and in vivo studies. Part. Fibre Toxicol. **5**, 14 (2008)
48. K. Jensen, Y. Kembouche, E. Christiansen, N. Jacobsen, H. Wallin, C. Guiot, O. Spalla, O. Witschger, *The Generic NANOGENOTOX Dispersion Protocol* (The National Research Centre for the Working Environment, Copenhagen, 2011)
49. PROSPECT, *Protocol for Nanoparticle Dispersion* (2010)
50. J.S. Taurozzi, V.A. Hackley, *Preparation of Nanoparticle Dispersions from Powdered Material Using Ultrasonic Disruption*, National Institute of Standards and Technology NIST SP 1200-2, 15 (2012)
51. J.S. Taurozzi, V.A. Hackley, M. R. Weisner, *Preparation of Nanoscale TiO2 Dispersions in an Environmental Matrix for Eco-Toxicological Assessment*, National Institute of Standards and Technology NIST SP 1200-5, 12 (2012)
52. Cytodiagnostics, Surfactant Stabilized Gold Nanoparticles. (2014), http://www.cytodiagnostics.com/store/pc/Surfactant-Stabilized-Gold-Nanoparticles-c141.htm

53. C.-P. Lienemann, A. Heissenberger, G.G. Leppard, D. Perret, Optimal preparation of water samples for examination of colloidal material by transmission electron microscopy. Aquat. Microb. Ecol. **14**, 205 (1998)
54. J. Stirling, A. Curry, B. Eyden, *Diagnostic Electron Microscopy: A Practical Guide to Tissue Preparation and Interpretation* (Wiley, Chichester, 2012)
55. Dune Sciences, Smart Grids: Functionalized grids for advanced imaging. (2010), http://www.dunesciences.com/files/SMARTGrids_Brochure.pdf
56. D.M. Cao, Powder TEM Sample preparation for Powder Sample. (2006), http://mcc.lsu.edu/TEM%20sample%20preparation.html
57. M. De Graef, *Introduction to Conventional Transmission Electron Microscopy* (Cambridge University Press, Cambridge, 2003)
58. D. Williams, C. Carter, *Transmission Electron Microscopy*, vol. 2 (Springer, New York, 1996). ISBN 0-306-45324-X
59. P.-J. De Temmerman, J. Lammertyn, B. De Ketelaere, V. Kestens, G. Roebben, E. Verleysen, J. Mast, Measurement uncertainties of size, shape, and surface measurements using transmission electron microscopy of near-monodisperse, near-spherical nanoparticles. J. Nanoparticle Res. **16**, 1 (2013)
60. H. Masuda, K. Gotoh, Study on the sample size required for the estimation of mean particle diameter. Adv. Powder Technol. **10**, 159 (1999)
61. H.G. Merkus, *Particle Size Measurements: Fundamentals, Practice, Quality* (Springer, Pijnacker, 2009)
62. N. Chakroune, G. Viau, S. Ammar, L. Poul, D. Veautier, M.M. Chehimi, C. Mangeney, F. Villain, F. Fiévet, Acetate-and thiol-capped monodisperse ruthenium nanoparticles: XPS, XAS, and HRTEM studies. Langmuir **21**, 6788 (2005)
63. S. Link, Z.L. Wang, M. El-Sayed, Alloy formation of gold-silver nanoparticles and the dependence of the plasmon absorption on their composition. J. Phys. Chem. B **103**, 3529 (1999)
64. S.-W. Lee, W.M. Sigmund, Formation of anatase TiO_2 nanoparticles on carbon nanotubes. Chem. Commun. (Camb). **6**, 780–781 (2003)
65. S. Sun, H. Zeng, Size-controlled synthesis of magnetite nanoparticles. J. Am. Chem. Soc. **124**, 8204 (2002)
66. F. Zhang, S.-W. Chan, J.E. Spanier, E. Apak, Q. Jin, R.D. Robinson, I.P. Herman, Cerium oxide nanoparticles: size-selective formation and structure analysis. Appl. Phys. Lett. **80**, 127 (2002)
67. R. Jin, Y. Cao, C.A. Mirkin, K. Kelly, G.C. Schatz, J. Zheng, Photoinduced conversion of silver nanospheres to nanoprisms. Science **294**, 1901 (2001)
68. M. Li, H. Schnablegger, S. Mann, Coupled synthesis and self-assembly of nanoparticles to give structures with controlled organization. Nature **402**, 393 (1999)
69. I. Srnová-Šloufová, F. Lednický, A. Gemperle, J. Gemperlová, Core-shell (Ag) Au bimetallic nanoparticles: analysis of transmission electron microscopy images. Langmuir **16**, 9928 (2000)
70. Y. Xu, M. Yamazaki, P. Villars, Inorganic materials database for exploring the nature of material. Jpn. J. Appl. Phys **50**, 11RH02-1–11RH02-5 (2011)
71. S.J. Pennycook, P.D. Nellist, Z-contrast scanning transmission electron microscopy, in *Impact of electron scanning probe microscopy on materials research*, ed. by D. Rickerby, G. Valdrè, U. Valdrè (Kluwer Academic, Amsterdam, 1999), p. 161. ISBN 0-7923-5939-9
72. M. Shiojiri, T. Yamazaki, Atomic resolved HAADF-STEM for composition analysis. JEOL News **38**, 54 (2003)
73. S. Pennycook, D. Jesson, High-resolution Z-contrast imaging of crystals. Ultramicroscopy **37**, 14 (1991)
74. P. Hartel, H. Rose, C. Dinges, Conditions and reasons for incoherent imaging in STEM. Ultramicroscopy **63**, 93 (1996)
75. P.A. Midgley, M. Weyland, J.M. Thomas, B.F. Johnson, Z-Contrast tomography: a technique in three-dimensional nanostructural analysis based on Rutherford scattering. Chem. Commun. **10**, 907–908 (2001)

76. J.R. Morones, J.L. Elechiguerra, A. Camacho, K. Holt, J.B. Kouri, J.T. Ramírez, M.J. Yacaman, The bactericidal effect of silver nanoparticles. Nanotechnology **16**, 2346 (2005)
77. J. Gonzalez, J. Hernandez, M. López-Haro, E. Del Rio, J. Delgado, A. Hungria, S. Trasobares, S. Bernal, P.A. Midgley, J.J. Calvino, 3 D characterization of gold nanoparticles supported on heavy metal oxide catalysts by HAADF-STEM electron tomography. Angew. Chem. Int. Ed. **121**, 5417 (2009)
78. T. Akita, K. Tanaka, M. Kohyama, M. Haruta, HAADF-STEM observation of Au nanoparticles on TiO_2. Surf. Interface Anal. **40**, 1760–1763 (2008)
79. H. Yu, M. Chen, P.M. Rice, S.X. Wang, R. White, S. Sun, Dumbbell-like bifunctional Au-Fe3O4 nanoparticles. Nano Lett. **5**, 379 (2005)
80. S. Utsunomiya, R.C. Ewing, Application of high-angle annular dark field scanning transmission electron microscopy, scanning transmission electron microscopy-energy dispersive X-ray spectrometry, and energy-filtered transmission electron microscopy to the characterization of nanoparticles in the environment. Environ. Sci. Technol. **37**, 786 (2003)
81. T. Epicier, K. Sato, F. Tournus, T. Konno, Chemical composition dispersion in bi-metallic nanoparticles: semi-automated analysis using HAADF-STEM. J. Nanoparticle Res. **14**, 1 (2012)
82. R.F. Egerton, *Electron Energy-Loss Spectroscopy in the Electron Microscope*, 3rd edn. (Springer, New York, 1996)
83. X. Zhang, K.-Y. Chan, Water-in-oil microemulsion synthesis of platinum-ruthenium nanoparticles, their characterization and electrocatalytic properties. Chem. Mater. **15**, 451 (2003)
84. J. Mock, M. Barbic, D. Smith, D. Schultz, S. Schultz, Shape effects in plasmon resonance of individual colloidal silver nanoparticles. J. Chem. Phys. **116**, 6755 (2002)
85. S. Pokrant, M.C. Cheynet, S. Irsen, *ELNES: A Promising Method for Structural and Chemical Nanoparticle Analysis?* (Verlag der TU Graz, 2009)
86. S. Turner, S. Lazar, B. Freitag, R. Egoavil, J. Verbeeck, S. Put, Y. Strauven, G. Van Tendeloo, High resolution mapping of surface reduction in ceria nanoparticles. Nanoscale **3**, 3385 (2011)
87. F. Wang, M. Malac, R.F. Egerton, Energy-loss near-edge fine structures of iron nanoparticles. Micron **37**, 316 (2006)
88. O. Stéphan, A. Vlandas, R. de la Concha, A. Loiseau, S. Trasobares, C. Colliex, *Probing electronic states in nanotubes and related-nanoparticles at the nanometer scale*, Conference Series-Institute of Physics, Philadelphia; Institute of Physics; 1999, (2004) p. 437
89. H. Sauer, S. Nepijko, M. Klimiankou, HRTEM and EELS characterization of TiO_2 nanoparticles in Ti-doped zeolite. Microsc. Microanal. **9**, 192 (2003)
90. A. Santos-Beltrán, S. Maldonado-Ruiz, R. Martinez-Sanchez, F. Espinosa-Magana, H. Flores, V. Gallegos-Orozco, ELNES of Al-Al_4C_3 nanoparticles produced by mechanical milling. Microsc. Microanal. **14**, 362 (2008)
91. C. Carlson, S. Hussain, A. Schrand, L.K. Braydich-Stolle, K. Hess, R. Jones, J. Schlager, Unique cellular interaction of silver nanoparticles: size-dependent generation of reactive oxygen species. J. Phys. Chem. B **112**, 13608 (2008)
92. J.E. Choi, S. Kim, J.H. Ahn, P. Youn, J.S. Kang, K. Park, J. Yi, D.-Y. Ryu, Induction of oxidative stress and apoptosis by silver nanoparticles in the liver of adult zebrafish. Aquat. Toxicol. **100**, 151 (2010)
93. E.-J. Park, J. Yi, Y. Kim, K. Choi, K. Park, Silver nanoparticles induce cytotoxicity by a Trojan-horse type mechanism. Toxicol. In Vitro. **24**, 872–878 (2010)
94. Y. Pan, S. Neuss, A. Leifert, M. Fischler, F. Wen, U. Simon, G. Schmid, W. Brandau, W. Jahnen-Dechent, Size-dependent cytotoxicity of gold nanoparticles. Small **3**, 1941–1949 (2007)
95. C.M. Goodman, C.D. McCusker, T. Yilmaz, V.M. Rotello, Toxicity of gold nanoparticles functionalized with cationic and anionic side chains. Bioconjug Chem. **15**, 897 (2004)
96. B.D. Chithrani, A.A. Ghazani, W.C. Chan, Determining the size and shape dependence of gold nanoparticle uptake into mammalian cells. Nano Lett. **6**, 662 (2006)
97. C.D. Walkey, J.B. Olsen, H. Guo, A. Emili, W.C. Chan, Nanoparticle size and surface chemistry determine serum protein adsorption and macrophage uptake. J. Am. Chem. Soc. **134**, 2139 (2012)

98. A.K. Suresh, D.A. Pelletier, W. Wang, J.L. Morrell-Falvey, B. Gu, M.J. Doktycz, Cytotoxicity induced by engineered silver nanocrystallites is dependent on surface coatings and cell types. Langmuir **28**, 2727 (2012)
99. OECD, *The Price of Prejudice: Labour Market Discrimination on the Grounds of Gender and Ethnicity. Technical Annex*. (Organisation for Economic Co-operation and Development, 2008)
100. W.C. Krumbein, L.L. Sloss, *Stratigraphy and Sedimentation* (W.H. Freeman, San Francisco, 1963)
101. NIST 960-1, *Particle Size Characterization* (2001)
102. E. Roduner, Size matters: why nanomaterials are different. Chem. Soc. Rev. **35**, 583 (2006)
103. G. Nichols, S. Byard, M.J. Bloxham, J. Botterill, N.J. Dawson, A. Dennis, V. Diart, N.C. North, J.D. Sherwood, A review of the terms agglomerate and aggregate with a recommendation for nomenclature used in powder and particle characterization. J. Pharm. Sci. **91**, 2103 (2002)
104. H.G. Brittain, Representations of particle shape, size, and distribution. Pharm. Technol. **25**, 38–45 (2001)
105. ASTM, F1877-05 Standard Practice for Characterization of Particles (2010)
106. NIST, *Glossary of Morphology Terms*. (Center for analytical chemistry, National Institute of Standards and Technology, Gaithersburg, 2005)
107. P.J. Barrett, The shape of rock particles, a critical review. Sedimentology **27**, 291 (1980)
108. USP, *Optical Microscopy, General Test 776, USP 24* (The United States Pharmacopeial Convention, Rockville, 2000), p. 1965
109. OECD, *Synthetic Amorphous Silica and Silicates—SIDS Initial Assessment Report for SIAM 19, OECD SIDS* (UNEP Publications, Berlin, 2004)
110. M. Hassellöv, J. Readman, J. Ranville, K. Tiede, Nanoparticle analysis and characterization methodologies in environmental risk assessment of engineered nanoparticles. Ecotoxicology **17**, 344 (2008)
111. W.D. Pyrz, D.J. Buttrey, Particle size determination using TEM: a discussion of image acquisition and analysis for the novice microscopist. Langmuir **24**, 11350 (2008)
112. ISO 9276-2, *Representation of Results of Particle Size Analysis, Part 2: Calculation of Average Particle Sizes/Diameters and Moments from Particle Size Distributions*. (International Organization for Standardization, Geneva, 2001)
113. ISO 9276-1, *Representation of Results of Particle Size Analysis, Part 1: Graphical Representation*. (International Organization for Standardization, Geneva, 1998)
114. iTEM, iTEM is the image analysis platform for transmission-electron microscopy. (2014), http://www.soft-imaging.net/en/eu/eng/2343_5832.htm
115. Visilog, *Visilog is the Reference Environment for Creating Image Processing Applications*. (2014)
116. OMERO, *OMERO is Client-Server Software for Visualization, Management and Analysis of Biological Microscope Images*. (2014), http://www.openmicroscopy.org/site
117. Fiji, Fiji is an image processing package based on ImageJ. (2014)
118. ImageJ, Image processing and analysis in Java (2014)
119. K. Franks, A. Braun, J. Charoud-Got, O. Couteau, V. Kestens, A. Lamberty, T.P.J. Linsinger, G. Roebben, *Certified Reference Material ERM®-FD304: Certification of the Equivalent Spherical Diameters of Silica Nanoparticles in Aqueous Solution* (European Union, Luxembourg, 2012)
120. A. Braun, K. Franks, V. Kestens, G. Roebben, A. Lamberty, T.P.J. Linsinger, *Certified Reference Material ERM®—FD100: Certification of Equivalent Spherical Diameters of Silica Nanoparticles in Water* (European Union, Luxembourg, 2011)
121. C. Singh, S. Friedrichs, M. Levin, R. Birkedal, K.A. Jensen, G. Pojana, W. Wohlleben, S. Schulte, K. Wiench, T. Turney, O. Koulaeva, D. Marshall, K. Hund-Rinke, W. Kördel, E. Van Doren, P.-J. De Temmerman, M. Abi Daoud Francisco, J. Mast, N. Gibson, R. Koeber, T.P.J. Linsinger, C. Klein, *NM-Series of Representative Manufactured Nanomaterials: Zinc Oxide NM-110, NM-111, NM-112, NM-113 Characterisation and Test Item Preparation, EUR 25066 EN–2011* (Publications Office of the European Union, Luxembourg, 2011)

122. K. Rasmussen, A. Mech, P.-J. De Temmerman, J. Mast, K.A. Jensen, M. Levin, S.H. Nielsen, I. Koponen, P. Clausen, R. Birkedal, Y. Kembouche, D. Rousset, S. Bau, B. Bianchi, O. Witschger, O. Spalla, C. Guiot, B. Shivachev, C. Motzkus, G. Pojana, A. Bilanicova, A. Marcomini, D. Gilliland, P.N. Gibson, H. Rauscher, H. Stamm, *Synthetic Amorphous Silicon Dioxide (SAS; NM-200, NM-201, NM-202, NM-203 and NM-204) Characterization, Stability and Homogeneity, EUR 26046* (Publications Office of the European Union, Luxembourg, 2013)
123. K. Rasmussen, J. Mast, P.-J. De Temmerman, E. Verleysen, N. Waegeneers, F. Van Steen, J.C. Pizzolon, L. De Temmerman, E. Van Doren, K. Jensen, R. Birkedal, M. Levin, S.H. Nielsen, I.K. Koponen, P.A. Clausen, V. Kofoed-Sørensen, Y. Kembouche, N. Thieriet, O. Spalla, C. Guiot, D. Rousset, O. Witschger, S. Bau, B. Bianchi, C. Motzkus, B. Shivachev, L. Dimowa, R. Nikolova, D. Nihtianova, M. Tarassov, O. Petrov, S. Bakardjieva, D. Gilliland, F. Pianella, G. Ceccone, V. Spampinato, G. Cotogno, N. Gibson, C. Gaillard, A. Mech, *Titanium Dioxide, NM-100, NM-101, NM-102, NM-103, NM-104, NM-105: Characterisation and Physico-Chemical Properties* (Publications Office of the European Union, Luxembourg, 2014)
124. F.W. Leong, M. Brady, J.O.D. McGee, Correction of uneven illumination (vignetting) in digital microscopy images. J. Clin. Pathol. **56**, 619 (2003)
125. T. Chen, W. Yin, X.S. Zhou, D. Comaniciu, T.S. Huang, Illumination Normalization for Face Recognition and Uneven Background Correction Using Total Variation Based Image Models. Computer Vision and Pattern Recognition, 2005. CVPR 2005. IEEE Computer Society Conference on, IEEE, (2005) p. 532
126. Olympus, Olympus Stream. (2014), http://www.olympus-ims.com/en/microscope/stream/
127. I. Grishin, K. Thomson, F. Migliorini, J.J. Sloan, Application of the Hough transform for the automatic determination of soot aggregate morphology. Appl. Opt. **51**, 610–620 (2012)
128. J. Zhao, M.A. Brubaker, J.L. Rubinstein, TMaCS: A hybrid template matching and classification system for partially automated particle selection. J. Struct. Biol. **181**, 234 (2013)
129. EFSA, Scientific opinion: the potential risks arising from nanoscience and nanotechnologies on food and feed safety. EFSA J. **958**, 1 (2009)
130. Z. Chu, Y. Huang, Q. Tao, Q. Li, Cellular uptake, evolution, and excretion of silica nanoparticles in human cells. Nanoscale **3**, 3291 (2011)
131. J.C. Russ, *The Image Processing Handbook* (CRC, Boca Raton, 2011)
132. M.N. Pons, H. Vivier, K. Belaroui, B. Bernard-Michel, F. Cordier, D. Oulhana, J.A. Dodds, Particle morphology: from visualisation to measurement. Powder Technol. **103**, 44 (1999)
133. ISO 9276-3, *Representation of Results of Particle Size Analysis, Part 3: Adjustment of an Experimental Curve to a Reference Model.* (International Organization for Standardization, Geneva, 2008)
134. D. Freedman, P. Diaconis, On the histogram as a density estimator: L 2 theory. Z. Wahrscheinlichkeit. **57**, 453 (1981)
135. D.W. Scott, Scott's rule. Wiley Interdiscip. Rev. Comput. Stat. **2**, 497 (2010)
136. D.W. Scott, Sturges' rule. Wiley Interdiscip. Rev. Comput. Stat. **1**, 303 (2009)
137. A.M. Brasil, T.L. Farias, M.G. Carvalho, A recipe for image characterization of fractal-like aggregates. J. Aerosol Sci. **30**, 1379–1389 (1999)
138. A.M. Brasil, T.L. Farias, M.G. Carvalho, Evaluation of the fractal properties of cluster-cluster aggregates. Aerosol Sci. Tech. **33**, 440–454 (2000)
139. A.M. Brasil, T.L. Farias, M.G. Carvalho, Ü.Ö. Köylü, Numerical characterization of the morphology of aggregated particles. J. Aerosol Sci. **32**, 489 (2001)
140. Ü.Ö. Köylü, G.M. Faeth, T.L. Farias, M.G. Carvalho, Fractal and projected structure properties of soot aggregates. Combust. Flame **100**, 621 (1995)
141. S. Bau, O. Witschger, F. Gensdarmes, O. Rastoix, D. Thomas, A TEM-based method as an alternative to the BET method for measuring off-line the specific surface area of nanoaerosols. Powder Technol. **200**, 190 (2010)

142. S.C. Brown, V. Boyko, G. Meyers, M. Voetz, W. Wohlleben, Toward advancing nano-object count metrology: a best practice framework. Environ. Health Perspect. **121**, 1282 (2013)
143. C. Motzkus, T. Macé, F. Gaie-Levrel, S. Ducourtieux, A. Delvallee, K. Dirscherl, V.D. Hodoroaba, I. Popov, O. Popov, I. Kuselman, K. Takahata, K. Ehara, P. Ausset, M. Maillé, N. Michielsen, S. Bondiguel, F. Gensdarmes, L. Morawska, G.R. Johnson, E.M. Faghihi, C.S. Kim, Y.H. Kim, M.C. Chu, J.A. Guardado, A. Salas, G. Capannelli, C. Costa, T. Bostrom, Å.K. Jämting, M.A. Lawn, L. Adlem, S. Vaslin-Reimann, Size characterization of airborne SiO2 nanoparticles with on-line and off-line measurement techniques: an interlaboratory comparison study. J. Nanoparticle Res. **15**, 1 (2013)
144. S.B. Rice, C. Chan, S.C. Brown, P. Eschbach, L. Han, D.S. Ensor, A.B. Stefaniak, J. Bonevich, A.E. Vladár, A.R. Hight Walker, J. Zheng, C. Starnes, A. Stromberg, J. Ye, E.A. Grulke, Particle size distributions by transmission electron microscopy: an interlaboratory comparison case study. Metrologia **50**, 663 (2013)
145. N.C. Bell, C. Minelli, J. Tompkins, M.M. Stevens, A.G. Shard, Emerging techniques for submicrometer particle sizing applied to Stober silica. Langmuir **28**, 10860 (2012)
146. W. Anderson, D. Kozak, V.A. Coleman, Å.K. Jämting, M. Trau, A comparative study of submicron particle sizing platforms: accuracy, precision and resolution analysis of polydisperse particle size distributions. J. Colloid Interface Sci. **405**, 322 (2013)

Index

F.L. Deepak et al. (eds.), *Advanced Transmission Electron Microscopy*,
DOI 10.1007/978-3-319-15177-9